THÈSE de DOCTORAT

de l'UNIVERSITÉ PARIS 7 - DENIS DIDEROT

École Doctorale: Constituants Élémentaires, Systèmes Complexes

Specialité: Champs, Particules, Matière

et

de l'UNIVERSITÀ DEGLI STUDI DI MILANO

Dottorato di Ricerca in Fisica, Astrofisica e Fisica Applicata

presentée par

Maria Elena MONZANI

CHARACTERIZATION AND CALIBRATION OF THE BOREXINO DETECTOR FOR SOLAR AND SUPERNOVA NEUTRINOS

Soutenue le 21 Janvier 2005 devant le jury composé par:

Gianpaolo BELLINI	Directeur de Thèse
Hervé DE KERRET	Directeur de Thèse
Giulio MANUZIO	Examinateur
Marco PALLAVICINI	Rapporteur
Charling TAO	Rapporteur
François VANNUCCI	Président du jury

To Mgr. Luigi Giussani,
in the 50th anniversary of
Communion and Liberation

À la mémoire de la petite Teresa

Et j'ai voulu de nouveau me serrer contre le tombeau vide, mettre ma main dans le trou de la croix, comme cet âpotre dans celui des mains et des pieds et du coeur.

Mais ma petite fille Violaine a été plus sage!

Est-ce que le but de la vie est vivre? est-ce que les pieds des enfants de Dieu sont attachés à cette terre misérable?

Il n'est pas de vivre, mais de mourir! et non point de charpentier la croix, mais d'y monter et de donner ce que nous avons en riant!

De quel prix est le monde auprès de la vie? et de quel prix la vie, sinon pour s'en servir et pour la donner?

Et pourquoi se tourmenter quand il est si simple d'obéir et que l'ordre est là?

C'est ainsi que Violaine toute prompte suit la main qui prend la sienne.

(Paul Claudel, *L'annonce fait à Marie*, Éd. Gallimard, Paris, 1940)

Acknowledgements

At the end of this work, is a great pleasure for me to acknowledge all the people that made possible the achievement of my thesis.

Fist of all, I thank my thesis advisors, Gianpaolo and Hervé, for their help and encouragement; my co-advisor, Marco, for his interest in my work and for his talk at the ISAPP School in 2004; my "unofficial" advisor, Emanuela, for the innumerable forms of help and kindness she provided me.

I thank all the Borexino members which helped me under various respects; fist of all the "on-line" people, for the wonderful experience of these three years of work: Alessandro, Andrew, Daniela, Davide D., Kevin, Marco, Olivier and Tristan; the CTF-analysis group, for the interesting discussions: Aldo, Andrea P., Barbara, Davide F., Gioacchino, Laura C., Sandra and Silvia; the PMT group, for their help during the Air-Runs: Augusto B., George, Massimo and Paolo L.; all the other members of the Borexino group in Milano (Marco G. and Sergio), Gran Sasso (Andrea I., Augusto G., Christian L., Laszlo, Ludwig, Stefano G.) and Paris (Alain, Didier, Michel and Serge); finally I thank prof. Vignaud and all the staff of the PPC Laboratory at Collège de France for their hospitality.

I thank all my friends at Gran Sasso Lab for their affection during the last five years: Alba, Carlo, Cristina, Federica, Maria, Paolo and Stefano.

I thank my parents, for their help and support: since their first visit to Gran Sasso Lab, they wondered how was it possible that their little girl liked to work in such a "peculiar" place; but nevertheless, they always provided my with comprehension and encouragement: I would not have made it, without them!

I thank Fr. Giussani, for that day of fifty years ago, when he decided to abandon teaching in the seminary of Venegono and throw himself into the fray (becoming an High School teacher): this was the first day of an adventure which reached me many years later and upset my life. I due to Fr. Giussani most of what I am now; and especially I due to him the discovery that "the unknown generates fear, the mystery generates amazement": without this experience, the scientific work would not have been possible for me. Along with him, I thank my friend Giorgio, for sharing with me the amazing experience of his life during the last three years and for accompanying me in many difficult steps.

I thank my friends Caterina, Chapeau, Fanta and Ninja, for their firm and faithful friendship: thanks to them, I experienced that whatever happens in my life is for me (and not against me). I thank all the other friends of the physics community, for several reasons that I do not list here: Benny, Cate & Marco, Marisa, Melissa, Nicola, Silvia P., Cawlo, Giovanni & Simona, Rossella, Silvia I., Caggio, Cella, Francy B., Mario, Matteo D.A., Noda, Redde, Angelo, Bolzi, Cecilia, Francy G., Samu, Simo P., Ben, Diego, Emilio, Giuliano, Paolo M., Rover, Tommy C., Tommy M., Tossico, Ciccio, Decio, Fefe, Krissy, Manu, Paola F., Ale, Ave (AZUICT), Chicco, Jack, Maria, Delo, Ire, Ivan, Jo, Moro, μ, Vale P., 2, Astea, Cheba, Jackie, Marmo, Cucciolo, Francesca and Maddalena. I also thank my "mathematician" friend Giacomo, for his affection to me (and for his frankness).

I thank all the girls I lived with during these three years: Daniela G., Elena, Laura, Marta, Valeria F. (Minù, I'm coming to see you!), Paola, Sara, Caterina, Valeria R., Viviana, Lucia, Chiara & Chiara ("appa" Grossich); Letizia, Maria Chiara, Daniela, Sara, Maria ("appa" Saldini); Daniela and Silvia ("appa" Jenner); Luciana ("appa" Scarlatti). I am grateful to all of them, for their infinite patience with me, and for taking care of all I could need (food, sleep, holidays, encouragement...). I also thank the "appa" Lombardia boys, for hosting me during the long weekends and nights when I was writing my thesis.

I thank all my friends in L'Aquila (and surroundings): Alessia & Gabbriele, Angelo (I'm waiting for you in Milano!), Antonella, Ercole, Federica & Fabbio, Giorgio, Graziella & Matteo (and Giovanni), Marco, Marta & Paolo, Mimmo, Mirko, Peppe, Stefano (good luck for your new life in Trento!), Valentina and Vincenzo.

I thank all my friends in Paris ("et environs"): Aña G., Anna C., Cécile, Claudia & Jeff (and my little sister, Laetitia), Daniel, Isabelle, Marco F., Meriem, Paulo; Agnese, Ambrogio, Delphine D., Eric W., François B., Katja, Ilaria P., Ilaria R., Lele, Luca S., Marta, Mauro B., Mauro Z., Mimmo, Pasha, Violaine; Alessandra & Silvio (and my favorite nightmare, Matteo), Chiara B., Chiara N., Corentin, Delphine J., Dino, Elena M., Elo & Mirco, Ezio & Rosella, Geneviève & Paul (and Madeleine), Giovanni D., Irene M., Ivanah, Jerôme, Julie C., Julie F., Laura & Paolo, Laurence, Luca, Ludovic, Pauline S., Peter, Tina & Lionel. I thank them all, because they succeeded in making me to feel at home: and what in principle could be a bad luck, become a wonderful adventure. I also thank all the people who went and see us: Davide, Widmer, Desa, Francesco, Maria, Michael, Pippo (I'll never forget your songs during that lunch at the Latin Quartier!), Benny, Francy, Giovanni, Ilaria and Martina.

Finally, I want to remember two people, who left me very early and that I miss so much. The first one was my first master, Roberto: even if he never understood why a "resonable" person like me could abandon my piano studies to enter the physics faculty, he was always very proud of me: I hope he is still very proud of me now! The second one was a little baby, Teresa: she left me well before I had time to love her; but nevertheless she took the time to teach me that the accomplishment of my life does not rely on what I can realize, but on what I belong to. Along with Teresa, I thank her mother, Marta, and all of them who were with me since the beginning of the whole story: Giovanni, Francesca, Matteo, Paolo, Simona and Valentina.

Contents

Introduction

Since the detection of the first neutrinos from the sun in 1967, the physics of solar neutrinos has been one of the most exciting fields of the entire scientific domain. During the last 40 years, thousands of physicists, chemists, astronomers and engineers have produced an amazing community effort to improve nuclear physics, astrophysics and detectors, so that the subject could become a precision test of stellar evolution and of the weak interaction theory. Although in the last six years our understanding of the neutrino properties has been greatly improved thanks to the results of the Super-Kamiokande and SNO experiments [49, 2], 99% of the solar neutrino spectrum lies in a mostly unexplored region, because no measurement on solar neutrinos has ever been performed by a real time detector with the sub-MeV sensitivity.

The Borexino experiment (presently in its final installation phase at the Gran Sasso Laboratories, Italy) has been designed and built in order to explore the sub-MeV region of the solar neutrino spectrum, namely the monochromatic ^8Be line at $860keV$ (9% of the total solar flux). This measurement represents a real experimental challenge, because it requires extremely low radioactivity levels for all the detector components, with contamination values which have never been reached before.

The Borexino detector is composed of 300 t of liquid scintillator, observed by an array of 2212 photomultipliers. The complete detector is designed in order to reduce γ-ray background in the core via a graded shielding, made of different layers of increasingly radio-pure materials.

^7Be solar neutrino detection is the main goal of Borexino, but the detector can be used to study neutrinos (or anti-neutrinos) from other sources, namely anti-neutrinos from the Earth interior (or from nuclear power reactor), and neutrinos and anti-neutrinos from Supernova explosions.

In this thesis, the characterization and calibration of the Borexino detector has been performed, both for sub-MeV solar neutrino detection, and for detection of neutrinos from other sources; a particular attention has been devoted to the high energy neutrinos emitted during Supernova events, because the reconstruction of their energy spectrum and arrival time requires the use of special tools.

The extremely low radioactivity levels required for Borexino have been reached for the first time in 1995, when a prototype of the detector (Counting Test Facility) was built to detect contamination levels as low as 10^{-16} g/g, for U an Th radioactive isotopes in the scintillator.

The CTF data taking has been resumed in 2000 (after a detector upgrade), for the final qualification of the Borexino components. In particular, a measurement campaign concerning the scintillator quality has been performed: during this campaign, several purification methods have been tested on the scintillator and showed encouraging results. In this thesis, a detailed data analysis of the different purification tests is presented, concerning the effectiveness of the methods in removing from the scintillator the most dangerous contaminants for Borexino. Besides that, some supplementary results on scintillator characterization are described: namely, the study of the pulse shape discrimination capabilities of a large scintillation detector such as the CTF.

The aim of this thesis has been to study the whole detector capabilities, and to operate it at the performance level demanded by physics. The neutrino signal identification in a wide energy range and the ^{7}Be neutrino flux measurement, require a precise energy and position reconstruction and an accurate detector stability monitor.

During the last three years, the Borexino read-out system has been installed, completed and fully tested: my personal work concerned many aspects of this finalization procedure, as listed below.

First of all, a complete Data Base of the experiment has been designed and implemented, containing all the relevant informations of the detector, from the PMT layout and electronics configuration to the fluid handling parameters and scintillator properties; the stored informations will be essential to reconstruct and interpret all the Borexino data.

After the installation of phototubes and electronics, the full system has been tested in realistic operation conditions, performing real runs, with the detector empty (the so-called “Air-Runs”). During these tests, several run conditions were applied, in order to test different sub-sets of the system.

First of all, the generation of pure electronics events (produced by pulsing directly the channels) allowed a global study of the electronics performances, as well as an accurate debugging on a single channel basis. With these events, it was possible to find out and solve both a problem on the digital boards (concerning the time measurement of the single hit) and a problem on the analog boards (concerning the charge measurement). Several pure dark noise runs were also acquired, allowing an accurate test of the photomultipliers.

For stability monitor purpose, a calibration system was designed for the Borexino PMTs, allowing to keep under control the working conditions of the phototubes and of the electronics chain: an extensive test of this system was performed as well. The synchronous pulses delivered by the calibration system allowed an accurate test of the time measurement precision of our read-out system, along with an estimation of the final time resolution of the detector. Furthermore, the illumination conditions of the PMTs being adjustable, the laser events allowed an estimation of the dynamical range of our electronics.

Several tests have been also performed through the insertion of some radioactive sources in the Borexino sphere. These sources were made up of some small samples of ^{222}Rn loaded scintillator, therefore these measurements represented a realistic test of our read-out system, in operating conditions. The behavior of our entire read-out chain was analyzed, showing very good global performances. In particular, the energy and position reconstruction capabilities of the detector have been evaluated, demonstrating that the system is ready and operational for Borexino data taking.

Besides the standard “solar neutrino” read-out system, a second electronics chain has been designed and installed in Borexino, with the specific aim to provide further informations on the high energy range up to the 10 MeV region and beyond. The target of this high energy electronics is the detection of: the anti-neutrinos from the Earth interior and from the nuclear reactors, the ^8B solar neutrino spectrum, the neutrino and anti-neutrino reactions from a Supernova event.

This further read-out system has also been tested during the Borexino “Air-Runs”, both with laser and radioactive source data. The results of these tests showed the very good general behavior of the system, and its finalization is underway, especially concerning the adjustment of the dynamical range of the boards.

In the first chapter of this thesis, the solar neutrino physics is introduced; in chapter 2, are described the physics goals and the detector design of the Borexino experiment, while the detection possibilities concerning non-solar neutrino physics are explained in chapter 3. In chapter 4, the Counting Test Facility is described, with particular emphasis on scintillator characterization.

The Borexino read-out system is delineated in chapter 5, while the main tests results of the read-out chain are reported in chapter 6. In chapter 7, are sketched the features of the PMT laser calibration system, along with the calibration system test results. Finally, in chapter 8 is described the high energy electronics, with the respective test results.

Chapter 1

Solar Neutrino Physics in 2004

The physics framework of the Borexino experiment is the experimental research on solar neutrinos. Many experiments have been realized in that field during the last 40 years; some of these experiments are now mentioned among the milestones of the elementary particle physics and have opened a “New Window on the Universe”, as documented in the Press Release of the 2002 Nobel Prize in Physics (awarded to Raymond Davis Jr and Masatoshi Koshiba “for pioneering contributions to astrophysics, in particular for the detection of cosmic neutrinos” [79]).

These “historical” experiments (before 1999) have provided several measurements of the flux of neutrinos coming from the sun; their common result is a deficit in neutrino fluxes, if compared to the predictions of the Standard Solar Model: this fact is known as *solar neutrino problem*. This problem has been for more then 30 years one of the major concerns of the physicists, both in theoretical and in experimental field; the final solution of such a *puzzle* has recently been proved to rely on the propagation mechanism of neutrinos, especially inside the matter [49, 2, 3, 40] (the so-called oscillation mechanism will be described in section 1.3).

The study of a so long-standing problem has induced a deep investigation of the reliability of solar and particle physics models (especially, the Solar Standard Model and the Standard Model of Electro-Weak Interaction have been carefully reviewed), since the solution of the *solar neutrino problem* could in principle rely both on the neutrino production mechanism (solar astrophysics) or on the neutrino propagation properties (particle physics). On the other hand, both fields took great advantages from the studies on solar neutrinos: in astrophysics, neutrino experiments allowed a direct verification of the theories on the stellar evolution and on the nuclear origin of the stellar energy (it is useful to remind that neutrinos are the only probe which allow the direct observation of the sun core); in particle physics, solar neutrino experiments can be used (and have effectively been used, like in [2, 3]) to determine non-standard properties of neutrinos themselves, like the non-conservation of the leptonic number and the introduction of a non-zero mass term.

In this chapter, we will first illustrate the Standard Solar Model, and its predictions on solar neutrino fluxes; then we will describe the results of the first experiments on solar neutrinos, explaining the details of the *solar neutrino problem*; we will explore the possible solutions to the problem, both in the astrophysics and particle physics fields; finally we will describe the experiments which helped in finding out the present solution (including experiments on atmospheric and reactor neutrinos): this last section will allow us to outline the experimental framework of Borexino.

1.1 The Standard Solar Model (SSM)

The interpretation of solar neutrino experiments relies on a theoretical model of the Sun which predicts the neutrino fluxes, along with their spectral composition (since the energy of emitted neutrinos depends on the particular reaction that produces them, the spectral distribution is a crucial point of solar models).

The most commonly accepted solar model (SSM) [82] is built up according to the following assumptions:

- **Hydrostatic Equilibrium:** the gravity force inside the star is supposed to be balanced by the outward pressure of the particle gas; such an assumption is mandatory in the model, because any deviation from the hydrostatic equilibrium condition would rapidly lead to the collapse or to the explosion of the star;

- **Thermal Equilibrium:** the net energy flux through each layer in the stellar core is balanced by the energy production due to the nuclear reactions; on the contrary of the thermal equilibrium, the hydrostatic one can be violated for long periods during the life of the star: during these phases, energetic equilibrium is granted by the gravitational energy, through contractions and expansions of the star;

- **Radiative Equilibrium:** the total luminosity of the star does not depend on the particular mechanism of energy production, but only on the temperature gradient between the layers of the star; the outward energy flux is mainly due to radiative transport, that is to photons diffusion: for this reason, the opacity of stellar medium is one of the critical parameters of computations;

- **Convective Equilibrium:** whenever the radiative equilibrium is not stable, convective motions are generated inside the star, which allow the reduction of temperature gradients inside the single layers; these convective motions provide, on the other hand, an effective mixing of the material inside each convective zone: this mechanism produces then a chemical homogeneity on a macroscopic scale;

- **Only nuclear reactions can provide a modification in isotopic abundances:** the Sun is supposed to be chemically homogeneous at its formation time; this means that inside the zones not affected by convective mixing, local changes in abundances can be produced only by nuclear reactions.

The SSM is the iterative resolution of a set of state equations (namely the equations describing the above mentioned equilibrium conditions), with well defined boundary conditions, such as the present mass, total luminosity, radius and age of the Sun:

- Mass: $M_\odot = 1.99 \cdot 10^{33}\ g$
- Luminosity: $L_\odot = 3.844 \cdot 10^{33}\ erg/sec$
- Radius: $R_\odot = 6.96 \cdot 10^{10}\ cm$
- Age: $t_\odot = 4.57 \cdot 10^{9}\ y$

As already mentioned, the thermal equilibrium of the Sun is granted by the energy produced in nuclear reactions. The main reactions (98% of the total energy) belong to the proton-proton ($p-p$) chain in figure 1.1; its energy balance gives:

$$4p \longrightarrow {}^4He + 2e^+ + 2\nu_e + 26.03\ MeV\ . \tag{1.1}$$

The 3% of the released energy is transformed into neutrinos kinetic energy.

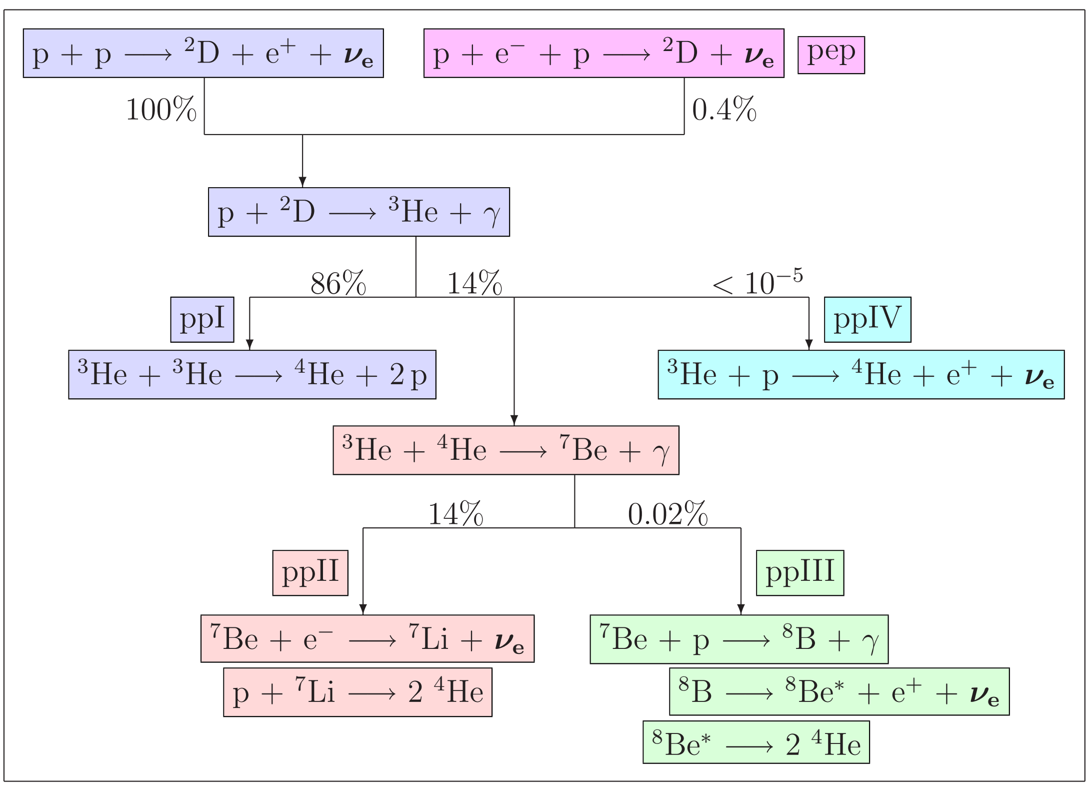

Figure 1.1: The proton-proton chains.

The second chain, hypothesized by Bethe in 1939, is the Carbon-Nitrogen-Oxygen cycle (CNO), in fig. 1.1: the energy balance is similar to the previous one, but is mediated by the ^{12}C:

$$4p \rightarrow {}^4He + 2e^+ + 2\nu_e + 25.3\ MeV\ . \tag{1.2}$$

The slightly lower energy gain in this second cycle is due to the major contribution to neutrinos kinetic energy. Most of the solar models assume the CNO cycle to contribute only marginally to the luminosity of our star: this assumption is confirmed by the study of isotopic abundances inside the Sun (isotopic abundances are extrapolated from stellar atmosphere composition, which can be observed directly) and, more recently, from precise measurements of solar neutrino fluxes [21].

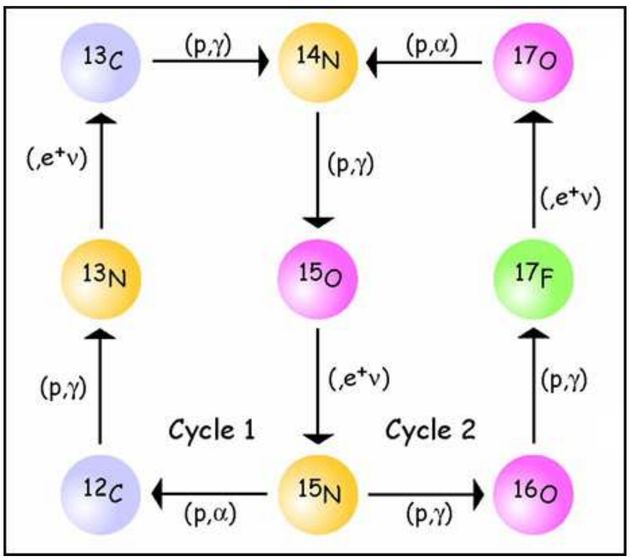

Figure 1.2: The CNO cycles.

1.1.1 Solar neutrino fluxes

As will be described later, several successful predictions have been inferred from the SSM: among them, we can recall the mass-luminosity relationship, the *Hertsprung-Russell diagram* explanation in evolutionary terms, as well as an amazing agreement with Helioseismological measurements (see 1.2.3). The most famous model is the *Bahcall-Pinsonneault* (B-P) one; the main features of this model are described in [24]: we only recall that it includes diffusion for Helium and heavy elements and that it takes into account all new measurements on input parameters like medium opacity[1].

[1] Other solar models, like the one described in [85, 86], give similar results, concerning both the neutrino fluxes calculations and the agreement with helioseismological measurements (see section 1.2.3).

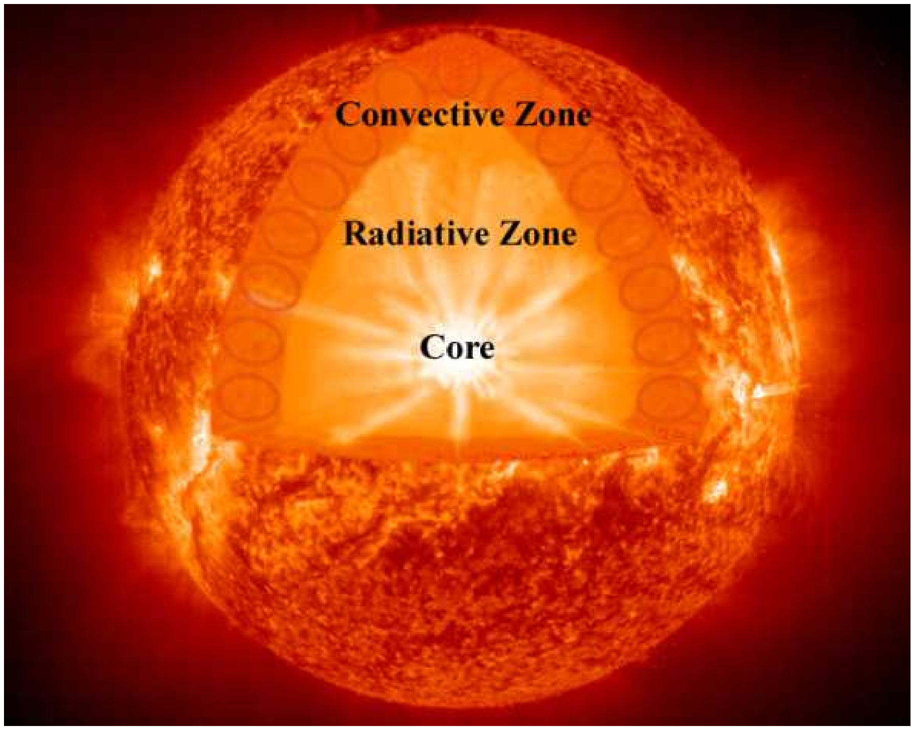

Figure 1.3: A cross section of the sun, where core and convective zone are shown.

The Bahcall-Pinsonneault model is commonly used for solar neutrino fluxes computations; a rough estimate of such a flux can be obtained as follows:

- the Sun is supposed to be in an equilibrium state: the produced thermal energy is then equal to the energy irradiated from the surface;
- the solar energy flux reaching our planet is:

$$S = 8.5{\times}10^{11}\ MeV cm^{-2} s^{-1};$$

- each 13 MeV of produced thermal energy, a neutrino is emitted[2];
- therefore, the approximate neutrino flux is:

$$\Phi_\nu = S/13 = 6{\times}10^{10}\ \nu_e\ cm^{-2} s^{-1}. \tag{1.3}$$

The Bahcall-Pinsonneault model allows the calculation of spectral shape of the solar neutrino flux [23], as shown in fig. 1.4; in table 1.1 neutrino fluxes are listed with their errors (due to all uncertainties on input parameters) [23].

[2]This assumption explains why the Sun luminosity constraint infers the total neutrino flux and not the $p-p$ one [19].

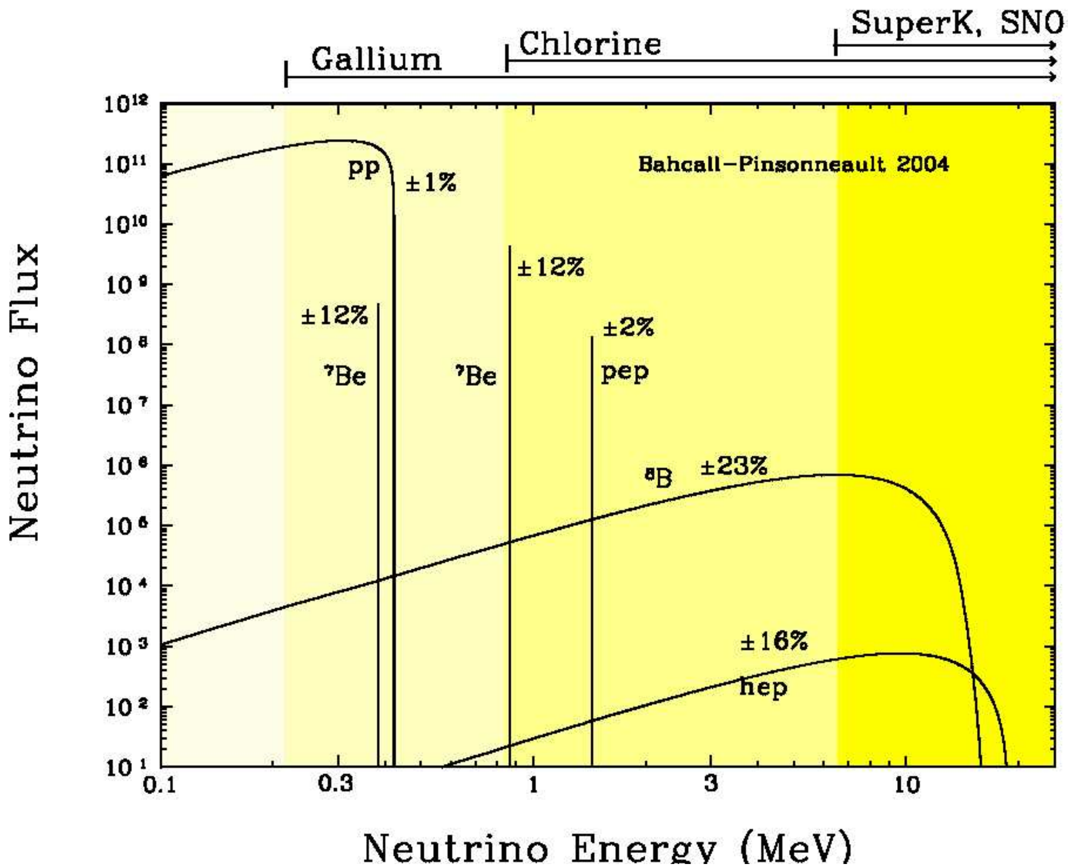

Figure 1.4: Solar neutrino spectrum for the $p-p$ chain reactions.

Source	$E_\nu(MeV)$	Flux ($10^{10}cm^{-2}s^{-1}$)
pp	$0 \to 0.42$	$5.94 \times 10^0(1 \pm 0.01)$
pep	1.44	$1.40 \times 10^{-2}(1 \pm 0.02)$
hep	$0 \to 18.8$	$7.88 \times 10^{-7}(1 \pm 0.16)$
^7Be	0.86(90%) 0.38(10%)	$4,86 \times 10^{-1}(1 \pm 0.12)$
^8B	$0 \to 14.06$	$5.79 \times 10^{-4}(1 \pm 0.23)$
^{13}N	$0 \to 1.7$	$5.71 \times 10^{-2}(1^{+0.37}_{-0.35})$
^{15}O	$0 \to 1.2$	$5.03 \times 10^{-2}(1^{+0.43}_{-0.39})$
^{17}F	$0 \to 1.7$	$5.91 \times 10^{-4}(1 \pm 0.44)$

Table 1.1: Expected fluxes for solar neutrino sources, with all uncertainties.

1.2 The solar neutrino problem before 2001

1.2.1 Radiochemical and water Čerenkov experiments

Before 2001, the solar neutrino flux had been measured by five experiments: three radiochemical experiments (Homestake, Gallex and Sage) and two water Čerenkov experiments (Kamiokande and Super-Kamiokande). Before describing the details of each experiment, it is useful to remark that the realization of each of them constitutes a big technological challenge: since solar neutrinos have a very small interaction cross section ($\simeq 10^{-44} \div 10^{-43}\ cm^2$), a huge target volume ($> 100\ t$) has to be built in each detector, in order to get a reasonable signal/background ratio; furthermore, all the background has to be dramatically reduced, concerning natural radioactivity of employed materials and cosmic rays induced background (for this reason, solar neutrino experiments are located underground, inside tunnels or mines, under thick rock layers).

- **Homestake**: the first solar neutrino experiment was installed in the late 60's in the Homestake gold mine (South Dakota), at a depth of 4200 meters of water equivalent (*mwe*) [39, 38]; the original concept of the Homestake detector was designed by Ray Davis, acknowledged for this work with the 2002 Nobel Prize in Physics [79]. Detector target is made of $2.2{\times}10^{30}$ ^{37}Cl atoms, in the form of 615 t of tetrachloroethylene (C_2Cl_4); neutrino detection interaction is:

  $$\nu_e +^{37} Cl \rightarrow e^- +^{37} Ar. \tag{1.4}$$

  This reaction has an energy threshold of 0.814 MeV, therefore it is sensitive to ^8B and ^7Be neutrinos, but not to the $p-p$ ones; moreover, this reaction is a charged current mediated interaction, then is only sensitive to electron neutrinos.

  The experiment is radiochemistry based: ^{37}Ar atoms are periodically extracted (^{37}Ar decays back into ^{37}Cl, with the emission of Auger electrons; mean life of ^{37}Ar is 35 days); then they are inserted in low background proportional counters and observed during 250 to 400 days (7 to 11 mean lives).

  The result for solar neutrino flux (after 25 years of runs) is [24]:

  $$(2.56 \pm 0.23)\ SNU^3$$

  to be compared with the SSM prediction [23]:

  $$(8.5 \pm 1.8)\ SNU$$

  (the 77% and 14% of this flux are due to the ^8B and ^7Be neutrinos respectively, while the contribution of *pep* and CNO neutrinos is lower then 1 SNU).

- **GALLEX and SAGE:** both experiments are based on the reaction

  $$\nu_e +^{71} Ga \rightarrow e^- +^{71} Ge^*$$

[3] 1 $SNU = 10^{-36}$ interactions per target atom per second;

featuring a very low energy threshold ($0.2332\ MeV$); this threshold allows to detect neutrinos produced in the first reaction of the solar chain, the $p-p$ fusion (accounting for 91% of the total solar neutrino flux).

The **GALLEX** experiment was located underground at Gran Sasso National Laboratories (LNGS, Italy), at 1400 m rock depth (3800 mwe); detector target is composed of 30.3 t of dissolved Gallium, in the form of 60 m^3 of $GaCl_3$. Germanium atoms produced in the reaction are chemically extracted every $\sim$ 30 days ($\tau_{Ge} = 16.4\ d$); their activity is then measured with the same method as the Homestake experiment.

The final measured flux (after 6 years of GALLEX, 1991-1997) is [58]:

$$(77.5 \pm 6.2(stat)\ ^{+4.5}_{-4.3}(syst))\ SNU.$$

The B-P model foresees the following neutrino rate, for a Ga experiment [23]:

$$(131\ ^{+12}_{-10})\ SNU,$$

with a partial contribution of 60% from the $p-p$ reaction, and of 29% from ^7Be.

The GALLEX collaboration, in order to demonstrate the reliability and the precision of their results, performed a set of calibration runs using two very strong (and calibrated) neutrino sources ($> 60\ PBq$ of ^{51}Cr); the combined result for 1994 and 1996 runs can be expressed in terms of the ratio between the neutrino source strength (derived from the measured rate of ^{71}Ge production, divided by the directly determined source strength; this combined ratio (for the two source experiments) is [59]:

$$0.93 \pm 0.08,$$

which shows that the $> 40\%$ deficit of solar neutrino flux observed by GALLEX cannot be attributed to experimental artifacts.

GALLEX was concluded in 1997; after a complete reconstruction of proportional counters and related electronics, the experiment was restarted in 1998 with the name of GNO (GNO was definitively closed in 2003). The combined neutrino flux measured in GALLEX/GNO, for the period from 1991 to 2003, is [36]:

$$(69.3 \pm 4.1(stat) \pm 3.6(syst))\ SNU.$$

The **SAGE** experiment is located in Baksan underground Laboratory (4700 mwe) in the Northern Caucasus Mountains; the target volume are 50 t of Gallium in metallic state [1]. The average measured flux (during the period from 1990 to 2003) is [36]:

$$(66.9\ ^{+3.9}_{-3.8}(stat)\ ^{+3.6}_{-3.2}(syst))\ SNU.$$

The ratios between measured and expected fluxes in Ga experiments are then:

GALLEX/GNO	$(52.9 \pm 6.4)\%$
SAGE	$(51.1 \pm 6.2)\%$

- **Kamiokande:** it was located in the Kamioka mine (Japan), at 2700 *mwe* depth; neutrinos are detected through the Čerenkov light produced in the scattering reaction $(\nu_x + e^- \rightarrow \nu_x + e^-)$ on the electrons of the 680 t of ultra-pure water which compose the fiducial volume; light is detected by means of 948 photomultipliers (with a 20 inch photocathode). The energy threshold of this experiment is 7.5 MeV: this threshold is not due to the physics of the scattering process, but to the necessity to remove background events produced by natural radioactivity of materials (mainly water). Because of this threshold, only ^8B neutrinos can be detected. Thanks to the scattering process, also non-electronics neutrinos can be detected (with a cross section of $\sim 1/6$ of the electron one).

  Kamiokande has been the first experiment *in real time*, namely capable to identify and reconstruct single events; for this reason, the detector was able to measure not only the total neutrino flux, but also the direction and energy of neutrinos[4]. In this way, the solar origin of neutrinos was demonstrated for the first time, since electrons are mainly scattered along the Sun-Earth vector (see figure 1.5).

  Published results [47] report a measured ^8B neutrino flux of:

  $$(2.80 \pm 0.19(stat) \pm 0.33(syst)) \times 10^6 cm^{-2} s^{-1},$$

  which is $(48 \pm 12 \pm 13)\%$ of the standard solar models.

  The Kamiokande detector was also the first one capable to detect supernova neutrinos in 1987 (see chapter 2); for this reason (as well as for solar neutrino observation), Kamiokande spokesperson Masatoshi Koshiba was awarded of the Nobel Prize in Physics in 2002 [79].

- **Super-Kamiokande:** this experiment is an enlargement of the Kamiokande concept, with bigger dimensions (50000 t of water, 22500 t of which are fiducial volume, observed by 11146 20 inch PMTs) and a lower threshold (5 MeV).

  Super-Kamiokande phase I started in May 1996 and finished in July 2001[5]; ^8B solar neutrino flux observed during 1496 days of live time is [64]:

  $$(2.35 \pm 0.02(stat) \pm 0.08(syst)) \times 10^6\ cm^{-2} s^{-1}.$$

[4] Čerenkov detector measure the energy of each scattered electron, reconstructing then energy and direction of the incoming neutrinos.

[5] In July 2001, during some routine maintenance jobs, detector underwent a big accident: approximately 50% of PMTs imploded during a water filling of the detector; after a re-positioning of the 5182 survived PMTs, the experiment was restarted in December 2002 with the so-called phase II (data taking will continue until autumn 2005; the upgrade of the detector to the original PMT coverage is foreseen in 2006).

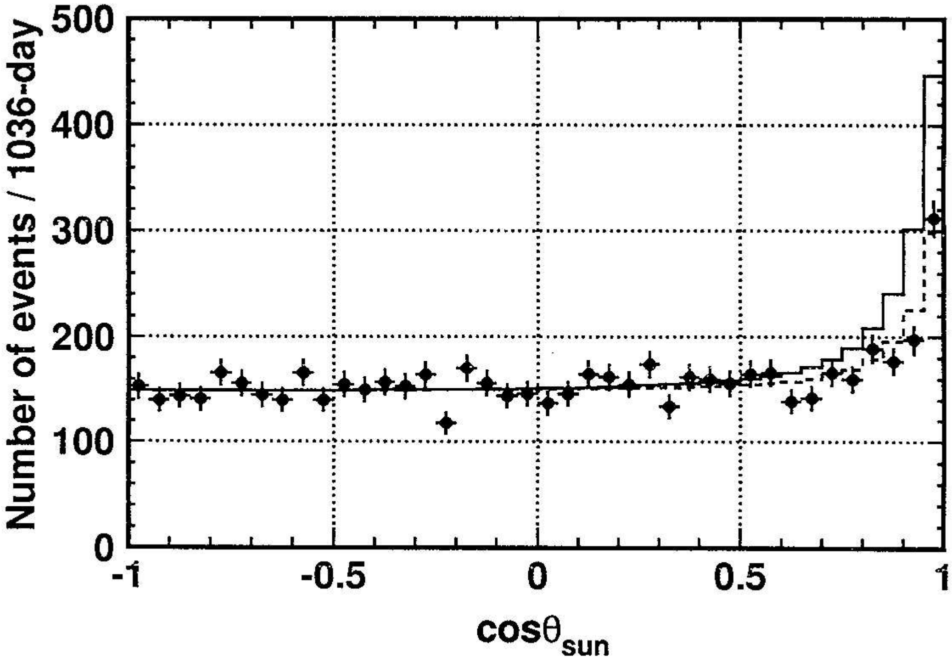

Figure 1.5: Angular distribution of Kamiokande data; the solid line shows the prediction from SSM and the dashed line shows the best fit to the data, assuming a flat background in the distribution [47].

This value is in agreement with the Kamiokande one (with smaller errors) and represents $(40.6 \pm 9.3 \pm 9.4)\%$ of the predicted standard flux.

Due to its real time capability, Super-Kamiokande has been the first experiment able to measure precisely day/night effects (expected from neutrino oscillations in matter) and annual modulations (see figure 1.6) of the solar neutrino flux (produced by the eccentricity of the Earth's orbit), as well as the ^8B spectral shape: all these informations are now used in the global solar neutrino oscillations analysis (see section 1.4).

In 1998, the Super-Kamiokande collaboration obtained the first evidence for neutrino oscillations, through the observation of atmospheric neutrinos [49]; these results will be explained in section 1.4.

1.2.2 Data analysis: three neutrino problems

In table 1.2 are reported the comparisons between solar neutrino experiments results and SSM predictions. The measured solar neutrino fluxes are always lower than the predictions: the discrepancy between the predicted and the measured rates is beyond the uncertainties.

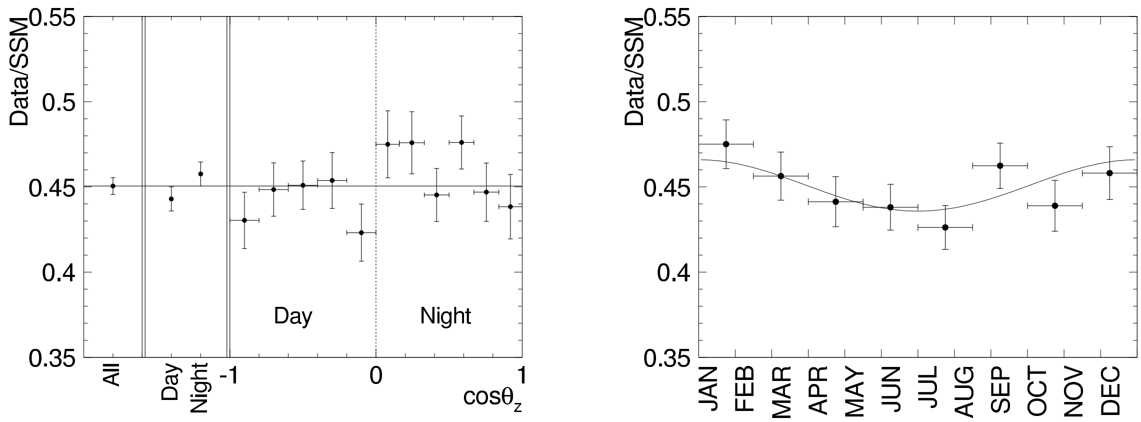

Figure 1.6: Left: the solar zenith angle (θ_z) dependence of the solar neutrino flux in Super-Kamiokande (error bars show statistical error only); the horizontal line shows the flux for all data. Right: seasonal variation of the solar neutrino flux; the curve shows the expected seasonal variation of the flux introduced by the eccentricity of the Earth's orbit (error bars show statistical error only); figures are taken from [51].

Experiment	Observed Flux	Expected Flux [23]	Obs./Expected
Homestake $^{37}Cl(\nu_e, e^-)^{37}Ar$ $E_{th} = 0.81 MeV$	(2.56 ± 0.23) SNU	(8.5 ± 1.8) SNU	(30.1 ± 6.9) %
Gallex $^{71}Ga(\nu_e, e^-)^{71}Ge$ $E_{th} = 0.23 MeV$	$(69.3 \pm 4.1 \pm 3.6)$ SNU	$(131\ ^{+12}_{-10})$ SNU	(52.9 ± 6.4) %
Sage $^{71}Ga(\nu_e, e^-)^{71}Ge$ $E_{th} = 0.23 MeV$	$(66.9\ ^{+3.9}_{-3.8}\ ^{+3.6}_{-3.2})$ SNU	$(131\ ^{+12}_{-10})$ SNU	(51.1 ± 6.2) %
Kamiokande $e^-(\nu_x, \nu_x)e^-$ $E_{th} = 7.5 MeV$	$(2.80 \pm 0.19 \pm 0.33)$ $\times 10^6 cm^{-2} s^{-1}$	(5.79 ± 1.33) $\times 10^6 cm^{-2} s^{-1}$	(48 ± 13) %
Super-Kamiokande $e^-(\nu_x, \nu_x)e^-$ $E_{th} = 5 MeV$	$(2.35 \pm 0.02 \pm 0.08)$ $\times 10^6 cm^{-2} s^{-1}$	(5.79 ± 1.33) $\times 10^6 cm^{-2} s^{-1}$	(40.6 ± 9.4) %

Table 1.2: Summary of measured and expected fluxes in solar neutrino experiments.

Actually, a deeper analysis of the results [18] leads to three different "solar neutrino problems" (see figure 1.7):

1. **calculated versus observed neutrino rates:** the difference (by a factor of three or more) between the chlorine measurement of Ray Davis and the

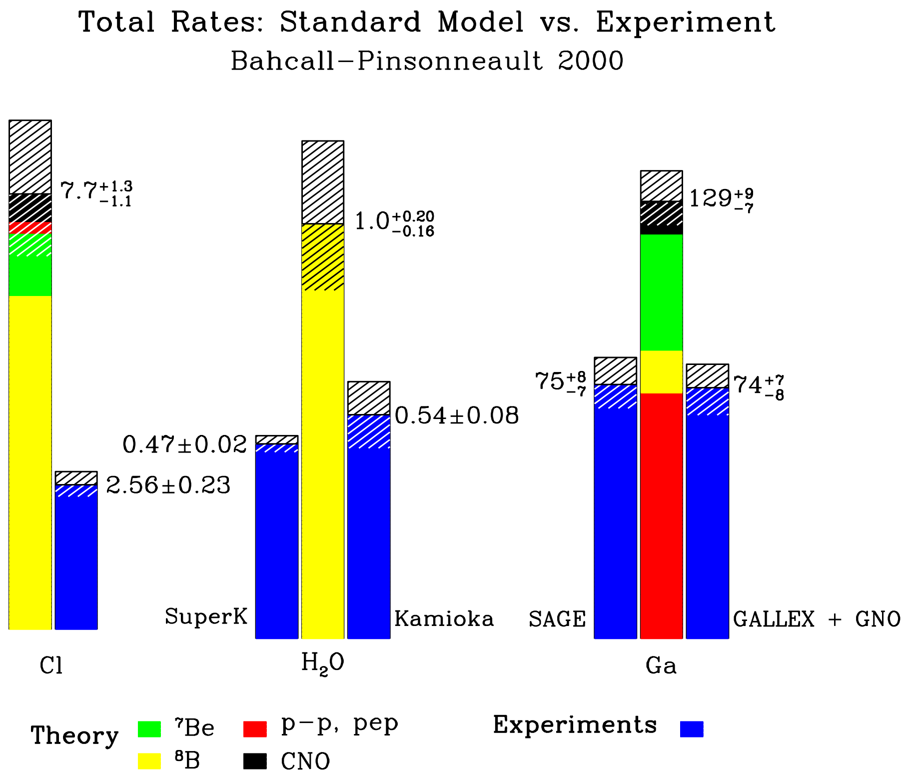

Figure 1.7: Comparison between calculated and observed neutrino rates in 2000 [24].

standard solar model prediction has been the only solar neutrino problem for two decades. The problem was strengthened at the beginning of the 1990s by the measurement by the Kamiokande experiment: in this case, the discrepancy is approximately a factor of two. The difference in absolute rates is the first "solar neutrino problem";

2. **incompatibility between Chlorine and Kamiokande experiments:** in 1990 a second solar neutrino problem was pointed out, namely, the rate of just the ^8B neutrinos observed in Kamiokande exceeds the total measured rate in the chlorine experiment if the energy spectrum of the solar neutrinos is not changed by new neutrino physics. This problem is exacerbated by the fact that significant contributions are also expected in the chlorine experiment from ^7Be and CNO neutrinos (the predicted rate from the ^7Be neutrinos is well determined, especially since the related ^8B neutrinos are observed to be depleted only by a factor of two);

3. **Gallium experiments: no room for ^7Be neutrinos:** the GALLEX and

SAGE experiments present the third, essentially independent solar neutrino problem. The total observed rate is accounted for by the *pp* neutrinos, whose flux can be calculated to an accuracy of 1%; therefore, the gallium experiments do not leave any room for the reliably calculated ^7Be neutrinos (this is the reason why the third solar neutrino problem is sometimes referred to as "the problem of the missing ^7Be neutrinos"). Moreover, both the GALLEX and SAGE experiments have been directly calibrated with a radioactive source (^{51}Cr) that emits neutrinos with similar energies to the ^7Be neutrinos.

The "problem of the missing ^7Be neutrinos" was the first hint that the solution of the puzzle should have a physical (not astrophysical) nature; actually, the ^7Be neutrinos suppression cannot be explained by modification of solar models, since the ^8B neutrinos detected in Kamiokande are produced in a competitive reaction with the missing ^7Be neutrinos, but solar model explanations that reduce the predicted ^7Be flux reduce much more the predictions for the observed ^8B flux. For this reason, an independent measurement of the ^7Be neutrino flux appeared strategic since 1990, in order to demonstrate the physical origin of the solar neutrino problems: the main purpose of the Borexino experiment is indeed a measurement of ^7Be neutrinos.

1.2.3 Astrophysical solutions

Since the publication of the first Homestake results, a big improvement of the solar models took place in order to calculate more accurately solar neutrino fluxes: in this way, a deep understanding of solar fluxes was obtained; the theoretical models have gradually been refined as improved input data, more accurate physics description and more precise numerical techniques have been employed. In the meanwhile, there have been many studies of "non-standard" solar models that were designed to "solve" the solar neutrino problem: some of these models adopt different input parameters (such as the metallicity of the sun or the radius of the convective zone), some other use different values for nuclear cross sections (for example, cross section of the process $^3He +^4 He \to^7 Be + \gamma$ is set to zero in one of these models), some hypothesize an artificially mixed sun core or suppress diffusion for helium and heavy elements [24].

None of these models succeeded in solving the puzzle; moreover, they show a big disagreement with helioseismological measurements. Helioseismology studies oscillatory phenomena that occur inside the sun (and that can be observed on its surface), in order to make accurate determinations of quantities such as: the interior sound speeds, the density profile, the interior rotational speed, the depth of the convective zone, the helium abundance and the heavy-element to hydrogen ratio in the convective zone, and even the radius of the sun. Opacity calculations and equation of state calculations can be therefore tested and improved by comparing theory with observation of solar eigenfrequencies.

In figure 1.8, is shown the excellent agreement between the measured sound speeds and the SSM computed ones, in the range from 0.05 $R_\odot$ to 0.95 $R_\odot$ (the

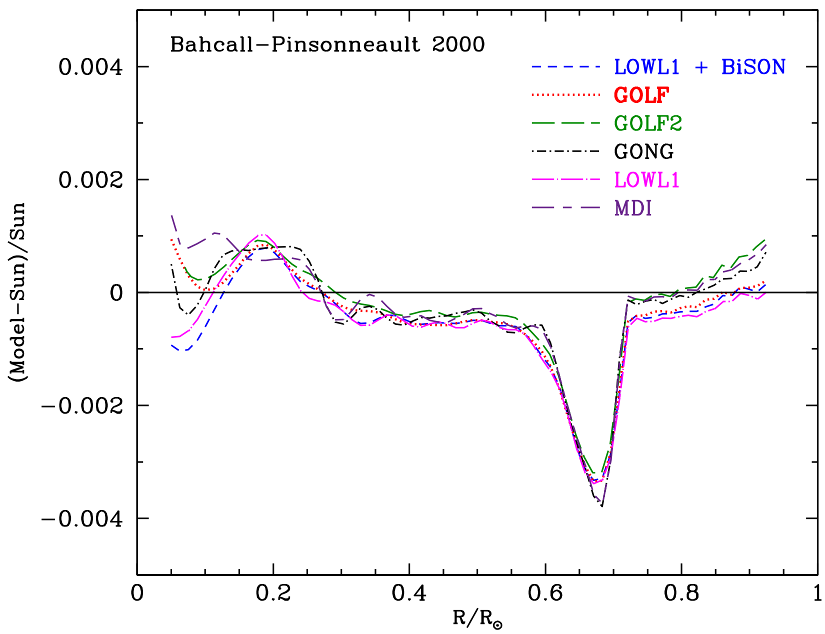

Figure 1.8: Comparison between the sound speeds computed in solar model and the ones measured in six helioseismological experiments [24].

fractional difference is actually shown, as a function of the radial position in the sun). In figure 1.9, the error on sound speed predictions is instead compared with the error bound on neutrino measurements: the picture is basically identical to the previous one, but the vertical scale has been enlarged in order to point out that the relative error is much smaller then the needed variations in the model (between 0.3 and 0.8), which could justify the observed neutrino fluxes (the arrow marked "^7Be lowered" indicates the variation needed for a 1σ compatibility with Gallium experiments).

All these consideration about helioseismological measurements have to be summed to the ones reported in the previous paragraph, namely to the impossibility to fit all the neutrino experiments in the different regions of the sun spectrum with some adjustment of the solar model parameters; therefore, a reasonable conclusion should be to rely on the SSM, focusing on the neutrino propagation mechanism for finding out a viable solution for the solar neutrino puzzle.

1.3 Neutrino oscillations

The solution of the solar neutrino problem relies on the attribution of non conventional properties to neutrino particles. In this paragraph, the main features of "non standard" neutrinos will be described.

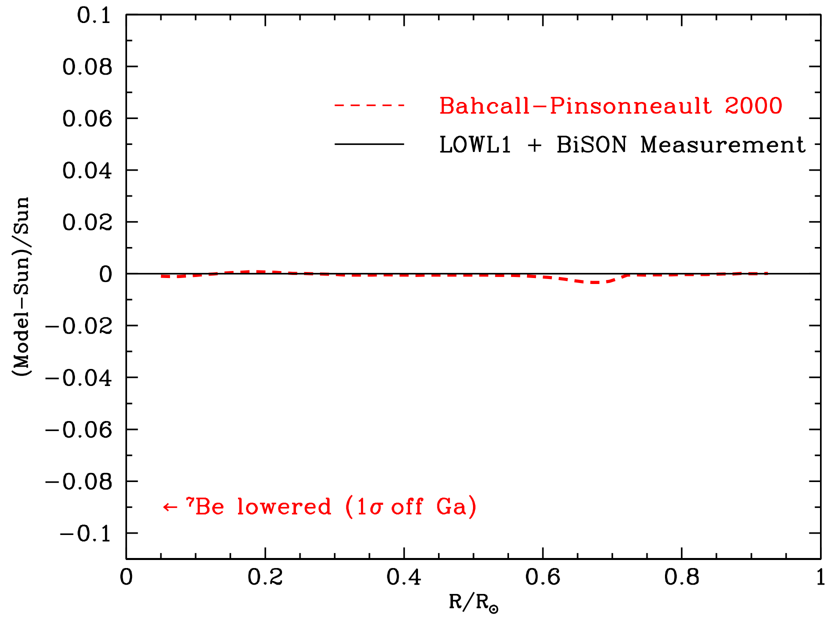

Figure 1.9: The difference between computed and measured sound speeds, compared to the 1σ compatibility region with Gallium experiments [24].

1.3.1 Neutrino masses

In the framework of the Standard Model of the Electro-Weak Interactions (SM)[6], the neutrino is described as a stable elementary particle, with spin 1/2 and zero mass; therefore, the SM neutrino is in a definite helicity state: the neutrino has only the left-handed component ν_L, while the anti-neutrino has only the right-handed one ν_R.

It is nevertheless straightforward to extend the SM to accommodate neutrino masses in the same way that this model accommodates quark and charged lepton masses. When a neutrino ν is assumed to be massless, the SM does not contain the chirally right-handed neutrino field ν_R, but only the left-handed field ν_L that couples to the W and Z bosons. To accommodate the ν mass in the same manner as quark masses are accommodated, we add ν_R to the Model. Then we may construct the “Dirac mass term”

$$\mathcal{L}_D = -m_R \overline{\nu}_L \nu_R + h.c. \ , \tag{1.5}$$

in which m_D is a constant. This term, which mimics the mass terms of quarks and charged leptons, conserves the lepton number L that distinguishes neutrinos and negatively-charged leptons on the one hand from anti-neutrinos and positively-charged leptons on the other. Since everything else in the SM conserves L, we then have an L-conserving world. In such a world, each neutrino mass eigenstate ν_i differs

[6]Some general review on this topic can be found in [55, 72, 42].

from its antiparticle $\overline{\nu}_i$, the difference being that $L(\overline{\nu}_i) = -L(\nu_i)$. When $\overline{\nu}_i \neq \nu_i$, we refer to the $\nu_i - \overline{\nu}_i$ complex as a "Dirac neutrino".

Once ν_R has been added to our description of neutrinos, a "Majorana mass term",

$$\mathcal{L}_M = -m_R \overline{\nu_R^c} \nu_R + h.c. \;, \tag{1.6}$$

can be constructed out of ν_R and its charge conjugate, ν_R^c. In this term, m_R is another constant. Since both ν_R and $\overline{\nu_R^c}$ absorb ν and create $\overline{\nu}$, $\mathcal{L}_M$ mixes ν and $\overline{\nu}$. Thus, a Majorana mass term does not conserve L. There is then no conserved lepton number to distinguish a neutrino mass eigenstate ν_i from its antiparticle. Hence, when Majorana mass terms are present, $\overline{\nu}_i = \nu_i$. That is, for a given helicity h, $\overline{\nu}_i(h) = \nu_i(h)$. We then refer to ν_i as a "Majorana neutrino".

Suppose the right-handed neutrinos required by Dirac mass terms have been added to the SM. If we insist that this extended SM conserve L, then, of course, Majorana mass terms are forbidden. However, if we do not impose L conservation, but require only the general principles of gauge invariance and renormalizability, then Majorana mass terms like that of equation (1.6) are expected to be present. As a result, L is violated, and neutrinos are Majorana particles.

If neutrino are massive particles, typically both mass terms (Dirac and Majorana) are possible. In this case, for a single neutrino generation, the Dirac-Majorana mass term is described by the lagrangian:

$$\mathcal{L}^{mass} = -\frac{1}{2} \left(\overline{\nu}_L, \overline{\nu_R^c}\right) \begin{pmatrix} m_L^M & m^D \\ m^D & m_R^M \end{pmatrix} \begin{pmatrix} \nu_L^c \\ \nu_R \end{pmatrix} + h.c. \;, \tag{1.7}$$

where m^D is the usual Dirac mass term, while m_L^M and m_R^M are the two Majorana mass terms; if CP is conserved for leptons, the mass matrix is real and the mass eigenstates are Majorana neutrinos.

The experiments produce upper limits to neutrino masses and show how light the neutrino should be with respect to the charged leptons of the same generations. Many theoretical procedures can be invoked, in order to produce very small neutrino masses: amongst them, the most natural one is the "see-saw" mechanism, in which both Dirac and Majorana mass terms are present [55]. If in (1.7) we set $m_L^M = 0$ (that is to say we introduce only the Majorana term constructed out of ν_R and its charge conjugate) and $M \equiv m_R^M \gg m_D$ (that is to say we introduce a very large mass term), the mixing matrix can be diagonalized with two eigenstates, $m_1 \simeq M$ and $m_2 \simeq (m^D)^2/M$. In this case, M can be an arbitrary large mass; a natural choice for this mass scale is suggested by the renormalizability constraint to be as large as the GUT scale ($\sim 10^{15}\ GeV$). Since m_D is the typical electro-weak scale ($\sim 100\ GeV$), m_2 can be reduced down to $10^{-3}\ eV$.

1.3.2 Experimental limits to neutrino masses

Until now, no attempt for the direct determination of neutrino masses has been successful; nevertheless, upper bounds on neutrino masses have been set, according to various methods:

- **Kinematic limits to neutrino masses:** the most common technique for the ν_e mass determination relies on tritium β decay ($^3H \longrightarrow ^3 He + e^- + \overline{\nu}_e$); m_ν is computed from the β spectrum, close to the end-point. The lowest limits to ν_e mass have been set by two similar experiments (Moscow and Mainz), using an electrostatic spectrometer with magnetic collimation; Moscow experiment uses a gaseous tritium source, while Mainz experiment uses a molecular tritium film condensed on an aluminium layer. The best upper limits are:

$$m_{\nu_e} \leq 2.5\, eV \quad (95\% C.L.) \qquad \text{(Moscow [67])},$$

$$m_{\nu_e} \leq 2.2\, eV \quad (95\% C.L.) \qquad \text{(Mainz [32])}.$$

  Concerning ν_μ mass determination, the most efficient process is pion decay ($\pi^+ \longrightarrow \mu^+ + \nu_\mu$). Present limits are referred to an experiment held at the Paul Scherrer Institut (Switzerland); the experiment implies a proton beam colliding on a graphite target to produce π^+; π^+ decay in $\mu^+ + \nu_\mu$ is analyzed by means of a muon spectrometer and of a micro-strip detector. The upper limit quoted for this experiment is [14]:

$$m_{\nu_\mu} \leq 170\, KeV \quad (90\% C.L.).$$

  The present upper limit to ν_τ mass has been set studying τ decay in pions and a ν_τ; this decay has been analyzed by the ALEPH experiment, during the LEP runs from 1991 to 1995; combining 3 and 5 pions decays, the following limit for m_{ν_τ} has been established [25]:

$$m_{\nu_\tau} \leq 18.2\, MeV \quad (95\% C.L.).$$

- **Double beta decay experiments:** the $0\nu\beta\beta$-decay ($(A, Z) \rightarrow (A, Z+2) + 2e^-$) is the most promising process to investigate the Majorana nature of neutrinos: this decay, if observed, would signal violation of the total lepton number conservation. The process can be mediated by an exchange of a light Majorana neutrino, or by an exchange of other particles: however, the existence of $0\nu\beta\beta$-decay requires Majorana neutrino mass, no matter what the actual mechanism is. As long as only a limit on the lifetime is available, limits on the effective Majorana neutrino mass $< m_{\beta\beta} >$ can be obtained[7].

  Present limits on half-life measurements of $0\nu\beta\beta$-decay are in the range $10^{21} \div 10^{25}\ yr$ (depending on nuclear isotope and experimental technique) [42], while

[7] $< m_{\beta\beta} >= \sum_{i=1}^{n} U_{1j}^2 m_{\nu_j}$, where n is the number of neutrino generations and ν_j is a Majorana neutrino.

the best available limits on $< m_{\beta\beta} >$ have been obtained with enriched ^{76}Ge detectors and are in the range [42][8]: $< m_{\beta\beta} > < (0.33 \div 1.35)\ eV$ (at 90% $C.L.$)[9]. Very interesting results, in the eV range, have been obtained also with other isotopes, like ^{130}Te, ^{116}Cd, ^{136}Xe, ^{100}Mo and ^{128}Te.

- **Cosmological and astrophysical limits to neutrino masses:** some fundamental properties of neutrinos can be deduced by astrophysics and cosmology measurements. Copious numbers of neutrinos were produced in the early universe: if these neutrinos have non-negligible mass, they can make a non-trivial contribution to the total energy density of the universe during both matter and radiation domination[10]. The contribution of neutrinos to the energy density of the universe depends upon the sum of the mass of the light neutrino species:

$$\Omega_\nu h^2 = \frac{\sum_i m_i}{94.0\ eV}$$

(note that the sum only includes neutrino species light enough to decouple while still relativistic).

Combining data from Cosmic Microwave Background and from measurements of large scale structures, the following limit on energy density in neutrinos can be set [83]:

$$\Omega_\nu h^2 < 0.0076 \quad (95\% C.L.).$$

This implies that

$$\sum_i m_i < 0.76\ eV \quad (95\% C.L.).$$

Finally, upper limits on neutrino masses can be inferred from the observation of neutrino bursts from supernova explosions. During the explosion of 1987A supernova, about $4 \cdot 10^{15} \nu / m^2$ neutrinos reached the earth during a few seconds. The Kamiokande detector was capable to observe these supernova neutrinos [79]; from the time distribution of the burst data, some upper limits could be calculated on electron neutrino mass [61], ranging from a few eV to 24 eV (depending on different models and calculations).

[8]Presently, the only claim for positive observation of $0\nu\beta\beta$-decay comes from [65]: this result is still unconfirmed.

[9]The extrapolation from half-life to effective Majorana mass is complicated by big uncertainties on nuclear matrix elements: this explains the wide range in effective mass limits.

[10]Furthermore, neutrinos can influence smaller scale fluctuations during matter domination, changing the shape of CMB angular power spectrum and suppressing the amplitude of fluctuations; they also can leave an observable imprint on the galaxy large scale structure power spectrum [83].

1.3.3 Mixing of the mass eigenstates and vacuum oscillations

If neutrinos are massive, there is a spectrum of three or more neutrino mass eigenstates ν_i $(i = 1, 2, 3, ...)$, that are the analogues of the charged-lepton mass eigenstates e,μ and τ. If lepton mix, neutrino flavor eigenstates ν_l $(l = e, \mu, \tau)$, are not supposed to be coincident with mass eigenstates, but to be a superposition of the mass eigenstates. In this case, such a superposition can be represented through a mixing matrix [72]:

$$\nu_l = \sum_{i=1}^{3} U_{li}\nu_i \ , \tag{1.8}$$

where U is an unitary matrix $(U^\dagger U = I)$. In this representation, neutrino mass limits quoted in 1.3.2 have to be referred to the dominant state for each generation (for example, the limit on ν_e mass applies to the ν_1 state).

A mixing scenario for neutrinos was first proposed in 1967 by B. Pontecorvo [74]: at that time, only one generation of neutrinos was known. Pontecorvo assumed a nonzero neutrino mass and supposed that the neutrino observed in interactions with elementary particles was a superposition of two Majorana neutrinos with different masses. In this case, an oscillatory phenomenon $\nu_L \leftrightarrow \bar{\nu}_L$ would have been possible in a neutrino beam. Later on, after the discovery of a second neutrino generation, oscillations $\nu_{eL} \leftrightarrow \nu_{\mu_L}$ between different flavors were considered.

Therefore, the mixing hypothesis allows the possibility of neutrino oscillations, namely the possibility that an electron neutrino (for example) could be detected as a muon neutrino at some distance from its emitting source. In case of two neutrino generations[11], the equation (1.8) can be parameterized with a mixing angle θ [72]:

$$\begin{pmatrix} \nu_e \\ \nu_\mu \end{pmatrix} = \begin{pmatrix} \cos\theta & \sin\theta \\ -\sin\theta & \cos\theta \end{pmatrix} \begin{pmatrix} \nu_1 \\ \nu_2 \end{pmatrix}. \tag{1.9}$$

We are interested in computing the probability for a neutrino with a well-defined starting flavor ν_α, created at a time $t = 0$ in $x = 0$ by a weak process, to interact as another flavor neutrino ν_β, in a detector at a distance $x = L$ from its production site.

The time evolution of mass eigenstates ν_i $(i = 1, 2)$ follows Schrödinger equation:

$$\nu_i(t) = e^{-iE_i t}\nu_i(0), \qquad \text{where} \quad E_i = \sqrt{\overline{p}^2 + {m_i}^2} \ . \tag{1.10}$$

Since $m_1 \neq m_2$, the flavor eigenstates ν_e, produced at $t = 0$, evolve in time into a

[11] Even if the two neutrino generations case is not realistic, its study is useful, since typically the three generations problem can be reduced to a pair of simpler two generations problems; a description of the complete 3 ν formalism can be found in [45].

superposition of ν_e and ν_μ states. If we set $\nu_i \equiv \nu_i(0)$,

$$\begin{aligned}
\nu_e(t) &= \cos\theta e^{-iE_1 t}\nu_1 + \sin\theta e^{-iE_2 t}\nu_2 \\
&= \left[\cos^2\theta e^{-iE_1 t} + \sin^2\theta e^{-iE_2 t}\right]\nu_e + \left[\cos\theta\sin\theta\left(e^{-iE_2 t} - e^{-iE_1 t}\right)\right]\nu_\mu \\
&= A_{ee}(t)\nu_e + A_{e\mu}(t)\nu_\mu \ . \qquad (1.11)
\end{aligned}$$

Using equation (1.11), the probability for the state $\nu_e(t)$ to be in a flavor eigenstate ν_e or ν_μ at a time t can be computed:

$$P(\nu_e \to \nu_e; t) = |A_{ee}(t)|^2 = 1 - \frac{1}{2}\sin^2 2\theta\,[1 - \cos(E_2 - E_1)t] \qquad (1.12)$$

$$P(\nu_e \to \nu_\mu; t) = |A_{e\mu}(t)|^2 = \frac{1}{2}\sin^2 2\theta\,[1 - \cos(E_2 - E_1)t] \ . \qquad (1.13)$$

When neutrino masses are small compared to their momentum, we can write:

$$E_i = \sqrt{\overline{p}^2 + m_i{}^2} \simeq |p| + \frac{m_i^2}{2|p|} \ , \qquad \text{where} \quad t \simeq L \ , \qquad (1.14)$$

and L is the distance covered by neutrinos in the time t (we recall that $c \equiv 1$ in our equations). The equation (1.13) can therefore be rewritten as:

$$P(\nu_e \to \nu_\mu; t) = \frac{1}{2}\sin^2 2\theta\left[1 - \cos\frac{\delta m^2}{2|p|}L\right] = \sin^2 2\theta \sin^2\frac{\pi L}{\lambda_0} \ , \qquad (1.15)$$

where $\delta m^2 = |m_2^2 - m_1^2|$ and $\lambda_0 = 4\pi E/\delta m^2$ is the *oscillation length in vacuum* (we recall that $|p| \simeq E$). Substituting the numerical values, we obtain:

$$\lambda_0 = \frac{4\pi E_\nu}{\delta m^2} \simeq 2.47 \cdot \left(\frac{E_\nu}{1MeV}\right)\cdot\left(\frac{1eV^2}{\delta m^2}\right)\ m \ . \qquad (1.16)$$

Maximum oscillation amplitude is present if $\theta = \pi/4$ (this case is called *maximal mixing*).

The first consequence of the oscillation mechanism is the non-conservation of leptonic number l for each family: in case of neutrino oscillation ($\nu_\alpha \leftrightarrow \nu_\beta$), lepton flavor is not conserved and $\delta l = \pm 1$: in the Dirac neutrino case, the global conserved symmetry is the total leptonic number ($l_e + l_\mu + l_\tau$), while in the Majorana case the total leptonic number is not conserved.

The second consequence is the possibility to study the order of magnitude of neutrino masses difference, also in the regions well below 1 eV. Looking at equations (1.15) and (1.16), it is easy to conclude that the δm^2 sensitivity for an experiment depends on the E/L ratio, since $\delta m^2[eV^2] \approx E[MeV]/L[m]$. Depending on the experiment type, this ratio can be in the range between 10^2 and 10^{-11} eV^2.

1.3.4 Matter enhanced neutrino oscillations

The previously discussed oscillation mechanism is based on the vacuum propagation of ultra-relativistic neutrinos:

$$\nu_i(t) = \nu_i e^{i(px - E_i t)} \simeq \nu_i e^{-it\frac{{m_i}^2}{2p}} \tag{1.17}$$

When propagation takes place in matter, the phase factor ipx becomes $ipnx$, where n is the refraction index. The possibility for a neutrino to change its lepton flavor is therefore modified [87] and oscillations can be enhanced in special conditions [70]: the model describing such a phenomena is known as MSW, from the initials of the physicists who first discussed it.

The refraction index in matter is different from 1 due to the weak interactions of neutrinos:

$$n_l = 1 + \frac{2\pi N}{p^2} f_l(0) \ , \tag{1.18}$$

where N is the density of diffusion centers and $f_l(0)$ is the forward scattering probability amplitude for l-flavored neutrinos (neutrino absorption can be neglected and only the real component of $f_l(0)$ is considered).

The origin of the MSW effect is connected to the fact that electron neutrinos can interact in matter also through charged current interactions with electrons. While all neutrino species have the same interactions in matter due to the neutral currents, the ν_e weak interaction eigenstates (because of their charged current interactions), as they propagate in matter, experience a slightly different index of refraction than the ν_μ and ν_τ weak interaction eigenstates: this different index of refraction for ν_e alters the time evolution of the system from what happens in vacuum.

The computation of the Feynman diagrams for charged and neutral current interactions holds (for energies much lower than the W boson mass):

$$\Delta f(0) = f_e(0) - f_\alpha(0) = -\sqrt{2}\frac{G_F p}{2\pi} \ , \tag{1.19}$$

where α is a non-electronic neutrino flavor and G_F is the usual Fermi constant. We then obtain a contribution to the time evolution of the neutrino beam:

$$\nu_e(x) = \nu_e(0)e^{ipnx} = \nu_e(0)e^{-\sqrt{2}G_F N_e x} \ . \tag{1.20}$$

Therefore, an *oscillation length in matter* λ_{0m} can be defined:

$$\lambda_{0m} = \frac{2\pi}{\sqrt{2}G_F N_e} \simeq \frac{1.7\times 10^7}{\rho[g\ cm^{-3}]\frac{Z}{A}}\ m \ , \tag{1.21}$$

where N_e is the electron density in matter. Let's point out that, on the contrary to λ_0, λ_{0m} is independent from neutrino energy. Including the forward scattering in matter, we obtain the time evolution equation for mass eigenstates ν_1 and ν_2:

$$i\frac{d}{dt}\begin{pmatrix} \nu_1 \\ \nu_2 \end{pmatrix} = \begin{pmatrix} \frac{{m_1}^2}{2p} + \sqrt{2}G_F N_e \cos^2\theta & +\sqrt{2}G_F N_e \sin\theta\cos\theta \\ +\sqrt{2}G_F N_e \sin\theta\cos\theta & \frac{{m_2}^2}{2p} + \sqrt{2}G_F N_e \sin^2\theta \end{pmatrix}\begin{pmatrix} \nu_1 \\ \nu_2 \end{pmatrix} \tag{1.22}$$

This matrix can be diagonalized, and the *mixing angle in matter* is:

$$\tan 2\theta_m = \tan 2\theta \left(1 + \frac{\lambda_0}{\lambda_{0m}} \sec 2\theta\right)^{-1} . \tag{1.23}$$

The difference between the matrix eigenvalues gives the effective oscillation length in matter:

$$\lambda_m = \lambda_0 \frac{\sin 2\theta_m}{\sin 2\theta} = \lambda_0 \left[1 + \left(\frac{\lambda_0}{\lambda_{0m}}\right)^2 + \frac{2\lambda_0}{\lambda_{0m}} \cos 2\theta\right]^{-1/2} , \tag{1.24}$$

while the ν_e survival probability at a distance L from the production site is:

$$P(E_\nu, L, \theta, \delta m^2) = 1 - \sin^2\theta_m \sin^2 \frac{\pi L}{\lambda_m} , \tag{1.25}$$

where θ_m e λ_m depend on the vacuum oscillation parameters θ and λ_0.

Three different possibilities arise for λ_0 and λ_{0m}:

- $|\lambda_0| \ll \lambda_{0m}$: matter has no substantial effects on oscillations;
- $|\lambda_0| \gg \lambda_{0m}$: the oscillation amplitude is suppressed by the factor $\lambda_{0m}/|\lambda_0|$, and the effective oscillation length $\lambda_m \simeq \lambda_{0m}$ does not depend on vacuum oscillation parameters;
- $|\lambda_0| \simeq \lambda_{0m}$: in this case the oscillation effect is enhanced (*resonant*); in the particular case $\lambda_0/\lambda_{0m} = -\cos 2\theta$, we obtain $\sin^2 2\theta_m = 1$ (that is to say $\theta_m = \pi/4$) and the effective oscillation length is: $\lambda_m = \lambda_0/\sin^2 2\theta$. For a material where $Z/A \simeq 1/2$, the resonance condition can be written as:

$$\frac{E_{nu}[MeV]}{\delta m^2[eV^2]} \simeq 0.65 \times 10^{-7} \frac{\cos 2\theta}{\rho[g\ cm^{-3}]} .$$

1.4 Neutrino oscillation experiments

On the experimental side, oscillation phenomena can be studied by means of a known neutrino source ν_α and observing either the appearance of a second neutrino flavor ν_β at a given distance (*appearance* experiments), or measuring a possible reduction of the initial flux (*disappearance* experiments).

Equations in (1.15) and (1.16) can be merged into:

$$P(\nu_e \to \nu_\mu; t) = \sin^2 2\theta \sin^2 \frac{\delta m^2 L}{4E_\nu} \simeq \sin^2 2\theta \sin^2 \left(1.27 \frac{L[m]}{E_\nu[MeV]} \delta m^2[eV^2]\right) , \tag{1.26}$$

from which we can understand that the sensitivity of a given oscillation experiment depend on its L/E ratio, which determines the detectable values of δm^2 and $\sin^2 2\theta$. In figure 1.10 the experimental sensitivity is shown for each experiment type.

In the following, a somewhat historical account of the determination of the ν oscillation parameters is adopted.

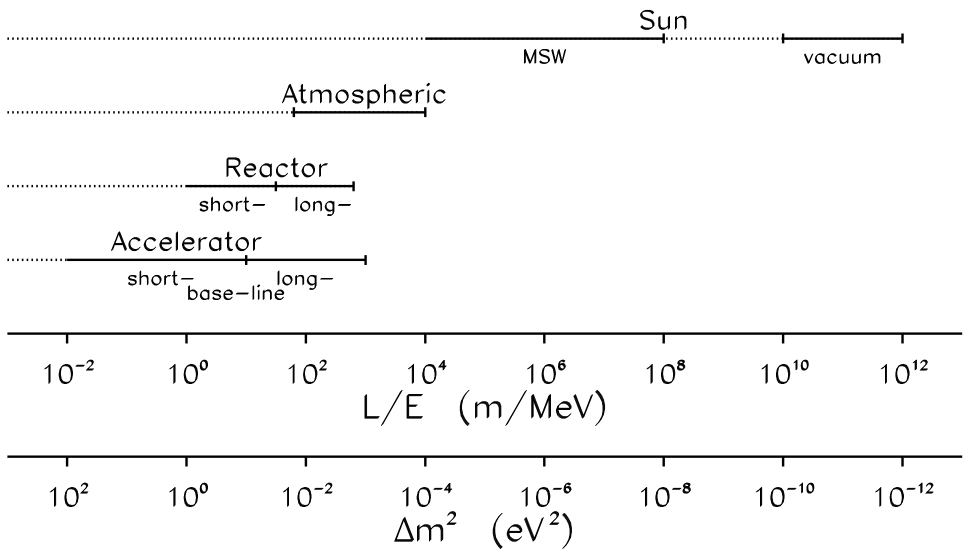

Figure 1.10: L/E regions accessible to the different experiment categories.

1.4.1 Solar neutrino experiments as oscillation experiments

Solar neutrino experiments can be considered as oscillation experiments, where the neutrino source is the Sun and the original neutrino flavor is electronic; solar neutrino experiments are disappearance experiments, because the suppression of the observed flux is due to the conversion of electron neutrinos into other flavor neutrinos, not interacting in the detector (in case of radiochemical experiments) or interacting with a lower cross-section (for water Čerenkov experiments). L/E ratio yields:

$$\frac{L}{E} \simeq \frac{10^8}{10^{-3}} \cdot \frac{km}{GeV} = 10^{11}\frac{m}{MeV} \Longrightarrow \delta m^2 \simeq 10^{-11} eV^2 \ , \tag{1.27}$$

therefore these experiments are sensitive to the smallest mass difference range.

Both vacuum and matter enhanced oscillations are studied: in case of vacuum oscillations, flavor conversion takes place in the Sun-Earth path, while in MSW scenario the resonance conversion condition is reached by neutrinos while travelling towards the Sun surface (or inside the Earth: in such a case, a day-night effect would be present). Furthermore, it can be hypothesized a scenario where electron neutrinos oscillate into sterile neutrinos (sterile neutrinos are neutrinos without a leptonic flavor, therefore they cannot interact in any detector).

The possible solutions in the parameter space (δm^2, $\tan^2\theta$) can be calculated (for active and sterile neutrinos), according to the results of Homestake, GALLEX/GNO, SAGE and Super-Kamiokande experiments (Kamiokande result is included in Super-Kamiokande one): for radiochemical experiments, only total fluxes can be taken into account, while for Super-Kamiokande spectral information and day-night effect are considered as well. With a global fit to the all the experimental results, several local minima for χ^2 can be found in the parameter space:

- **MSW solutions:** three solutions are present for matter enhanced oscillations: LMA (*Large Mixing Angle*), SMA (*Small Mixing Angle*) and LOW (*Low probability, Low mass*);

- **vacuum oscillations:** two different vacuum oscillation solutions are present, called VAC an JustSo^2;

- **sterile neutrino oscillations:** in this scenario, only one SMA and two vacuum solutions are possible.

In table 1.3 and figure 1.11 are reported the solutions for solar neutrino oscillations, deduced according to the above listed results; in this analysis, Super-Kamiokande spectra during day and night are included (the total Super-Kamiokande flux and day-night effect are not included, because their informations are present in spectral data) [22].

Solution	$\delta m^2 (eV^2)$	$tan^2\theta$	χ^2_{min}	g.o.f.
LMA	$4.2 \cdot 10^{-5}$	$2.6 \cdot 10^{-1}$	29.0	75%
SMA	$5.2 \cdot 10^{-6}$	$5.5 \cdot 10^{-4}$	31.1	66%
LOW	$7.6 \cdot 10^{-8}$	$7.2 \cdot 10^{-1}$	36.0	42%
VAC	$1.4 \cdot 10^{-10}$	$3.8 \cdot 10^{-1}$	37.5	36%
JustSo^2	$5.5 \cdot 10^{-12}$	$1.0 \cdot 10^{0}$	36.1	42%
Sterile SMA	$4.2 \cdot 10^{-6}$	$6.0 \cdot 10^{-4}$	32.5	59%
Sterile VAC	$1.4 \cdot 10^{-10}$	$3.6 \cdot 10^{-1}$	41.4	21%
Sterile JustSo^2	$5.5 \cdot 10^{-12}$	$1.0 \cdot 10^{0}$	36.5	40%

Table 1.3: Global fit to solar neutrino data, before SNO and KamLAND results (from [22]).

1.4.2 Atmospheric neutrinos and the Super-Kamiokande evidence

Atmospheric neutrinos are produced in the collision of primary cosmic rays (typically protons) with nuclei in the upper atmosphere. This creates a shower of hadrons, mostly pions: the pions decay into a muon and a muon neutrino; the muons decay to an electron, another muon neutrino, and an electron neutrino. Based on this kinematic chain, the flux ratio for muon neutrinos to electron neutrinos can be predicted; detailed calculations are somewhat complicated (kaons are also produced in the hadronic shower and some high energy muons reach the earth before decaying in flight to high energy neutrinos): however, the flux ratio calculation cancels out many uncertainties and the final estimated uncertainty in the flux ratio is about 5%.

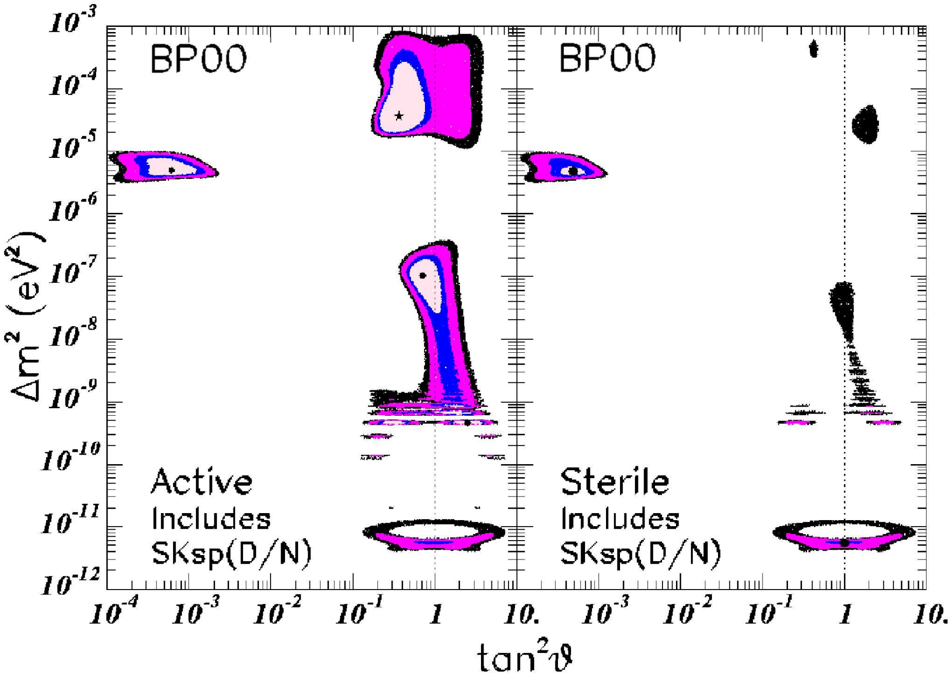

Figure 1.11: Allowed parameter regions for solar neutrino oscillations into active (left) and sterile (right) neutrinos, before SNO results; C.L. contours are 90%, 95%, 99% and 99.73% (3σ).

Super-Kamiokande experiment detects atmospheric neutrinos by their interaction on target water: the products of these reactions are usually "fully contained" in the detector volume. The neutrino flavor is tagged by detecting and identifying the final state lepton (muon or electron). Low energy ($E < 1\ GeV$) neutrinos typically react by quasi-elastic scattering, with only the lepton visible in the final state (at higher energies, the final state muon or electron is often accompanied by a pion or numerous hadrons). The properties of the incoming neutrino can be estimated from the properties of the Čerenkov ring: by measuring the number of events of each type, as a function of energy and direction, it is possible to find out if neutrino oscillations are affecting the results, because neutrino oscillations can effect the number of neutrinos detected as a function of distance travelled (which is determined by the arrival angle with respect to the vertical).

The first piece of evidence for neutrino oscillations is that an anomalous number of muon neutrino events is measured, compared to electron neutrino events. In [49] the following double-ratio was reported (for the sub-GeV energy range):

$$\frac{(N_\mu/N_e)_{data}}{(N_\mu/N_e)_{predicted}} = 0.63 \pm 0.03\ (stat.) \pm 0.05\ (syst.);$$

if the data agreed with the standard prediction of muon and electron neutrino pro-

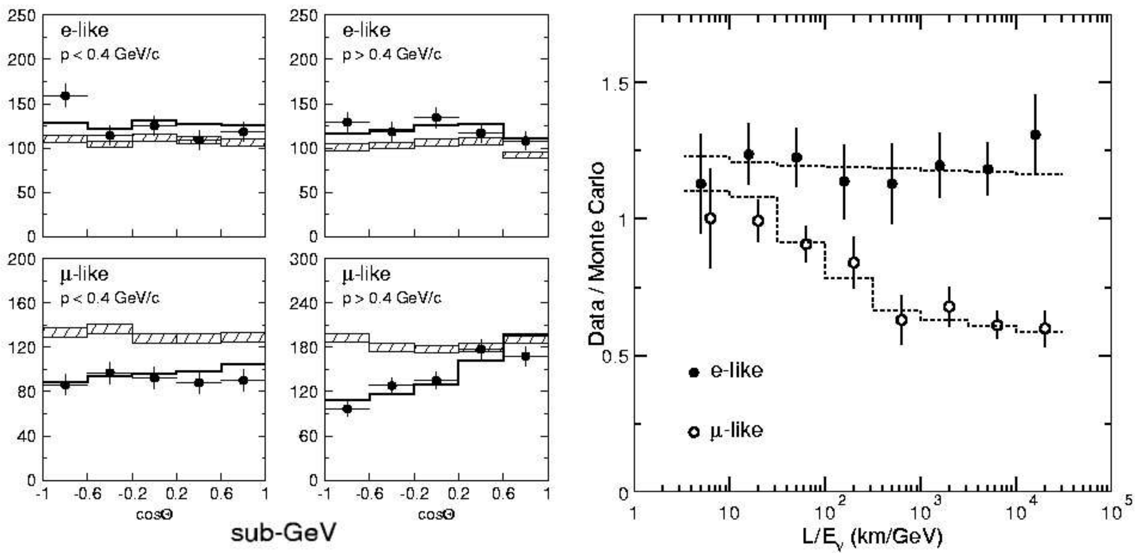

Figure 1.12: Left: zenith angle distribution of e-like and μ-like events for sub-GeV data sets; the hatched regions show the Monte Carlo expectation for no oscillations, while the bold line is the best-fit expectation for $\nu_\mu \leftrightarrow \nu_\tau$ oscillations; right: the ratio of the number of FC data events to Monte Carlo events versus reconstructed L/E_ν: the points show the expectations in absence of oscillations, the dashed lines show the expected shape for $\nu_\mu \leftrightarrow \nu_\tau$ oscillations (from [49]).

duction, this number should be about 1, while the measured number differs from 1 by more than 5 σ. In figure 1.12, the zenith angle distributions for sub-GeV events are shown (compared with the Monte Carlo predictions), as well as the L/E_ν distributions of e-like and μ-like events.

A second piece of evidence for neutrino oscillations is the measurement of a significant up-down asymmetry of high energy muon neutrino events. Above a few GeV, atmospheric neutrinos can be traced back to primary cosmic rays of energy greater than 10 GeV, which are not deflected very much by the earth's magnetic field; since cosmic rays arrive at the earth almost isotropically, the flux of atmospheric neutrinos should be symmetric in the cosine(zenith) distribution. We quantify this be calculating the up/down asymmetry: for high energy muon neutrino events, the following asymmetry was measured [48]:

$$A_\mu = \frac{up - down}{up + down} = 0.296 \pm 0.048\ (stat.) \pm 0.01\ (syst.);$$

the asymmetry for the predicted value was consistent with zero, therefore the above result differs from the expected one for 6 σ. The up/down asymmetry was consistent with zero for high energy electron neutrinos: the effect can be dramatically seen in the zenith angle distribution of high energy neutrino events (see figure 1.13).

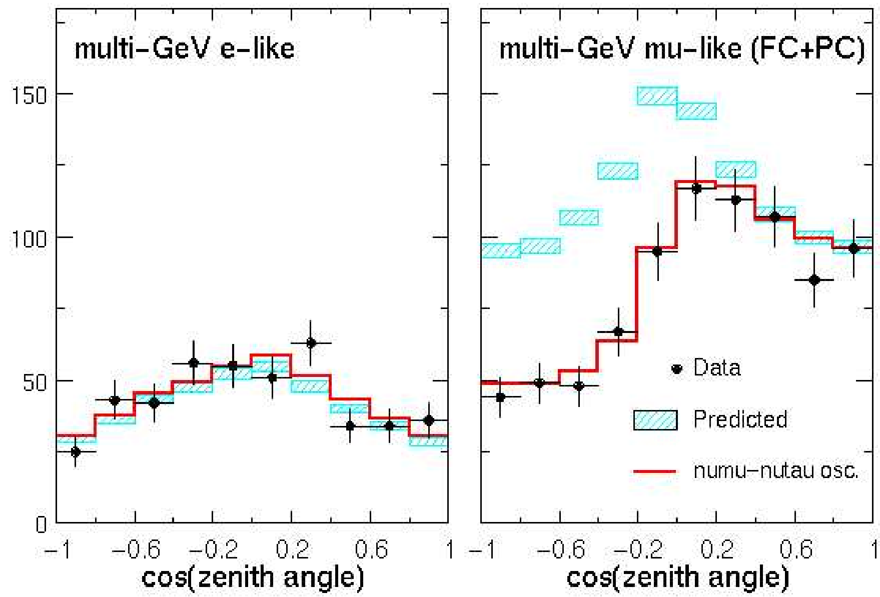

Figure 1.13: Zenith angle distribution for e-like and μ-like multi-GeV events; the blue hatched regions show the Monte Carlo predictions with their statistical uncertainties, while the red lines show the expected shape for $\nu_\mu \leftrightarrow \nu_\tau$ oscillations.

A third piece of evidence came from an independent data set. Muon neutrinos also interact in the rock around and below the detector, with the final state muon entering the detector: if the neutrino and muon come from above, these events are lost in the background of cosmic ray muons; but cosmic rays can't penetrate the earth from below, so upward-going muons must be neutrino induced. These upgoing muons where studied and it was found that their angular distribution, was in poor agreement with the standard prediction, but in good agreement with an hypothesis of neutrino oscillations [50].

Super-Kamiokande results on atmospheric neutrinos have been explained via $\nu_\mu \leftrightarrow \nu_\tau$ oscillations: $\nu_\mu \rightarrow \nu_e$ oscillations were excluded thanks to the CHOOZ results (see section 1.4.4). Allowed regions for oscillation parameters are shown in figure 1.14; at the moment of the publications of Super-Kamiokande results on atmospheric neutrino oscillations (1998), these data represented the best evidence of a physics beyond the Standard Model.

1.4.3 The SNO experiment: direct test of solar neutrino oscillations

The "final" solution to the solar neutrino puzzle was provided by the SNO experiment, which started data taking in May 1999 and released its phase-1 results in June 2001 [2] and April 2002 [3].

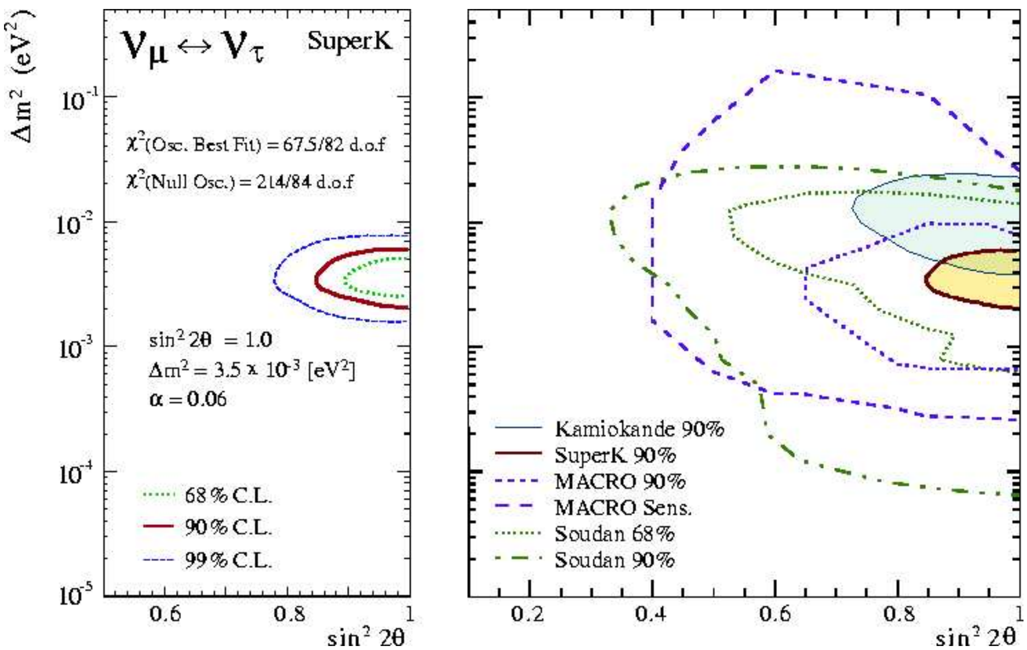

Figure 1.14: Allowed regions in parameter space for atmospheric neutrino oscillations; Super-Kamiokande data are compared to the results of lower sensitivity experiments.

The Sudbury Neutrino Observatory [31] is a 100 t heavy water Čerenkov detector, located in the Creighton mine, in Subdury (Ontario, Canada), at 6010 *mwe* depth. The detector layout is shown in figure 1.15: a 34 m high and 22 m wide cave hosts an acrylic sphere of 12 m diameter, which is filled with heavy water. Outside the sphere a geodetic structure is installed, were 9456 inwards-looking PMTs are mounted; the external volume of the acrylic vessel is filled with light water, providing hydrostatic support to the structure and passive shielding against the radioactivity from the PMT array and from the rock.

In the phase-1 data taking, neutrinos were detected in heavy water via three different interactions[12]:

- **Charged Current (CC):** $\nu_e + D \rightarrow e^- + p + p$; this reaction, which is sensitive only to electron neutrinos, is detected via the Čerenkov light produced by the emitted electron; electron has an energy highly correlated with that of the incoming neutrino, hence this reaction is sensitive to the energy spectrum of ν_e and to deviations from the parent spectrum;
- **Neutral Current (NC):** $\nu_x + D \rightarrow \nu_x + p + n$; this reaction is sensitive to all the active neutrino flavors and its cross section is independent from the

[12]Due to the radioactive background, the energy threshold of the experiment was 5 MeV, allowing only ^8B neutrinos detection.

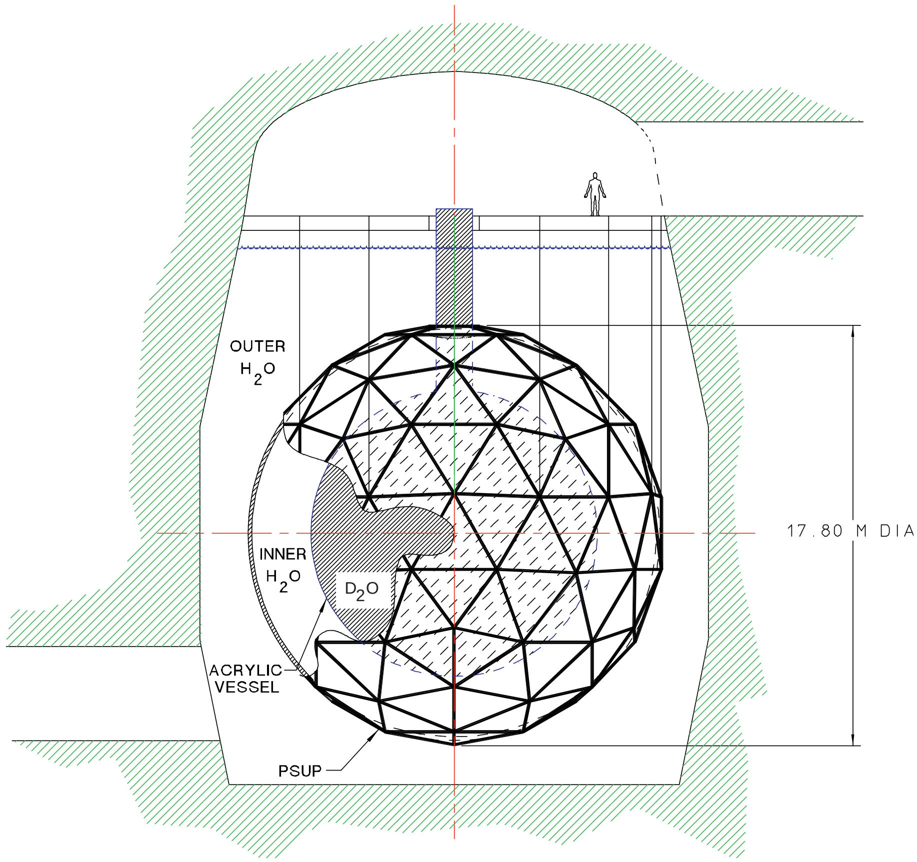

Figure 1.15: Detector layout of the SNO experiment.

specific flavor: therefore, it provides a determination of the total ^8B neutrino flux, while the CC/NC ratio allows to quantify eventual ν_e oscillations; to be detected, the resulting neutron must be absorbed, giving a 6.25 MeV photon: the photon subsequently must Compton scatter, imparting enough energy to electrons to create Čerenkov light;

- **Elastic Scattering (ES):** $\nu_x + e \rightarrow \nu_x + e$; this last reaction is sensitive to all neutrino flavors, but the $\sigma(\nu_e) \sim 6\sigma(\nu_{\mu,\tau})$; it is highly directional and establishes the Sun as the source of detected neutrinos; comparison of the ^8B flux deduced from the ES reaction to that measured by the CC reaction provided the first evidence of flavor transformation in solar neutrino flux.

Data published in June 2001 [2] reported the first ES and CC results as follows:

$$\begin{aligned}
\phi^{CC}_{SNO}(\nu_e) &= (1.75 \pm 0.07\ (stat.)\ ^{+0.12}_{-0.11}\ (sys.) \pm 0.05\ (theor.)) \times 10^6 cm^{-2} s^{-1} \\
\phi^{ES}_{SNO}(\nu_x) &= (2.39 \pm 0.34\ (stat.)\ ^{+0.16}_{-0.14}\ (sys.)) \times 10^6 cm^{-2} s^{-1}.
\end{aligned}$$

The ES result can be compared with the Super-Kamiokande measurement:

$$\phi_{SK}^{ES}(\nu_x) = (2.32 \pm 0.03\ (stat.)\ ^{+0.08}_{-0.07}\ (sys.)) \times 10^6 cm^{-2} s^{-1},$$

leading to the following ES-CC difference (under the assumption that the systematic errors are normally distributed):

$$\phi_{SK}^{ES}(\nu_x) - \phi_{SNO}^{CC}(\nu_e) = (0.57 \pm 0.17) \times 10^6 cm^{-2} s^{-1}\ (\text{or } 3.3\ \sigma).$$

These data are therefore evidence for a non-electronic active flavor component in the solar neutrino flux; the best estimation of $\phi(\nu_{\mu,\tau})$ is:

$$\phi(\nu_{\mu,\tau}) = (3.69 \pm 1.13) \times 10^6 cm^{-2} s^{-1},$$

while the total flux of active ^8B neutrinos is determined to be:

$$\phi(\nu_x) = (5.44 \pm 0.99) \times 10^6 cm^{-2} s^{-1},$$

in good agreement with the Solar Model Prediction:

$$\phi_{SSM} = (5.79 \pm 1.33) \times 10^6 cm^{-2} s^{-1}.$$

In April 2002 [3], also NC results where published, as well as improved CC results:

$$\begin{aligned}
\phi_{SNO}^{CC}(\nu_e) &= (1.76\ ^{+0.06}_{-0.05}\ (stat.)\ ^{+0.09}_{-0.09}\ (sys.)) \times 10^6 cm^{-2} s^{-1} \\
\phi_{SNO}^{ES}(\nu_x) &= (2.39\ ^{+0.24}_{-0.23}\ (stat.)\ ^{+0.12}_{-0.12}\ (sys.)) \times 10^6 cm^{-2} s^{-1} \\
\phi_{SNO}^{NC}(\nu_x) &= (5.09\ ^{+0.44}_{-0.43}\ (stat.)\ ^{+0.46}_{-0.43}\ (sys.)) \times 10^6 cm^{-2} s^{-1},
\end{aligned}$$

where all the fluxes are calculated assuming undistorted ^8B energy spectrum.

A simple change of variables resolves the data into electron and non-electron components:

$$\begin{aligned}
\phi(\nu_e) &= (1.76\ ^{+0.05}_{-0.05}\ (stat.)\ ^{+0.09}_{-0.09}\ (sys.)) \times 10^6 cm^{-2} s^{-1} \\
\phi(\nu_{\mu,\tau}) &= (3.41\ ^{+0.45}_{-0.45}\ (stat.)\ ^{+0.48}_{-0.45}\ (sys.)) \times 10^6 cm^{-2} s^{-1},
\end{aligned}$$

leading to a strong evidence (5.3 σ) for non-null $\nu_{\mu,\tau}$ flux, that is to say for flavor transformation consistent with the oscillation hypothesis (see figure 1.16).

Removing the constraint that the solar neutrino energy spectrum is undistorted, the total flux of active ^8B neutrinos can be estimated in:

$$\phi_{NC}^{SNO} = (6.42\ ^{+1.57}_{-1.57}\ (stat.)\ ^{+0.55}_{-0.58}\ (sys.)) \times 10^6 cm^{-2} s^{-1},$$

which accounts for all the flux predicted by the standard solar model ($\phi_{SSM} = (5.79 \pm 1.33) \times 10^6 cm^{-2} s^{-1}$); for this reason, the role of a sterile component in the solar neutrino flux is probably marginal, even if it cannot be excluded completely.

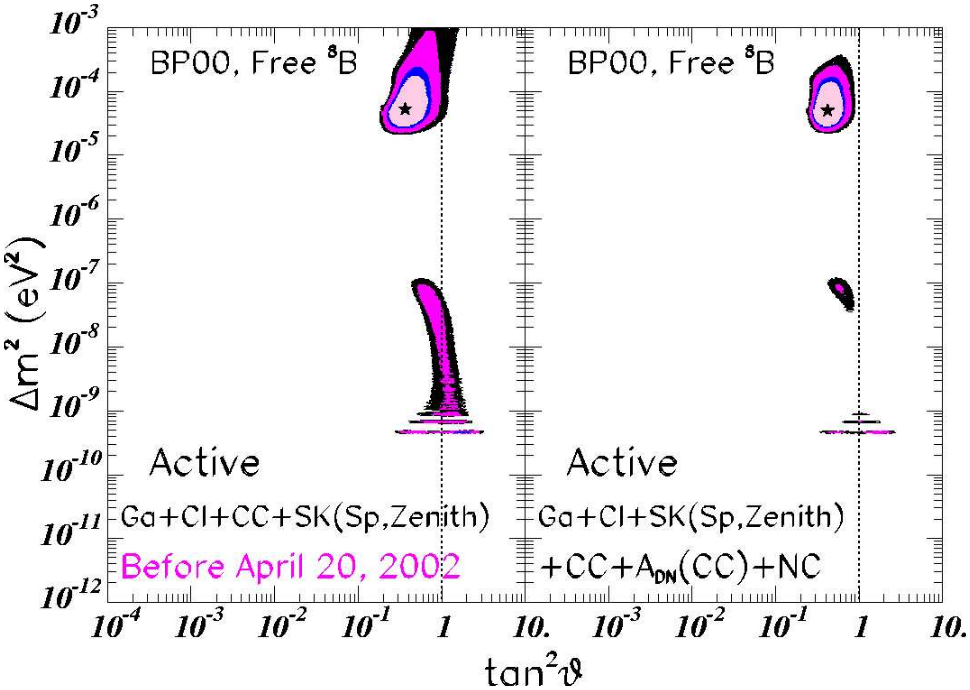

Figure 1.16: Allowed regions for neutrino oscillations computed with SNO CC data (left) and with the SNO NC data and improved CC data (right) [20].

After the end of phase-1 data taking, 2 tons of salt ($NaCl$) were added to SNO heavy water, in order to increase NC sensitivity (^{35}Cl has a large cross section for the capture of neutrons produced in NC reaction; the total energy of the γ-ray cascade emitted in the capture is 8.6 MeV). Phase-2 data taking took place from July 2001 until September 2003 and first data were released in September 2003 [4]. Results are consistent with the phase-1 data, even if they present smaller errors (as expected); effects of the SNO phase-2 measurement on the allowed region for oscillations will be discussed in the next subsection.

Finally, after the end of phase-2 data taking, the salt was removed from heavy water and the deployment of a Neutral Current Detector (NCD) has started. NCD are Helium-3 proportional counter tubes hung in a grid within the heavy water: ^3He has a very large cross-section for the capture of thermal neutrons, which produces an energetic proton-triton pair resulting in an electrical pulse in the counter wire. Some 800 meters of tubes have been deployed uniformly throughout the heavy water volume in strings up to 11 m, during the period between November 2003 and April 2004. Re-calibration of the detector is underway: phase-3 data taking is foreseen to start at the end of 2004.

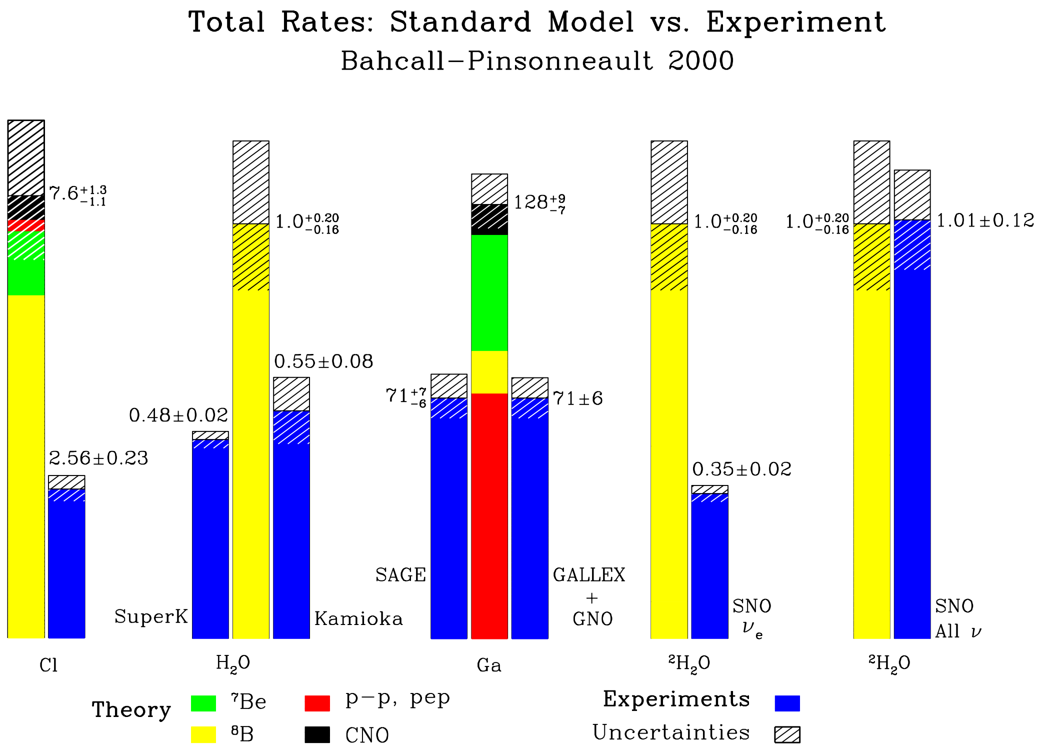

Figure 1.17: Comparison between calculated and observed neutrino rates in 2003, including SNO CC and NC measurements.

1.4.4 Reactor neutrino experiments before 2002

Reactor experiments are typically disappearance experiments; they are sensitive to the oscillations of electron anti-neutrinos (produced in the core of nuclear reactor plants) in non-electronic flavors. Anti-neutrinos are detected via inverse β decay on target protons: $\overline{\nu}_e + p \rightarrow n + e^+$ (threshold for $\overline{\nu}_e$ is 1.8 MeV); the positron annihilates yielding two gamma rays (511 keV each) and the neutron is thermalized and captured by a proton, releasing a 2.2 MeV gamma: the neutron mean thermalization time is 200 ms, therefore anti-neutrino events can be tagged by means of the delayed coincidence between the positron annihilation and the neutron capture. Two reactor experiments will be recalled here:

- **CHOOZ:** this experiment was located in the Ardenne region (France), close to two pressurized water reactors with a total thermal power of 8.5 GW; detector was installed at a distance of about 1 km from the neutrino source, in a 300 mwe underground laboratory. The detector target was contained in a welded cylindrical steel vessel, filled with a paraffinic liquid scintillator loaded with 0.09% gadolinium (which has a large neutron capture cross section) [11]: real target had a 5 t mass; a 17 t active buffer and a 91 t passive buffer were also present. After the April 1997 - July 1998 data taking, the total anti-neutrino rate and energy spectrum data were published [12], showing no deviations from the non-oscillation hypothesis; the measured versus expected ratio, averaged over the energy spectrum is: $R = 1.01 \pm 2.8\%(stat.) \pm 2.7\%(sys.)$.

Considering these results, the excluded parameters region for $\nu_e \leftrightarrow \nu_x$ oscillations is: $\delta m^2 > 7 \times 10^{-4}\ eV^2$ for maximal mixing and $sin^2\ 2\theta > 0.10$ for large δm^2 (as shown in figure 1.18). These constraints have three main consequences:

- provide an upper bound on δm^2 for solar neutrino oscillations: $\delta m^2_{12} < 7 \times 10^{-4}\ eV^2$;
- provide an upper limit on θ_{13} mixing parameter: $sin^2\ 2\theta_{13} < 0.10$[13];
- exclude the Super-Kamiokande region for atmospheric neutrino oscillations: electron neutrinos are not involved in atmospheric oscillations and the Super-Kamiokande result has to be explained via $\nu_\mu \leftrightarrow \nu_\tau$ oscillations.

- **Palo Verde:** this experiment was performed at the Palo Verde Nuclear Generating Station in Arizona (USA); the plant consists of three identical pressurized water reactors with a total thermal power of 11.63 GW. The detector was located in a shallow underground site (32 mwe), 890 m from two of the reactors and 750 m from the third. The segmented detector consisted of 66 acrylic cells, filled with 11.34 t of Gd-loaded liquid scintillator; a mineral oil buffer and a water (105 t) buffer were present. The obtained observed versus expected ratio was [30]: $R_{obs}/R_{calc} = 1.01 \pm 0.024\ (stat.) \pm 0.053\ (syst.)$, consistent with the non-oscillation hypothesis.

  Two different analysis of Palo Verde data have been performed: the standard "reactor power" analysis and the "swap" analysis (based on a swapped set of cuts for coincidence events); the second method allows to reduce systematics via a direct background subtraction: therefore it enhances the experiment sensitivity. Nevertheless, the Palo Verde final sensitivity never reached the CHOOZ sensitivity (Palo Verde and CHOOZ excluded regions are shown in figure 1.18).

[13] A recent paper on the global neutrino oscillation analysis performed in a 3 ν formalism, can be found in reference [45].

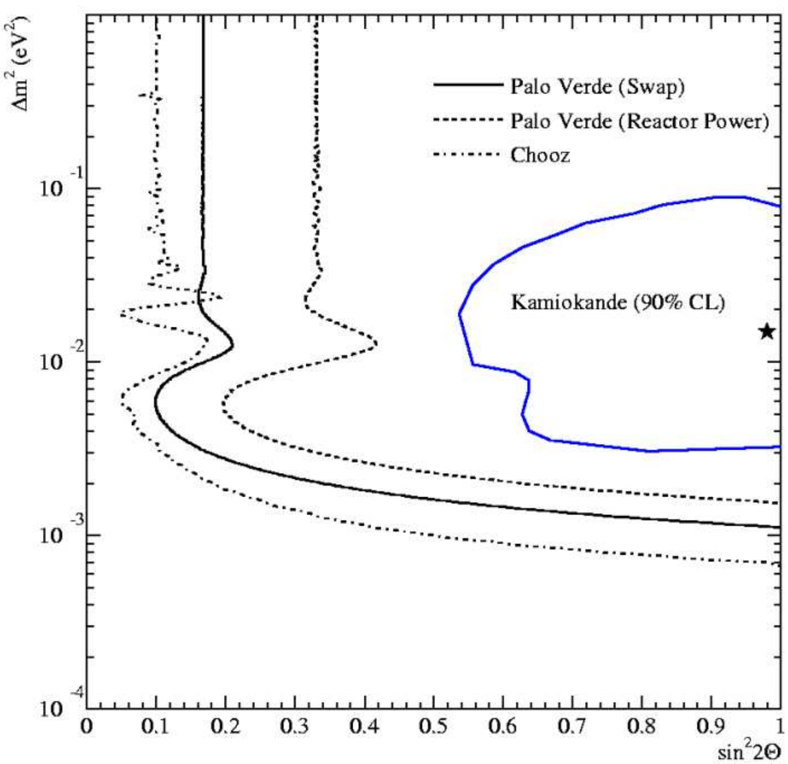

Figure 1.18: Exclusion plot for the CHOOZ and the Palo Verde (two analysis) experiments, compared to the Super-Kamiokande allowed region for atmospheric neutrino oscillations (from [30]).

1.4.5 The KamLAND result: solar neutrino oscillation parameters

KamLAND (Kamioka Liquid scintillator Anti-Neutrino Detector) is a large anti-neutrino detector built in the old Kamiokande cave, at the Kamioka mine (Japan) [62]. It was designed to study the flux and energy spectra produced by anti-neutrinos from local Japanese commercial reactors (most of the Japanese reactors are located within 150-200 kilometers from the detector location). KamLAND is a disappearance anti-neutrino oscillation experiment (it detects $\overline{\nu}_e$ via the inverse beta decay, as the other reactor neutrino experiments): at an average distance of 180 km from the anti-neutrino source, the L/E ratio for reactor anti-neutrinos is similar to the solar neutrino range; therefore, the KamLAND observatory can be used to determine the solar neutrino oscillation parameters.

As shown in figure 1.19, the neutrino target is 1 $kton$ of liquid scintillator (LS) contained in a 13 m diameter spherical balloon made of transparent nylon film. A buffer of mineral oil between the balloon and an 18 m diameter spherical stainless-steel containment vessel shields the LS from external radiation. An array of 1879

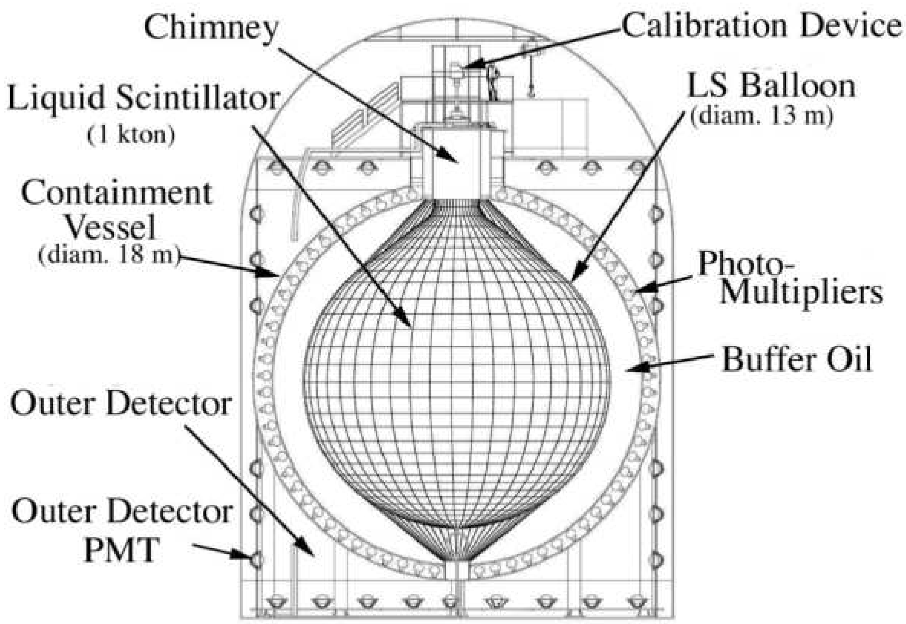

Figure 1.19: Schematics of the KamLAND detector.

PMTs, mounted on the inner surface of the containment vessel, completes the inner detector system, featuring a total photo-cathode coverage of 34%. The containment vessel is surrounded by a 3.2 *kton* water Čerenkov detector with 225 PMTs: this outer detector absorbs γ-rays and neutrons from the surrounding rock and provides a tag for cosmic-ray muons.

The KamLAND experiment started taking data in January 2002 and released first result about reactor anti-neutrino disappearance at the end of 2002 [40], while new data about anti-neutrino spectral distortion are in publication [13]. As shown in figure 1.20, the ratio of the number of observed reactor $\overline{\nu}_e$ events to that expected in the absence of neutrino oscillations is [40]:

$$(N_{obs} - N_{BG})/N_{expected} = 0.611 \pm 0.085\ (stat.)\ \ \pm 0.041\ (syst.);$$

the probability that this result is consistent with the no disappearance hypothesis is less than 0.5% (in other words, the null hypothesis is excluded at $> 4\ \sigma$).

Since a negligible reduction of $\overline{\nu}_e$ is predicted for SMA, LOW and vacuum solutions, the LMA region is the only remaining oscillation solution consistent with the KamLAND result and CPT invariance (CPT invariance is required for equivalence between ν_e and $\overline{\nu}_e$ results). In figure 1.21 are shown the allowed regions for reactor and solar neutrino oscillation parameters, after the release of KamLAND spectral distortion data [13] and SNO salt data [4]: the best fit-points for oscillation parameters are:

$$\delta m^2 = 8.2^{+0.6}_{-0.5} \times 10^{-5}\ eV^2; \qquad tan^2\theta = 0.40^{+0.09}_{-0.07}$$

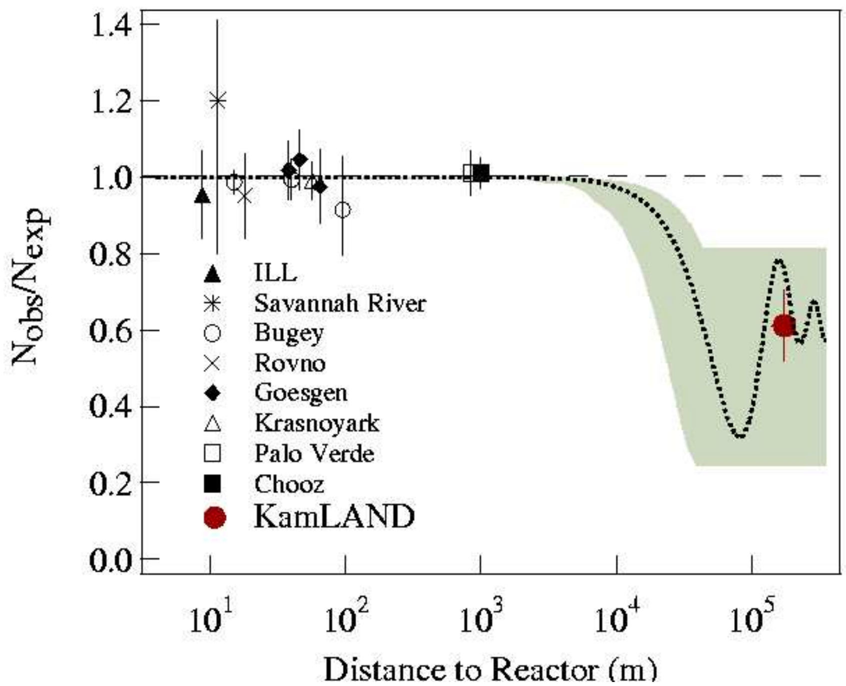

Figure 1.20: First result of KamLAND experiment: ratio of observed to expected anti-neutrino flux as a function of distance from nuclear reactors; the shaded region indicates the range of flux predictions corresponding to the 95% C.L. LMA region, found in a global analysis of the solar neutrino data.

1.4.6 Accelerator neutrino experiments

Accelerator experiments study the $\nu_\mu \leftrightarrow \nu_e$ (or $\overline{\nu}_\mu \leftrightarrow \overline{\nu}_e$) channel, through the appearance of electron neutrinos in a muon neutrino beam. The main feature of accelerator experiments is the sensitivity to small $sin^2 2\theta$ values (see figure 1.10). Depending on the source-detector distance, we distinguish between Long and Short Baseline experiments. The main results have presently been obtained in the following experiments:

- the **LSND** experiment (Los Alamos, new Mexico) studies the proton beam produced by a LINear ACcelerator: protons interact on target, generating a π^+ beam; from the π^+ decay, μ^+ and ν_μ are produced. 30 m away from the beam stopper, a scintillator detector is installed, looking for $\overline{\nu}_e$ coming from the $\overline{\nu}_\mu$ beam (if oscillations take place). An excess of $\overline{\nu}_e$ events has been found [43]: therefore, a new parameter region for oscillations ($0.2 < \delta m^2 < 4eV^2$, $\sin^2 2\theta \simeq 10^{-2}$) has been established (see figure 1.22). LSND results are partially contradicted by KARMEN (see below) and no confirmation experiment has been concluded yet;

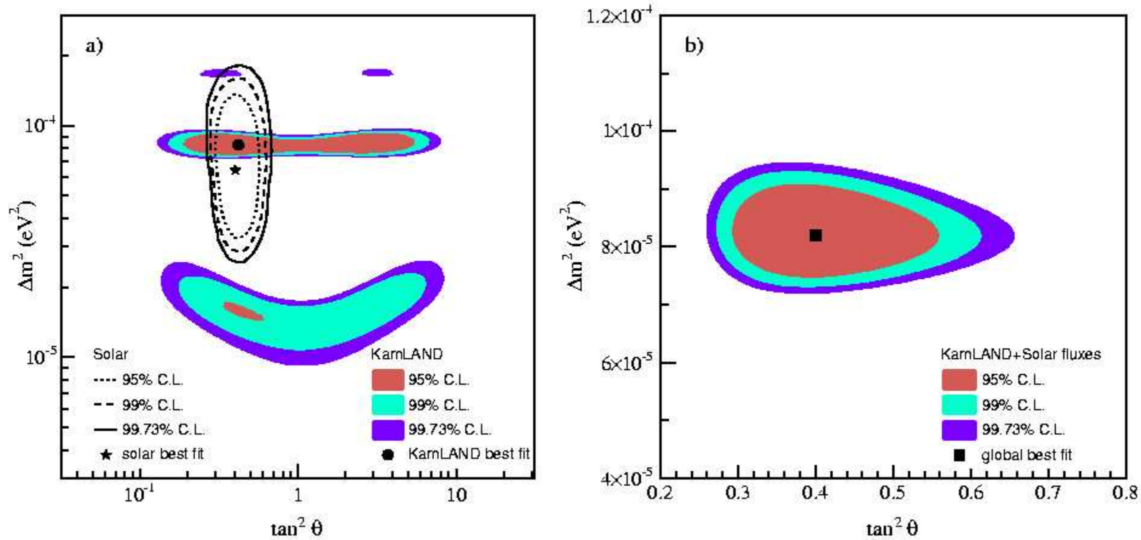

Figure 1.21: Left: allowed regions of neutrino oscillation parameters from KamLAND anti-neutrino data (shaded regions) and solar neutrino experiments (lines); right: result of a combined two-flavor neutrino oscillation analysis, under the assumption of CPT invariance (from [13]).

- the **KARMEN** experiment studies the same channel of LSND, using the proton source of the ISIS accelerator (Rutherford Appleton Laboratories, Karlsruhe) [43]; in this case, the distance between detector and source is 18 m. No excess $\overline{\nu}_e$ events has been measured in this experiment, therefore the LSND result was not confirmed: moreover, the KARMEN results exclude a big portion of the neutrino parameter region favored by LSND, even if not all of it (see figure 1.22);

- the **NOMAD** experiment used the CERN wide band neutrino beam from the 450 GeV PS [43]. The NOMAD $\nu_\mu \to \nu_e$ search has shown no excess of ν_e events and excluded a portion of the LSND allowed region (see figure 1.22);

- the **NuTeV** experiment at Fermilab used the 800 GeV primary proton beam from the Tevatron [43]; separate searches for $\nu_\mu \to \nu_e$ and $\overline{\nu}_\mu \to \overline{\nu}_e$ oscillations have been performed, by appearance of ν_e and $\overline{\nu}_e$, respectively. The NuTeV experiment confirmed the KARMEN and NOMAD results, as shown in figure 1.22;

- the **MiniBooNE** experiment at Fermilab is designed to cover the entire parameter range favored by LSND (the experiment was proposed by the same collaboration as LSND), with a completely different experimental setup by looking for both ν_μ disappearance and ν_e appearance from $\nu_\mu \to \nu_e$ in a ν_μ beam [43]. MiniBooNE uses the 8 GeV booster at Fermilab's main injector to produce a neutrino beam: the Čerenkov detector is installed at a distance of 500 m from the neutrino production point; MiniBooNE started data taking in 2002, but no results on neutrino oscillations have been published yet: expected sensitivity for a 2 years data taking is shown in figure 1.22;

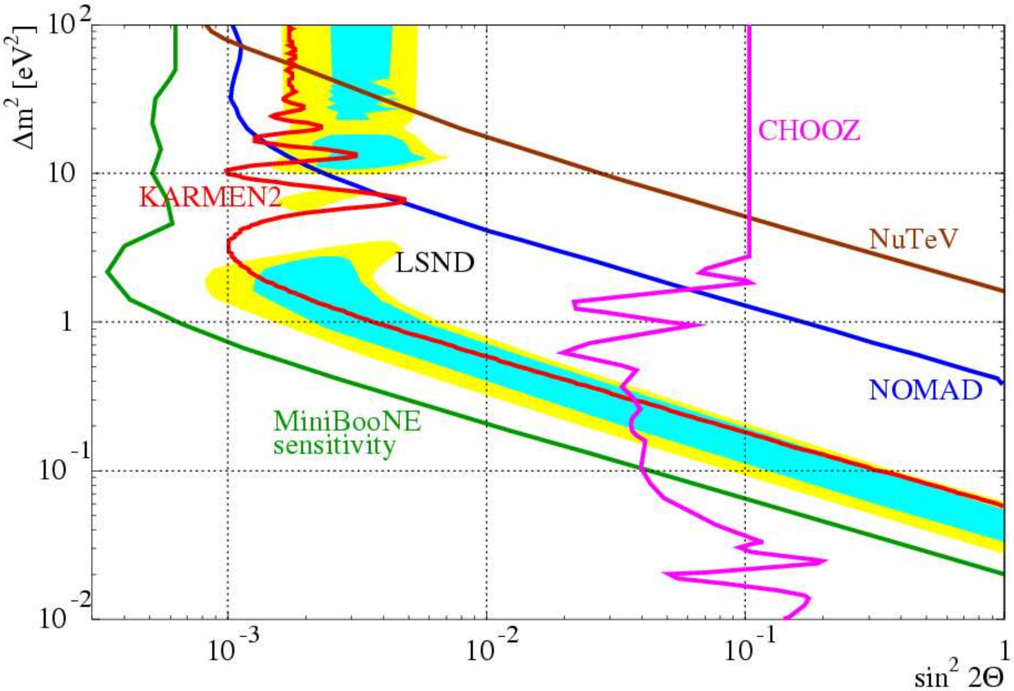

Figure 1.22: MiniBooNE expected $\nu_\mu \to \nu_e$ sensitivity, compared to the results of the above mentioned experimental searches, including the limit from the CHOOZ reactor experiment (from [43]).

- **K2K** is a long baseline neutrino oscillation experiment: a wide-band ν_μ neutrino beam is generated in the KEK 12 GeV PS and a neutrino beam-line. The far detector is Super-Kamiokande, which is located at a distance of 250 km from the neutrino production site. Various beam monitors along the beam line and two different types of front detector (a scintillating fiber detector and a 1 $kton$ water Čerenkov detector) have also been constructed at KEK site. The K2K experiment started in early 1999 and two data taking phases took place (corresponding to the Super-Kamiokande accident and recovery, see section 1.2.1); results on both ν_μ disappearance ($\nu_\mu \leftrightarrow \nu_\tau$ oscillations) and ν_e appearance ($\nu_\mu \leftrightarrow \nu_e$ oscillations) confirm existent results from atmospheric and reactor neutrinos respectively (see figure 1.23) [63];

- **MINOS** is designed to detect neutrinos delivered by the Main Injector accelerator at Fermilab (NuMI); two detectors, functionally identical, will be placed in the NuMI neutrino beam: one at Fermilab and the second one in Soudan iron mine, 732 km away. MINOS will be able to precisely measure the oscillation parameters in the $\nu_\mu \to \nu_\tau$ channel, but the experiment can also be sensitive to the presence of $\nu_\mu \to \nu_s$ oscillations, as well as to improve $\nu_\mu \to \nu_e$ limits. The far detector is installed and atmospheric neutrino data taking started in July 2003; the near detector installation is close to completion and neutrino beam delivery is foreseen for early 2005 [80].

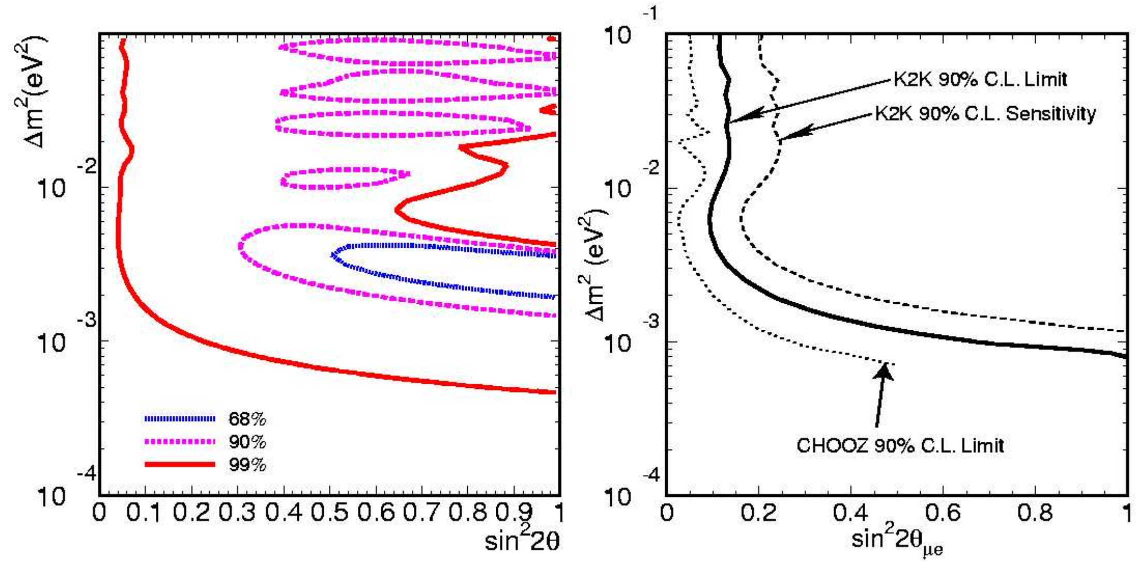

Figure 1.23: K2K results: allowed region for ν_μ disappearance (left) and exclusion plot for $\nu_\mu \to \nu_e$ oscillations (right), compared to CHOOZ result.

Chapter 2

Borexino: physics goals and detector design

The Borexino experiment is devoted to the real time detection of low energy ($\leq 1MeV$) solar neutrinos. This energy region is more sensitive to neutrino oscillations: in particular, the importance of the monochromatic ^7Be line ($0.862MeV$, 90%) has been explained in section 1.2.2. No direct measurement of ^7Be neutrinos has been performed yet.

An international team composed by Italian, German, American, Russian, Hungarian and French physicists is collaborating for the realization of this challenging project.

Technical developments were realized in order to reach and detect unique low levels of radioactive contaminations. Cosmic ray induced radioactivity is reduced locating the experiment underground and is detected via hardware veto. Natural radioactive elements like uranium, thorium and their daughter nuclei, radon and krypton gases, ^{14}C and potassium, etc. decay with an energy release in the region of interest. Only via a strict materials selection and an effective scintillator purification, the signal to background ratio of the experiment can reach a value of ~ 1.

The detector is now in its final assembly phase in the underground laboratories of Gran Sasso (LNGS), Italy.

2.1 Physics goals

Solar neutrino detection in Borexino is based on the well known technique of liquid scintillator spectroscopy. The non standard aspect consist in the use of an unsegmented volume composed by 300 *tons* of ultra-pure liquid scintillator surrounded by 1000 tons of passive buffer. About 2200 photomultipliers detect the scintillation light.

The detection reaction is neutrino elastic scattering off the electrons contained in the scintillator ($\nu + e^- \rightarrow \nu + e^-$). Electron neutrinos can interact with electrons via charged and neutral current reactions, while muon and tau neutrinos only undergo

Figure 2.1: A view of the Gran Sasso mountain, with the external buildings of the Gran Sasso National Laboratories of INFN.

neutral current reactions; for this reason, in the energy range of interest, $\sigma_\mu \sim \frac{1}{5}\sigma_e$. The reaction cross section is well defined in the frame of electro-weak theory [84]:

$$\sigma_e(q,T) = 101.0 \times 10^{-46} \cdot \left[1 - 0.18\frac{T}{q} + 0.090\left(1 - \frac{1.62}{T}\right)\left(\frac{T}{q}\right)^2\right] \; cm^2 \qquad (2.1)$$

$$\sigma_{\mu,\tau}(q,T) = 21.7 \times 10^{-46} \cdot \left[1 - 0.84\frac{T}{q} + 0.42\left(1 + \frac{0.60}{T}\right)\left(\frac{T}{q}\right)^2\right] \; cm^2 \;, \qquad (2.2)$$

where T and q are neutrino and electron energy (respectively). At ^7Be neutrino energies, these cross sections are approximately: $6{\cdot}10^{-45}\,cm^2$ for ν_e and $1.2{\cdot}10^{-45}\,cm^2$ for ν_μ and ν_τ.

In this section, basic considerations about the neutrino signal expected in Borexino (in standard and non standard scenarios) will be discussed, together with the main sources of background.

2.1.1 Neutrino signal in the SSM case

The signal from monochromatic ^7Be neutrinos in Borexino will show the typical Compton edge shape in the scattered electron energy spectrum, with an end-point at $0.66\,MeV$ (a simulated signal shape, in absence of background, is shown in figure 2.2); this shape will represent the basic signature for the reaction (the scintillation photon emission is isotropic so the directionality of the reaction is lost). In the energy window between 0 and 0.66 MeV, we expect an event rate of ~ 0.5 scattered electrons each day per ton of target material, in a standard scenario where neutrinos do not oscillate.

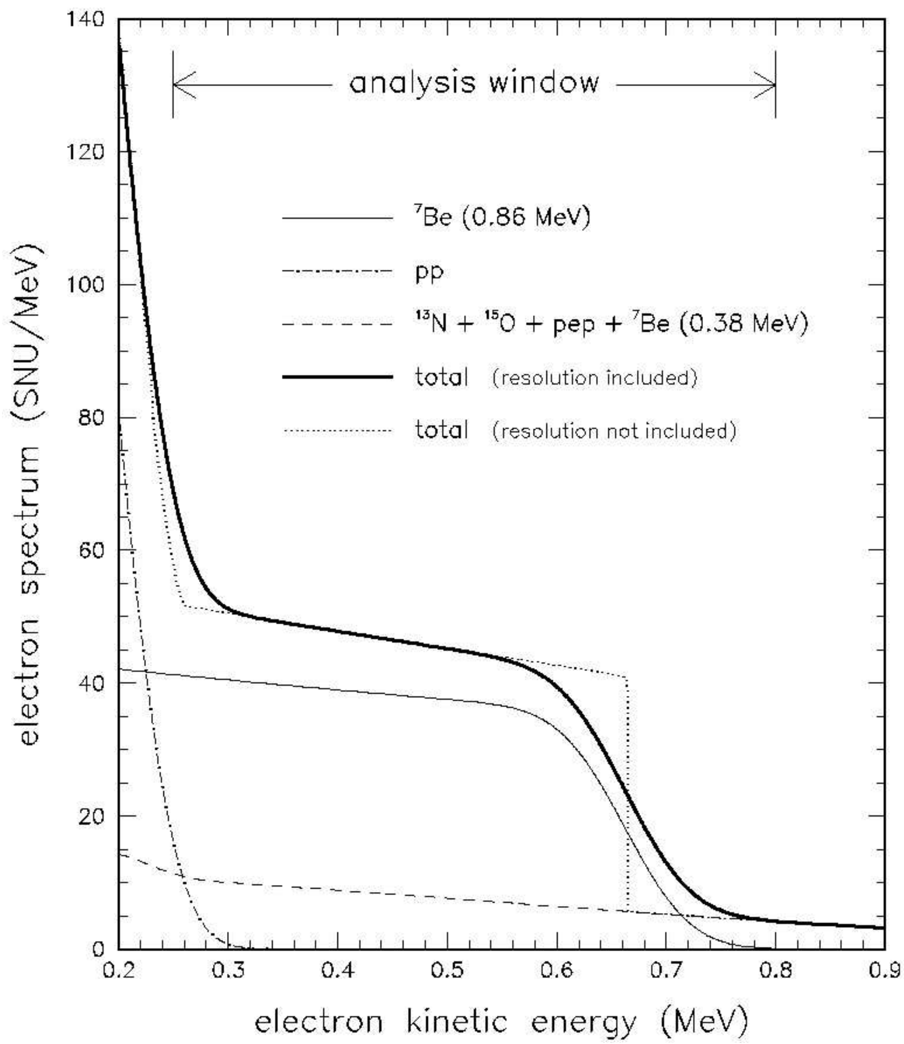

Figure 2.2: Simulated energy spectrum of recoil electrons in Borexino, for different sources of solar neutrinos; the effects of energy resolution are also shown (from [44]).

A $\pm 3.5\%$ time variation of the signal during the year is expected from the variation of solid angle in the Earth orbit. Even if the effect is very small, it can be used as a confirmation of the solar origin of detected neutrinos.

2.1.2 Neutrino signal in oscillation scenario

The solutions to the Solar Neutrino Problem in terms of neutrino oscillation will provide a substantial reduction of the flux measured by Borexino due to flavor conversion. The flux reduction depends on the specific case of neutrino oscillation; as described in chapter 1, the possible solutions[1] are [20]:

- **MSW effect:** in case of LMA and LOW solutions, ^7Be electron neutrinos undergo an incomplete flavor conversion, hence resulting in a partial suppression of the SSM signal; expected rates are: $64\% \pm 7\%$ and $58\% \pm 5\%$ of the SSM, respectively; for the LOW solution, the observation of an earth regeneration effect is expected, featuring a day-night asymmetry of $23\% \pm 12\%$;
- **Vacuum oscillations:** in this scenario the expected rate is $40\% \pm 14\%$ of the SSM; the annual variation of the signal is enhanced to $\sim 25\%$ and also a day-night effect of the $\sim 8\%$ is present. In figure 2.3, the annual modulations in two vacuum solutions are shown, compared to the non oscillation case.

The survival probabilities for solar neutrinos in the three different scenarios are reported in figure 2.4, while the predicted event rates are listed in table 2.1.

Neutrino Source	SSM	LMA	LOW	VAC
pp	1.3	0.8	0.7	0.8
^7Be	45.7	29.2	26.5	18.2
pep	2.0	1.0	0.9	1.4
^{13}N	4.2	2.2	1.9	2.2
^{15}O	5.5	2.5	2.4	3.0
Total	58.7	35.7	31.5	25.6

Table 2.1: Neutrino signals expected in Borexino in counts per day in the energy window $0.25 - 0.8\ MeV$, in SSM case and for three oscillations scenarios.

2.1.3 Internal background

Without an event by event signature for neutrino events, it is mandatory to have a low background counting rate which is lower than the neutrino signal. The foundation of a “new technology” was requested in order to detect these rare low energy

[1] We refer here to the allowed solutions after the SNO NC publication (LMA, LOW and VAC solutions) even if, after the KamLAND results, only the LMA solution remains valid.

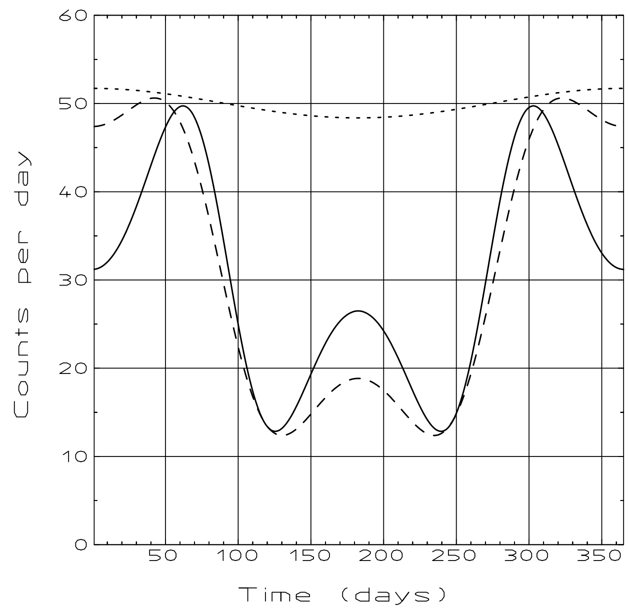

Figure 2.3: Annual modulations of the expected countrate in Borexino, in the non oscillation case and for two different vacuum solutions ($\delta m^2 = 4.2 \cdot 10^{-10} eV^2$ and $\delta m^2 = 3.2 \cdot 10^{-10} eV^2$); from [8].

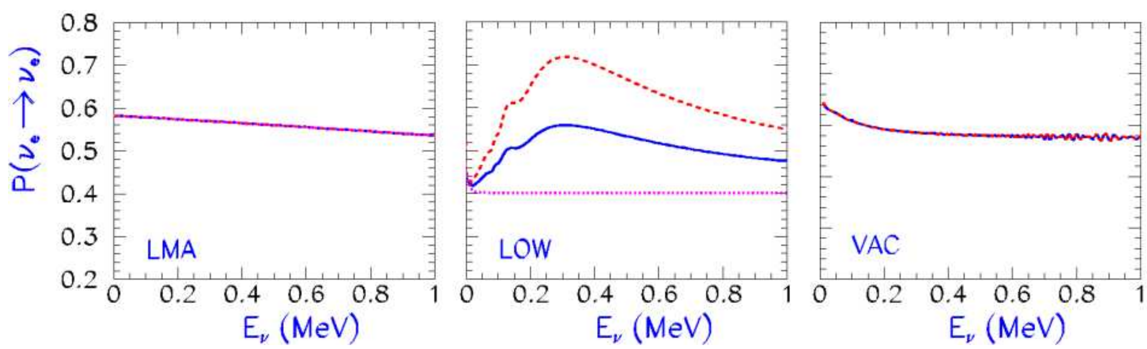

Figure 2.4: Survival probabilities for sub-MeV solar neutrinos, in three different oscillation scenarios: the dotted line (purple) does not include earth regeneration, the dashed line (red) includes regeneration at night and the full line (blue) refers to the day-night averaged survival probabilities (from [20]).

events in real time [8]; the background sources have been classified into three different classes: internal, external and surface background.

Intrinsic background contained in the liquid scintillator is classified as *Internal Background*. The most important internal sources of background for Borexino are:

- ^{14}C**:** the β particles ($Q = 156\ keV$) emitted by ^{14}C decay set the low energy threshold of the experiment at $\sim 250\ keV$. In spite of the threshold, some ^{14}C events can fall into the so-called *Neutrino Window* (NW, $0.25 - 0.8\ MeV$), due to the energy resolution of the detector. Another issue is represented by the pile-up events (pile-up is a coincidence event composed by two ^{14}C decays reconstructed in the fiducial volume); due to the possible difficulties in separating via software two events very close in time ($\tau \leq 100\ nsec$), this pair of events can be confused with a higher energy single event.

By means of Monte-Carlo simulations of the experiment, it is possible to estimate the number of ^{14}C events mimicking a neutrino signal, in case of both single and pile-up events. With a $^{14}C/^{12}C$ ratio of a few 10^{-18}, the total ^{14}C rate (above 70 keV) would be in the 10 Hz range (in 300 *tons* of liquid scintillator), but the number of ^{14}C events above 250 keV would remain lower than 1 $count/day$: therefore, this rate would represent a tolerable background. As described in [7], the $^{14}C/^{12}C$ ratio in Borexino scintillator, as measured in CTF, amounts to $\sim 10^{-18}$, therefore it satisfies the above constraints;

- **^{238}U, ^{232}Th and ^{40}K:** Borexino can tolerate levels of U and Th not greater than $10^{-16}g/g$. This level was detected in scintillator for the first time in CTF-1, demonstrating the conceptual feasibility of the experiment (see chapter 4). If we consider a level of $10^{-16}\ g/g$ for U and Th and $10^{-14}\ g/g$ for K_{nat}, we find in the NW $\sim 26\ \beta + \gamma$ events/day and $\sim 122\ \alpha$ events/day in a $100 - ton$ fiducial volume (FV), assuming secular equilibrium for U and Th[2].

  Some of these events can be identified off-line, as we will explain later (see chapter 4). One of the possible rejection techniques is based on delay coincidences identification (an identification efficiency of 95% would reduce the background down to $\sim 25\ \beta + \gamma$ events/day and $\sim 118\ \alpha$ events/day in the FV); a second method is based on pulse shape discrimination analysis, relying on the fact that the time profile of the pulse produced by an α event in liquid scintillator is different from the one due to a β event [71] (with an identification efficiency of 90%, the α background would lower down to ~ 34 events/day in the FV); finally, while tagging delayed coincidence events, the activity of the parent isotopes is also known: then a statistical subtraction of these isotopes can be applied[3] (a 95% efficiency could furthermore reduce the background down to $\sim 13\ \beta + \gamma$ events/day and $\sim 19\ \alpha$ events/day in the FV);

- **^{222}Rn:** radon is a noble gas produced in the ^{238}U chain, characterized by very large diffusion coefficients in air and through various materials. Radon contamination can come from a direct contact with air or through emanation of environmental materials. In order to reduce possible contaminations a strict selection of all materials involved in the detector construction was realized via

[2] These numbers have to be compared with the expected neutrino rates, as reported in table 2.1.
[3] The effectiveness of such a method can be enhanced by means of a spectral analysis [46].

a new radon emanation measurement technique developed by the Heidelberg group [60, 78, 10];

- **^{85}Kr, ^{39}Ar:** these rare-gas radioisotopes are much less abundant in atmosphere than the radon; nevertheless, ^{85}Kr was identified as a background source through CTF measurements, via a $\beta - \gamma$ coincidence analysis (see section 4.3). Both nuclides are crucial for the experiment, because of their long lifetime and of the β particles emission, falling in the energy range of the neutrino signal. The acceptable concentration limits in nitrogen (used for tanks blanket or water and PC stripping) are: 0.31 *ppm* ^{39}Ar and 0.14 *ppt* ^{85}Kr (0.44 μBq $^{39}Ar/m^3$ and 0.14 μBq $^{85}Kr/m^3$).

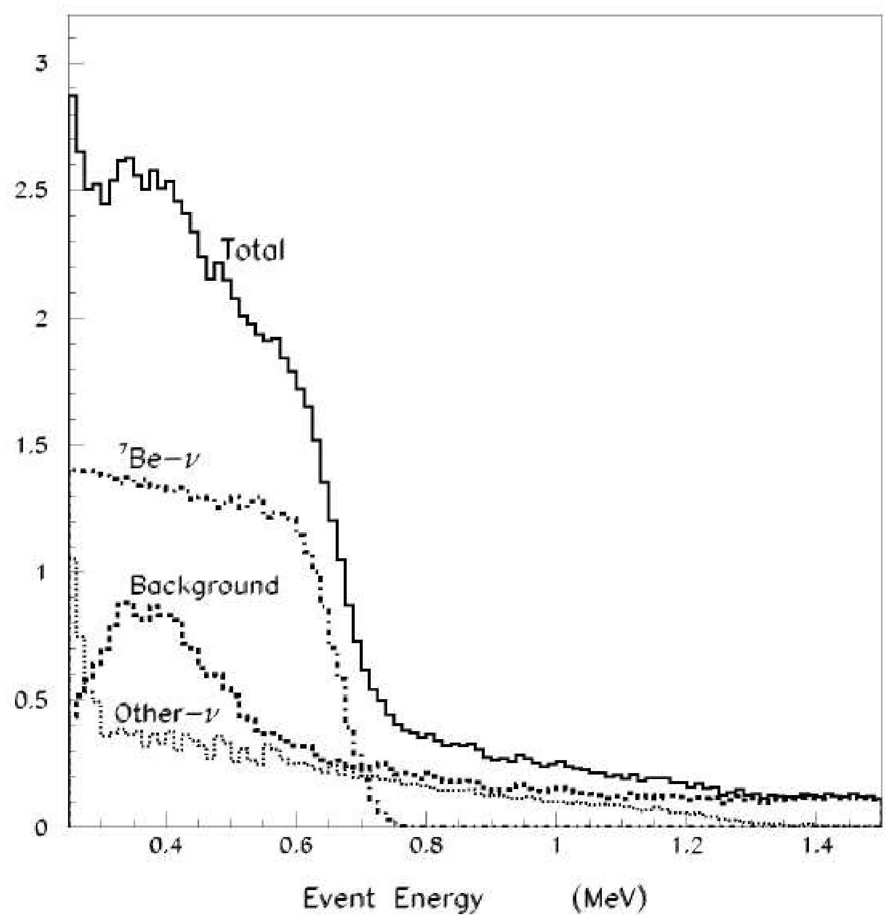

Figure 2.5: Monte Carlo simulation of ν signals (in arbitrary units) and background: the $^7Be-\nu$ signal expected from the SSM (dotted-dashed), the signal from all other neutrino sources together (dotted), the expected background with all the described cuts (dashed), the sum spectrum from all events (solid line).

2.1.4 Surface background

Possible contaminants coming from the Inner Vessel materials (see section 2.2) are classified as *Surface Background*. The nylon film used in Inner Vessel construction meets the most stringent cleanliness requirements, since it is the only material in direct contact with the liquid scintillator. Radon exposure during production and installation was kept under a strict control in order to avoid the build-up of Radon daughters [73] (among them, we recall the ^{210}Pb, whose half-life is greater than $22\ yr$); furthermore, several different materials have been measured before the choice of the adopted film [34].

2.1.5 External background

The γ-rays emitted outside the Inner Vessel create what we call *External Background*. The suppression of this flux played a major role in the detector construction: a systematic measurement and selection of the materials were realized in order to reduce this contamination. The principal sources of such a background are: photomultipliers and light concentrators, rock walls of the experimental hall, environmental materials composing the detector. Some of the fundamental contributions to the number of γ events entering the Neutrino Window are reported in table 2.2.

It is useful to point out that the radial distribution of these events can allow an off-line identification and an efficient rejection; actually, the Borexino fiducial volume will be optimized depending on the observed external activity.

Component	^{238}U (g/g)	^{232}Th (g/g)	^{nat}K (g/g)	Total Mass (g)	Rate in NW (ev/day/100ton)
2000 PMTs	$3 \cdot 10^{-8}$	$1 \cdot 10^{-8}$	$2 \cdot 10^{-5}$	$38 \cdot 10^{6}$	0.06
Light guides	$2 \cdot 10^{-10}$	$1 \cdot 10^{-9}$	$3 \cdot 10^{-7}$	$6 \cdot 10^{6}$	0.01
PC Buffer	$1 \cdot 10^{-15}$	$1 \cdot 10^{-15}$	$5 \cdot 10^{-12}$	$8.7 \cdot 10^{8}$	≤ 0.004
^{222}Rn in Buffer					0.03
Nylon Vessel	$2 \cdot 10^{-11}$	$2 \cdot 10^{-11}$	$1 \cdot 10^{-8}$	$5 \cdot 10^{4}$	≤ 0.04
SSS	$2 \cdot 10^{-10}$	$1 \cdot 10^{-9}$	$3 \cdot 10^{-7}$	$3.7 \cdot 10^{7}$	≤ 0.007
Cables	$2.1 \cdot 10^{-8}$	$2.4 \cdot 10^{-8}$	$7 \cdot 10^{-6}$	$2 \cdot 10^{5}$	≤ 0.003
Rock					≤ 0.005
Total					0.11 ± 0.05

Table 2.2: Expected external and surface backgrounds in the fiducial volume coming from the different sources; detector components will be described in section 2.2

2.1.6 Muon induced background

A separate background issue for Borexino is due to the residual muon flux at Gran Sasso depth. Estimated muon flux in Borexino will be $\sim 25\ \mu/day/m^2$: this rate will contribute significantly to the total experimental rate.

Muons crossing the scintillator are easily rejected, due to the huge energy amount of these events, compared to the neutrino ones; nevertheless, muon interactions can mimic neutrinos in the following cases:

- muon crossing the buffer liquid: if muons interact in the liquid outside the Inner Vessel, they can lose energy via Čerenkov effect; a fraction of the produced light can be detected in PMTs, simulating a scintillation event. These events can be disentangled due to the "up-down" asymmetry of the associated Čerenkov light (details are given in chapter 4); moreover, a dedicated muon tagging system has been installed in the detector (see below);

- radioactive isotopes production: muon interactions in scintillator can induce the creation of radioactive elements, even if the absence of isotopes heavier than $^{12,13}C$ in the liquid scintillator limits the cosmogenic radioactivity problem. The possible long lived radioactivities from a carbon target that can hardly be vetoed by the muon signal are: ^{11}B,^{11}C,^{10}C and ^{7}Be[4]; among them, the only dangerous element for Borexino is ^{7}Be, which decays via a 487 keV γ. Considering the very low production rate for ^{7}Be in underground laboratories ($\sim$ 0.4 atoms/day in 100 ton of scintillator [57]), the best solution to this problem is to minimize the cosmic ray exposure of the scintillator during the transport (^{7}Be half-life is 53 days: therefore, a persistent background for several months could arise from a long exposure): presently, the main component of Borexino scintillator reaches the Gran Sasso Lab in less than 2 days from its production time;

- neutron production: muons can produce neutrons due to the interaction on the different detector media; these neutrons are then captured by protons, producing a 2.2 MeV γ-ray: if such a capture takes place in buffer liquid, a fraction of the γ energy can reach the active scintillator volume, simulating a scintillation event in the NW.

2.2 Borexino detector

Borexino is located in Hall C of the Gran Sasso Laboratories (LNGS). The Laboratories are located besides the Gran Sasso tunnel (10.4 km long) on the highway connecting Teramo to Rome, at about 6 km from the west entrance. They consist of three experimental halls, named hall A, B and C, and a series of connecting tunnels

[4] A detailed discussion on cosmogenic background rejection can be found in [46].

and service areas. The three experimental halls are $\sim 70\ m$ long and about $18\ m$ high and large. The laboratory is located at $963\ m$ over the sea level and the maximum thickness of the rock overburden is $1400\ m$, corresponding to $3800\ mwe$. As already pointed out, the residual muon flux at Gran Sasso depth is $\sim 25/d/m^2$. The radioactive elements in the rock of the hall produce a $\gamma - ray$ flux of $\sim 10^8/d/m^2$ [8].

Figure 2.6: A recent picture of the Hall B of the Gran Sasso Laboratories, after the decommissioning of the MACRO experiment.

2.2.1 Detector structure

The Borexino detector is designed in order to reduce $\gamma - ray$ background in the core via a graded shielding. This approach is realized through different layers of increasingly radio-pure materials. The detector structure is sketched in figure 2.8: starting from the interior we find the following parts:

- **Liquid Scintillator:** the selected mixture is composed by pseudocumene (PC, 1,2,4-trimethylbenzene, $C_6H_3(CH_3)_3$) as a solvent and by the fluor PPO (2,5-diphenyloxazole, $C_{15}H_{11}NO$) as a solute, at a concentration of $1.5\ g/l$. The studies realized by the collaboration about this scintillator are reported in [9, 6] and the main characteristics are summarized in table 2.3. Due to the needed external background rejection, only the internal $100\ t$ of scintillator will be used as target (Fiducial Volume), selected by means of "software" cut; the remaining $190\ t$ of scintillating mixture will be used as an active buffer;

Figure 2.7: A pictorial view of the Gran Sasso Underground Lab, where the experimental halls and the interconnection tunnels are shown.

General Characteristics	
Total Mass	$\sim$ 290 tons (8.5 m diameter IV)
FV Total Mass	100 tons (6 m diameter software cut)
Density	0.88 g/cm^3
Optical Characteristics	
Primary Light Yield	$\sim 10^4$ photons/MeV (@380 nm)
Peak Emission wavelength	365 nm
Attenuation length	$\geq 5m$ (@430 nm)
Decay lifetime without abs/reem	~ 3.5 $nsec$ (β particles)
Decay lifetime with abs/reem	~ 5 $nsec$ (β particles)
Physical Characteristics	
α-quenching (E)	$Q(E) = 20.3 - 1.3E[MeV]$
Radioactivity Characteristics	
^{238}U	$(3.5 \pm 1.3) \cdot 10^{-16} g/g$
^{232}Th	$(4.4 \pm 1.5) \cdot 10^{-16} g/g$
$^{14}C/^{12}C$	$(1.94 \pm 0.09) \cdot 10^{-18}$

Table 2.3: Main characteristics of Borexino liquid scintillator.

- **Inner Vessel and Radon Barrier:** the Inner Vessel is the 8.5 m diameter nylon sphere containing the scintillating mixture. It is made by a 125 μm thick transparent nylon; the chosen polymer is the Sniamid ADS40T (nylon-6

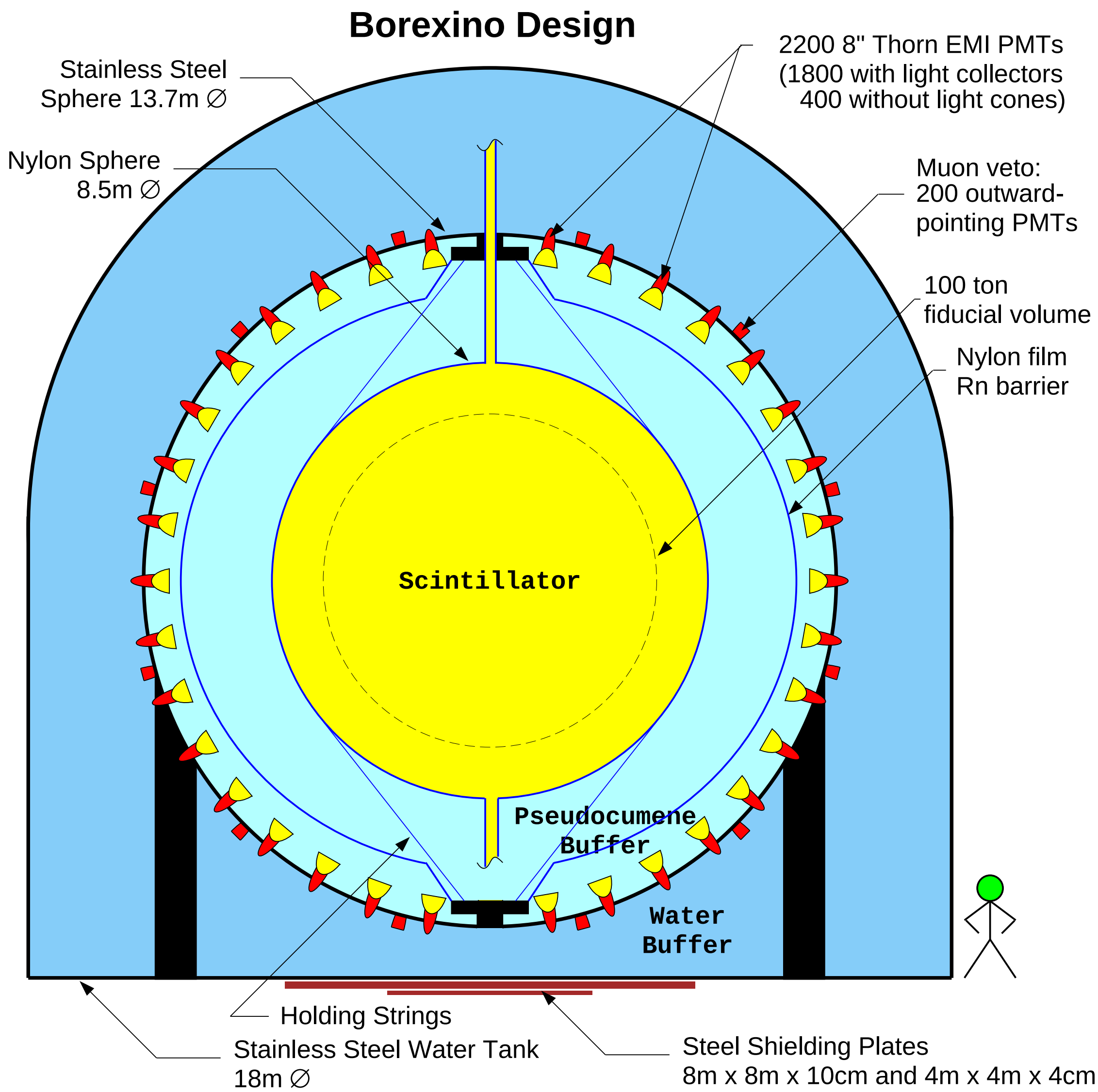

Figure 2.8: A schematic view of Borexino detector.

copolymer), characterized by a very low radio emanation activity. The vessel is anchored to the detector by means of a system of strain gauges (a set of ropes equipped with loan cells, in order to monitor buoyancy forces and mechanical stability). A second nylon vessel (made of the Nylon-6 Capron B73ZP polymer) has been installed outside the previous one (11 m of diameter): its purpose is to reduce radon diffusion from outside to the inner part of the detector. Many details on Inner and Outer Vessel fabrication can be found in [34, 73]; the installation of the two vessels happened in Gran Sasso in April 2004 (see pictures);

Figure 2.9: Two phases of Nylon Vessels construction in Princeton cleanroom (May 2002).

- **Buffer Liquid:** the Inner Vessel volume will be inserted in a passive buffer liquid, providing the suppression of γ-rays produced by external radioactivity. In order to reduce practically the buoyancy force on the IV to zero, a buffer liquid composed by pure PC was selected (this solution allows also to prevent optical effects at the interface between the two different materials, in case of a mismatch of refraction indexes). The total needed mass is $\sim$ 1040 tons; a light quenching compound DMP (dimethylphthalate) [37] is added with a concentration of 5 g/l in order to reduce the scintillation light produced by γ-rays coming from the external background in the buffer. The light mean free path lengths and Čerenkov light emission yield, important for the muon veto, are not affected by the presence of DMP;

- **Stainless Steel Sphere (SSS):** a 13.7 m diameter, $8 \div 10$ mm thick stainless steel sphere (SSS) contains the scintillator (and buffer liquid) and it is used as a support structure for the PMTs. It is sustained by 20 legs which are welded on the base plate of the water tank. The sphere divides hermetically the 2 m external shield layer of ultrapure water from the inner scintillator;

- **Phototubes and Light Concentrators:** the 2212 PMTs installed in Borexino have been produced by the ETL company (with the label ETL9351) and have a 20 cm photocathode diameter. They are installed inside the sphere and connected by feed-through across the sphere wall to a single cable outside the sphere. The back-end sealing has been designed to be compatible for operation in PC and in water. 1800 PMTs are equipped with light concentrators to enhance the geometrical coverage to the $\sim 30\%$. The other 400 are dedicated to the internal muon veto system;

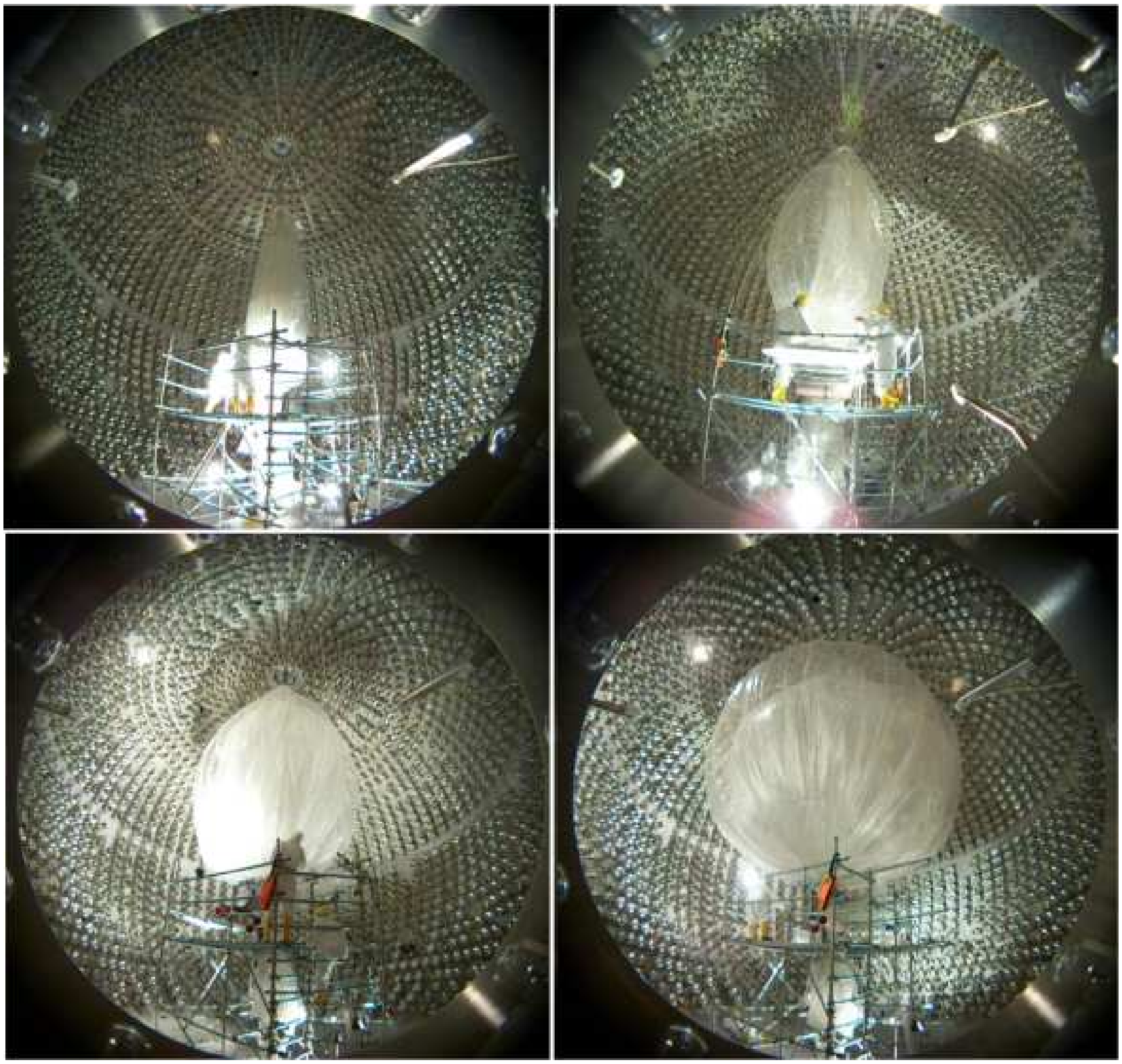

Figure 2.10: Four steps in nylon vessels installation and inflation inside Borexino detector (April 2004).

- **Muon Veto:** the muon rejection detector consists of an internal and an external component. The internal detector is featured by the 400 internal PMTs without light concentrators; it has been designed in order to detect muons crossing the buffer liquid: its operation principle relies on the light distribution of these events (the PMTs without concentrator are most sensitive to the light coming from the external volume of the SSS). Other 210 PMTs have been mounted outside the sphere and will work as outer muon veto, detecting Čerenkov light produced in the water buffer; a complete encapsulated sealing design was developed for the outer muon veto PMTs. The overall muon veto system has been designed in order to establish a muon identification which

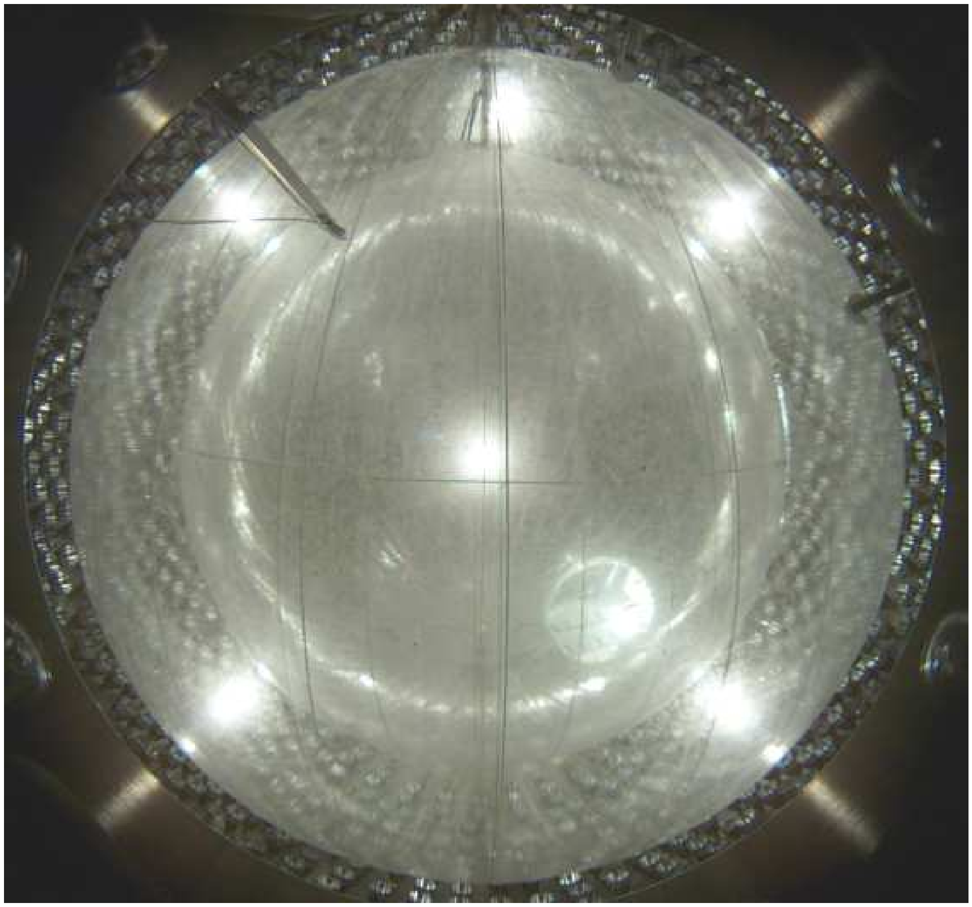

Figure 2.11: Final nylon vessels position in the Borexino Sphere, after the completion of the inflation with synthetic air: outer and inner vessels are clearly visible.

suppresses this background by a factor 10^4;

- **Water Buffer and Water Tank:** Overall containment of the detector is provided by a domed cylinder external tank 18 m in diameter and 16.7 m high. Deionized water provides at least a 2 m shielding against external gamma and neutron radiation. In order to increase the cosmic ray detection efficiency, the water tank internal wall is covered by *Tyvek* sheets, which reflect the Čerenkov light irradiated by cosmic rays crossing water.

2.2.2 Auxiliary systems

Auxiliary systems maintain the detector operative and allow manipulation of the different liquids:

- **Water Purification Plant:** $\sim$ 2000 t of ultrapure water are used as a shield against external background and as a highly transparent Čerenkov medium; $\sim$

Figure 2.12: Installed outer muon veto PMTs: the encapsulation of PMTs is clearly visible, as well as the calibration optical fiber; white material is the *Tyvek* covering of water tank internal walls.

1000 for CTF shield, different tons for cleaning the detector and the auxiliary system are used as well. The production system is based on reverse osmosis process and can provide 2 m^3/h of ultrapure water;

- **Scintillator Storage, Purification and Handling:** a very complex plant is installed in Hall C, in order to store 300 t of liquid scintillator in 4 storage tanks and to handle and purify all the amount of scintillator needed for Borexino. The system consists of electro-polished stainless steel plumbing and radon tight valves and fittings. On-line purification is based on four systems: gas removal, water extraction, distillation and solid column chromatography. All these systems are under test and improvement using the CTF detector (see chapter 4);

- **Nitrogen Distribution System:** pure and ultra-pure nitrogen is used for various purposes in Borexino, like stripping columns and blanket of the tanks. The nitrogen plant consists of three 6 m^3 storage tanks, two atmospheric evaporators and a water bath electric heater to produce regular nitrogen of up to 250 m^3/h. High purity nitrogen is produced by charcoal column purification of the liquid nitrogen prior to evaporation: it can supply up to 100 m^3/h of nitrogen [8]. A plant for low $^{39}Ar -^{85} Kr$ nitrogen ($LAKN_2$) is also present: liquid nitrogen meeting the required Ar and Kr concentrations is produced by an external company and delivered to Gran Sasso in a special tank, which is used also as a storage; the LAK gaseous N_2 is produced by direct evaporation from the storage tank and feeded into hall C through a dedicated line;

- **Signal Processing and Data Acquisition:** the Borexino read-out system will be described in its details in chapter 5.

Chapter 3

Non-solar neutrino physics with the Borexino detector

While the basic objective of Borexino is the direct observation and measurement of the solar $^7Be - \nu$ flux, the facility can be applied to a broad range of frontier questions in particle physics, astrophysics and geophysics. The unique low energy sensitivity and ultra-low background in Borexino bring new capabilities to attack problems in these fields. Much of this research can be undertaken simultaneously with solar ν observations; in particular, antineutrino ($\overline{\nu}_e$) spectroscopy can be performed simultaneously with a distinct tag independent of solar$-\nu$ spectroscopy.

3.1 Anti-neutrino detection in Borexino

The best method to detect ($\overline{\nu}_e$) is the classic Reines reaction of capture by protons in the scintillator liquid: $\overline{\nu}_e + p \to n + e^+$. The positron visible energy (kinetic energy $+1.02\ MeV$ annihilation energy) yields $E = E(\overline{\nu}_e) - Q$, where the threshold energy is $Q = 1.8\ MeV$. The $\overline{\nu}_e$ tag is made possible by the delayed coincidence between the positron signal and the $2.2\ MeV$ $\gamma-$ray emitted by neutron capture on proton, after a $200\ \mu s$ delay; the tag suppresses background by a factor ~ 100, therefore the presence of an active buffer is not crucial: in favorable circumstances, the entire scintillator mass ($300\ t$) may be utilized. Overall, a signal rate of a few $\overline{\nu}_e$ event per year in $300\ t$ appears measurable. The most interesting $\overline{\nu}_e$ sources are supernovae, the Sun itself, the Earth and nuclear power reactors, which can be distinguished from each other mainly by the characteristically different energy spectra of the signals.

3.1.1 Anti-neutrinos from the Earth's interior

The Earth emits a very small heat flux, with an average energy value of $\phi_H = 80\ mW/m^2$; integrating over the whole Earth surface, we obtain nevertheless an important heat flux of $\Phi_H = 40\ TW$. The source of this energy is not understood quantitatively, but the radiogenic heat from the decay of U and Th in the Earth's crust is currently believed to account for $\sim 40\%$ of the total 40 TW heat flow. The radiochemical composition of the Earth can in principle be studied by detecting the $\overline{\nu}_e$ emitted by the decay of radioactive isotopes; confirming the abundance of certain radio-elements could establish important geophysical constraints on the heat generation within the Earth [68].

The main contribution of the radiogenic heat should be due to the two decay chains ^{238}U and ^{232}Th and the decay of the ^{40}K (^{235}U and ^{87}Rb provide smaller contributions). Borexino can make a basic contribution to testing geothermal models, by detecting $\overline{\nu}_e$ emitted by these nuclides in the energy range of $(1.8 \div 3.3)$ MeV. The energy threshold of the detecting reaction is 1.8 MeV; the terrestrial antineutrino spectrum above 1.8 MeV has a 2-component shape (see figure 3.1): the high energy component (~ 2 MeV in the emitted positron spectrum) coming from the U chain only and the low energy component (~ 1.2 MeV) coming with contributions from both U and Th chains: this signature could allow individual assay of U and Th abundance in the Earth.

Combining data from Borexino (Eurasian plate) with those from the KamLAND detector or similar (interface of Asian and oceanic crusts), the relative distribution of U/Th in the continental and oceanic crusts may be probed. Depending on the geophysical model, $\overline{\nu}_e$ rates between 10 and 60 ev/yr can be expected in Borexino.

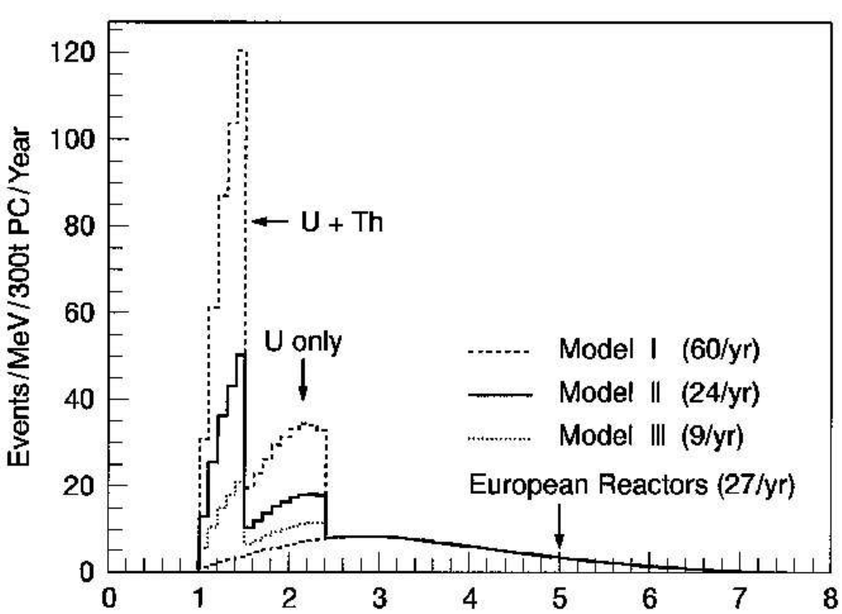

Figure 3.1: The expected shape of terrestrial antineutrinos in Borexino, according to three different geophysical models (from [75]).

3.1.2 Long-baseline $\overline{\nu}_e$ from European reactors

The $\overline{\nu}_e$ fluxes from astrophysical sources (including the Earth) are essentially model-dependent; on the contrary, nuclear power reactors emit $\overline{\nu}_e$ with a known flux and spectral shape, with energies up to $\sim 8\ MeV$. Borexino is sensitive to this flux from power reactors situated all over Europe (European reactors produce about 500 $GW$of thermal power) at an average baseline distance of $\sim 800\ km$ (Italy has no nuclear power reactors): reactor anti-neutrino flux will account for $\sim 30\ ev/yr$ in Borexino. Since the distances to the reactors are known, and the fuel composition and operating cycle of the reactors can also be known very well, the multi-reactor $\overline{\nu}_e$ event rate and the positron spectrum in Borexino can be calculated with an error lower than 3%.

The well defined set-up offered by this combination makes an ideal terrestrial long-baseline experiment for a model-independent search for ν oscillations. Evidence for neutrino oscillations would come from the disappearance of these neutrinos and from distortions in their spectral shape. As usual, the characteristic oscillation length varies inversely with energy (1.26): therefore, reactor neutrinos, with energies up to 8 MeV, allow very small mass differences to be probed. In Borexino, the sensitivity for vacuum ν oscillations is in the range $\delta m^2 \simeq (10^{-3} \div 10^{-5})\ eV^2$, filling the gap between the results of the CHOOZ experiment and solar neutrinos. The European reactor-Borexino combination is also suitable to probe neutrino oscillations in the LMA-MSW area, as is done in the KamLAND experiment.

3.1.3 Anti-neutrinos from the Sun

The SSM predicts no $\overline{\nu}_e$ emission from the Sun. However, non-standard physics can create $\overline{\nu}_e$ by some conversion mechanisms. For instance, a non-vanishing neutrino magnetic moment at the level of $10^{-12} \div 10^{-11}\ \mu_B$ could lead to the presence of anti-neutrinos in the solar neutrino spectrum. This scenario could play a subdominant role in the physics of solar neutrinos, the MSW-LMA being the dominant one. The mechanism of neutrino-antineutrino conversion due to spin-flavor precession (SFP) induced by neutrino transition magnetic moment was discussed for the first time as a possible solution to the Solar neutrino deficit problem: the interaction of the neutrino magnetic moment with solar magnetic fields could produce the required spin-flavor precession, with a flavor conversion into μ or τ antineutrinos. Because of the maximal mixing inherent in the model, the resulting μ/τ anti-neutrinos would in turn oscillate into $\overline{\nu}_e$ thanks to the vacuum oscillation mechanism; they would then be detected as $\overline{\nu}_e$ when reaching the Earth.

Recently, the interest in a large neutrino magnetic moment was revised, due to the new experimental data available from KamLAND detector [41]. In the energy range $8.3 < E_{\nu_e} < 14.8\ MeV$, no candidate anti-neutrino events were observed in KamLAND, during a 185.5 live days measurement period; considering the expected background, the computed limit on solar $\overline{\nu}_e$ flux in the above energy range is: $\phi_{\overline{\nu}_e} <$

$3.7 \times 10^2\ cm^{-2}\ s^{-1}$ at the 90% $C.L.$, corresponding to an upper limit on the neutrino conversion probability of 2.8×10^{-4} at the 90% $C.L.$ (normalizing to the solar $^8B\ \nu_e$ flux). Expected Borexino sensitivity to solar anti-neutrinos can be estimated by the CTF performances (see chapter 4); it will be comparable to the KamLAND sensitivity (even if with a much smaller target mass), but will be in a wider energy range due to its distant location from nuclear reactors.

3.2 Supernova neutrino detection in Borexino

A typical Type II supernova explosion at a distance of 10 kpc would produce in Borexino a burst of around 110 neutrino events, reaching the detector within a time interval of about 10 s [35]. Most of these events would come from the reaction channel $\bar{\nu}_e + p \rightarrow e^+ + n$, while about 30 events would be induced by the interaction of the supernova neutrinos on ^{12}C in the liquid scintillator: the detection of the neutrino interactions with ^{12}C atoms, is an unique feature of Borexino and KamLAND detectors. Borexino can clearly distinguish between the neutral-current excitations $^{12}C(\nu, \nu')^{12}C^*$ and the charged-current reactions $^{12}C(\nu_e, e^-)^{12}N$ and $^{12}C(\bar{\nu}_e, e^+)^{12}B$, via their distinctive event signatures. The ratio of the charged-current to neutral-current neutrino event rates and their time profiles, with respect to each other, can provide a handle on supernova and non-standard neutrino physics (neutrino mass and flavor oscillation).

3.2.1 Supernova explosions

As explained in section 1.1, at any time during its life a star is in hydrostatic equilibrium: the nuclear energy counter-balances the gravitational energy. Every time the fuel reservoir is exhausted and the resistance to gravitational pressure drops, the star starts collapsing: the temperature of the core increases and new fusion reactions (higher Z) are triggered. By the end of their lives, stars as massive red giants (Mass $> 8M_\odot$) present an "onion" structure, with a very dense core composed of heavy elements, such as Ni and Si, and a gaseous external Hydrogen envelope: for a $18M_\odot$ star at the end of its life, the Silicon core is 10^8 times more dense than the Hydrogen layer.

When ^{57}Fe is produced at the core, by Silicon burning, the star enters the final stage of its life. Energy keeps flowing out, fuel is exhausted, the core pressure drops and the core loses its support. As a consequence, the star implodes under its own weight. To have an idea of the dimensions involved, the diameter of the core drops from 8000 to 20 km and the density increases 7 orders of magnitude in less than a second [81].

The temperature rises to $5 \times 10^9\ K$ ($0.5 MeV/particle$) and the density of the core ($> 10^{10}\ g/cm^3$) makes it a degenerate Fermi gas. The contraction becomes a free-fall and stops only when the core density reaches the nuclear density ($10^{14}\ g/cm^3$).

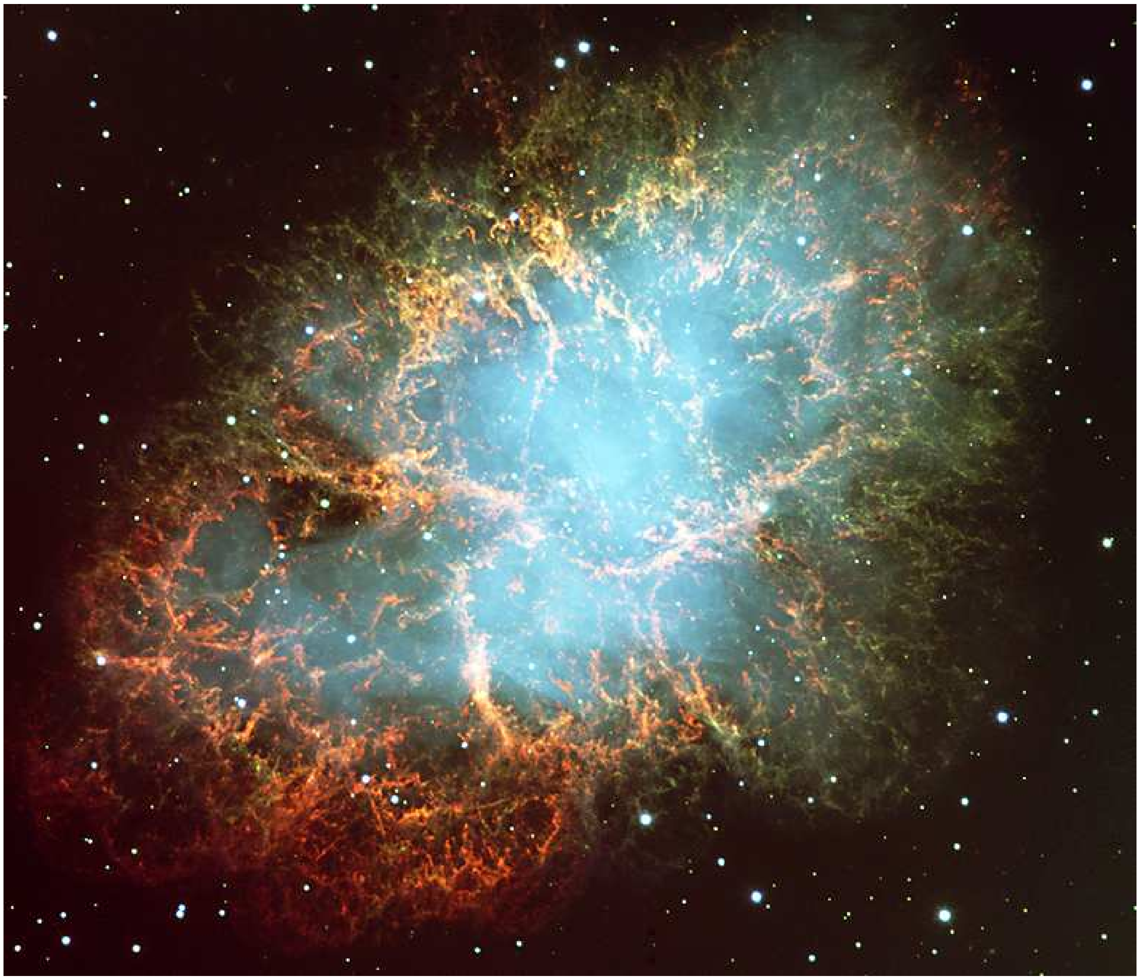

Figure 3.2: A spectacular three color composite image of the well-known Crab Nebula, from the ESO FORS2 instrument (November 10, 1999); it is the remnant of the 1054 supernova explosion: the green light is predominantly produced by hydrogen emission from material ejected by the exploded star, while the blue light is predominantly emitted by synchrotron emission of relativistic electrons; credit: European Southern Observatory.

Here the strong force enters and nucleons start repelling. This is the time when the core bounces, matter starts being released, a shock front starts moving outwards in a rapid expansion and a powerful explosion takes place, ejecting the star's outer layers into space. All that will be left behind is a neutron star. Supernova explosions destroy the most massive stars at the end of their evolution.

The main classification for supernovae is in type I and II. Type I supernovae are usually generated by white dwarfs, with mass $M \sim 1\, M_{\odot}$, and leave no remnant. Type II are the most common type: they are formed by red giants with mass

$M > 8\, M_\odot$ and they leave a neutron star behind.

The frequency of supernova explosions in our Galaxy has been calculated in several independent ways. An analysis based on theories of the stellar evolution, the luminosity function of nearby stars and a model of stellar population yields a rate of $(2.6 \pm 1.3)/century$. A comparison with the occurrence of supernovae in other galaxies gives a consistent result: $(3 \pm 1)(H_0/75)^2/century$.

During the last 2000 years, though, only four supernovae from core collapse (both type I and II) have been identified in our Galaxy, within 4 kpc from the Sun, in the years 185, 1054, 1181, 1670. This gives a rate of $(0.2 \pm 0.1)/century$. It is a real puzzle that no more near supernovae have been observed in the last four centuries: a simple Poisson statistics calculation shows that the probability of not having any supernova in the last 100 years is only 8.2%, assuming a mean galactic rate of $2.5/century$. Thousands supernovae are being observed in distant galaxies, but to date the most interesting to us is SN1987A [81] in the nearby LMC, whose neutrinos have been detected by the Kamiokande [61] and IMB detector [29].

3.2.2 The role of neutrinos in the Supernova explosion

The gravitational collapse events associated with type II supernovae and neutron star formation are copious producers of neutrinos. As stated in [81], regardless of the detail of the collapse, core bounce and explosion processes, in order to form a remnant neutron star there must be an energy release equal to the binding energy $\varepsilon_B \simeq 3 \times 10^{53}\ ergs$. The total light emitted in the supernova outburst is about 1% of this energy; the remainder of the binding energy comes off in the form of neutrinos.

Neutrinos are produced at different stages of the supernova event, through different processes, but most of the binding energy of the star is carried away by the $\nu\bar{\nu}$ pairs produced during the thermal cooling phase of the hot remnant core. These neutrinos, created in pair-production processes such as: $e^+ + e^- \rightarrow \nu_i + \bar{\nu}_i$, are the most efficient energy carriers and constitute the main neutrino signal we can receive, on Earth, from the supernova event [81].

The $\nu_i - \bar{\nu}_i$ pairs produced during the cooling phase do not immediately escape the core. The reason is the weak interaction: at densities $> 10^{11}\ g/cm^3$ the scattering of neutrinos off nuclei happens so often that the neutrinos get trapped. Despite this, the neutrino mean free path remains large, so that they are still efficient energy carriers and they can escape as soon as they pass the neutrino-sphere, defined as the surface within which neutrinos are trapped. This occurs at a density $\sim 5 \times 10^{10}\ g/cm^3$.

The temperature of the neutrino-sphere characterizes the energy distribution spectrum of the neutrinos. ν_μ and ν_τ and their antiparticles present lower opacities than ν_e and $\bar{\nu}_e$, since they interact only via neutral current weak interaction (ν_e and $\bar{\nu}_e$ also do charged current). This means their neutrino-sphere is deeper inside the core and their spectrum is hotter than the one of ν_e and $\bar{\nu}_e$. Moreover, the neutrino decoupling takes place in a neutron rich matter, less transparent to ν_e than $\bar{\nu}_e$. The temperature hierarchy is, then: $T_{\nu_e} < T_{\bar{\nu}_e} < T_{\nu_x}$ (ν_x refers to ν_μ, ν_τ and

Figure 3.3: A very famous picture (with enlargement) of the SN1987A, in the Large Magellanic Cloud, from the NASA Hubble Space Telescope (the three-color image is composed of several pictures of the supernova and its neighboring region taken with the Wide Field and Planetary Camera 2 in Sept. 1994, Feb. 1996 and July 1997): the supernova remnant, surrounded by inner and outer rings of material, is set in a diffuse cloud of gas. The presence of bright gas clouds is a sign of the youth of this region, which still appears to be a new stars fabrication field; credit: Hubble Heritage Team (AURA/STScI/NASA).

their antiparticles).

The theoretical prediction is that all the neutrino species are produced in the cooling phase with the same luminosity, in agreement with an equipartition principle: this means there will be more ν_e than ν_μ and ν_τ, since their average energy is lower. The expected neutrino spectra from a supernova with binding energy $\varepsilon_B = 3 \times 10^{53}\ erg$ are shown in figure 3.4.

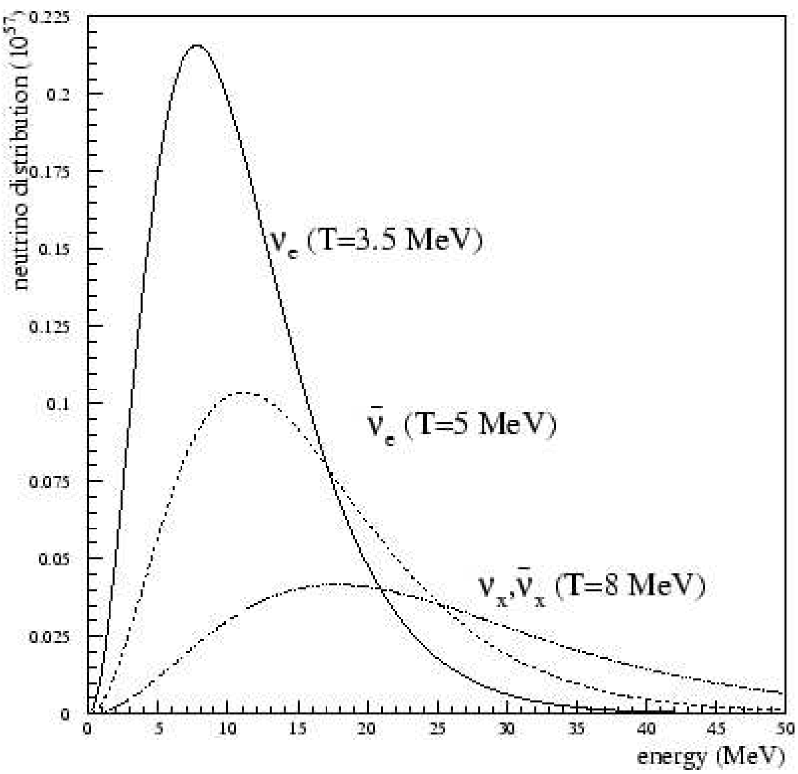

Figure 3.4: Neutrino thermal spectra, for $\varepsilon_B = 3 \times 10^{53}$ $ergs$: the solid line is the ν_e spectrum, the dashed one is for $\bar{\nu}_e$ and the dotted line is the spectrum of ν_μ, ν_τ.

3.2.3 Supernova neutrino signatures in Borexino

The neutrino flux from a supernova event will interact in the Borexino sensitive volume through the following reactions:

Scattering on electrons:

$$\nu + e^- \to \nu + e^-.$$

This is a "pointing" reaction with no threshold, sensitive to all leptonic flavor. The cross section for neutrino-lepton scattering can be estimated with the formalism of the standard electro-weak theory; if the incoming neutrino energy is $E_\nu >> m_e$, we obtain:

$$\sigma = \frac{2G_F^2 m_e E_\nu}{\pi}\left[c_L^2 + \frac{1}{3}c_R^2\right].$$

The total cross section for $\nu - e$ scattering is then linearly proportional to the neutrino energy: $\sigma(E_\nu) = \tilde{\sigma} \cdot E_\nu$, with $\tilde{\sigma} \simeq$ constant. The numerical values are:

$$\begin{aligned}
\sigma(\nu_e) &= 9.20 \times 10^{-45}\ E_\nu[MeV]\ cm^2 \\
\sigma(\bar{\nu}_e) &= 3.83 \times 10^{-45}\ E_\nu[MeV]\ cm^2 \\
\sigma(\nu_{\mu,\tau}) &= 1.57 \times 10^{-45}\ E_\nu[MeV]\ cm^2 \\
\sigma(\bar{\nu}_{\mu,\tau}) &= 1.29 \times 10^{-45}\ E_\nu[MeV]\ cm^2.
\end{aligned}$$

These cross sections can be averaged over the proper thermal neutrino spectrum, with $E_{thr} = 0$; it is then straightforward to calculate the expected number of events of this type in Borexino, as a consequence of a supernova collapse: in 300 t of liquid scintillator there would be ~ 5 scattering events due to a type II supernova with binding energy $\varepsilon_B = 3 \times 10^{53}$ erg at 10 kpc distance.

Inverse β decay of the proton:

$$\bar{\nu}_e + p \rightarrow e^+ + n.$$

This reaction, with an energy threshold of 1.80 MeV, is the favorite channel for the detection of supernova neutrinos.

The total cross section for this reaction, for sufficiently low energy, is given by:

$$\sigma = \frac{G_F^2 E_{\bar{\nu}}^2}{\pi} |\cos^2\theta_c|^2 \left[1 + 3\left(\frac{g_A}{g_V}\right)^2\right].$$

This approximation is valid for neutrino energies up to about 50 MeV; in our case, the average $\bar{\nu}_e$ energy is $\langle E_{\bar{\nu}_e}\rangle = 16\ MeV$ and only 0.3% of the $\bar{\nu}_e$ spectrum is above 50 MeV. It is safe, then, to assume the cross section for this reaction depends on the neutrino energy as $\sigma(E_\nu) = \bar{\sigma}(E_\nu - 1.3)^2$, with $\bar{\sigma}$ = constant = $9.5 \times 10^{-44}\ cm^2/MeV^2$.

The expected event number in Borexino (300 t sensitive volume) results to be ~ 79 counts, for the "usual" 10 kpc type II supernova.

Reactions on ^{12}C:

Although the main supernova signal comes from the $\bar{\nu}$ capture, the reactions of neutrino capture on ^{12}C are particularly interesting in detectors based on organic scintillator, such as Borexino. Three different reactions are possible:

- charged current capture of $\bar{\nu}_e$:

$$\begin{aligned}
\bar{\nu}_e +^{12} C \rightarrow\ & ^{12}B + e^+ & Q = 13.37\ MeV \\
& ^{12}B \rightarrow^{12} C + e^- + \bar{\nu}_e & \tau_{1/2} = 20.20\ ms
\end{aligned}$$

- charged current capture of ν_e:

$$\begin{array}{lll} \nu_e +^{12} C \rightarrow & ^{12}N + e^- & Q = 17.34\ MeV \\ & ^{12}N \rightarrow^{12} C + e^+ + \nu_e & \tau_{1/2} = 11.00\ ms \end{array}$$

- inelastic scattering of ν_x:

$$\begin{array}{lll} \nu_x +^{12} C \rightarrow & ^{12}C^* + \nu_x' & E_{thr} = 15.11\ MeV \\ & ^{12}C^* \rightarrow^{12} C + \gamma & E_\gamma = 15.11\ MeV \end{array}$$

All these three reactions on ^{12}C can be tagged in Borexino: both $^{12}C(\nu_e, e^-)^{12}N$ and $^{12}C(\bar{\nu}_e, e^+)^{12}B$ present a delayed coincidence of an electron and a positron, with a few milliseconds delay; while the inelastic scattering $^{12}C(\nu, \nu')^{12}C^*$ is followed by a mono-energetic γ ray at 15.11 MeV.

The cross sections for the neutrino-carbon reactions are complicated by the presence of nuclear matrix elements: for this reason, they have been investigated theoretically and experimentally over the past 20 years and are now well established. The agreement between the theoretical predictions to the measured data is good and a combined theoretical and experimental average value for the $^{12}C(\nu_e, e^-)^{12}N$ reaction, can be set as $\langle\sigma\rangle_{exp} = 9.2 \times 10^{-42} cm^2$ [35]. The cross section measurements were averaged over the neutrino energies relevant to the experiments, namely neutrinos from muon decay at rest: it is straightforward to scale these measured values to give averaged cross sections for supernova neutrinos. Since ^{12}N and ^{12}B are "mirror nuclei", the matrix elements and energy-independent terms in the cross section are essentially identical (only the Coulomb correction differs when calculating the $\bar{\nu}_e$ rates).

The neutral-current cross section can also be extracted from the experimental $^{12}C(\nu, \nu')^{12}C^*$ cross section data. Using an averaged value $\langle\sigma\rangle_{exp} = 10 \times 10^{-42} cm^2$ and assuming the contribution of ν_e and $\bar{\nu}_\mu$ to the nuclear inelastic scattering to be the same, we scaled this data for supernova neutrino fluxes and energies. These calculations allow to estimate the following event numbers in Borexino (300 t): 23 neutral-current events, 4 events due to $\bar{\nu}_e$ capture on ^{12}C and less than one event due to ν_e capture, from a typical Galactic supernova at 10 kpc.

The contributions of the different neutrino flavors to the neutral current reaction $^{12}C(\nu, \nu')^{12}C^*(15.11\ MeV)$ are shown in figure 3.5, where incoming neutrino energy spectra are compared with their convolution with the cross section: the summed contribution of ν_μ, ν_τ (and their antiparticles) gives the only significant fraction of events above threshold; the summary of expectations on supernova neutrino events from the various contributions is listed in table 3.1.

3.2.4 Neutral current detection capabilities

The neutrino burst from a supernova rises steeply and decays exponentially in time: the neutrino luminosity, decays exponentially in time as $L_\nu \sim e^{t/\tau_\nu}$, with $\tau_\nu \sim 3$

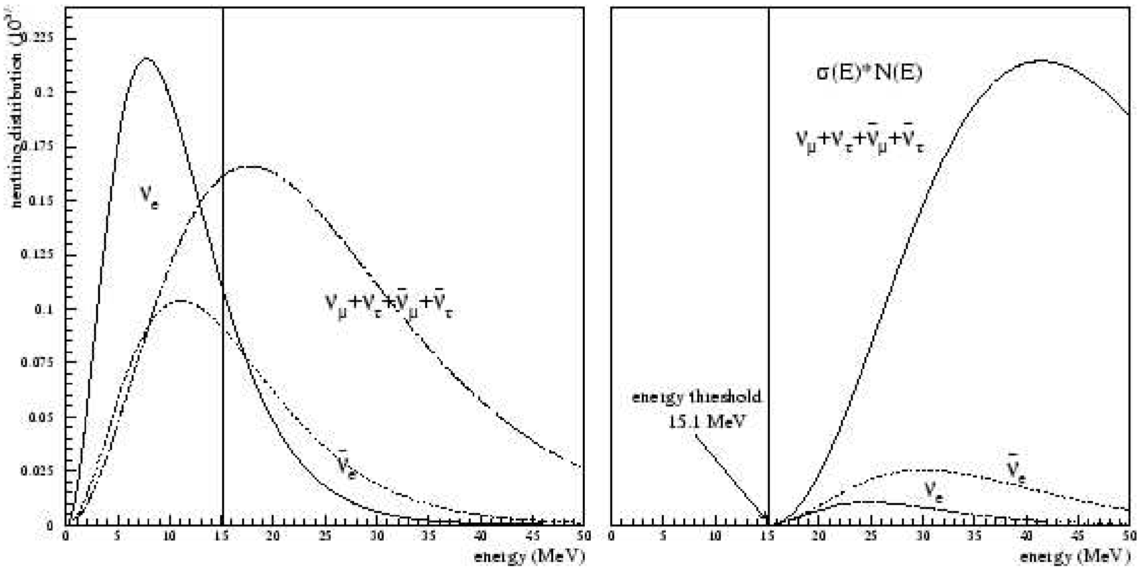

Figure 3.5: Contribution of the different neutrino flavors to the neutral current reaction $^{12}C(\nu,\nu')^{12}C^*(15.11\ MeV)$: incoming neutrino energy spectra (left) and their convolution with the cross section (right). The solid line is the ν_e distribution, the dashed line is the $\bar{\nu}_e$ profile and the dotted line represents the summed contribution of the other flavors (ν_μ, ν_τ and their antiparticles).

reaction channel	$\langle E_\nu \rangle$ [MeV]	$\langle \sigma \rangle$ $[cm^2]$	N_{events}
$\nu_e - e$	11	1.02×10^{-43}	2.37
$\bar{\nu}_e - e$	16	6.03×10^{-44}	0.97
$\nu_x - e$	25	3.96×10^{-44}	0.81
$\bar{\nu}_x - e$	25	3.25×10^{-44}	0.67
total $\nu - e$			4.82
$\bar{\nu}_e + p \rightarrow e^- + n$	16	2.70×10^{-41}	78.9
$^{12}C(\nu_e, e^-)^{12}N$	11	1.85×10^{-43}	0.6
$^{12}C(\bar{\nu}_e, e^+)^{12}B$	16	1.87×10^{-42}	4.1
$\nu_e +^{12} C$	11	1.33×10^{-43}	0.4
$\bar{\nu}_e +^{12} C$	16	6.88×10^{-43}	1.5
$\nu_x +^{12}$ C	25	3.73×10^{-42}	20.9
total $^{12}C(\nu,\nu')^{12}C^*$			22.9

Table 3.1: Predicted neutrino events in Borexino (300 t), due to a supernova explosion at a distance of 10 kpc, with $\varepsilon_B = 3 \times 10^{53}$ $ergs$ binding energy release.

sec. In a low-background solar neutrino detector, a burst of 100 events in a time window of 10 seconds is easily identified. The ability to separate the neutral-current events in a liquid scintillator detector from the $\bar{\nu}_e - p$ reactions determines whether interesting neutrino physics can be explored.

The inverse β decay of the proton produces a neutron. In Borexino, this neutron thermalizes and walks in the detector until it is captured by hydrogen: $n+p \rightarrow d+\gamma$, with a mean capture time $\tau_{1/2} = 250\ \mu s$ and $E_\gamma = 2.2\ MeV$. The large homogeneous detection volume in Borexino ensures efficient neutron capture and efficient detection of the 2.2 MeV γ. These events can be tagged by the delayed coincidence between the initial e^+ from the $p(\bar{\nu}_e, e^+)n$ reaction and the neutron capture γ ray.

On the other hand, if an hypothetical detector lacks the low-energy threshold of Borexino or is not able to contain the neutron produced by the $\bar{\nu}_e - p$ reaction, it will not be able to exploit the delayed coincidence signature to identify these events. Consequently, the $\bar{\nu}_e - p$ events appear as single positrons. The challenge in such a detector is then to distinguish the 15.1 MeV γ of ^{12}C neutral-current excitation from the continuum spectrum produced by these positrons.

Efficient detection and resolution of the 15.1 MeV γ will also be possible in Borexino. Figure 3.6 depicts an example of the singles spectrum from all supernova neutrino events that would occur in Borexino within a time window of 10 seconds. Even if the $\bar{\nu}_e - p$ positrons are not tagged by the delayed neutron capture γ ray, the 15.1 MeV peak is well resolved on top of the positron spectrum. The energy resolution in Borexino, simulated here with the design light collection statistics of 400 photoelectrons/MeV, allows the neutral-current events to be identified. The large, homogeneous volume of liquid scintillator effectively contains the total energy of this γ ray.

3.2.5 Neutrino mass limits from time of flight

The detection of a supernova neutrino burst in our galaxy has the potential to probe non-standard physics. In particular, the Borexino neutral current detection capability will be a powerful tool in exploring non- standard features of neutrinos, like mass and flavor oscillations.

As explained in section 1.3.1, the present limits on neutrino masses, obtained in laboratory experiments, are still unsatisfactorily high, especially for ν_μ and ν_τ:

$$\begin{gathered} m_{\nu_e} < 2.2 \div 2.5\ eV \\ m_{\nu_\mu} < 170\ keV \\ m_{\nu_\tau} < 18.2\ MeV \end{gathered}$$

The limits on the masses of ν_μ and ν_τ could be significantly improved through a study of the arrival time of neutrinos of different flavors.

Suppose the neutrino flux is composed of two species, one with mass and the other massless. The massive neutrinos will reach Earth with a delay (with respect to the massless species) that can be estimated with a simple relativistic calculation:

$$\Delta t = \frac{D}{2c}\left(\frac{m_\nu}{E_\nu}\right)^2,$$

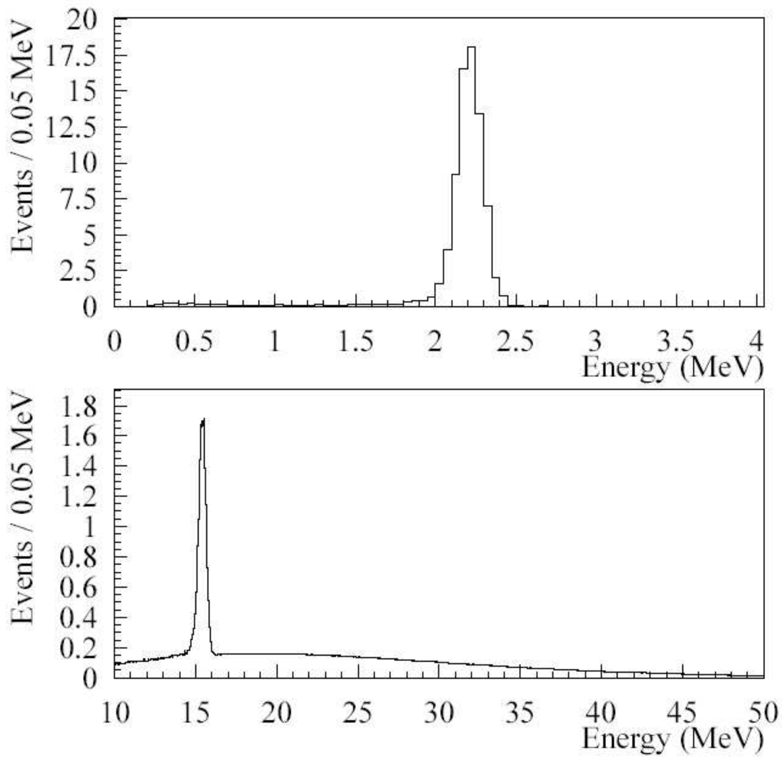

Figure 3.6: Simulated singles spectrum from supernova neutrinos in Borexino, in two different energy windows. In the lower energy spectrum there will be a peak at 2.2 MeV, due to the capture of neutron produced in the $p(\bar{\nu}_e, e^+)n$ reaction. In the higher energy end of the spectrum ($E > 10\ MeV$), the 15.1 MeV γ rays from neutral-current excitation of ^{12}C are well resolved from the continuum of e^+ events from $p(\bar{\nu}_e, e^+)n$.

where D is the distance to the supernova. Measuring this time delay requires being able to distinguish the massive species from the massless neutrino interactions. Ideally, knowledge of the emission time distribution is also required as is a precise measurement of E.

In Borexino, the neutral-current excitation is dominated by ν_μ and ν_τ, due to their higher average energy; 91% of the neutral-current events come from the heavy flavor neutrinos. Their relative contribution to the neutral-current event rate is illustrated in figure 3.5. The $\bar{\nu}_e - p$ charged-current events provide the "time stamp" for the massless species: thus, in Borexino, determining the time delay between the neutral-current and charged-current events provides a handle on the mass of ν_μ and/or ν_τ.

The arrival time delay delay is convoluted with the emission time distribution, which presents big uncertainties; nevertheless, it was shown [27, 28] that model-specific details relating to the emission time profile of neutrinos from a supernova do not have a pronounced effect on the arrival time distribution, since the overwhelming consideration in analyzing the time delay for massive neutrinos is the time constant of the exponential decay of the neutrino luminosity; the averaged quantities such as:

$$\Delta t = < t >_{NC} - < t >_{CC}$$

can then be used as sensitive probes for extraction of the neutrino mass from supernova neutrino data.

We considered a model for a supernova neutrino burst that rises linearly, reaching maximum in the first ~ 20 ms after the core bounce; the sharp increase is then followed by an exponential decay, with lifetime $\tau \sim 3$s. Figure 3.7 shows the expected time distribution of the $^{12}C(\nu,\nu')^{12}C^*$ events in Borexino, for two scenarios. In both cases, ν_e is assumed massless and: (a) ν_μ is massless and ν_τ is massive $\Rightarrow$ 46% of the $^{12}C(\nu,\nu')^{12}C^*$ events are delayed; (b) ν_μ and ν_τ are both massive $\Rightarrow$ 91% of the $^{12}C(\nu,\nu')^{12}C^*$ events are delayed.

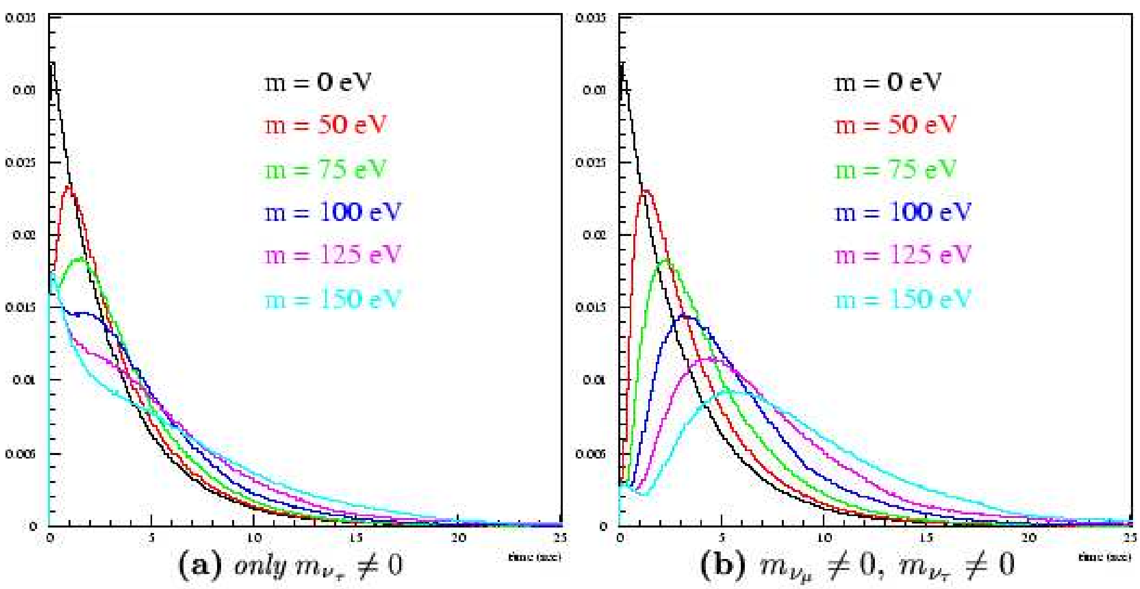

Figure 3.7: Time distribution for the $^{12}C(\nu,\nu')^{12}C^*$ events, for two cases: (a) 46% of the events are from massive neutrinos (ν_τ); (b) 91% of the events are massive (ν_μ and ν_τ).

Figure 3.8 shows the distribution of average time of arrival of the $^{12}C(\nu,\nu')^{12}C^*$ events, for different values of the heavy neutrino mass. It is based on the results of a Monte Carlo simulation of 10^5 supernovae (distance 10 kpc) producing ^{12}C neutral-current events in Borexino [35]. The arrival times for the, on average, 23 events were drawn from the distributions shown in figure 3.7. Time zero is the theoretical instant of the earliest possible arrival (possibly determined by the earliest detection of $\bar{\nu}_e$). To obtain Δt, we subtract the average arrival time of the light neutrinos, that is $\langle t \rangle_{CC} = 3$ s.

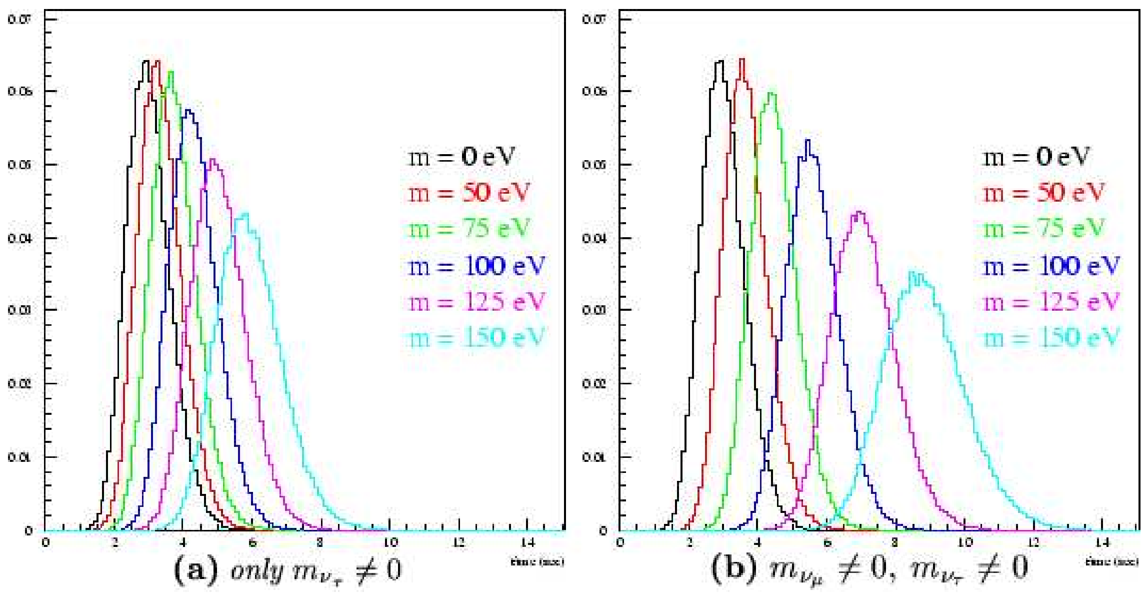

Figure 3.8: Monte Carlo distribution of the average time of the $^{12}C(\nu,\nu')^{12}C^*$ events, for a sample of 10^5 supernovae at 10 kpc (in this model, $t = 3$ s is the average arrival time of the massless neutrinos).

The interpretation of these plots, in terms of neutrino mass limits, goes as follows.

- Consider scenario (a), where ν_τ is massive (46% of the neutral-current events are delayed). From the data set, the average arrival time of the charged-current events is subtracted from the average arrival time of the neutral-current events, giving a value for Δt. Given a measured delay, allows one to set a mass limit, such that:
  - if $\Delta t = -0.5\,s \;\Rightarrow\; m_{\nu_\tau} < 46\ eV$ $(90\%\ CL)$
  - if $\Delta t = 0 \;\Rightarrow\; m_{\nu_\tau} < 79\ eV$ $(90\%\ CL)$
  - if $\Delta t = +0.5\,s \;\Rightarrow\; m_{\nu_\tau} < 103\ eV$ $(90\%\ CL)$
- Similarly, for scenario (b) in which both ν_μ and ν_τ are massive, with $m_{\nu_\mu} \simeq m_{\nu_\tau}$ (as might arise for small Δm_{23}), mass limits are extracted such that:
  - if $\Delta t = -0.5\,s \;\Rightarrow\; m_{\nu_{\mu\tau}} < 33\ eV$ $(90\%\ CL)$
  - if $\Delta t = 0 \;\Rightarrow\; m_{\nu_{\mu\tau}} < 55\ eV$ $(90\%\ CL)$
  - if $\Delta t = +0.5\,s \;\Rightarrow\; m_{\nu_\tau} < 71\ eV$ $(90\%\ CL)$

  Conversely, a measured average arrival time delay of $\Delta t = +1.0$ s allows one to exclude a massless ν_τ at greater than 90% confidence level. These limits are only slightly worse than what might be achievable in Super-Kamiokande

(50 eV sensitivity [28]), and in SNO (30 eV sensitivity [27]): it is remarkable that the limits in Borexino are comparable, given the much higher statistics expected in these much larger detectors.

3.2.6 Neutrino oscillations from reactions on ^{12}C

Neutrino oscillations can be probed by comparing the supernova neutrino event rates for different reactions. The extent of limits on Δm^2 depend on the L/E ratio which, for distances of kilo-parsecs, is many orders of magnitude lower than presently explored regions (e.g. solar neutrino vacuum oscillations).

We will consider the implications of vacuum oscillations on the detection of supernova neutrinos in Borexino: the main consideration is that higher energy ν_μ could oscillate into ν_e, resulting in an increased event rate since the expected ν_e energies are just at or below the charged-current reaction threshold. The cross section for $^{12}C(\nu_e, e^-)^{12}N$ increases by a factor of 35 if we average it over a ν_e distribution with $T = 8\ MeV$, rather than 3.5 MeV. The gain in cross section for $^{12}\mathrm{C}(\bar{\nu}_\mathrm{e}, \mathrm{e}^+)^{12}\mathrm{B}$ is a factor of 5. The large increase in the ν_e induced reaction rate is a pseudo-appearance signature for oscillations.

We assign the probability α_μ to have $\nu_e \leftrightarrow \nu_\mu$ conversion and α_τ to have $\nu_e \leftrightarrow \nu_\tau$, and define $\beta = \alpha_\mu + \alpha_\tau$. Thus, depending on the value of β, we have the combinations of event numbers reported in table 3.2 and displayed in figure 3.9 (the number of charged-current and neutral-current events, as a function of the parameter β, are shown with a 1 σ error band corresponding to the statistics for a supernova at 10 kpc).

channel	$\beta = 0$	$N = N(\beta)$	$\beta = 0.1$	$\beta = 0.5$	$\beta = 0.9$
$^{12}C(\nu_e, e^-)^{12}N$	0.6	$0.6(1 + 15.1\beta)$	1.5	5.1	8.8
$^{12}C(\bar{\nu}_e, e^+)^{12}B$	4.1	$4.1(1 + 2.3\beta)$	5	8.8	12.6
$^{12}C(\nu, \nu')^{12}C^*$	23	23	23	23	23

Table 3.2: Number of NC and CC events on ^{12}C, as a function of an overall conversion probability $\beta = \alpha_\mu + \alpha_\tau$, where $\alpha_\mu = P(\nu_e \leftrightarrow \nu_\mu)$ and $\alpha_\tau = P(\nu_e \leftrightarrow \nu_\tau)$.

A comparison between the number of events from $^{12}C(\bar{\nu}_e, e^+)^{12}B$, $^{12}C(\nu_e, e^-)^{12}N$ and $^{12}C(\nu, \nu')^{12}C^*$ might, then, give strong constraints on the mixing parameters (the constant neutral-current rate fixes the flavor-independent luminosity). Though the statistics are low, the effect on the charged-current rates are significant.

Therefore, the charged-current and neutral-current reactions on ^{12}C offer an important tool for probing neutrino oscillations. The distinctive charged-current reactions feature delayed β decays, correlated in time and space with the neutrino interactions, allowing both ν_e and $\bar{\nu}_e$ to be easily identified in a flavor-oscillation analysis.

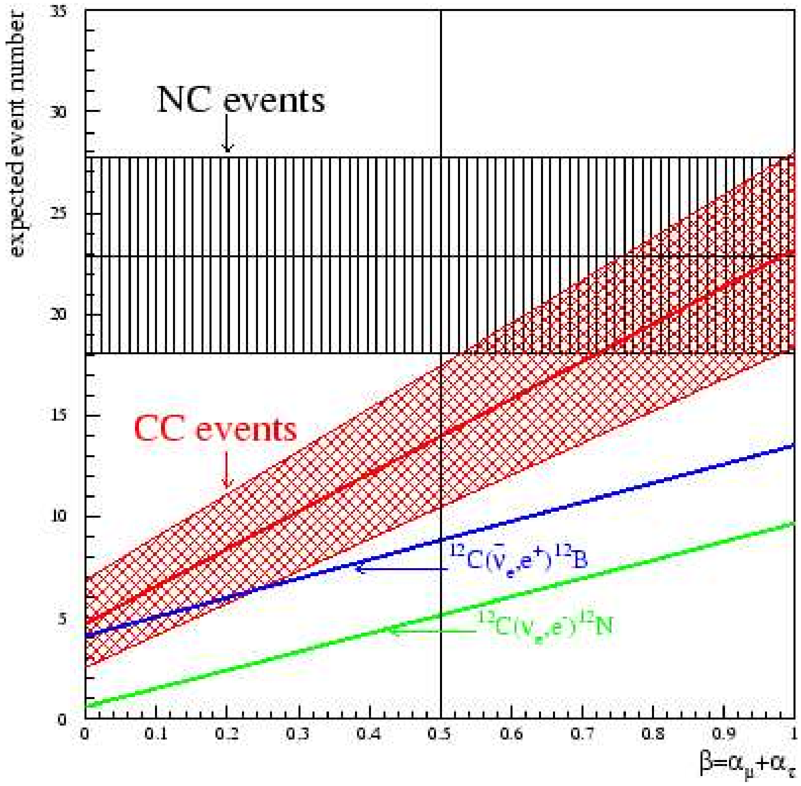

Figure 3.9: Number of NC and CC events on ^{12}C, as a function of an overall conversion probability $\beta = \alpha_\mu + \alpha_\tau$. The error bands refer to the case of a supernova at 10 kpc with $\varepsilon_B = 3 \times 10^{53}$ $ergs$.

3.2.7 Detection of supernova neutrinos by $\nu - p$ elastic scattering

In a recent study [26], it was pointed out that also the neutrino-proton elastic scattering reaction ($\nu + p \to \nu + p$) can be used for the detection of supernova neutrinos in scintillator detectors. The neutrino-proton elastic scattering has been observed at accelerators at GeV energies, but has never been demonstrated to be a realistic detection channel for low-energy neutrinos: for this reason, this reaction is presented separately from the "standard" detection channels.

The $\nu - p$ scattering could play an important role in supernova physics, because it would give a powerful tool to study the energy distribution trough the six neutrino channels. The four flavors ν_μ, ν_τ, $\bar{\nu}_\mu$ and $\bar{\nu}_\tau$ are expected to carry away about 2/3 of the supernova binding energy, and are expected to have a higher temperature than ν_e or $\bar{\nu}_e$. However, there is no experimental basis for these statements, and at present, numerical models of supernovae cannot definitively address these issues either. If there is no spectral signature for the neutral-current detection reactions, then neither the total energy carried by these flavors nor their temperature can be separately determined from the detected number of events: the $\nu - p$ represents an exception to this statement, since the measured proton spectrum is related to the incident neutrino spectrum, which helps in reconstructing the total energy and temperature of ν_μ, ν_τ, $\bar{\nu}_\mu$ and $\bar{\nu}_\tau$.

The theoretical cross section for neutrino-proton elastic scattering has been confirmed by extensive measurements at GeV energies. At the energies considered here, the total cross section yields [26]:

$$\sigma = \frac{G_F^2 E_\nu^2}{\pi}(c_V^2 + 3c_A^2).$$

This cross section is of the same form as the total cross section for the charged-current reaction $\bar{\nu}_e + p \rightarrow e^+ + n$, but is approximately 4 times smaller. However, this is compensated in the yield by the contributions of all six flavors, as well as the higher temperature assumed for ν_μ and ν_τ ($T = 8\ MeV$ instead of $5\ MeV$): thus, the total yield from $\nu + p \rightarrow \nu + p$ is larger than from $\bar{\nu}_e + p \rightarrow e^+ + n$, when the detector threshold is neglected.

The elastically-scattered protons will have kinetic energies of a few MeV. Obviously, these very non-relativistic protons will be completely invisible in any Čerenkov detector like Super-Kamiokande. However, such small energy depositions can be readily detected in scintillator detectors such as KamLAND and Borexino. The proton recoil spectrum for KamLAND detector is shown in figure 3.10 (left): in Borexino, the spectrum will have the same shape, but the total numbers will be reduced by a factor 4.7 (taking into account the reduced number of target protons).

For highly ionizing particles like low-energy protons, the quenching effect in scintillator has to be considered; the observable light output E_{equiv} is given by Birk's Law:

$$\frac{dE_{equiv}}{dx} = \frac{dE/dx}{1 + K_B(dE/dx)}$$

where k_B is a constant of the scintillation material, assumed to be $k_B \simeq 0.015$ for KamLAND and $k_B \simeq 0.010 \div 0.015$ for Borexino[1]. Visible proton spectrum for KamLAND is shown in figure 3.10: the effect of the quenching is a significant shift of the spectrum towards lower energy values.

In absence of threshold, ~ 133 scattered protons would be detected in Borexino; but the real number of $\bar{\nu}_e + p \rightarrow e^+ + n$ events will be determined by the natural radioactivity of the scintillator (namely by the ^{14}C countrate): since the supernova event rate will be of the order of 10 Hz, an acceptable threshold could be slightly lower than in the solar neutrino case ($\sim 200\ keV$), where the ^{14}C rate will be of the Hz order. In these conditions, $\sim 45 \div 55\%$ of the $\nu - p$ signal would be conserved (depending on the real quenching factor that will be measured in the scintillator), giving a total countrate comparable with the $\bar{\nu}_e + p \rightarrow e^+ + n$ one.

[1]The value $k_B = 0.015$ has been measured in laboratory measurement but never published; some recent studies on CTF-III data (see chapter 4) suggest a value closer to 0.010.

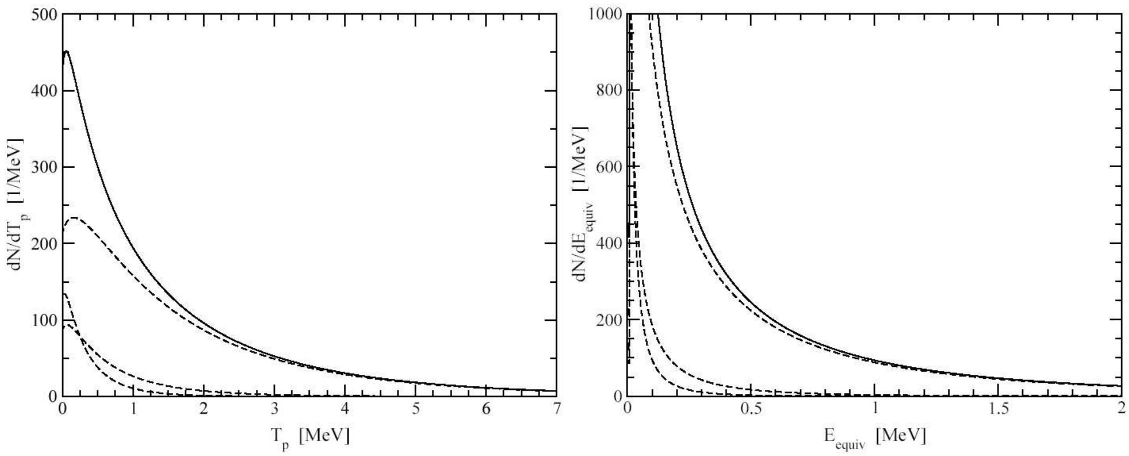

Figure 3.10: Left: the theoretical proton spectrum in KamLAND, for a standard supernova at 10 *kpc*; the contributions from ν_e, $\bar{\nu}_e$ and the sum of ν_μ, ν_τ, $\bar{\nu}_\mu$ and $\bar{\nu}_\tau$ are shown with dashed lines; the solid line is the sum spectrum for all flavors. Right: the same spectrum, with the quenching effect taken into account.

As already explained, the measured proton spectrum is related to the incident neutrino spectrum; therefore, it is possible to measure separately the total energy and temperature of ν_μ, ν_τ, $\bar{\nu}_\mu$ and $\bar{\nu}_\tau$, each with uncertainty of order 10% in KamLAND. In Borexino, there will be about 4.7 times fewer free proton targets than assumed for KamLAND; however, the quenching is lower in pure scintillator, so that the precision in Borexino will be about 20% or better [26].

Chapter 4

The Counting Test Facility (CTF) of Borexino

The $R\&D$ of the Borexino experiment has been a great technological challenge, mainly concerning the radio-purity issue for the chosen materials. The Counting Test Facility (CTF) was designed to test the feasibility of the Borexino concept: the CTF is a large-scale Borexino prototype, with a total mass of $\sim 4\,t$ of scintillator. The detector CTF was designed for ^{238}U, ^{232}Th and ^{14}C spectroscopy (mainly in the energy range below 1 MeV) and for the study of the optical response of a big volume of liquid scintillator. The sensitivity for neutrino interaction, ^{40}K and ^{7}Be is not sufficient in CTF because the surface/volume ratio limits the self-shielding.

In the following, the three CTF campaigns will be described, as well as the main results.

4.1 Feasibility of Borexino: CTF-1

The goal of the first CTF campaign (CTF-1, January 1995 - July 1997) was to study the feasibility of Borexino, showing the possibility to reach the required contamination levels: $\sim 5 \times 10^{-16} g/g_{scintillator}$ for U and Th and a $^{14}C/^{12}C$ ratio $\simeq 10^{-18}$.

4.1.1 Structure of the detector

CTF is located near Borexino, in the Hall C of the Gran Sasso underground laboratories: the detector layout is shown in figures 4.1 and 4.2; a comprehensive description of the detector can be found in [5]. The active detector is composed of $\sim$ 4 m^3 organic liquid scintillator (PC+PPO), contained in a 0.5 mm thick nylon spherical vessel of 2 m diameter (Inner Vessel). The light emitted from the scintillator is detected by 100 PMTs placed on a spherical open structure 2.3 m far from the IV.

All the structure is immersed in $\sim$ 1000 t of ultra-pure water, contained in a carbon steel tank (D200): the water provides a 4.5 m shield from γ-ray background from the rock of the hall and a 2.3 m shield from the PMT induced background.

The absence of a PC buffer (IV is directly immersed in water), yields a big buoyancy force on the Inner Vessel itself: mechanical stresses on the nylon layer are important and the IV spherical shape is difficultly maintained.

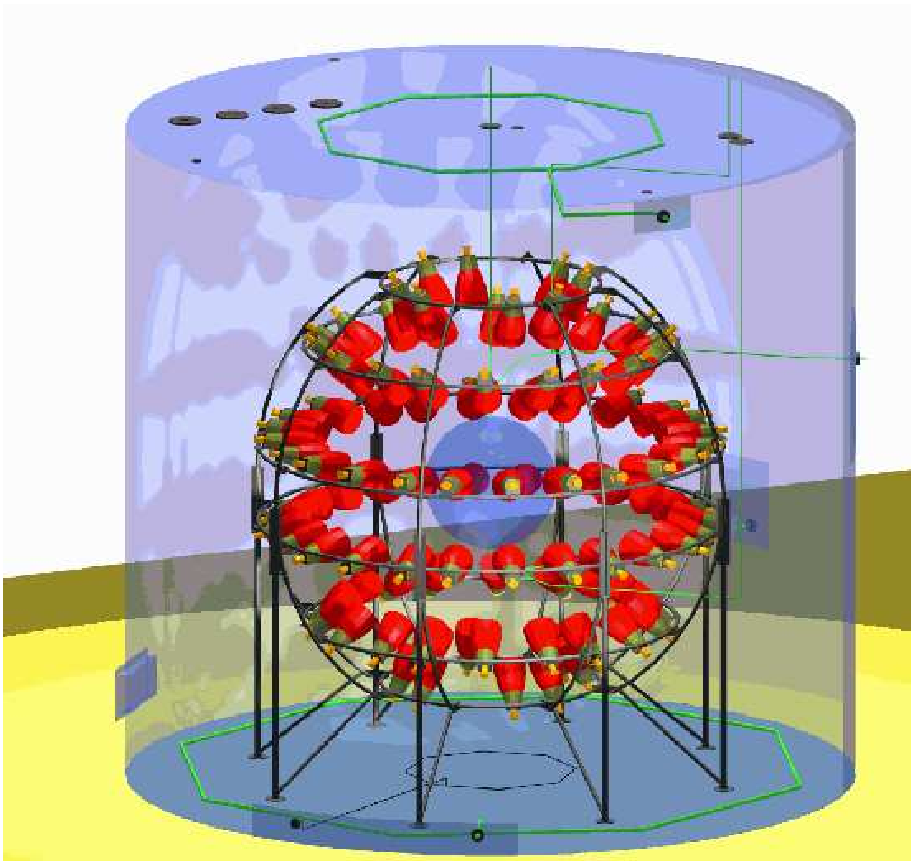

Figure 4.1: Draft of the Counting Test Facility structure.

A water purification plant is placed near the CTF tank; water is purified through filtration, reverse osmosis, deionization, ion exchange, and nitrogen stripping [5]. The plant reduces the U and Th concentration of the raw water from 10^{-10} g/g to 10^{-14} g/g. The radon content in water after nitrogen stripping is reduced to ~ 20 mBq/m^3.

A fluid handling system performs the filling and the emptying of the inner vessel with different liquids (water, liquid scintillator), circulates the scintillator through the purification system and maintains a pressure control on the inner vessel content. A purification system containing sub-micron filtration, water extraction, vacuum distillation, and nitrogen stripping was constructed to actively remove radioactive impurities [5]. Filtration removes suspended dust particles larger than 0.05 μm. Water extraction is effective at removing ionizable species, such as metals (U, Th, Po). Vacuum distillation removes low volatility components such as metals and dust

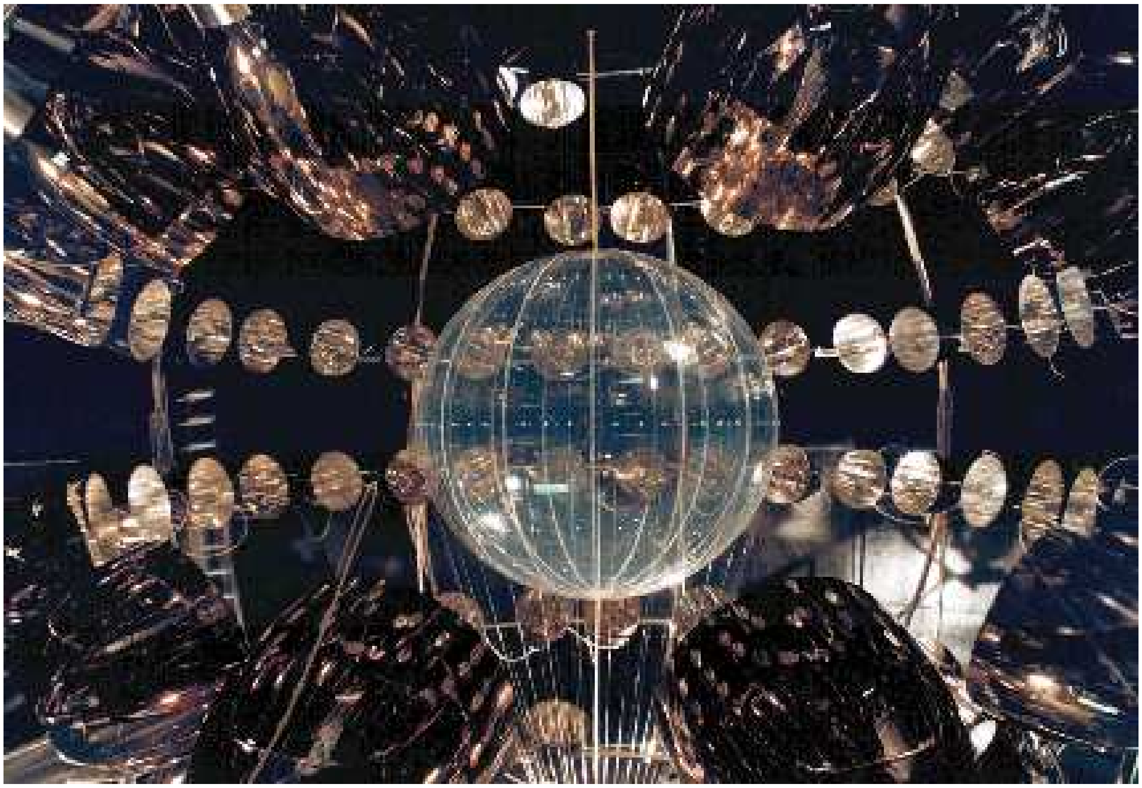

Figure 4.2: A picture taken inside the D200 tank, during the CTF-1 data taking.

particles. Nitrogen stripping removes dissolved gas impurities, such as ^{85}Kr, as well as water and oxygen dissolved in the scintillator.

The scintillation light is detected by 100 20 cm diameter photomultiplier tubes (Thorn EMI 9351). The tubes have a cathode efficiency of $\sim$ 25% (at 380 nm), transit time spread of 1 ns, dark noise of $\sim$ 500 Hz, low afterpulse ($\sim$ 2.5%) and amplification of 10^7; the dynodes of the PMT are shielded against magnetic fields with mu-metal collar. The PMTs are coupled to "truncated string cone" light concentrators, which collect the light from the scintillator containment vessel: the geometrical coverage of the scintillator region is 21%. The PMTs and their assembly components were selected to minimize the radioactivity; the final γ-ray activity of each tube assembly is ~ 3.8 Bq.

4.1.2 Main results of the test

The CTF installation was completed in early 1995. The detector was filled with water in January 1995 and the scintillator filling happened in February-April 1995. The data taking went on continuously since it was filled with water (in January 1995), until July 1997. The main results of CTF-1 are described in [5, 9, 7, 6] and can be summarized as follows:

- **Measurement of extremely low radioactive contamination:** the investigated radioactive elements represent the fundamental sources of background in Borexino. As mentioned above, the radioactive contaminants which were investigated are: ^{238}U and ^{232}Th chains, the primordial ^{40}K; the noble gases ^{222}Rn and ^{85}Kr; the cosmogenic element ^{14}C. The CTF-1 main results are summarized in Tab. 4.1, where for some elements are reported also the corresponding measurements realized with Neutron Activation Analysis (NAA) [10].

  NAA measures directly the concentration of ^{238}U and ^{232}Th nuclei, while CTF detects the delayed coincidences $^{214}Bi(\beta\gamma) -^{214} Po(\alpha)$ ($\tau = 236\ \mu s$) and $^{212}Bi(\beta\gamma) -^{212} Po(\alpha)$ ($\tau = 432.8\ ns$). In other words CTF is sensible to the $^{226}Ra -^{214} Po$ segment of ^{238}U chain and to the entire segment following ^{226}Ac in the ^{232}Th chain: if CTF and NAA measurements are in agreement, secular equilibrium can be assumed.

Element	PC (CTF)	PC (NAA)
^{238}U	$(3.5 \pm 1.3) \cdot 10^{-16} g/g$	$\leq 2 \cdot 10^{-16}$
^{232}Th	$(4.4 \pm 1.5) \cdot 10^{-16} g/g$	$\leq 2 \cdot 10^{-15}$
$^{14}C/^{12}C$	$(1.94 \pm 0.09) \cdot 10^{-18}$	-
^{40}K	$\leq 2.4 \cdot 10^{-11} g/g$	$\leq 4 \cdot 10^{-12}$

Table 4.1: Radioactivity levels of the scintillator, measured in CTF and with NAA.

- **Radon contamination studies:** *Rn* emanation from the materials and its diffusivity in liquids and through solids were found to be fundamental problems to be addressed in a low energy experiment. During CTF-1 data taking, a high *Rn* activity was observed in the shielding water ($\sim 30\ mBq/m^3$), probably due to emanation of the materials in the tank: to overcome this problem, Borexino design was modified, with the addition of a Radon Barrier (as described in chapter 2).

- **Evaluation of the purification efficiency:** before any purification, other contaminants were observed, besides the above listed ones: ^{85}Kr, ^{210}Po and ^{210}Bi, coming probably from the contact with air during the scintillator preparation (especially for ^{210}Po and ^{210}Bi, which are Radon daughters). The applied purification sequence reduced the total rate in the Neutrino Window from 470 ± 90 internal events/day down to a value consistent with zero (21 ± 47 events/day) [9]; the energy spectra before and after the purification are shown in figure 4.3.

- **Optical properties of the scintillator:** fundamental performances of the detector-scintillator system were measured by means of the insertion of radioactive sources inside the Inner Vessel; the total light yield was found to

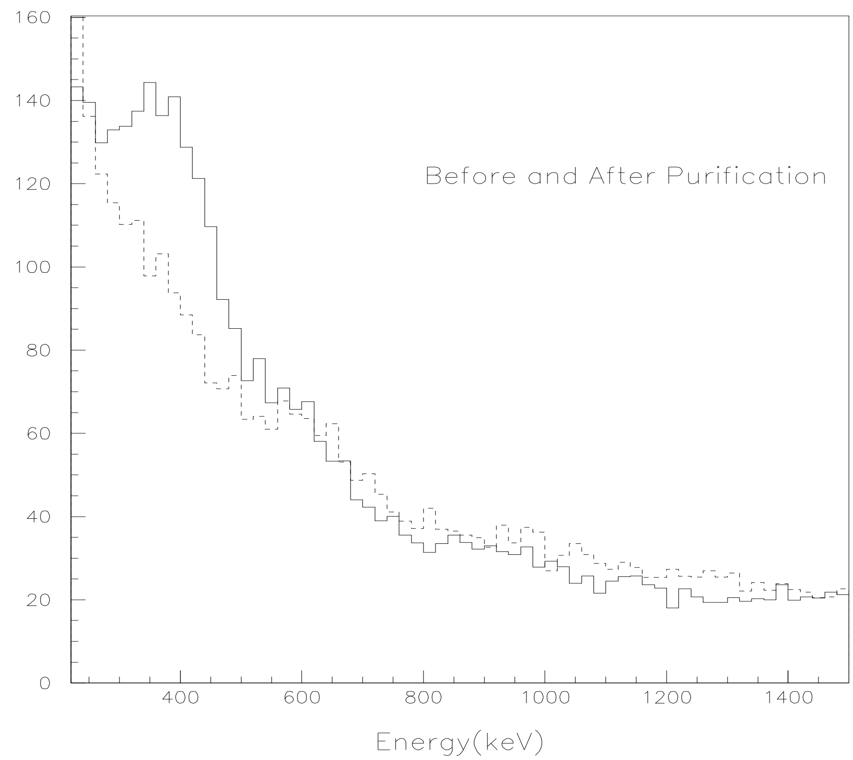

Figure 4.3: Energy spectrum of CTF events, before (continuous line) and after (dashed line) the scintillator purifications.

be $\sim 300\ p.e./MeV$, the spatial resolution $\sim 12\ cm$ and energy resolution $\sim 9\%$ at $825\ KeV$. Furthermore, the study of a big volume of liquid scintillator in a 4π geometry has given interesting results about light propagation processes; involved mechanisms are discussed in [6] and are: light absorption and re-emission on the fluor and elastic scattering on the solvent. Results were computed in two ways: by the comparison between the results obtained with a "full angle" and a "window" ^{222}Rn source; by the comparison of ^{222}Rn source data with Monte-Carlo simulation. It was evaluated that $52 \div 56\%$ of the scintillation light is directly detected, while $\sim 28\%$ is absorbed and re-emitted, $\sim 11\%$ is scattered and $\sim 9\%$ experience both processes. Due to these effects, the effective scintillator decay time of $\sim 3.5\ ns$ increases to $4.5 \div 5.0\ ns$.

- α/β **discrimination analysis:** in liquid scintillators, α decays can be separated from β events using the PSD (Pulse Shape Discrimination) analysis; the selection method applied in CTF-1 is known as "Tail to Total ratio" and will be described in CTF-2 section. The identification efficiency of β events in CTF-1 is 98.5% at $751\ keV$ (^{214}Po peak), with an associated α misidentification of 5%. At lower energies, $300 \div 600\ keV$ (^{210}Po, ^{222}Rn and ^{218}Po peaks) the efficiency on β events decreases to 93%, with an associated α misidentification of 11% (the distribution of the discrimination parameter for low energy events is shown in figure 4.4).

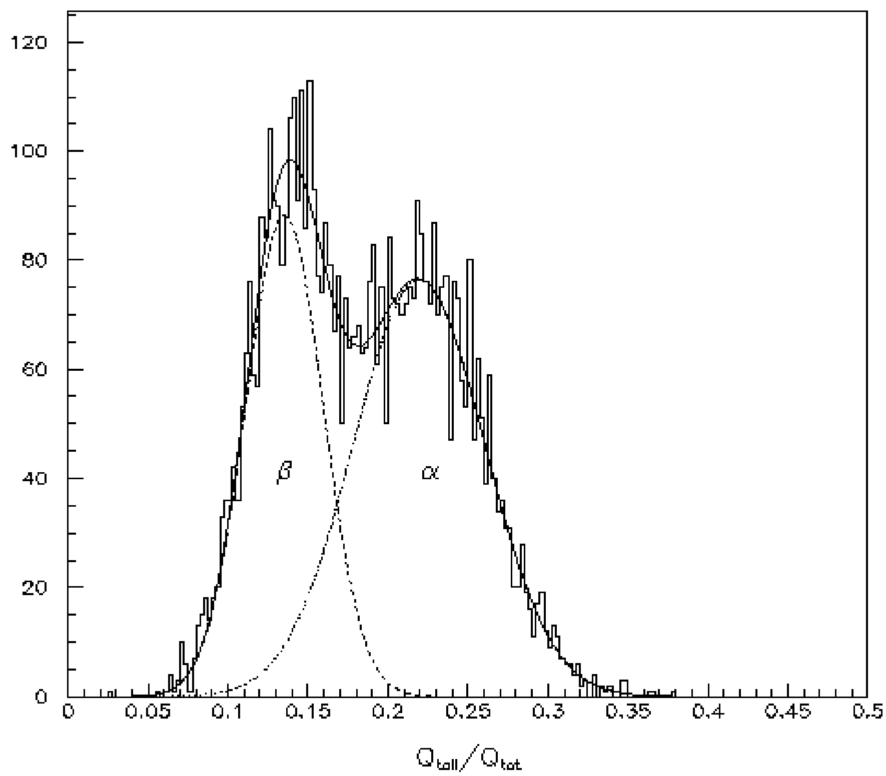

Figure 4.4: Behavior of the α/β discrimination parameter at low energies.

4.2 Quality control for Borexino: CTF-2

From May to September 2000, a second phase of the data taking (CTF-2) took place, with an improved detector setup: this second campaign was mainly devoted to test a backup solution for the scintillating mixture. The liquid scintillator used at this stage was a phenylxylylethane (PXE, $C_{16}H_{18}$) with p-diphenylbenzene (paraterphenyl, P-TP) as fluor (at a concentration of $2\,g/l$) and $1,4$-bis-(2-methylstyrol)-benzene (bis-MSB, at $50\,mg/l$) as wavelength shifter (detailed characteristics of the scintillating mixture are reported in [16]).

4.2.1 Detector upgrade

For CTF-2 data taking, detector was completely rebuilt [15]:

- 100 new phototubes were installed, of Borexino type (Thorn EMI 9351 of 20 cm diameter); a completely new sealing design was developed for these PMTs;

- electronics was redesigned, in order to meet data taking requirements; a new board (Digital Pulse Shape Analyzer) was installed, in order to improve α/β discrimination capabilities: details about the board are reported in [76], while its implementation in CTF is described in [71]; the main results are described in section 4.2.4;

- an additional nylon screen between the scintillator vessel and PMTs (against radon penetration) was installed, as it will be done in Borexino as well (Radon barrier);

- the detector was equipped with a carefully designed muon veto system, consisting of 2 rings of 8 PMTs each, installed at the bottom of the tank; muon veto PMTs are looking upward and have no light concentrators. The muon veto system was optimized in order to have a negligible probability of registering the scintillation events in the Neutrino Window; its performances were calculated by a Monte-Carlo method accounting for specific features of the light propagation in the CTF and checked by means of a radioactive source, which allowed to tune-up Monte-Carlo parameters [15].

4.2.2 Sequence of measurements

The CTF-2 campaign can be divided into four distinct phases:

1. **Water run:** first data were taken during May 2000 with both the inner vessel and the external tank filled with water. These data were used to test and tune the electronics and to determine criteria to identify muon events.

2. **Scintillator filling:** loading of the scintillator into the Inner Vessel was done in four batches of 1 ton each separated by short periods of data taking. Filling operations lasted from June 3 until July 15, 2000.

3. **Data taking:** data were taken from July 16 until September 5, 2000, corresponding to 52 days with 4.2 t of PXE. The Inner Vessel was valved off and no operations were performed during this period.

4. **Calibration:** after completion of the data taking period, a series of calibration measurements with a ^{222}Rn point-like source were carried out. The source was moved inside the inner vessel to map the detector response and tune the position reconstruction software[1].

[1]Some details about the Borexino and CTF position reconstruction algorithm are given in section 7.4.

4.2.3 Detector performances

- The pulse height-energy relation can be derived from the ^{214}Po alpha peak, together with the laboratory measured quenching factors: due to its short mean life of 236.6 μs, the ^{214}Po decay can easily be tagged; the ^{214}Po stems mainly from ^{222}Rn introduced during scintillator loading and therefore is homogeneously distributed in the scintillator volume. The alpha particle has an energy of 7.69 MeV, which in the scintillator is quenched to an equivalent beta energy of (950 ± 12) keV according to laboratory measurements [16]. In the CTF, the peak position corresponds to (304 ± 3) photoelectrons, leading to a yield of (320 ± 8) photoelectrons per MeV.

- The pulse height-energy relation is also a parameter of the ^{14}C fit (see below), which is performed in the energy range from 70 to 150 keV, resulting in a somewhat higher value of 340 photo electrons per MeV (here, no ionization quenching is taken into account[2]).

- The energy resolution can be derived from the width of the ^{214}Po alpha peak and corresponds to $\sigma(E)/E \simeq 8.7\%$, or $\sigma(E)/\sqrt{E} \simeq 2.6\ keV^{1/2}$. A value of $\sigma(E)/\sqrt{E} \simeq 2.5\ keV^{1/2}$ is obtained from the spectral analysis of the ^{14}C spectrum at energies between 70 and 150 keV.

- The spatial resolution was studied with a localized ^{222}Rn source at various positions inside the Inner Vessel. Values of $\sigma_{x,y} \simeq 12\ cm$, $\sigma_z \simeq 13\ cm$ at 600 keV were obtained at center of the detector. The resolution degraded up to 15% close to the surface of the Inner Vessel.

4.2.4 α/β discrimination

To distinguish α from β particles by pulse shape discrimination, two different methods have been implemented in CTF-2: the "standard" charge integration method (already used in CTF-1) and the "new" Optimum Filter method, which is applied to the data from the newly designed and installed Digital Pulse Shape Analyzer (DPSA) [76].

The charge integration method

For the first method, the analog sum of the charge signal from all PMTs is split into several identical signals and sent to a charge sensitive ADC with different time delays. The total charge information is obtained from the integration of the entire charge pulse signal ($0 \div 500\ ns$), while the slow component is integrated in the time window $48 \div 548\ ns$[3]. The so-called "Tail to Total ratio" parameter ($r48/tot$) can be

[2] A detailed analysis of the photo electron yield including a model with ionization quenching is presented in [17].

[3] The choice of the time interval for integration was optimized during the CTF-1 data taking.

used as discrimination parameter as displayed in figure 4.4. The operation principle of the method is based on the difference between the α and $\beta - \gamma$ excitations: for the first, the slow component of the charge signal has a bigger importance ($\sim 25\%$) than for the second ($\sim 10\%$) [71, 77]; the time evolution of the scintillator signal for α and β particles in a lab scale setup is shown in figure 4.5.

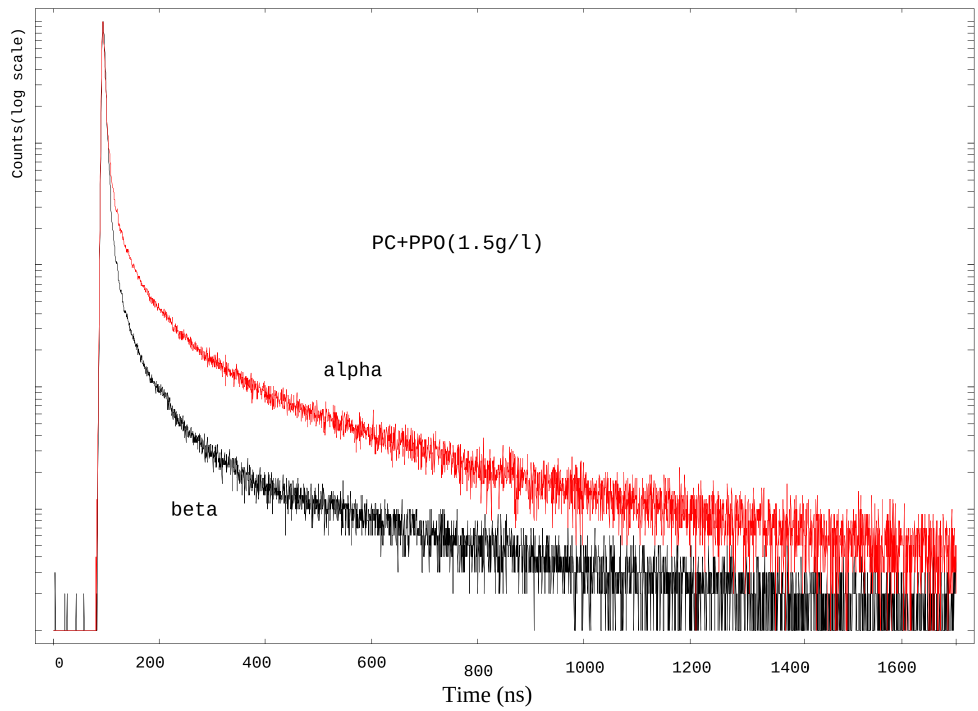

Figure 4.5: The time evolution of the scintillator signal for α and β particles in a lab scale setup of a few cm^3 (the scintillating mixture is the same of Borexino).

The discrimination efficiency can be derived from a clean data sample of α and β events in the same energy range, namely from events belonging to the ^{214}Bi – ^{214}Po coincidence; only ^{214}Bi events in the same energy range of the ^{214}Po events ($0.6 \div 1.3\ MeV$) were considered [16, 71]. Fixing the β acceptance efficiency at 98%, leads to an α rejection of 88%; applying a radial cut of $r < 90\ cm$ on the ^{214}Bi and ^{214}Po samples, the α identification efficiency increases to 91%[4]; finally, a 60 cm radial cut further improves α rejection to 94%[5].

For the lower energy region ($0.3 \div 0.6\ MeV$), the particle identification capability decreases dramatically: α/β discrimination can be applied only to the inner 60 cm

[4]This improvement is due to the optical distortions occurring at the interface between water and scintillator: the difference in refraction index between the two media induces the total reflection of the photons in the last 10 cm of the IV; this effect alters the time shape of scintillation events.

[5]This more stringent radial cut allows to minimize the distortion on time spectra due to the different time of flight of the photons, when reaching PMTs lying on opposite sides of the IV.

of the detector and performances are significantly worst than in the high energy case: fixing the β acceptance efficiency at 93%, the α rejection capability is only 82%. The behavior of discriminating parameter is shown in figure 4.6 (left).

DPSA data and the Optimum Filter

The DPSA board [76] analyzes one of the copies of the analog sum of the charge signal from all PMTs; the board performs first an integration of the sum signal; then the integrated pulse is sampled every 8.3 ns by means of a 60 MHz FADCs pair (with 10 bit resolution).

The first step in the analysis of DPSA data is the identification of a pair of α and β reference pulse-shapes (this can be partially done by exploiting the ^{214}Bi –^{214}Po coincidences); then the DPSA signal for each event is processed through the so-called "Optimum filter", first proposed by Gatti and De Martini in 1962 [52] (for this reason, the discrimination parameter is often called "Gatti" parameter). The discrimination parameter is obtained from the following formula:

$$G_{\alpha\beta} = \sum_i P_i\, S_i = \sum_i \frac{\alpha_i - \beta_i}{\alpha_i + \beta_i}\, S_i \;, \tag{4.1}$$

where S_i are the n samples of the signal performed by the board, α_i and β_i are the sampled α and β reference pulse-shapes and, in our case, $n = 50$ [71].

The distribution of the "Gatti" parameter can be found in figure 4.6 (right), for low energy events reconstructed in the inner 60 cm of the detector: the improvement with respect to the $r48/tot$ parameter is well visible. In this case, fixing the β acceptance efficiency at 93%, leads to an α rejection capability of 94% (which means that the α contamination of the selected β sample decreases from 18% of the previous case down to 6%).

With the DPSA data, the radial cut can be released and α/β discrimination can be performed also in the external shells of the Inner Vessel; with a 90 cm radial cut, we obtain (for a 93% of β acceptance) a 90% of α rejection; with the 1 m radial cut (only events reconstructed out of the IV volume are discarded), α rejection is 88% (always fixing a 93% β acceptance).

4.2.5 PXE test results

- ^{14}C **analysis:** the counting rate below 200 keV is dominated by the ^{14}C beta decay with an endpoint of 156 keV. The ^{14}C concentration in the scintillator was determined by fitting a convolution of the theoretical beta spectrum and the energy dependent detector resolution function, plus a background contribution to the measured spectrum in the energy range from 70 to 150 keV [7]. The low energy spectrum together with the fit is displayed in figure 4.7: at lower energies there is a background contribution from Čerenkov events produced by γ in the shielding water. From the fit the ^{14}C activity is derived, which can

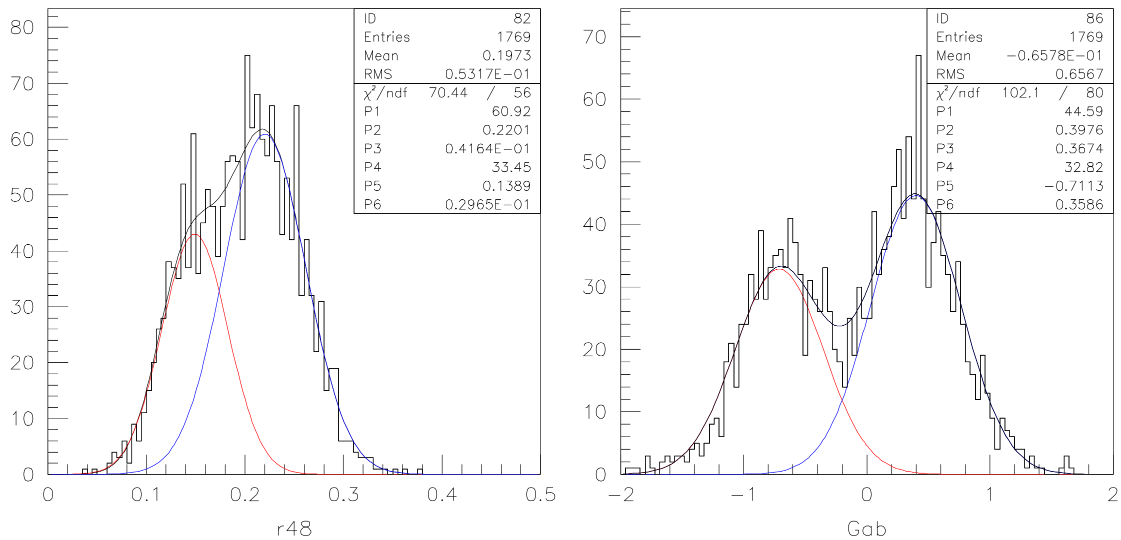

Figure 4.6: α/β discriminating parameter distribution for the $r48/tot$ and the "Gatti" parameters, in the low energy region and with a 60 cm radial cut.

be translated into a ratio of $^{14}C/^{12}C = (9.1 \pm 0.3\ (stat)\ \pm 0.3\ (syst)) \times 10^{-18}$. The systematic error is dominated by the uncertainty of the scintillator mass.

- ^{238}U **decay chain:** the ^{238}U decay chain is assayed via the delayed coincidence of the ^{222}Rn progenies $^{214}Bi(\beta) -^{214} Po(\alpha)$, with a half life of 236.6 μs (details on $^{214}Bi -^{214} Po$ analysis will be given in section 4.3). Assuming secular equilibrium of the decay chain (not expected to be the case here), the measured $^{214}Bi-^{214}Po$ rate can be expressed as an upper limit on the uranium-equivalent activity. During the CTF-2 campaign, the $^{214}Bi -^{214} Po$ activity was not homogeneously distributed within the scintillator volume, but most of the events were localized along the vertical symmetry axis of the detector. Nevertheless, an artefact due to false reconstruction could be excluded, because the reconstruction capability was tested with the insertion of a point like source which was located both on and off axis: the origin of these localized events could not be identified, however it can be excluded that they are related to the intrinsic scintillator impurities. To derive a number for the residual ^{222}Rn concentration homogeneously distributed in the scintillator, a cylindrical cut around the vertical axis was applied. For $R_{x,y} > 60\ cm$, a ^{222}Rn activity of $(27 \pm 5)\ \mu Bq/m^3$ was found, leading to an upper limit for the intrinsic ^{238}U scintillator contamination of $(2.3 \pm 0.4) \times 10^{-15} g/g$.

  Further radio-isotopes from the uranium decay chain of concern are the ^{210}Pb progenies ^{210}Bi and ^{210}Po. Secular equilibrium typically is perturbed even within this sub-chain, because of the characteristic lifetimes and the different chemistries involved. About 100 to 200 decays per day with α-like pulse shapes

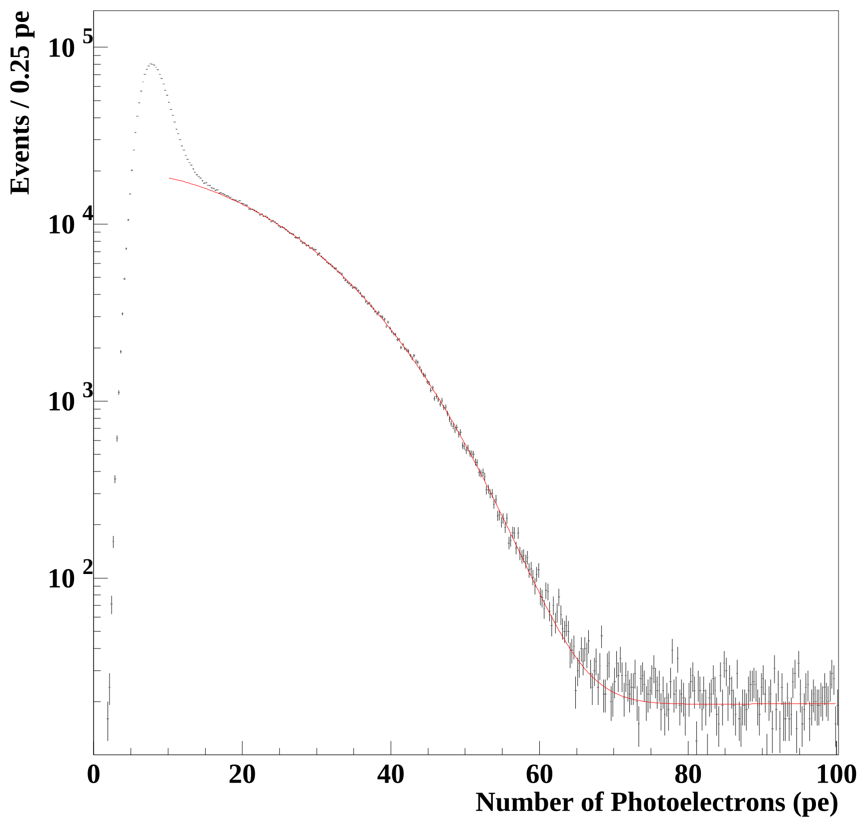

Figure 4.7: Data and fit of ^{14}C spectrum in CTF-2: the bin width is 0.25 $p.e.$ and the collection period is 153 hours (from [16]).

and with quenched energy depositions around 0.5 MeV can be attributed to ^{210}Po decays in the scintillator [71, 16].

- ^{232}Th **decay chain:** a limit for the intrinsic ^{232}Th contamination can be derived in a similar way as for ^{238}U, as in the ^{232}Th chain there is also a delayed coincidence, $^{212}Bi -^{212} Po$, with a half life of 299 ns. It can be distinguished from the $^{214}Bi -^{214} Po$ coincidence by the higher energy of the α decay and the shorter coincidence time, though the latter has to be considered as a background (details on the $^{212}Bi -^{212} Po$ analysis will be detailed in the next section). Secular equilibrium in the ^{232}Th chain is usually observed for ^{228}Th and its progenies; it can be broken between ^{232}Th and ^{228}Th. Assuming full secular equilibrium and including the branching ratio of $^{212}Bi(\beta) -^{212} Po(\alpha)$ of 64%, an upper limit on ^{232}Th activity of $1.7 \times 10^{-15} g/g$ (90% $C.L.$) can be established.

- **Residual backgrounds:** an estimation of the remaining background for the neutrino detection in Borexino is provided by the subtraction of all known contributions from the background spectrum measured in the CTF. In order to reduce the contribution from the external background, a radial cut ($r < 90\ cm$) has been applied. Also, all correlated events have been tagged and discriminated: at this stage, the residual activity in the neutrino window is 120 events per day and ton. As a next step, all muon induced events have been subtracted (74 events per day and ton); in this inner region of the detector, alpha events can be discriminated via their pulse shape (with an efficiency of $\sim 90\%$), leading to 48 events per day and ton. The resulting background spectra are shown in figure 4.8; clearly visible are the contributions from: ^{14}C, remaining alphas from ^{238}U and ^{232}Th chains, and a ^{40}K peak, which could be identified as external background originating from the Vectran strings that hold the Inner Vessel in place.

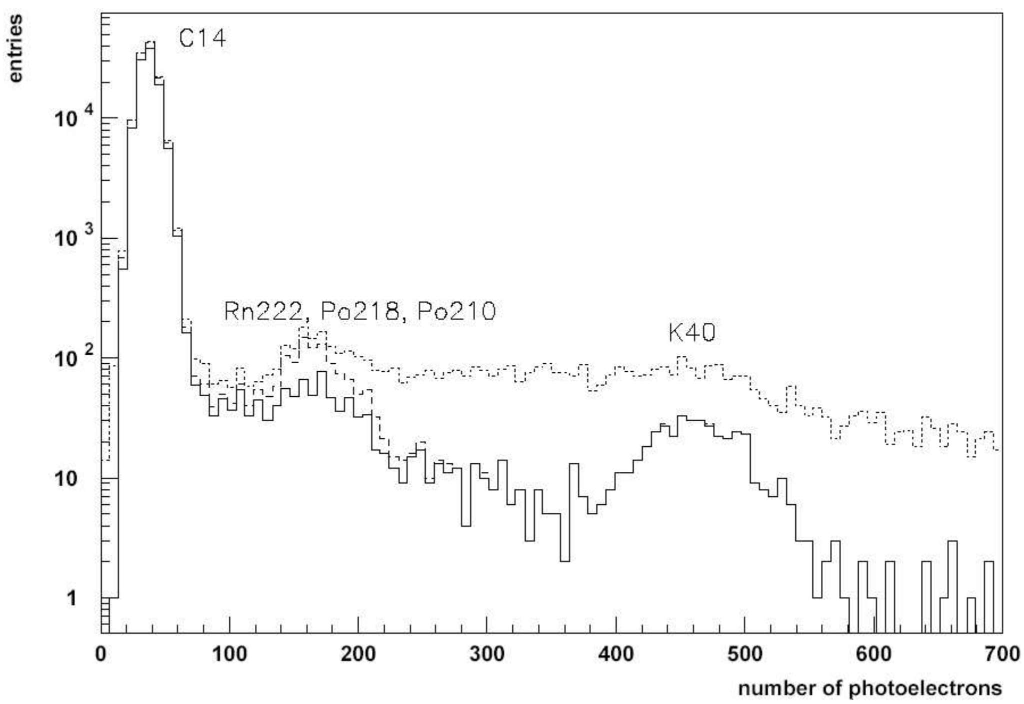

Figure 4.8: PXE data collected in CTF during a period of 7.3 days: only single events with $r < 90\ cm$ are shown (dotted line); in the next step, all muon events are removed (dashed line); in the final step, 90% of the alpha events are subtracted via PSD (solid line); figure from [16].

4.3 Test of the purification systems: CTF-3

The CTF has been restarted in November 2001 to test the quality of the Borexino scintillator (PC+PPO) (both from the optical and the radio-purity point of view) and to verify the efficiency of different purification methods (water extraction, Si-Gel column and distillation). Data taking with CTF-3 is still in progress.

During the CTF-2 campaign, a creep in the CTF nylon vessel was found; in 2001, a new vessels set (inner vessel + radon barrier) has been produced at Princeton facility. The new vessels have been installed in March 2001 and filled with water in June: in figure 4.9, an internal view of the detector filled with water is shown. Filling with scintillator happened in November and data taking with full detector started on November, 27.

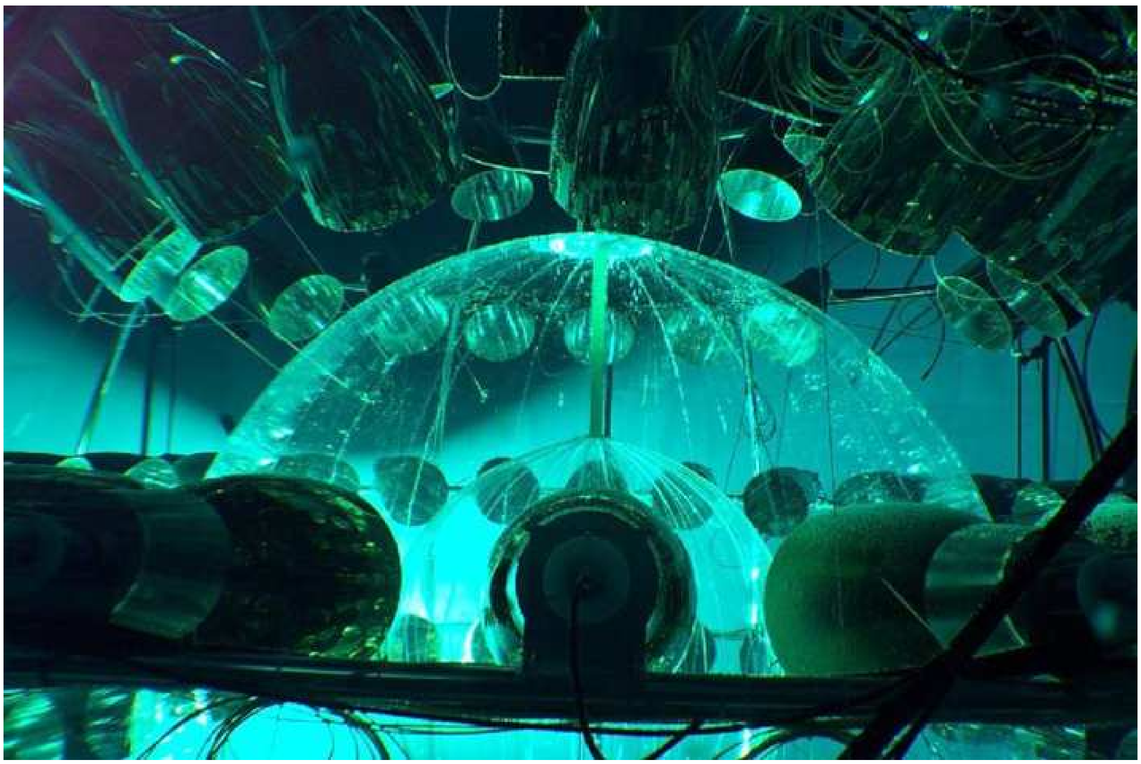

Figure 4.9: An internal view of the CTF detector, during the CTF-3 water run (June 2001).

Four batches of pseudocumene have been tested, belonging to different production periods (November 2001, January, April and June 2002) at the Sarroch plant (Sardinia, Italy) and showed very similar characteristics. The results described in the following sections have been obtained exploiting the spectral and position distribution of the events, together with the particle identification capability of the detector: the event energy is obtained as the sum of the collected photons, the event position is reconstructed by taking into account the photon arrival time at each PMT, while the distinction between alpha and beta particles is deduced via pulse shape discrimination methods. Different analysis techniques were applied to the same data and proved to be substantially in agreement with each other.

4.3.1 A starting point for scintillator quality

The first PC batch was procured on 23 Oct 2001 and arrived in Hall C on 25 Oct 2001; the amount of PC loaded in the IV was: $(4268 \pm 10)\ l$, corresponding to $(3756 \pm 9)\ Kg$. The following analysis concerns the data taking period from 28 Nov 2001 to 9 Jan 2002; the total measurement period is 41.75 days and the total run time is 33.59 days, with a live time of the detector (corrected for the trigger dead time, which is measured by a scaler) of 30.47 days.

The scintillator photon yield was found to be $(380 \pm 20)\ pe/MeV$ (obtained through a fit of the ^{14}C spectral shape), corresponding to the expected energy and position resolution (FWHM) of respectively 10% and 13 cm at 1 MeV.

^{238}U analysis

In the ^{238}U analysis, the long ^{214}Bi –^{214}Po coincidence is tagged. ^{214}Bi decays $\beta + \gamma$ to ^{214}Po (end-point 3.23 MeV, 100% BR). ^{214}Po in turn decays α (7.668 MeV[6]) with a mean life of 236.6 μs. These coincidences are selected by means of the following cuts:

- coincidence time between the 1^{st} and the 2^{nd} event is requested to be lower than 709.8 μs (3 τ). Acceptance: $\simeq 95\%$;
- coincidence time between the 1^{st} and the 2^{nd} event is requested to be bigger than 2 μs, in order to reject short time ^{212}Bi –^{212}Po coincidences (with 99% efficiency). Acceptance: $\simeq 99\%$;
- energy of 2^{nd} event is requested to lie between 540 KeV and 950 KeV. These boundaries correspond to a 3 σ cut around the center of the ^{214}Po events distribution, obtained with a sum of all the ^{214}Po events, selected using the previous 2 cuts. Acceptance: $> 99\%$.

Since the ^{214}Bi isotope reaches secular equilibrium with ^{222}Rn in about 33 minutes, ^{214}Bi –^{214}Po coincidences can be used as a monitor of the ^{222}Rn contamination in the detector. In figure 4.10, a plot of the ^{214}Bi –^{214}Po counts during the whole data taking period is shown. The plot is fitted with a negative exponential + a constant: the decay time ($(5.86 \pm 0.12)\ days$) is in a good agreement with ^{222}Rn mean-life (5.48 d). The ^{222}Rn activity at the end of the filling with scintillator (28 Nov 2001) was $(2660 \pm 50)\ c/d$, while the constant contribution to this decay curve is $(5.86 \pm 1.22)\ c/d$.

If we assume the constant contribution to be in secular equilibrium with ^{238}U this activity corresponds to a contamination of $(1.46 \pm 0.30) \times 10^{-15}\ g/g$ of ^{238}U equivalent. Looking at the plot in figure 4.10, one can realize that the constant of

[6] This α peak was measured to be quenched to 751 KeV in laboratory measurements and in CTF-1.

the ^{222}Rn fit is clearly determined by the last few days of data taking; since only a couple of runs were taken in a very low ^{222}Rn activity condition, the value of the constant is just an estimation of the real ^{238}U contamination, which can also be significantly smaller.

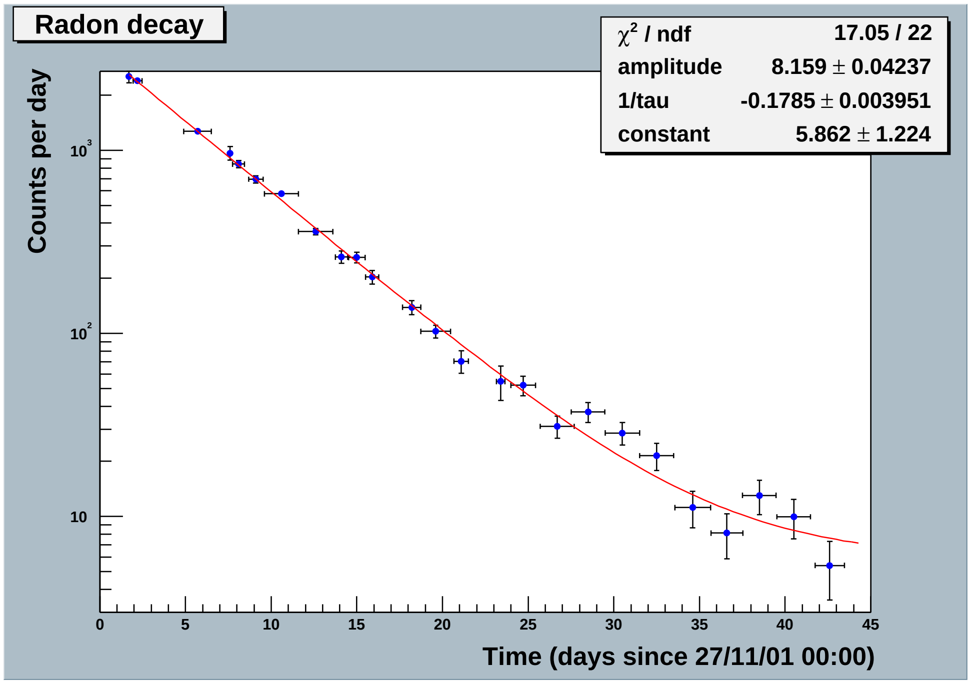

Figure 4.10: ^{222}Rn decay curve in log scale, fitted with exponential + constant (the constant is determined by the last few days of data taking).

^{232}Th analysis

In ^{232}Th analysis, the short term coincidence ^{212}Bi –^{212}Po is tag. ^{212}Bi decays β to ^{212}Po (end-point 2.25 MeV, 64% BR). ^{212}Po in turn decays α (8.79 MeV[7]) with a mean life of 432.8 ns. These short term coincidences are selected with the following cuts:

- energy of 1^{st} event is requested to be smaller than 2.49 MeV (2 σ above the the end-point energy) and bigger than 300 KeV. This second request is essential to reject some low energy events whose nature is presently not well understood. Acceptance is stated from simulated spectra: $\simeq$ 87%;
- energy of 2^{nd} event is requested to lie between 700 KeV and 1200 KeV. These boundaries are set by eyes around the distribution (marked in red in fig. 4.11),

[7]This α peak was measured to be quenched to 1.01 MeV in laboratory measurements and in CTF-1.

since the quenching factor in this region is not clear (see comments below). Acceptance: $> 99\%$;

- coincidence time between the the 1^{st} and the 2^{nd} event is requested to be lower than 2000 ns ($4.63\ \tau$)[8]. Acceptance: $\simeq 88\%$.

Only the period when the radon contamination was low enough (52 ev/d or smaller) was analyzed: 63 events were found, evenly distributed in a total live time of 17.58 days. The selected events can be seen in the scatter plots of figure 4.11. Background from ^{214}Bi –^{214}Po coincidences has been estimated assuming a flat decay curve in the $0-20\ \mu s$ time region and deducing the number of coincidence per μs that simulate both energy cuts from the $3-20\ \mu s$ time region where ^{212}Po events should be negligible: 0.53 $ev/\mu s$ in the considered live time. This in turn means that only $\simeq 1$ event of our 63 is due to ^{214}Bi –^{214}Po (we just subtract it). Random coincidence from other sources is instead negligible.

The daily rate of coincidence, accounting for background and acceptance of cuts is: $(4.7 \pm 0.6)\ ev/d$, corresponding to a contamination of $(6.2 \pm 0.8) \times 10^{-15}\ g/g$ of ^{232}Th equivalent.

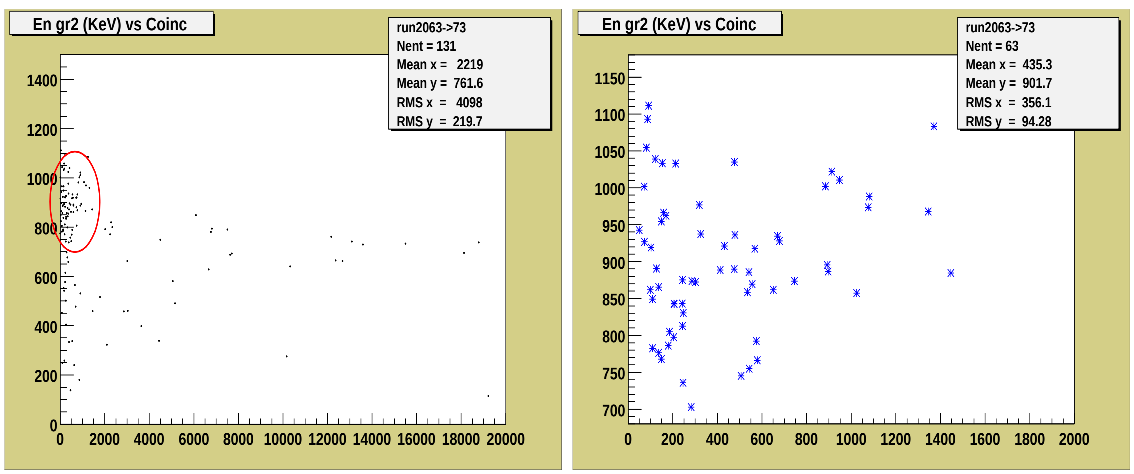

Figure 4.11: Left: a scatter plot of the 2^{nd} event energy versus the coincidence time. A clear cluster of ^{212}Po events can be seen around 900 KeV (circled in red). Right: a zoom of this cluster.

^{85}Kr analysis

^{85}Kr nuclei can decay β into ^{85}Rb ground state (687 KeV end-point energy; 99.57% BR) or into the metastable ^{85m}Rb (173 KeV end-point energy; 0.43% BR). The

[8]This time is also intrinsically larger than 50 ns due to the electronics dead time elapsing between two consecutive events, before a new trigger is armed.

^{85m}Rb in turns decays to ^{85}Rb emitting a 514 KeV γ-ray with a mean life of 1.46 μs[9].

These short term coincidences are tag with the following cuts:

- energy of 1^{st} event is required to be smaller than 274 KeV (3 σ above the the end-point energy). Acceptance: $\simeq$ 100%;
- energy of 2^{nd} event is required to lie between 300 KeV and 600 KeV (3 σ from the γ-ray energy). Acceptance (from simulated spectra): $\simeq$ 83%;
- coincidence time is required to be lower than 6000 ns (4.1 τ)[10]. Acceptance: $\simeq$ 95%.

Applying the described cuts, 19 events were found, evenly distributed in a total live time of 22.44 days. The average coincidence time comes out to be 1.93 μs, not too far from the expected value (1.46 μs). The average energy of the 2^{nd} event is 444 KeV, very close to the average value of simulated distributions (439 KeV).

A check for the incidence of background from random coincidence has also been made and this comes out to be negligible in the selected time-energy window. The daily rate of coincidence, accounting for acceptance of cuts is: (1.9 ± 0.7) ev/d, corresponding to (440 ± 160) $decays/d$ of ^{85}Kr .

Total countrate analysis

For the total countrate analysis, all the scintillation events in the energy region from 260 to 600 keV were considered (cosmic background events were rejected with the flag provided by the μ-veto system): in figure 4.12 the time evolution of the total countrate in this energy range is shown.

This time distribution has been fitted with a sum of two negative exponential, with the time constants of ^{222}Rn and ^{210}Po mean-lives (see below); the very good fit is a hint that the total countrate in this energy region is dominated by ^{222}Rn (+ ^{222}Rn daughters) and ^{210}Po decays (see below).

A "radial analysis" (i.e, the study of the event position distribution) for the events in the Neutrino Window ($250 - 800$ keV) has been applied to the data to disentangle the bulk contamination of the scintillator from the surface or external contamination [46]. The contamination coming form the surface was found to amount to approximately 1000 c/day: for this reason, all the following analysis of the total countrate will be performed with radial cuts on the selected events, in order to isolate the bulk activity form the surface/external one.

Figure 4.13 shows the spectral distribution of the internal countrate in the considered period (only the events within 60 cm from the center of the detector are

[9]Some of these γ-rays, especially those generated in the border regions of the IV volume, escape from the scintillator before loosing all their energy. The effect of this is a continuous spectrum superimposed on the peak distribution ranging from virtually zero energy to the peak value.

[10]This time is also intrinsically larger than 50 ns due to the electronics dead time.

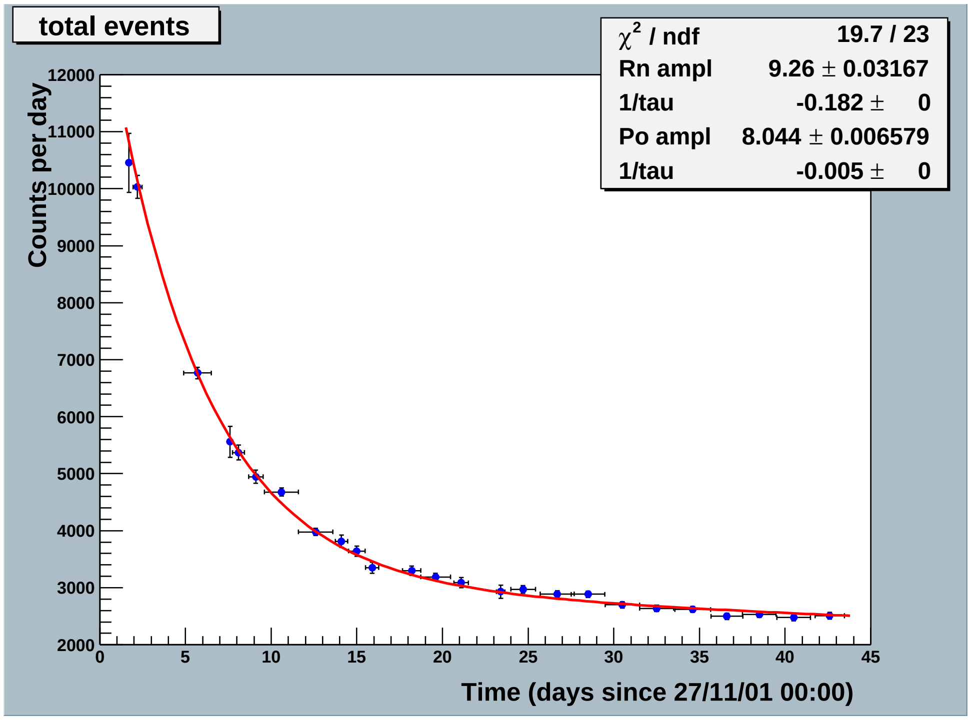

Figure 4.12: Total countrate in the energy range $260 - 600\ keV$, as a function of the date of the run (errors are statistical only).

selected): the peak at about $0.40 \div 0.50\ MeV$ is the sum of the activity from the ^{210}Po, the ^{222}Rn and the ^{218}Po, while the higher energy peak ($\sim 0.75\ MeV$) is due to the ^{214}Po decay; underlying there is the $\beta + \gamma$ activity from the ^{222}Rn chain and from the ^{40}K and ^{85}Kr; a shape analysis of this energy spectrum [46] indicates a significant contribution from ^{210}Po, as suggested by the time decay fit of the total activity.

α/β discrimination

In the above considered energy region, a continuous $\beta + \gamma$ spectrum is present: for this reason, the number of events in the α peak have to be computed using Pulse-Shape discrimination techniques.

α/β discrimination is performed in CTF using different techniques. The most effective one was found to be the so-called "Optimum filter" (or "Gatti method") applied to the pulses produced by the DPSA board [76], which was described in the previous section.

An optimization procedure of the DPSA data processing was performed at the beginning of the analysis procedure: the most important achievement was the optimization of the total integration time, which was found to be about 370 ns (DPSA data were therefore processed over a 367 ns interval).

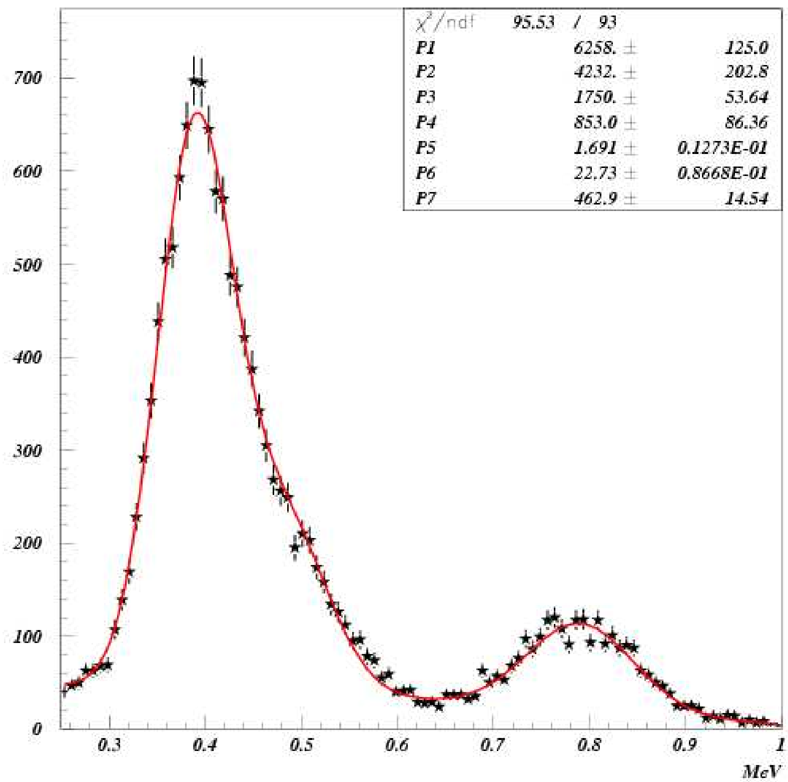

Figure 4.13: Spectral distribution of the internal countrate in the Neutrino Window (radial cut at 60 cm); the superimposed fit takes into account the contributions from: ^{210}Po, $^{210}Bi/^{40}K$, ^{85}Kr and ^{222}Rn sub-chain (plot from [46]).

The efficiency of this α/β discrimination method was evaluated on run 2048 data; since this efficiency depends critically on the geometrical distribution of the events, it was evaluated both on the whole detector and on an internal volume. The internal volume includes all the events reconstructed at a radius < 90 cm (from the center of the detector): this radial cut allows to exclude total reflections effects on the separation surface between scintillator and water.

The results of this evaluation are shown in figure 4.14: with no radial cut, for a 98% of β rejection efficiency we get a 90% acceptance for α events; with the 90 cm radial cut, for the same level of β rejection, α acceptance reaches the 94%.

Internal ^{210}Po analysis

^{210}Po decays α to stable ^{206}Pb (this is the last step of ^{238}U decay chain) with a mean-life of 200.2 d; the emitted α particle has an energy of 5.30 MeV[11]. The presence of an internal ^{210}Po contamination in scintillator (not in secular equilibrium with

[11]This α peak was measured to be quenched to 395 keV in laboratory measurements and CTF-1.

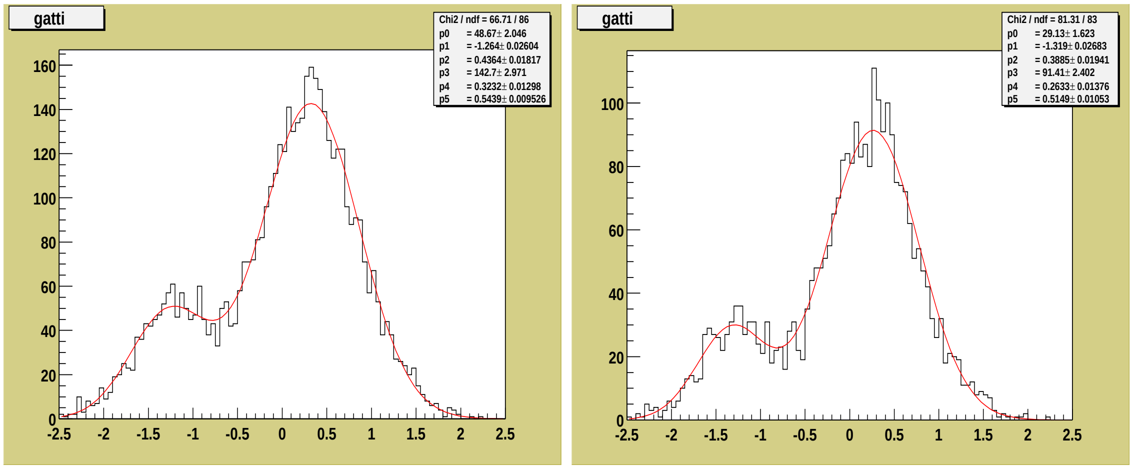

Figure 4.14: Evaluation of the α/β discrimination efficiency with the "Gatti" parameter, in the whole scintillator volume (left) and with a 90 cm radial cut.

its ancestor ^{222}Rn) is suggested by the spectral analysis of the energy distribution shown in figure 4.13; another hint comes from the time decay fit of the total internal contamination (figure 4.12); this second indication is however very weak, because the time decay fit of the total countrate is not really sensitive to the difference between a constant component and long decay time (200 d, to be compared to the 45 d of observation time). For this reason, a further analysis of the internal countrate has been performed, with the help of the α/β discrimination, which allowed to disentangle the low energy α peak ($0.4 \div 0.5$ MeV) from the underlying $\beta + \gamma$ spectrum.

In this energy region, α decays of ^{222}Rn and ^{218}Po are present, in addition to the ^{210}Po decay[12]: since the CTF energy resolution is not enough to separate these 3 peaks, ^{210}Po countrate estimation can be carried out by subtracting ^{222}Rn and ^{218}Po contributions from the total activity under the α peak (these contributions can be easily computed assuming the two isotopes to be in secular equilibrium with the ^{214}Bi –^{214}Po events[13], which are tagged by means of the delayed coincidence analysis described above).

In figure 4.15 is shown the time behavior of the residual internal α activity, after the statistical subtraction of the ^{222}Rn daughters contribution: it was obtained using a narrow radial cut (reconstructed radius < 70 cm) and scaling back the countrate to the total 4.2 m^3 volume; the resulting distribution is fitted with an exponential decay representing the ^{210}Po mean-life: the result of the fit shows that the distribution is consistent with the ^{210}Po hypothesis. The internal ^{210}Po activity at the beginning

[12]The peaks of ^{222}Rn (5.49 MeV) and ^{218}Po (6.02 MeV) were measured to be quenched respectively to 410 and 483 keV in laboratory and CTF-1.

[13]Secular equilibrium between these three isotopes is reached after ~ 33 min from the exposure time to the ^{222}Rn contamination.

of the run was estimated to be around 1800 c/d, with at least a 20% error[14].

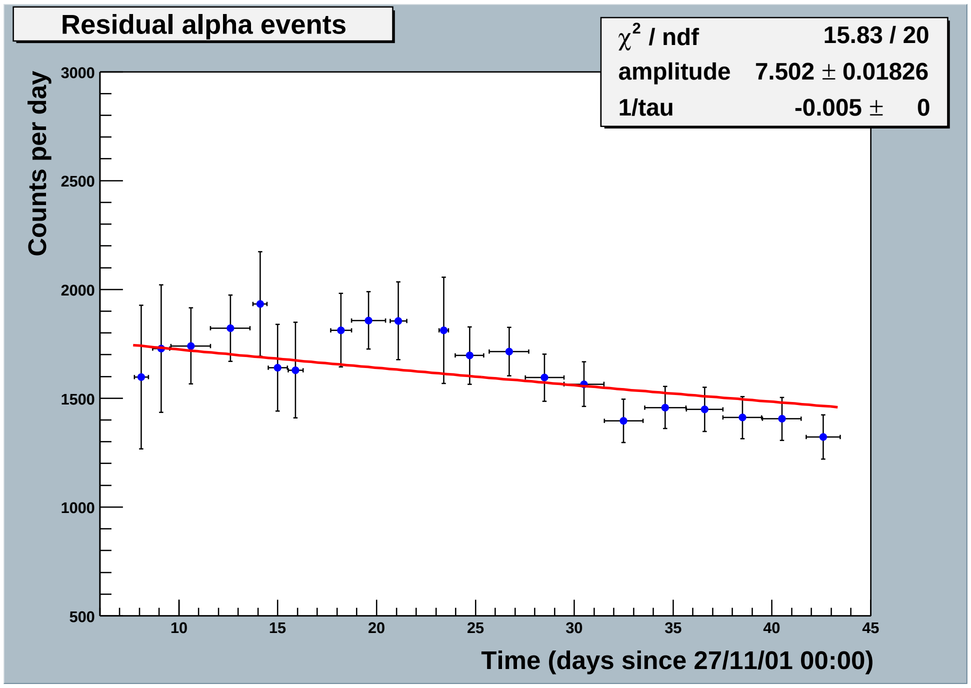

Figure 4.15: Estimation of the ^{210}Po internal contamination of the scintillator, during the first 1.5 months of data taking: the very first runs were discarded from this analysis, due to an electronics problem.

4.3.2 Results of the ^{14}C tests on the four PC batches

The four batches of pseudocumene which have been tested in CTF-3, belonged to different production periods at the Sarroch plant (November 2001, January, April and June 2002); they were measured right after their production (as soon as they arrived in Gran Sasso) and showed similar characteristics, concerning both the optical quality and the ^{14}C contamination.

The ^{14}C contamination test in the 1^{st} PC batch happened during the first month of data taking: as usual, ^{14}C activity was evaluated by means of a spectral fit of the low energy region (see figure 4.7); the result of the procedure is a measured $^{14}C/^{12}C$ rate of $(1.34 \pm 0.01) \times 10^{-18}$.

The other three PC samples were measured following this procedure: 50 l of the new PC were inserted in the CTF Inner Vessel via volumetric exchange with present scintillator; the observed increase or decrease in ^{14}C activity was studied,

[14] A precise estimation of the systematic error is not possible at present, since a calibration of the position reconstruction method is needed (it will probably happen in a few months from now); for this reason, the error on the reconstructed position of the events is not known exactly.

in order to evaluate the PC contamination with respect to the previous situation. The results of the tests were respectively: $(2.6 \pm 0.2) \times 10^{-18}$, $(4.4 \pm 0.2) \times 10^{-18}$ and $(4.4 \pm 0.4) \times 10^{-18}$ (expressed in terms of the $^{14}C/^{12}C$ ratio). The ^{14}C content of the scintillating mixture was found to be within the specifications (a few 10^{-18}) in all four cases.

In figure 4.16 is shown the total countrate in the $55 \div 80$ keV range, which is completely dominated by the ^{14}C activity; numbered periods indicate the four ^{14}C tests: in all three cases of new PC insertion, an increase of the countrate was observed, due to a higher ^{14}C contamination of the PC.

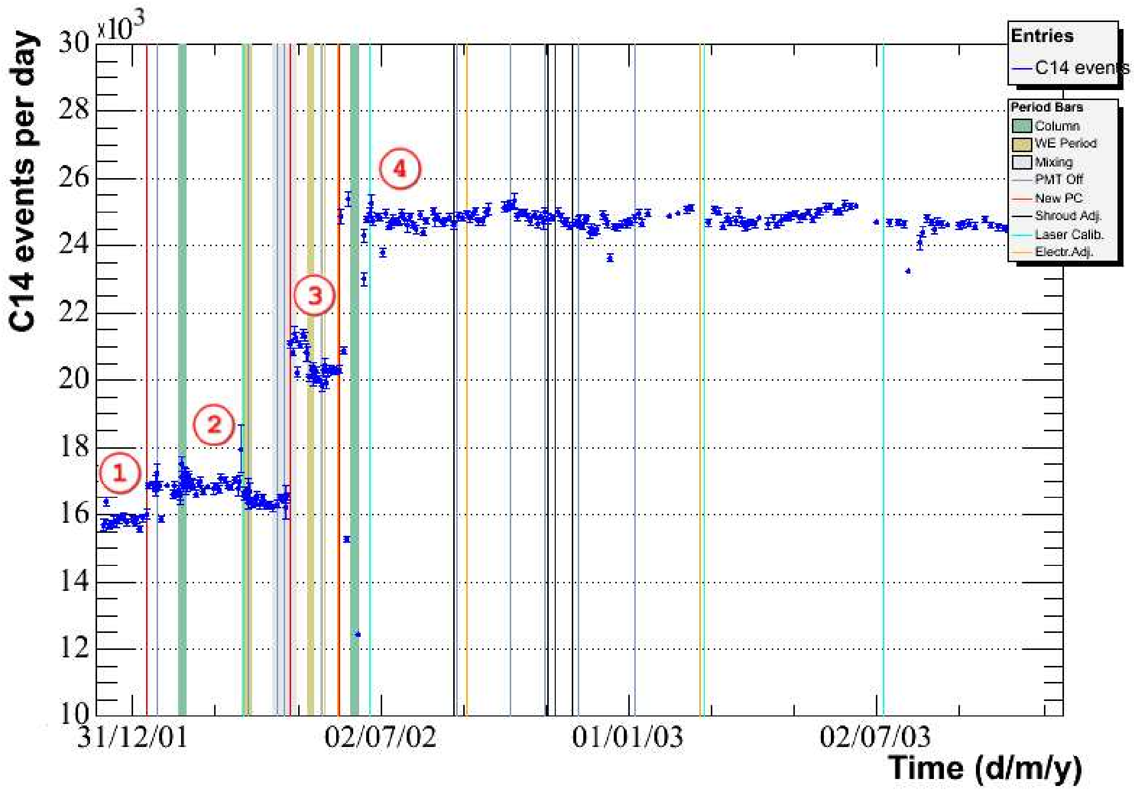

Figure 4.16: Plot of the total ^{14}C activity in the range $55 \div 80$ keV, during the first two years of CTF-3 data taking; numbered periods (red labels) are the four ^{14}C tests (from [46]).

4.3.3 The Si-Gel column purification system

The purification based on the Si-Gel column [16] was applied twice to the CTF scintillator (February and June 2002): the first time it was performed in the "loop" mode, that is to say the scintillator was circulated in a closed loop between the Inner Vessel and the purification column (the total scintillator mass present in CTF was processed about 6 times); the second time a "batch" test was performed: the scintillator was unloaded from the IV to a storage tank, processed through the column and loaded back to CTF (this procedure avoids the mixing between the purified and the "dirty" scintillator and in principle should give better results).

The main results of the loop purification test are the following:

- ^{238}U **:** after purification with the column, the ^{214}Bi –^{214}Po activity reduced to (3.1 ± 0.7) ev/day, corresponding to an ^{238}U contamination of $(7.6 \pm 1.7) \times 10^{-16}$ g/g: these numbers can be translated into a factor ~ 2 reduction in ^{238}U contamination;

- ^{232}Th **:** after the purification, the analysis indicated that the residual ^{212}Bi –^{212}Po events were due, at least in part, to surface contamination of the Inner Vessel and not to bulk contamination of the scintillator (the spectrum of the residual ^{212}Po events appeared shifted at lower energies than expected and the position reconstruction indicated a clustering of the events in the outer part of the IV volume). Therefore, in order to reduce the contribution of this surface contamination, a radial cut ($r < 50$ cm) has been applied in the analysis: the final value of internal ^{232}Th contamination was determined in $(1.4 \pm 1.1) \times 10^{-15}$ g/g, leading to a purification factor of ~ 4;

- ^{210}Po **:** a purification factor of ~ 2 was observed also for the internal ^{210}Po contamination, which reduced its activity to ~ 800 c/d (to be compared to the initial ~ 1600 c/d); a plot of the estimated internal ^{210}Po countrate[15] during and after the column loop test is shown in figure 4.17: the decrease in activity during the purification procedure is fitted with an exponential decay, which represents the ~ 2 purification factor, while the final ^{210}Po activity is fitted with a constant.

During the batch purification test, a further reduction factor of ~ 2.5 in internal ^{212}Bi –^{212}Po activity was obtained, leading to a final ^{232}Th contamination of $(5.2 \pm 1.4) \times 10^{-16}$ g/g; the ^{238}U contamination remained substantially unchanged ($(5.7 \pm 0.3) \times 10^{-16}$ g/g), with respect to the precedent water extraction tests (see below). Concerning the total internal contamination, an overall increase in activity was observed: the reasons for such an increase are not understood at present, but will be further investigated in the future, as described in section 4.3.5.

4.3.4 Test of the water extraction procedure

This purification procedure implies a liquid/liquid extraction column, where water flows counter-current to PC; the process efficiently removes impurities with a higher solubility in the aqueous phase, including K and most heavy metals in the ^{238}U and

[15]The internal activity was determined applying an 80 cm radial cut, and scaling back to the total scintillator volume.

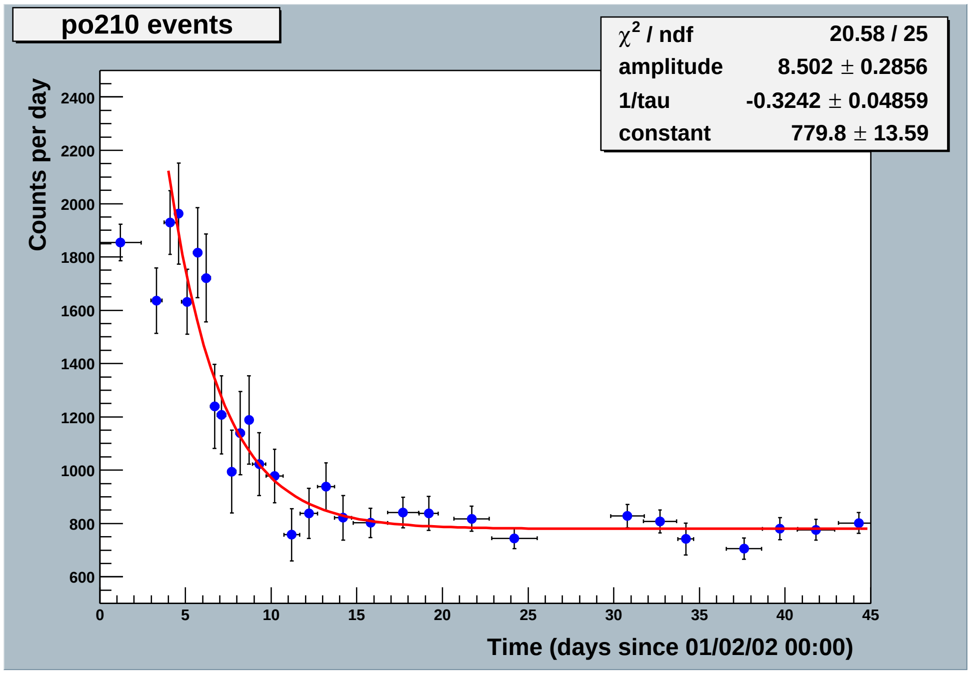

Figure 4.17: Estimated ^{210}Po activity during and after the loop column purification test: the countrate decrease during the purification procedure is fitted with an exponential decay, which represents the ~ 2 purification factor.

^{232}Th chains [9]. The test of the water extraction (and associated N_2 stripping) was done in a 8 day campaign during March 2002, where 13 inner vessel volumes were processed at a flow rate of 300 kg/hr.

Here are the main results of the test:

- **^{238}U :** after water extraction, the ^{214}Bi –^{214}Po activity reduced to (2.3 ± 0.6) ev/day, corresponding to an ^{238}U contamination of $(5.6 \pm 1.5) \times 10^{-16}$ g/g: these numbers indicate a small reduction in ^{238}U contamination, with respect to the starting point of $(7.6 \pm 1.7) \times 10^{-16}$ g/g. The countrate history for the ^{214}Bi –^{214}Po coincidence during the first year of CTF-3 data taking is shown in figure 4.18; the labelled regions indicate the ^{222}Rn lifetime fit for the periods following the main CTF-3 tests (first PC insertion, Si-Gel column in loop mode, water extraction purification, Si-Gel column in batch mode);

- **^{85}Kr :** N_2 stripping associated with water extraction has proved to be effective in reducing ^{85}Kr contamination: after the test, the residual rate of Kr events amounted to (30 ± 10) ev/day, which is consistent within 2σ with the activity expected from the Kr in the N_2 used for the stripping; overall reduction factor can be estimated to be about ~ 10;

- **^{210}Po :** the water extraction method, further reduced the internal ^{210}Po con-

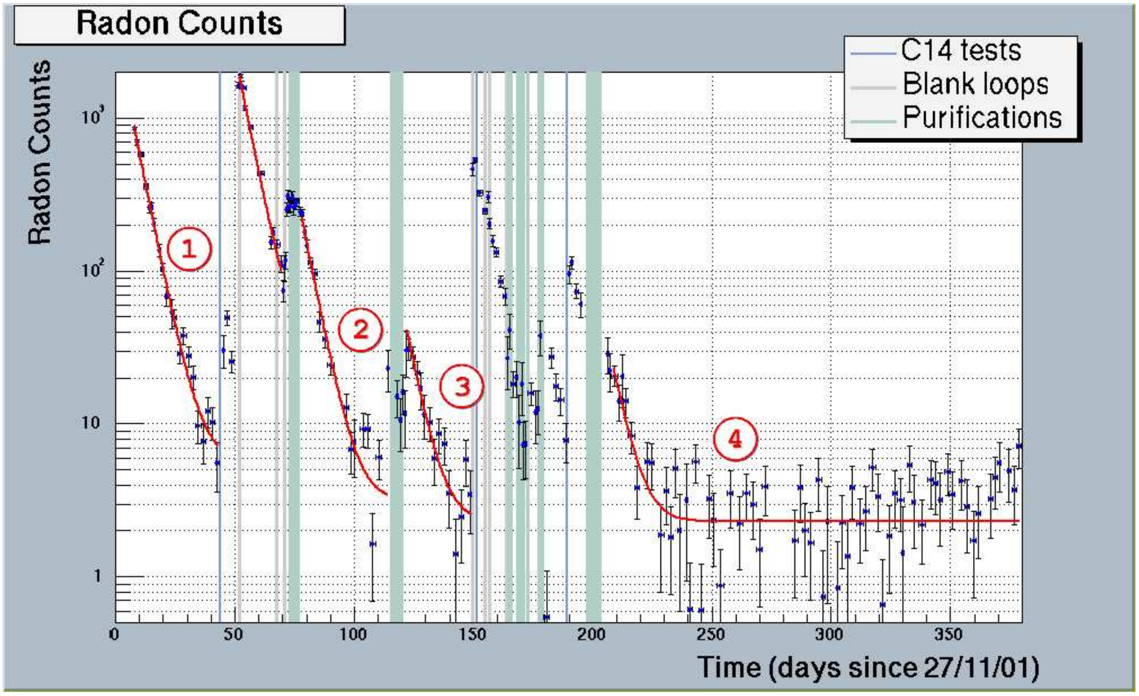

Figure 4.18: ^{214}Bi $-^{214}Po$ countrate history during the first year of CTF-3 data taking; numbered period represent: first PC insertion, loop column test, water extraction, batch column test.

tamination of a factor ~ 5; before the test, the estimated ^{212}Po activity was actually ~ 600 c/d, which reduced down to ~ 120 c/d after the test. The time behavior of the internal ^{210}Po countrate[16] before, during and after the column loop test is shown in figure 4.19: the decrease in activity during the purification procedure is fitted with an exponential decay, which represents the ~ 5 purification factor, while the starting and final ^{210}Po activities are fitted with a constant.

4.3.5 A proposal for the future measurements sequence

The CTF-3 operations have been stopped on August, 16 2002, due to the lack of some scintillator handling permissions from the LNGS. The CTF-3 operations will likely resume in the first months of 2005, after the discussion of the present work. An internal Borexino committee has been installed, with the commitment to propose a program to resume the operations. The main conclusion of the committee are listed here, along with their scientific motivation.

The main questions the next CTF tests should answer are:

[16]The internal activity was determined applying a 70 cm radial cut, and scaling back to the total scintillator volume.

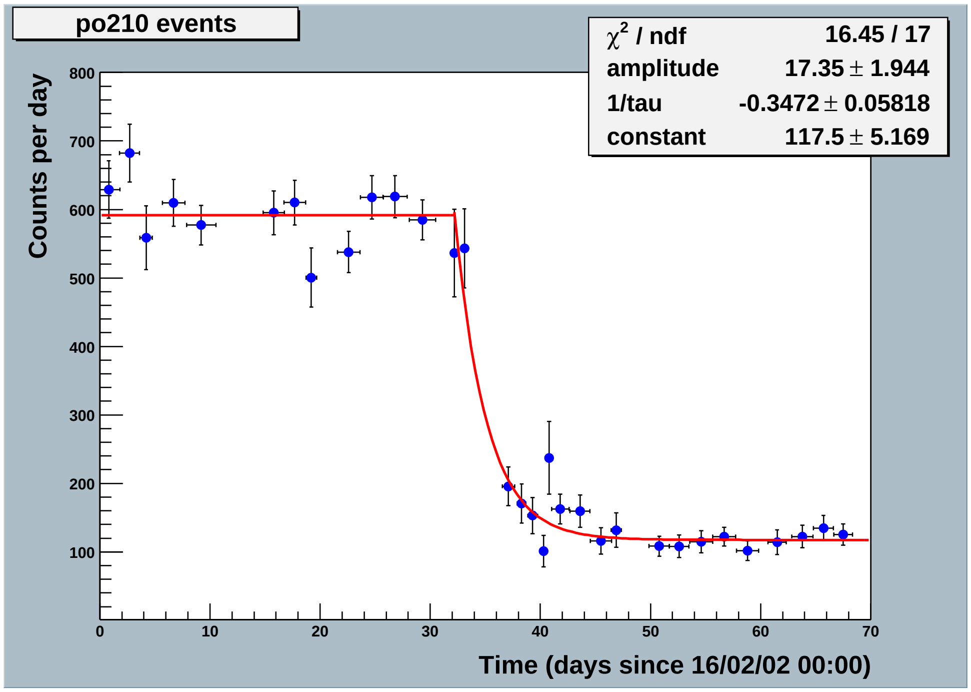

Figure 4.19: Estimated ^{210}Po activity before, during and after the water extraction test: the countrate decrease during the purification procedure is fitted with an exponential decay, which represents the ~ 5 purification factor.

- **how uncertain are the CTF-3 results?** as explained before, the present CTF-3 results suffer from an unknown systematic uncertainty, due to the missing calibration of the position reconstruction system: first of all, a calibration has to be performed, in order to certify the position reconstruction performances; this would definitely rule out the hypothesis that the observed countrate is not due to the bulk activity of the scintillator, but to a big surface or external activity;

- **is the ^{210}Po contamination present in PC or in PPO?** if a bulk ^{210}Po contamination is really there, we need to understand whether it comes from the PC itself or from the PPO; for the two components of our scintillating mixture, up to now two different purification procedures have been applied, based on the assumption that the main contamination comes from the PC (due to its bigger mass): if a specific test will contradict this assumption, a more aggressive purification procedure will be foreseen for the PPO as well;

- **why the purification tests did not give expected results?** both water extraction and Si-Gel purification gave lower results than expected: especially, the water extraction performances were inferior to what was achieved in CTF-1, and the batch Si-Gel column test seemed to dirty the scintillator instead of cleaning it (while the loop test showed a reduction in contaminations, even if lower than expected); at present, the most reasonable hypothesis is that the scintillator flows into some lines which are not really clean (in spite of the careful cleaning work done before the use of the line) and it undergoes a recontamination effect from the lines itself, before coming back to CTF: a check of the lines cleanliness is then desirable;

- **what is the present status of the PC in Storage Area?** $\sim 300\ t$ of pseudocumene are sealed in SA tanks since 2.5 years: before its use (and its purification), the PC has to be carefully checked (both on optical and radioactivity point of view), in order to study the possible contamination effects due to long stop in the SA tanks (contact with the Stainless Steel, possible ^{222}Rn emanation or leak, etc.);

- **what else can we do, for PC purification?** Among the three purification methods implemented in Borexino, the distillation has not been tested yet: this test is quite crucial, because the CTF-1 results indicate a big purification factor as a combined result of both water extraction and distillation (the separate effects of the two methods were not established with sufficient accuracy). After the distillation test, also water extraction and Si-Gel column will likely be repeated: but it is very important that this second round of purification tests takes place after the re-cleaning of the lines and the PPO tests, otherwise the possible inefficiencies of the method will be confused with other effects.

The proposed CTF tests sequence follows from the previous considerations and is composed of ten steps:

1. **position reconstruction calibration:** it will be made by means of a movable radon loaded source (like the one used in CTF-2) and an optical fiber. The radon source will help in reducing the uncertainties concerning radial analysis (and, if the quality of the source is very high, it will provide a cross-check of the α/β discrimination methods). Fiber optics will allow to study the validity of the Borexino concept for position calibrations;

2. **lines cleaning:** some lines in the purification skids have never been cleaned; before continuing the tests, these two groups of lines need a precision cleaning;

3. **blank test of the lines,** done by circulating the scintillator that is now in CTF through the purification skids and the Module 0 (the module containing the Si-Gel plant and some buffer tanks). The test should involve already cleaned lines; it will be done in two steps: the first time without going through the skids; the second time going through the skids. The test should be long enough to test also radon leaks in the lines;

4. **check the optical quality of the PC in the Storage Area:** if the optical quality is too bad, a supplementary purification program need to be established;

5. **a blank test of the PPO system:** all the lines involved in PPO plant will undergo a blank test, similar to the one done in the main lines; this test will allow the disentangle the possible contamination coming from the PPO itself from the effect of the lines;

6. **precision cleaning of remaining lines:** filling stations and other lines (not involved in previous tests) will be cleaned, before their use during Borexino filling (lines not involved in CTF tests will be cleaned later than others);

7. **PPO test:** it consists of an insertion in CTF of a few liters of "master solution" (a concentrated solution of PPO in PC). In principle, this test requires distillation plant to be operational, in order to check in the same time the procedure for Borexino; alternatively, a lab-scale procedure can be applied just to check PPO purity, and the full test will be performed later;

8. **test in CTF of the PC in the Storage Area:** of course, this test will be done only if the optical quality is not too bad; otherwise, either an attempt to improve the optical quality of the PC will be performed (for example by means of an intensive nitrogen stripping) or some new PC arrival (for the buffer liquid of Borexino) will be waited for;

9. **distillation test with Borexino skids:** for this test, the PC in the SA will be used (a sample of this PC will have been tested just before, so that a "pre-distillation" measurement of the same PC batch is not strictly needed). This is the most important test of all, but it cannot happen before the others: all the possible contamination sources (lines, PPO, etc.) have to be identified (or discarded) before doing it;

10. **possible further tests of Si-Gel column purification and water extraction:** this second round of tests will be decided upon the outcome of previous tests and will hopefully allow to define the final procedure for scintillator purification in Borexino.

Chapter 5

An overview of the Borexino read-out system

The design and the implementation of the Borexino read-out system is optimized for the measurement of the ^7Be solar neutrino flux. For each scintillation event, the energy and position informations have to be reconstructed: energy is needed for the spectral analysis of the neutrino signal, while position allows the determination of the Fiducial Volume (see chapter 2).

The scintillation light produced in events has then to be detected with high precision:

- the emitted photons have to be efficiently collected and their number accurately measured, because it determines the total energy of the event;
- the arrival time of each photon must be determined at the ns level, for precise reconstruction of the event position and for the exploitation of Pulse Shape Discrimination techniques (section 4.2.4).

In addition, the time difference between consecutive events has to be known precisely, to allow Delayed Coincidence analysis (a technique for identification of radioactive background). A determination of the absolute (astronomical) time of the event would provide this information, and would be useful for the field of Supernova Neutrinos (section 3.2).

The read-out system is based on the well-known technique of the Photomultiplier tubes; this chapter describes the main features of the Borexino PMTs, as well as the specific implementation of the electronics and data acquisition.

5.1 Borexino Photomultipliers

Borexino detector will use a large number of photomultipliers. At the first stage of the experiment a long test activity was carried out on several large photocathode

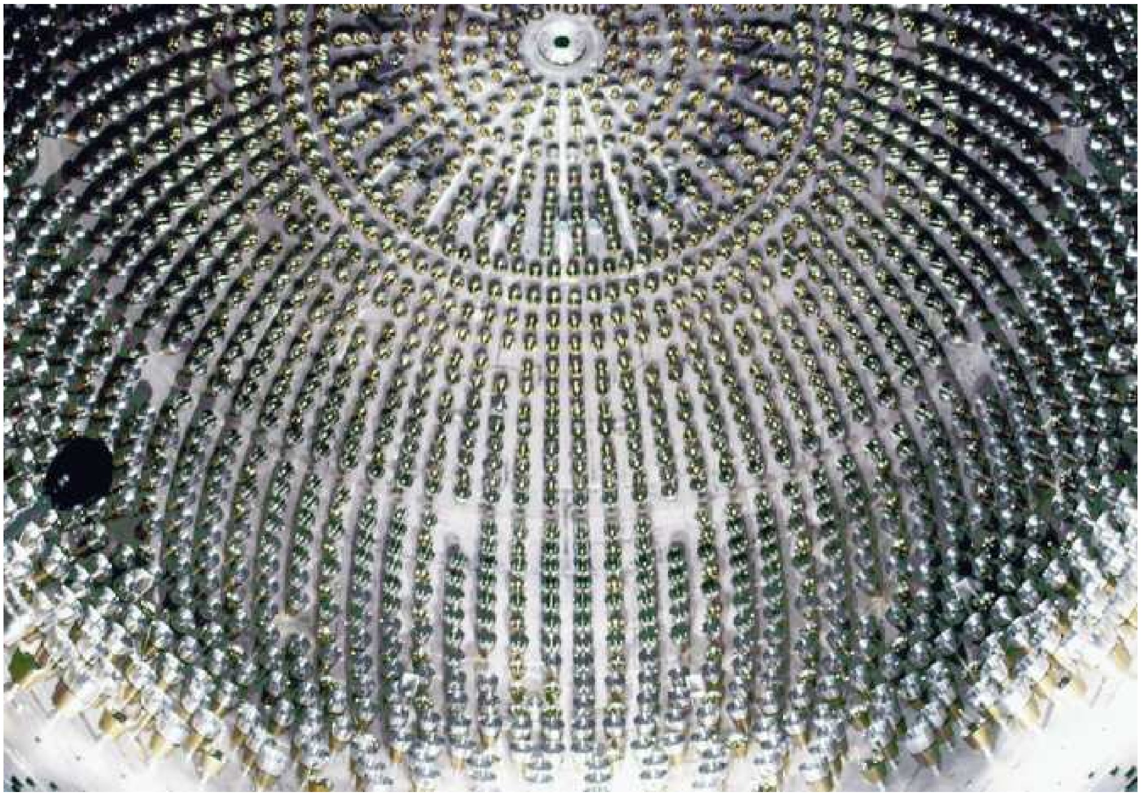

Figure 5.1: An internal view of the SSS, with 1993 installed PMTs, right after the dismount of the scaffolds used for installation (Nov 2001).

area tubes available on the market. The 8" E.T.L. 9351 phototube was identified as the best for the operation in the Borexino detector; the 9351 tube has an hemispherical photocathode with a curvature radius of $\sim 11\ cm$, thus resulting in a minimum projected area of 366 cm^2. The cathode is made of an emissive bi-alkali type layer ($CsKSb$), while the multiplier structure consists of 12 linear focused dynodes ($BeCu$). The bulb of the tube is made of a low radioactive Schott 8246 glass, carefully analyzed in the germanium facility at the underground Gran Sasso Laboratory.

The selection of PMTs was performed essentially by evaluating the impact of the main technical features of the candidate tubes on the overall detector performances. For this purpose, the principal characteristics of the tubes were thoroughly analyzed in operational conditions (the high priority parameters and their values are presented in table 5.1). Through a comparison between our measurements and all the statistical information available from the company, a table of specifications was produced; this specification table was stringent enough to fulfill all the requirements of the experiment, but in the same time it was practical enough so that a large fraction of the tubes were not rejected.

High Priority Parameters	
Photocathode quantum efficiency	$> 21\%$
After-pulses	$< 5\%$
Single *p.e.* transit time spread	$< 1.3\ ns$
Dark count rate	$< 20\ kHz$
Late pulses	$< 4\%$
Single *p.e.* peak to valley ratio	> 1.5

Table 5.1: High priority parameters for the choice of Borexino PMTs.

The adopted voltage divider scheme is suited for the twofold purpose of minimizing the simple photoelectron transit time spread and properly shaping the output analog signal for the subsequent front-end processing (signal and HV are coupled/decoupled at the input of the front-end electronics). The dividers are supplied with positive high voltage in the range of $1100 \div 2000\ V$. The voltage across the cathode and the first dynode is fixed (by means of two Zener diodes) to the value ($600\ V$) suggested by the manufacturer for the optimum PMT performance.

5.1.1 PMT encapsulation and mounting structure

The 2200 Borexino PMT's are mounted on the internal surface of the SSS. The sphere will be filled with PC, while the tank will be filled with water (see chapter 2). In this way, the front part of the PMT will be immersed in PC and the rear part in water. To ensure a reliable operation of the devices in such a complex environment, it was necessary to develop an encapsulation of the neck of the bulb and the divider in order to fulfill all the mechanical and environmental constraints. The design has been based upon the broad experience gained in the research and development of the Counting Test Facility (see chapter 4).

The base and the neck of the tube is enclosed in a cylindrical stainless steel housing whose external diameter is equal to $90\ mm$, as shown in figure 5.3. The housing is fixed to the glass of the neck of the tube through a PC proof epoxy resin, which acts as a structural adhesive as well as a protection barrier against the PC permeation. The end-cap of the cylindrical housing, welded to it and leak tested, carries the feed-through intended to ensure the mounting of the devices to the sphere.

The PMT installation is realized inserting the feed-through into a SSS hole and then securing it through a rear nut. An important role in this mounting is played by an isolating material (phenolic resin) that electrically decouples the device to avoid ground loops and also act as the groove for the Viton o-ring used to assure the tightness between the tank and the sphere. All the 2200 feeds-through have been tested by means of a custom made mass spectrometer, using argon as a trace gas to evaluate the leak rate. The feed-through is also designed to accommodate

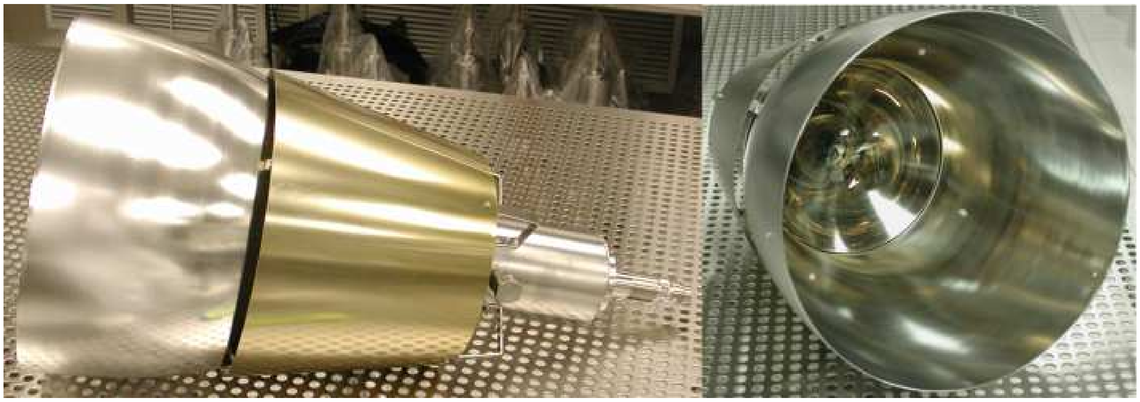

Figure 5.2: An assembled PMT in Clean Room, waiting for the installation in SSS: the optical concentrator, $\mu-$metal shielding and HV connector are visible (left), as well as a zoom of the photocathode area (right).

the underwater connector, which is screwed into the feed-through until its o-ring is properly compressed; a further potting with epoxy resin is realized, to have a second barrier against water infiltration.

The empty space inside the cylinder is filled with a inert organic oil: this oil prevents water condensation on the divider, without stressing the very delicate joints between the metal pins and the glass. A last barrier against PC is assured by an heat shrink teflon tube, glued between the glass neck of the PMT and the steel can. A fully assembled PMT, waiting for installation in the SSS, is shown in figure 5.2.

5.1.2 Light concentrators and $\mu-$metal

The intrinsic radioactivity of the photomultipliers used in Borexino does not allow to place them close to the center of the detector. In order to enhance the photon detection efficiency and to establish an energy resolution which meets the requirements of the experiment, 1800 PMTs out of a total of 2200 have been equipped with optical concentrators (OC). The OC is designed to collect scintillation photons emitted inside the inner vessel with high efficiency and its shape is calculated to reflect photons to the curved photocathode of the PMT if the incidence angle is below 32,5 degrees. The OC consists of high purity, soft aluminium which is processed to get its final shape (surface of a revolution body). The surface was electro polished to increase specular reflectivity (90% in the wavelength region of 370 to 450 nm) and the ageing tests confirmed a good resistivity against water and PC corrosion.

The EMI 9351 PMT, due to its large size, is very sensitive to the earth magnetic field, so it was necessary to shield it with a conic $\mu-$metal foil (0.5 mm thick) placed around the cathode and the base region. Ageing test showed that this material, in contact with pseudocumene, strongly catalyze an oxidation of the scintillator. It was mandatory to protect the $\mu-$metal with a lining (20 μm thick) of clear

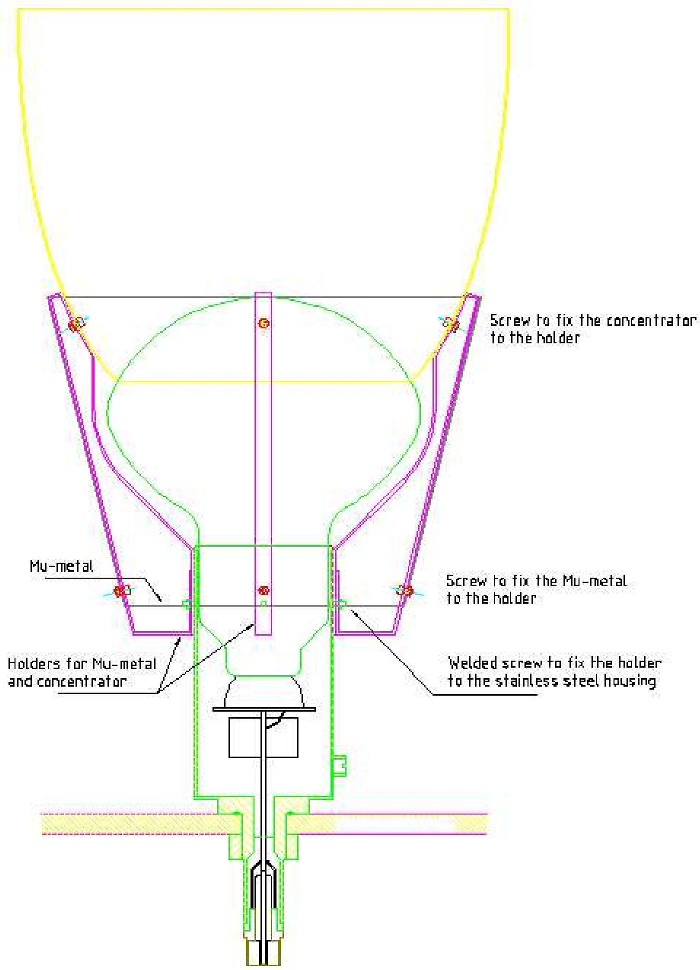

Figure 5.3: Layout of the PMTs assembly structure.

phenolic paint. The support of the $\mu-$metal and the light concentrators is sketched in figure 5.3 and it is realized with four holders at 90°, screwed on the housing of the tube.

5.1.3 Cables and connectors

In Borexino, cables and connectors will lie completely immersed in high purity water for a period of many years. This requires the use of materials explicitly developed for submarine applications. The assessment of the compatibility for our application implies of course the evaluation of possible effects caused by the concurrent presence of different materials as the development of localized corrosion and the release of impurities in water; as usual, the radioactivity level of the materials is also a major concern.

The transmission line is intended to conduct both the signal and the high voltage

Figure 5.4: A cluster of PMTs installed in the Northern Hemisphere of the SSS.

(HV), while ensuring the connection to a 50 Ω front-end where the decoupling of the HV and the signal is accomplished. The cable, that connects the device directly to the electronics, is a custom made RG213 coaxial 50 Ω cable. The outer jacket is made of solid extruded high density polyethylene, while an internal barrier is realized with a laminated copper foil, bounded to the braid with a copolymer coating. All the cables have an electrical length of $(282.1 \pm 0.25)\ ns$ ($\sim 57\ m$).

Underwater connectors will work in a non critical condition concerning pressure but an immersion time of many years required the help of a company with a big experience in long term applications in submarine field; they provided strong stainless steel connectors suitable for our 50 Ω RG213 cables, with Viton o-rings. Special attention was dedicated to the assembly of the connectors on cables, to optimize the overall electrical response of the line; dedicated tests with a dual port network were performed both at the company and at the experiment site.

All the Borexino cables (as well as the PMTs, the SSS holes, the electronics channels) are equipped with optical labels, on both extremities. After cables installation, these labels are read by means of a dedicated optical device and automatically inserted in the Data Base (the choice of an automatic procedure is intended to minimize errors due to manual transcription of the labels); in this way, it is possible to recover from the Data Base the cabling information from the SSS position to the corresponding electronics channel.

Figure 5.5: An internal view of the SSS, with the last mounted PMTs, after the installation and inflation of the Inner Vessel and Radon Barrier (June 2004).

5.1.4 Test of the PMTs and sealing design

Various testing stages have been foreseen in order to assess the quality and long term reliability of the PMT and of the encapsulation.

- As a first step, the device in its final configuration was immersed in deionized water inside a little steel tank to perform an accelerated ageing test under pressure and temperature. At the same time other prototypes were subjected to a long thermal cycling test for a comparison with the results of the finite element analysis.

- After this first campaign, a more realistic, long term and large scale test set-up was realized at Gran Sasso; 54 PMTs were immersed at the end of 1999 partially in pseudocumene and partially in water in a two liquid tank, explicitly designed to reproduce the main geometry, mechanics and environmental conditions of the experiment (the Two Liquid Test Tank is described in details in section 7.2.3). Since then all the PMTs have been working properly and all the main electrical, mechanical and chemical parameters are within the specifications.

- The PMTs delivered from the supplier (ETL) are tested at the factory, thus the operating voltage and the other performances are then reported on the data sheet by the manufacturer. Mainly, because of the difference in the dividers used by ETL and the ones used in Borexino, all the parameters should be measured again. For this purpose, a test set-up has been realized at the Gran Sasso in which it is possible to characterize, at the same time, 64 PMTs.

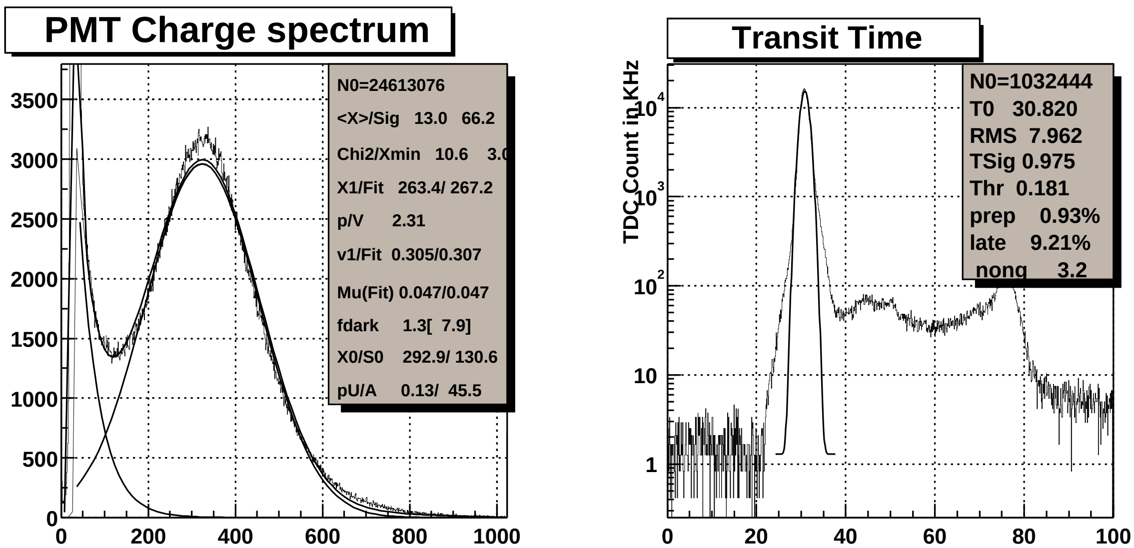

Figure 5.6: The charge spectrum and the transit time of a PMT, during the measurement in the Gran Sasso Dark Room.

The system consists in a dark room in which the tubes are allocated on a test table inside a compensation system for the Earth magnetic field. All the PMTs are illuminated with a solid state laser, whose beam is uniformly distributed and attenuated to reach the single photoelectron condition. The system performs a preliminary, but very accurate, high voltage tuning to set the real gain of each PMTs at a level of 2×10^7; several parameters are then acquired during a few hours test run and displayed as histogram in real time (see figure 5.6).

Most important parameters are: the charge spectrum, the transit time spread, the after-pulses and the mean number of photoelectrons detected by the corresponding tube. In figure 5.7 is shown the distribution of the transit time jitter of the PMTs presently installed in the SSS, as measured in dark room: the mean value of the distribution is $\sim 1.2\ ns$.

5.1.5 The HV power supply

Each photomultiplier needs to be supplied by a positive high voltage in the range of $1100 \div 2000\ V$, and by a current in the $100\ \mu A$ range. A suitable power supply

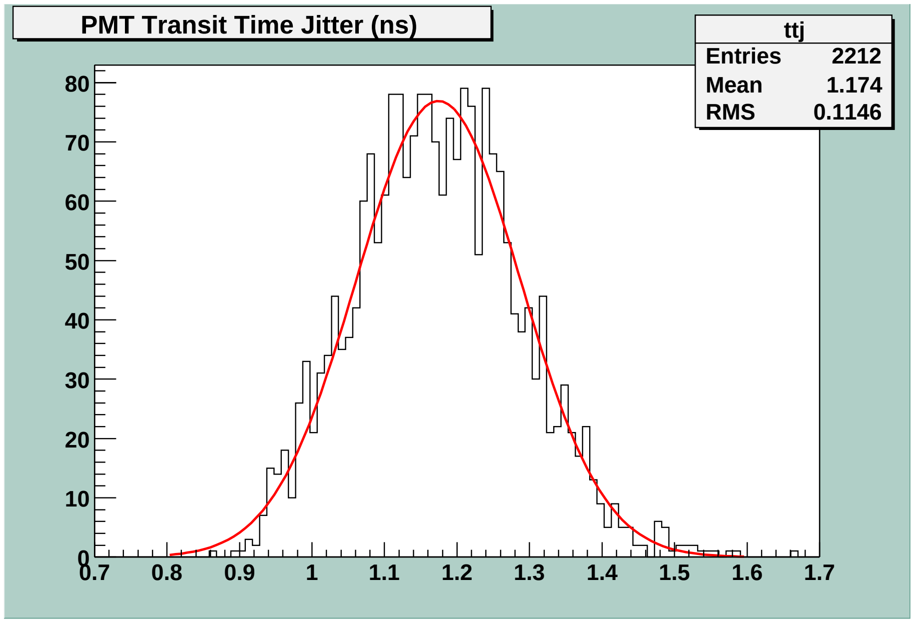

Figure 5.7: Distribution of the measured Transit Time Jitter for the Borexino PMTs.

system has been bought, based on the SYS527 modules (by C.A.E.N.): this model has been chosen thanks to its high modularity and its remote controlling features.

The system is organized in 14 independent crates (called "Mainframes"), with the same channels distribution of the Front-End and VME crates (see picture 5.9). Each mainframe can host up to 10 boards (24 channels each): in our case, 7 boards are enough to supply all the 160 PMTs associated to a crate.

Each crate may be controlled locally or remotely. Local control is performed manually through a key-pad and a LCD display located on the front panel. Remote control is realized either directly by means of a VT100 terminal, plugged in an RS232C connector, or by a network builded on a proprietary serial bus (CAENET), which allows to connect up to 98 units accessed by a master board installed in a PC. In our case, a program running on a dedicated PC (the "slow control", described in section 5.3) takes care of the control of the HV power supplies, which is a complex task, involving all the HV parameters (voltages, currents, etc.).

The modules bearing the output voltages are the A932AP Channel Boards (C.A.E.N.). They feature a primary high voltage channel, with 2.5 kV of maximum output, and 24 active distributor output channels, directly supplied by the primary channel. The internal primary channel has a complete set of programmable parameters: high voltage value (1 V resolution), current limit (1 μA resolution), ramp-up and ramp-down times, over-current behavior, alarms handling. Also the voltage on each distributed output can be independently programmed, but only inside a maximum drop of 900 V from the primary channel setting.

The output voltages are provided via two multi-conductor block-type connectors;

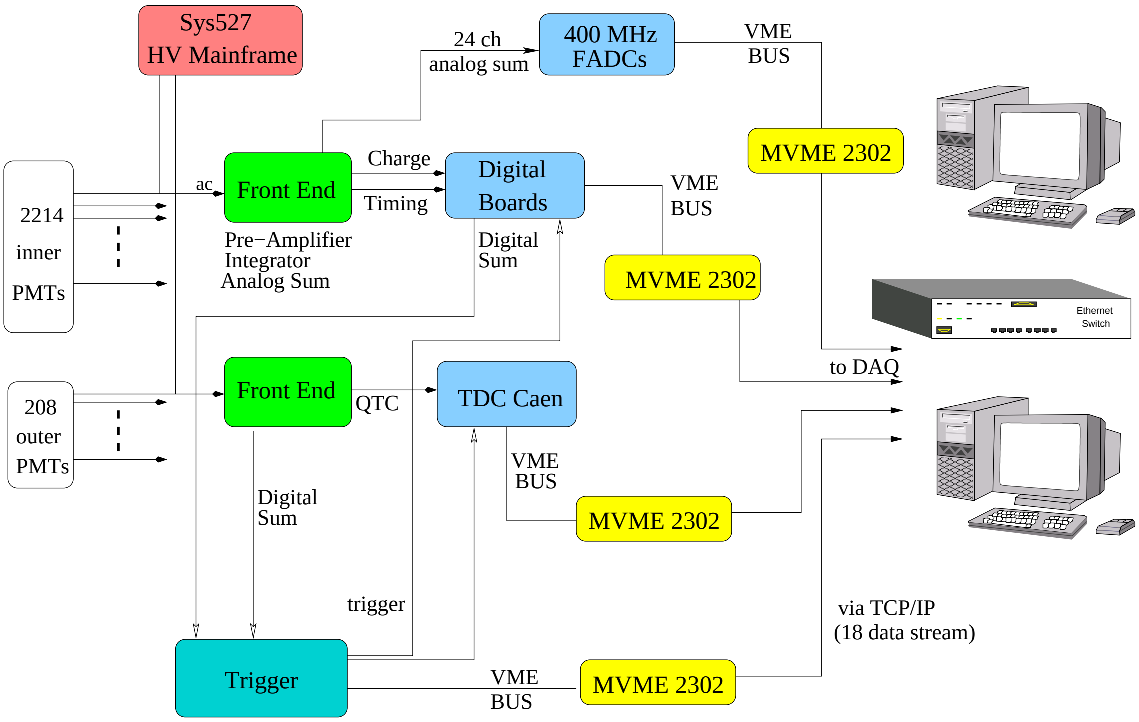

Figure 5.8: Block diagram of the electronics system for the Borexino detector.

the output connectors have two pins dedicated to realize the safety board interlock. This protection disables the primary HV generation when the distributor outputs are not connected to their loads (namely, when the connectors on the Front-End boards are not properly connected).

5.2 The "solar neutrino" electronics and trigger system

The design and the implementation of the main electronic system for Borexino, is optimized for the measurement of the ^7Be solar neutrino flux. The system is directly connected to the detector photomultipliers (PMT): for each of these, the arrival time and the collected charge for the single light pulse is measured.

The complete system is composed of the following (see figures 5.8 and 5.9): a front-end stage, which performs an analog processing of the PMT signal; a readout stage, used to digitize and store the signal processed by the front end and to measure the arrival time and the charge of each light pulse coming from the detector; a trigger stage, used to identify interesting events. In the following, a detailed description of each of the preceding stages is given.

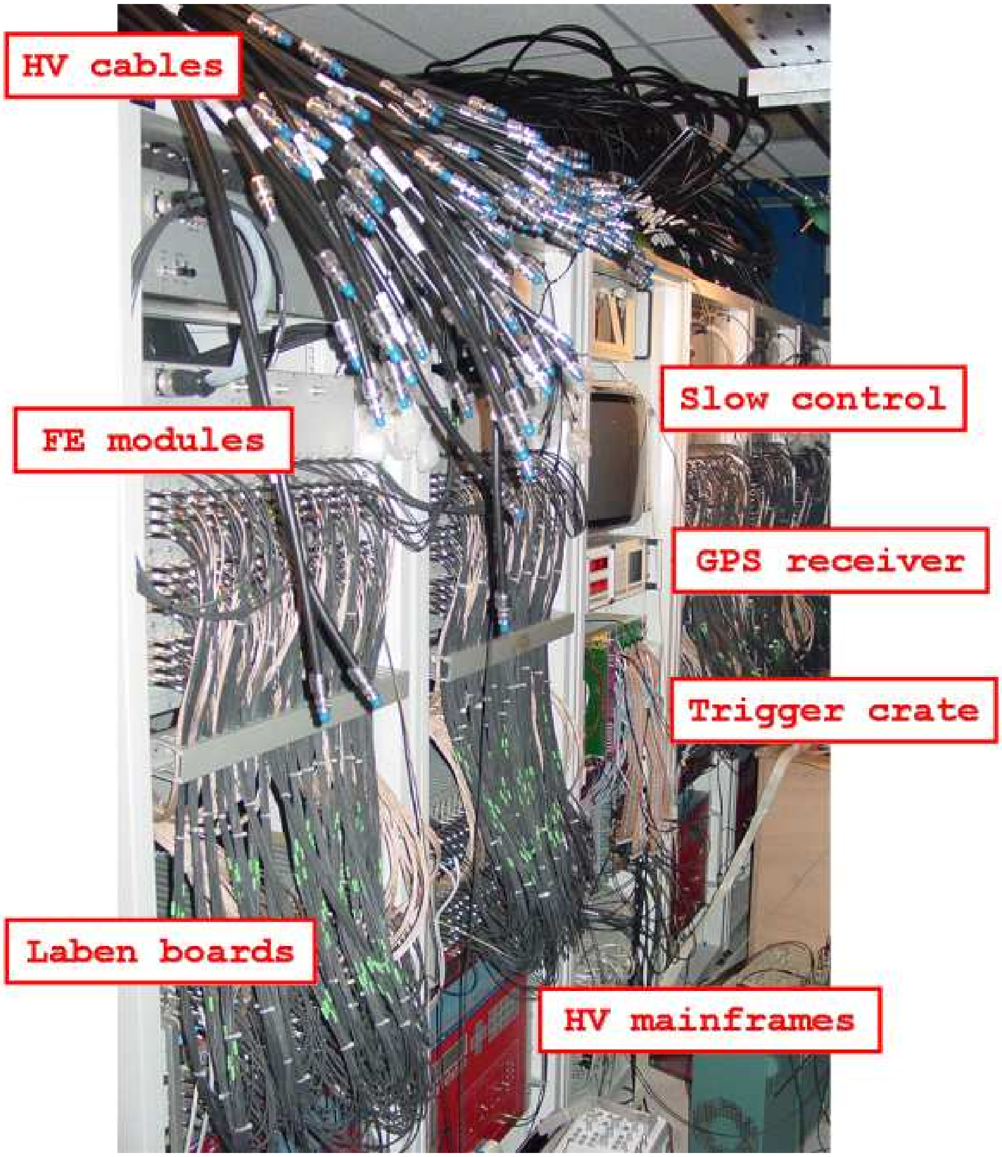

Figure 5.9: Layout of the Borexino electronics, as installed in the Counting Room: two of the 14 identical racks are well visible (left), as well as the trigger rack.

5.2.1 The analog front-end stage

A complete detailed description of the analog stage can be found in [66]. For each photomultiplier, a dedicated analog circuit is used to perform the following functions:

- connect the externally generated high-voltage PMT power supply to the coaxial cable;
- decouple the high-voltage PMT power supply from the signal (the Borexino

PMT use a single coaxial cable to carry both power supply and signal);

- provide the best impedance matching for the coaxial cable over a wide frequency range;
- provide a large rejection of the noise eventually coming from the HV power supply;
- amplify the signal and give a fast output, which will be used to identify the time information;
- integrate the PMT signal, which will be proportional to the charge and hence the energy of the pulse;
- eventually, inject an external signal for testing and calibration.

The main feature of this circuit is the original idea of a gateless charge integrator. Thanks to the AC coupling of the input signal (which is due to the HV present on the cable), it is possible to avoid the use of the switches as in the usual current integrators. The circuit is always integrating the input signal, owing to the fact that the total charge of every input pulse is equal to zero (due to the input capacitor).

The integrator output rises when the pulse arrives and decays approximately to zero (really the noise level) after the time constant of the input network which has been set to about 500 ns for optimum performances. As long as the time interval between two successive signals is larger than the time constant of the input network, the integrator output normally resets before the arrival of the next pulse.

The output of the integrator is stable for about 80 ns after the rising edge (the integration time), allowing to double the sample output: the first sample is taken on the baseline of the signal and used as reference, while the second one is taken on the maximum, as shown in figure 5.10. The difference between the two measurements is then proportional to the charge collected by the PMT. Using this differential measurement technique, it is also possible to solve some pile-up problems: if the second pulse arrives while the integrator is discharging, it can be possible to measure it, if the dynamic range is preserved.

This circuit is then housed on a 12 channel board and for each board an additional output which gives the sum of the input channels is also available. This output can be used for fast digitization using dedicated digitizers. The main reason for the presence of this output is the detection and measurement of high-energy scintillation events originated by the ^8B neutrinos or by a supernova explosion leading to saturated signals in the single PMT chain (as explained in chapter 8).

The whole front-end system has been carefully tested before the installation at Gran Sasso. The integrator transfer function (i.e. the output voltage versus the input charge) is very linear and the slope is $G = 247\ mV/p.e.$. The precision of the single photoelectron charge measurement is about 2.3%. The gain of the linear output is about 20 and the linearity is very good. The signal to noise ratio of the

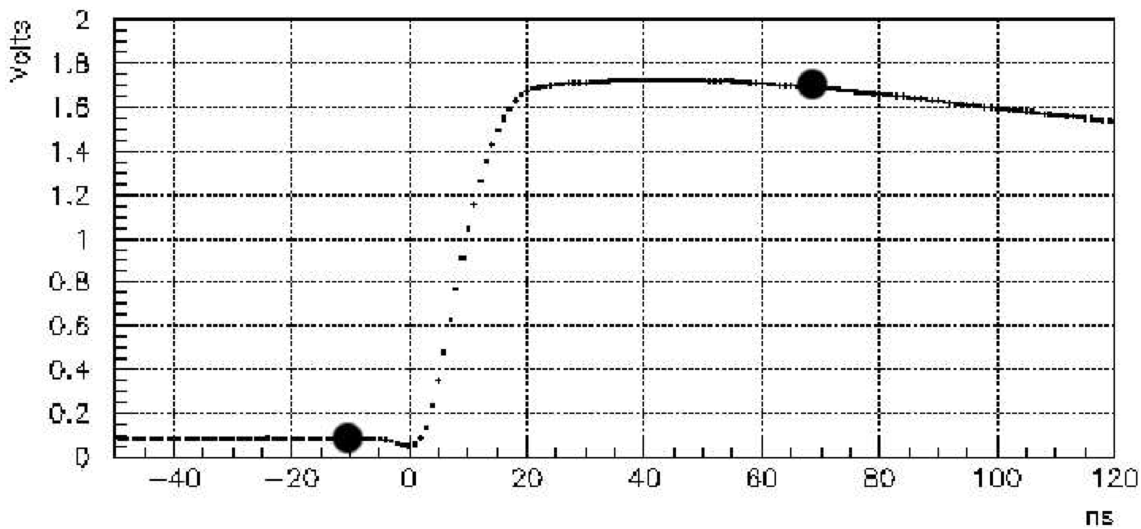

Figure 5.10: The charge measurement: the integrated pulse is sampled twice, before its rising edge and 80 *ns* later; the difference between the two values is proportional to the total charge in the pulse.

linear output is about 4×10^{-3} for a single photoelectron. The tests of the system after the installation are described in chapter 6.

5.2.2 The digital read out stage

A complete detailed description of the digital board can be found in [53, 54]. For the single channel, the arrival time of the pulse and the associated charge (energy) have to be measured. For this purpose, an 8 channel read-out card was designed and built for Borexino in collaboration with the Laben company. The card architecture is composed of two functional blocks: the first block is the single acquisition channel (replicated 8 times); the second block takes care of the control operations of the board.

The single acquisition channel

Borexino Front-End boards deliver a fast linear timing and an integrated signal to each channel of the acquisition board. The 8 channels of the acquisition board acquire asynchronously and continuously these pulses, if exceeding a given threshold; a fast ADC with 8 bit resolution and a Time to Digital Converter (TDC) with a resolution better than 500 *ps* perform the digital conversions.

The ADC and TDC data are temporary stored in a delay line (see below), in order to maximize the detection of the interesting delayed coincidences: when a trigger signal is received, the board starts the procedure for building the event. While waiting for trigger, the oldest data are continuously discarded, except if a

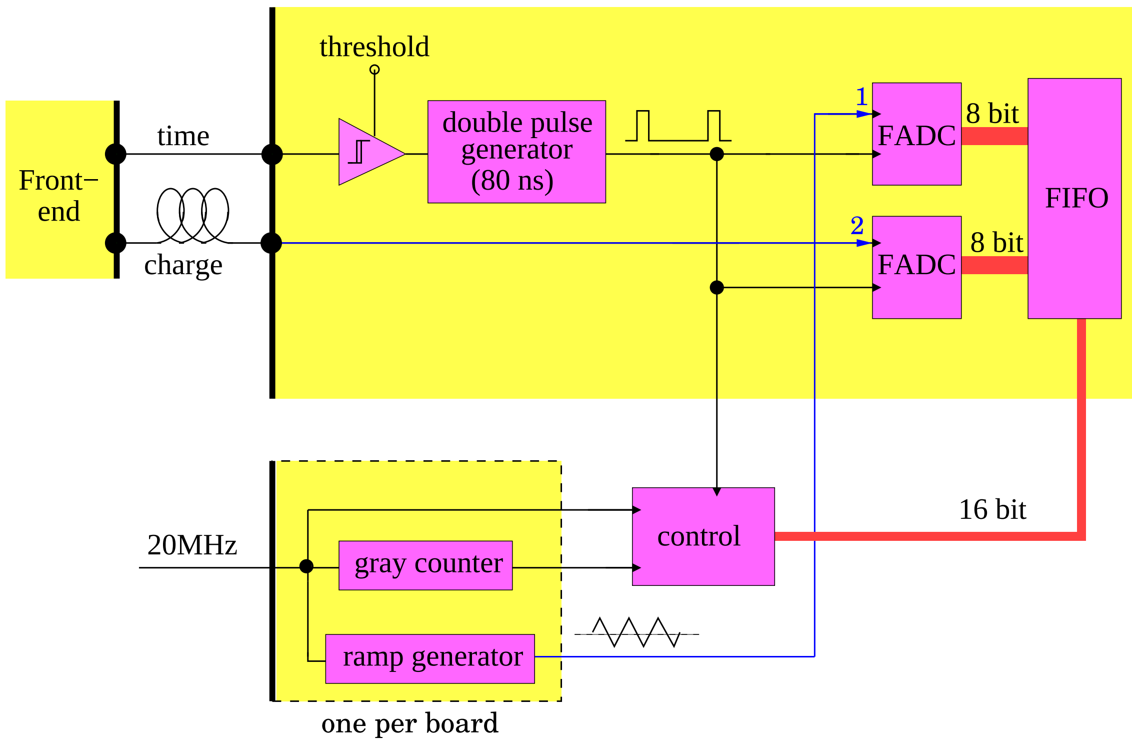

Figure 5.11: Schematics of the single acquisition channel in Laben boards.

special request of monitoring is sent to the board: upon this request the discarded hits can be analyzed by the board itself to produce time or charge histograms.

Each channel has two inputs coming from the front-end stage:

- the fast PMT signal which is an inverted and amplified copy of the PMT signal, used to fire the discriminator and to give the timing information;
- the integrated PMT signal which gives the energy information.

The functionalities of a single acquisition channel are the following (see channel diagram in figure 5.11):

- programmable dual threshold discriminator, receiving the timing input. The choice of the discriminator type has been done as a compromise between the time precision requirement, which constraints the threshold to be as low as possible (the 'walk effect' must be at the level of a fraction of ns, otherwise it would compromise the time resolution) and the need for discarding pulses smaller than the single photoelectron, requiring a higher threshold (between 1/3 and 1/2 of the mean height of the single *p.e.* signal): the channel is fired only if the photomultiplier signal crosses the high threshold, but the timing is related to the low threshold crossing. The output signal of the discriminator enables a double pulse generator that produces two pulses 80 ns delayed;

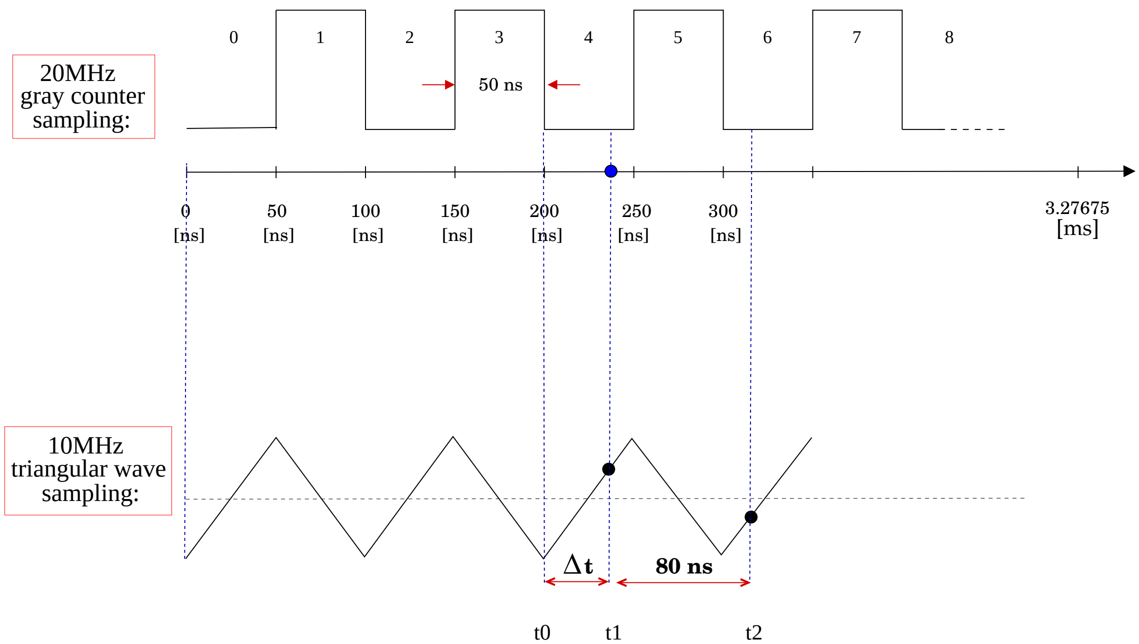

Figure 5.12: Timing informations provided for each event by the single acquisition channel: a sample of the 16 bit gray counter (50 ns resolution) and two samples of the 10 MHz triangular wave synchronous with the clock.

- the discrimination pulses are sent, as a trigger signal, to a dual input 8-bit FADC. The input of the first FADC is the integrated signal of the hit: a calibrated delay line between the front-end charge output and the Laben board input is intended to have the double sampling in coincidence, respectively, with the baseline and the peak value of the signal (see figure 5.10);

- Time to Digital Converter (TDC) with resolution better than 500 ps (see below);

- local FIFO buffer, 24 bit wide, 1024 word deep, used to temporarily store the data while the system is waiting for a possible trigger. The maximum trigger latency possible is 6.4 μs.

The TDC is composed of two sections:

1. the coarse timing is given by a 16 bit Gray coded counter driven by the 20 MHz general clock, which gives a resolution of 50 ns;

2. the fine timing is given by sampling twice with a 10 MHz triangular signal, generated on the board from the 20 MHz base clock. The operation is performed by the second 8-bit FADC, triggered by the dual pulse signal coming from the discriminator.

For the coarse time information, the Gray coded counter is used, because the input signal is asynchronous and there is the possibility to sample the output of the counter while it is not stable. The double-sampling technique is used to have the correct timing also if a sample occurs in a discontinuity of the triangular wave: it is assured that at least one sample is in the linear region of the signal (see figure 5.12).

The triangular wave generator and the Gray counter are common to the card and their output signals are distributed to all the channels on the board. The Gray code is then converted into binary before read out, in order to have the correct number without converting it by software. Using both the Gray counter and the interpolated ramp data, it is possible to obtain a resolution of 200 ps (RMS) and a maximum time span of 3.2 ms.

The main control block

The control block is common to all the 8 channels; the digital lines are managed by a Digital Signal Processor (DSP), which performs the following functions:

- board settings and controls,
- data monitoring,
- local data event building,
- local event buffering.

The main program flow of the DSP code consists in a continuous control of the channel FIFO status (see figure 5.13): while the DSP checks the FIFO waiting for a trigger, the oldest data are continuously discarded, except if a special request of monitoring is sent to the board. In this case, the DSP reads un-triggered data to build up histograms, which can be used for on-line analysis and control of the PMT's working point.

When an event triggers the Borexino Trigger Board (BTB), a Master trigger is delivered to the Laben boards with a latency of about 4 μs; this signal interrupts the DSP, which starts the procedure for building the event. All the hits registered in the digital delay lines are collected and stored in a 2 Kbytes memory with a header containing the event identifier. The depth of the event memory allows to store hundreds of the typical size Borexino events.

The memory bank is a dual port memory (2048 word deep, 32 bit wide), accessible both from the VME bus and from the DSP. It is divided into three separate banks: some locations are reserved for exchanging configuration and programming data, the main part is reserved for event data records and the remaining part is dedicated to store histograms.

Memory is organized on an event by event basis: for each event there are data coming from the channels, together with additional informations such as absolute time, trigger identifier, module identifier and so on. If a card contains no data for

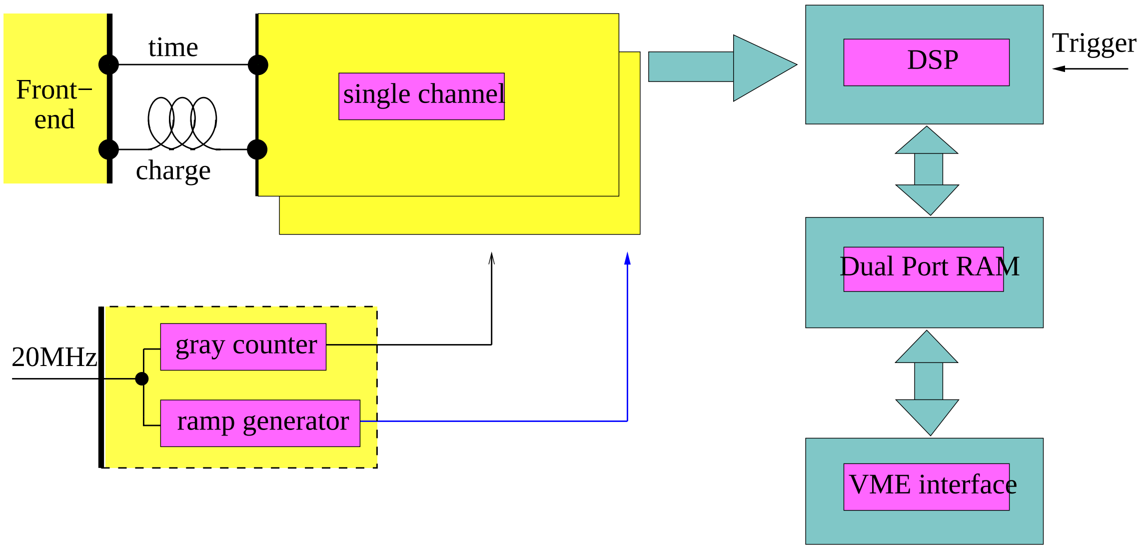

Figure 5.13: Schematics of the complete Laben board.

a particular event, an empty record is generated, to keep the system aligned. A dedicated process running on the Laben PPCs (see below) waits for interrupts from the VME Bus (issued by the Laben Trigger Backplane) to read the raw data, store them in a single data structure and send them to the event builder.

Performances

Several measurements were preformed on the board, before using controlled input signals, and after connecting the analog front-end stage.

The ADC integral and differential non-linearities are smaller than 0.5 LSB. The noise RMS measured in operating conditions (i.e. connecting the photomultiplier and the analog front-end to the inputs) is 0.5 LSB. The PMT single photoelectron peak is put at about 30 digits: the peak value corresponds to a charge of about 3.2 pC on the anode.

The TDC integral and differential non-linearities are less than 1 and 0.5 LSB respectively. As already reported, the timing resolution is about 0.5 LSB RMS, which corresponds to about 100 ps (RMS): this means that the contribution of the electronics to the time spread of the signal is negligible, the photomultiplier resolution being about 1 ns RMS. The measured dead time (the time interval in which the discriminator is in disable state) on the single channel is 145 ns, including the integration time of 80 ns.

The maximum continuous trigger rate allowed on the board has been tested up to 5 kHz, with one hit per channel: obviously the real maximum trigger rate depends on the data throughput, i.e. on the number of hits per event. It is expected that the experimental trigger rate above 250 keV would be in the order of $0.1 \div 1$ Hz, with an average value of $0.1 \div 0.2$ hits per channel per event: this data rate is well below the best performances of the board. Also in the case of acquisition of the ^{14}C β spectrum, with an energy threshold of 70 keV, the trigger rate would reach a few 10 Hz, and can be safely managed by the system.

5.2.3 Layout of the trigger system

The Borexino trigger system has been designed in order to optimize the detection of the scintillation events in the energy range of the ^{7}Be neutrino signal. Since the main Borexino background will be produced by the ^{14}C activity (a β spectrum with end-point at 156 keV), the main feature of the trigger will be the acquisition of the events above a given energy threshold, and the rejection of the low energy events.

For this reason, the Borexino trigger system is designed to perform the following functions:

- identify good scintillation candidate events, requiring that at least K PMTs have fired within a time window of 50 ns. The energy K can be programmed from 1 to 255; the time window can be adjusted between 30 and 70 ns using a switch in the Clock Generator front panel (see below);
- identify muon events, detected by the outer detector (described in section 2.2), which is provided by an independent trigger;
- provide test and calibration triggers, that can be generated via software, or automatically by an internal timer of the Borexino Trigger Board (BTB), or by means of an external independent pulser;
- provide the possibility to fire the laser system (chapter 7), or at least to receive a signal to flag laser events;
- handle the absolute time clock.

System components

The complete trigger system is depicted in figure 5.14 [69]. It is composed of 14 Trigger Backplanes (TBP), 5 Trigger Adder Boards (TAB), 1 Borexino Trigger Board (BTB), 1 Clock Generator (CKG), 1 Trigger Fan Out (TFO), 1 Muon Trigger Board (MTB), 1 Timing Unit, 1 Absolute Time Clock.

- **Trigger Backplanes:** each Laben crate is equipped with a TBP mounted in its rear; the TBP is devoted to provide a fast sum of the number of hits that have occurred in the crate in the last 50 ns and to deliver trigger signals to each Laben board.

  It works in this way: every time a timing input fires, a monostable signal is activated and kept active for three clock cycles of a dedicated line running at

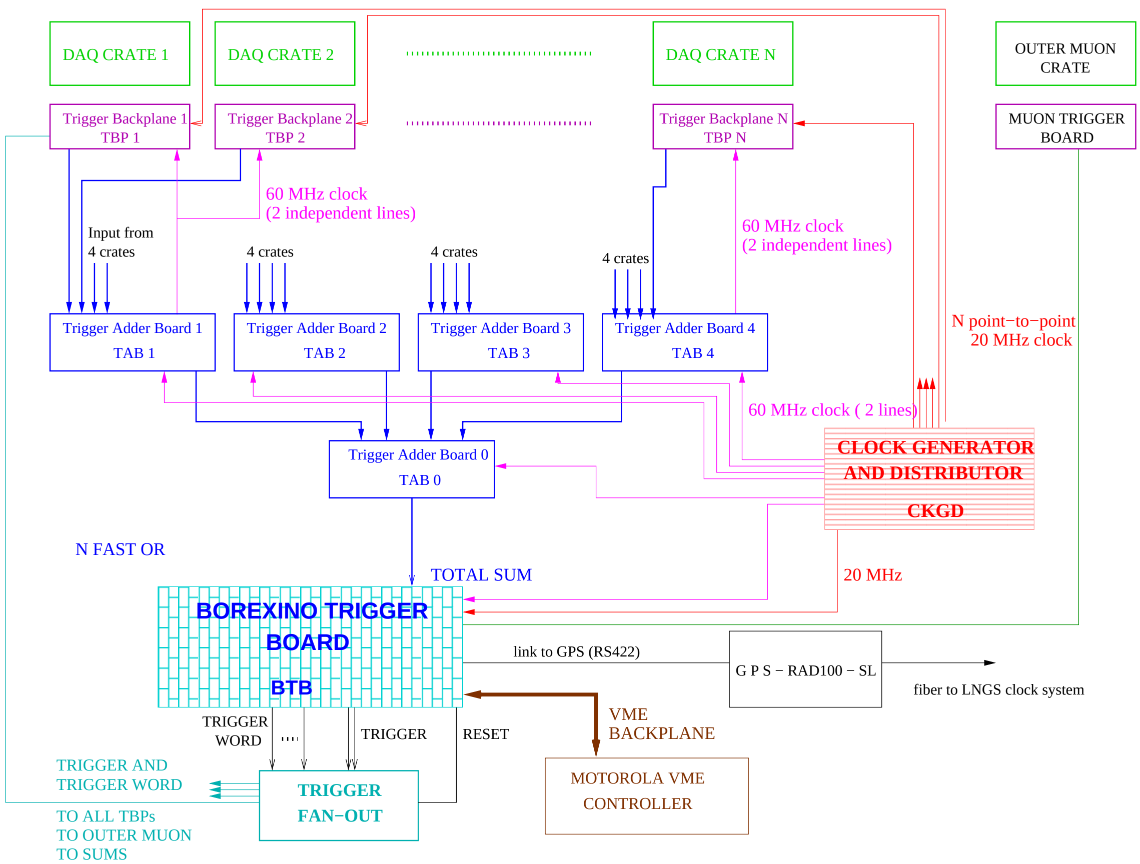

Figure 5.14: Block diagram of the Borexino trigger system.

60 MHz nominal: this means that the monostable is active for 50 ns. Every 16.7 ns, the TBP adds all the monostable outputs (on the all 160 channels in the crate) and produce an 8 bit sum that is sent synchronously to the TABs via a flat cable.

The TBP is also devoted to receive the 16 bit trigger ID that arrives together with the trigger signal and delivers it to the Laben boards. The DSP attaches this trigger ID to the header of each recorded hit, to allow the DAQ to associate each stored hit to the right trigger ID.

- **Trigger Adder Boards:** TABs are basically adders, capable to get the sums from the TBP and to make a further sum every 16.7 ns. Each TAB has four 8 bit inputs and one 8 bit output: to read all 14 crates and sum them up, 4 TABs are used, plus a fifth one to perform the final sum.

- **Clock Generator:** in order to count the hits occurring in a given time window, all Borexino TBPs and TABs must be properly synchronized. We do this by having a single clock generator for the whole system and distributing it with cables of equal length.

The CKG has a single 20 MHz oscillator, from which all other clocks are generated. Three clock lines are distributed to the whole system: a 20 MHz line that is used by the Laben board DSP, a 60 MHz line that is used by BTB and another 60 MHz line (adjustable from 30 to 70 MHz) that defines the trigger time window.

- **Trigger Fan-Out:** all the signals are distributed to all the racks via the TFO, that is mounted in the rear of the main trigger crate.

- **Timing Unit:** a dedicated NIM timing unit is installed in the trigger system, in order to generate a pulse with an adjustable rate (by default it is set around 200 Hz); this NIM pulse is converted to TTL and sent to the BTB input. The signal is used to pulse the trigger, which generates synchronous events for the calibration distribution system or the laser calibration system (see below).

- **Absolute Time Clock:** a GPS device is present in the trigger system, to have a global time synchronization of the events between various experiments all around the world (this feature can be very useful in the case of a supernova event, where all the possible data should be correlated).

  The system accesses the Gran Sasso clock system, whose precision is 100 ns. A local receiver of the clock is housed in the trigger crate; its synchronization with the main clock is updated every ms through a dedicated fiber-optic link.

  At each trigger a stop signal, synchronous with trigger signal, latches the time information from GPS clock, and writes it in some dedicated registers. This operation takes about 2 μs: when this process ends, an acknowledge allows the BTB to readout the 5 timing words (16 bit each); the DAQ will write the words in the trigger record of the event.

5.2.4 The Borexino Trigger Board

At the end of the summing procedure performed by TBP and TABs, the total number of PMTs fired in the given time window is available. This number feeds the trigger supervisor board called Borexino Trigger Board (BTB).

This is a custom designed unit which takes the total number of PMTs fired as input, can be programmed to work in several different conditions and generates the output signals needed by all the digital read-out cards to start the acquisition of an event. The BTB is a VME slave device that not only generates the needed signals, but also stores the conditions under which the triggers are generated on a local memory that can be accessed by the CPU crate controller. To have the maximum flexibility, the main control functions are implemented using a DSP, which runs a specific C code handling the whole triggering logic.

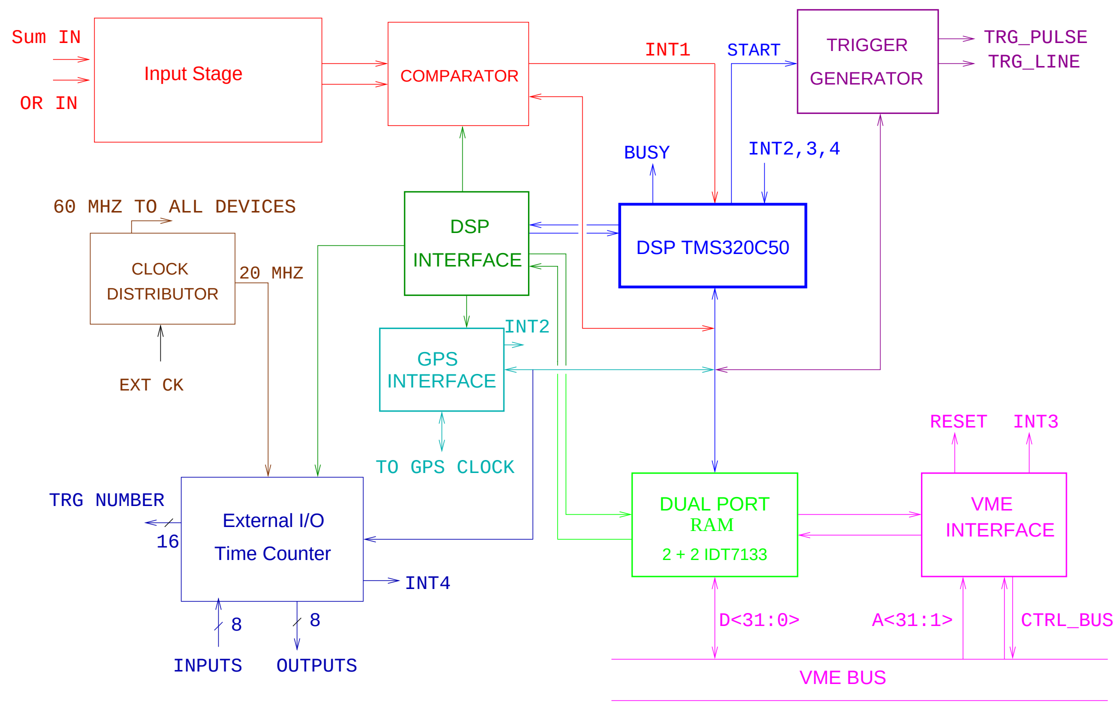

Figure 5.15: Block diagram of the Borexino Trigger supervisor Board (BTB).

The main operation performed by the BTB is the comparison of the final output from the TABs with the programmable threshold K. When the number of hits is above the threshold K, an interrupt to the BTB DSP is generated: in these conditions, the BTB flags the acquired event as a "Neutrino" event (see table 5.2).

If the Run condition is enabled, the two output trigger signals (TRIGGER, GATE) are generated and sent to all racks, via the Trigger Fan-Out: TRIGGER is the real trigger signal, while GATE determines the length of the data readout window inside the Laben boards (presently, the total data acquisition time is 7 μs); the TRIGGER signal increments also the trigger number 16 bit counter: this number is sent to all data acquisition crates and is stored with the acquired data for each event.

Other trigger types

Besides the "Neutrino" trigger type, the BTB allows the handling of several trigger types, depending on the trigger conditions. Each trigger type has a specific flag, which is stored in the trigger record of the event and is available for the analysis. Different trigger types have also different priorities, allowing the BTB to choose the most important event type in case of more than one valid trigger condition occurring at the same time. The list of all the trigger types, with their priorities, is available

Trigger Type	Trigger Type (dec)	Trigger Word (hex)	Priority
Neutrino	1	0x0001	1
MuonMTB	2	0x0402	2
MuonTotC	128	0x0880	3
Laser355	4	0x1004	4
Laser266	16	0x2010	5
Laser394	8	0x4008	7
Calibration	32	0x4020	6
Random	64	0x4040	8

Table 5.2: Complete list of the possible Trigger Types foreseen for Borexino.

in table 5.2.

- **Calibration triggers:** the time reconstruction algorithm used in the off-line code (see chapter 6) needs a pre-analysis of the raw data for the time alignment of the detector: this procedure can be done only if the data contains some synchronous events. The test and calibration signal distributor can deliver the same signal to all the front end boards: this system has been configured to generate the needed number of these events at the start of each run.

  The NIM Timing Unit generates a pulse with an adjustable rate, which is converted to TTL and sent to the BTB input: at the start of the run, the BTB firmware accepts all these external pulses (up to a programmable number), as real triggers, starts the procedure to generate the trigger signals, writes the trigger record flagging these events as Calibration (table 5.2) and generates an output signal. This TTL pulse, $\sim 2\mu s$ long, is converted in a signal similar to the typical photomultipliers signal and sent as input to the fan-out of the calibration signal distributor.

- **Random triggers:** the same 200 Hz pulse rate, generated with the NIM logic described above, handles also the timing laser and the random gates logic. We define a random gate a trigger interrupt generated from an external pulse at any arbitrary time; this allows us, for example, to study the dark noise of the photomultipliers. When the variable Random is enabled, the BTB serves the first triggers as Calibration triggers; then it serves all the interrupts received on its input as Random triggers.

- **Timing laser trigger:** the timing laser logic is done exactly in the same way of the Random trigger logic; if the variable Laser394 (Timing Laser) is enabled, after the first Calibration triggers, the rate of calibration pulses is served as Laser394 triggers. The triggers are then flagged as Timing Laser triggers (table 5.2) and a TTL pulse is sent to a BTB output line: this signal is used as an external trigger for the laser system.

- **Laser 355 and Laser 266:** both these two lasers (used for measurements of scintillator optical parameters) oscillate at a fixed frequency, of the order of 11 KHz, and cannot be driven by an external pulse. To couple these laser systems with the trigger board, their external synchronization signals are used as external triggers and sent (properly pre-scaled) to an input of the BTB. By default, the two lasers are disabled: if the user enables one of them, the BTB receives a pre-scaled signal as its input, and serves it as a Laser355 (or Laser266) trigger.

- **Outer Muon Triggers:** Two different trigger interrupts can be generated by the Muon Outer Detector: one based on the hit multiplicity and provided by the Muon Trigger Board and the other one based on the total charge. The two corresponding input lines on the BTB can be individually enabled or disabled; if they are enabled the BTB flags properly the two triggering conditions, as MuonMTB or MuonTotC (table 5.2) and generates an output on the output lines. In case both triggers fire, the trigger word will show this information.

5.3 The Data Acquisition software

The main Borexino electronics is composed of 14 identical racks ("Laben" racks), that perform complete analog signal handling, high voltage distribution, digitization and data processing, data transfer to the DAQ event builder; moreover, one Trigger rack is present, containing all components described in previous sections (see figure 5.9). In each rack, a VME crate is present, housing the digital boards: each VME crate hosts a Motorola Power PC (PPC), which is in charge of the data read-out from the boards and data transmission via network; a central CPU, collects data from all the PPCs, builds the overall event structure and writes it to the disk.

5.3.1 Computing architecture

The computing architecture is composed of the following elements: 17 PPCs, 2 Network Switches, 1 Terminal Server, 1 Network Hub, 5 PCs.

- **PPCs:** data from each VME crate is read by a Power PC; each PPC is a single slot VME board, with a standard Motorola Power PC Processor, 32 Mb RAM, Fast Ethernet (100 $Mbit/s$) interface and a console. These processors are diskless: their firmware is configured to load the operating system kernel from the network via a BOOTP request which is handled by the bxmon machine; each PPC mounts a dedicated disk on bxmon via NFS to load the application programs. All the PPC software is completely custom made, as well as the operating system (which is a version of the Linux Debian 2.1 release).

- **PCs:** central operations are handled by 5 Linux Debian PCs, that are named bxslow, bxbuild, bxweb, bxdb and bxmon; they are respectively devoted (mainly) to: electronics and HV slow control and monitor, event building, WEB server, Data Base server, system monitor (bxmon has also the crucial functions of PPC bootstrap and cross-compilation, and also provide the network bridge to the world).

- **Network Switches:** all elements of the computing system are connected to two dedicated Fast Ethernet Switches.

- **Terminal Server:** all PPCs are connected also to a Terminal Server via their console serial port. This is not needed during normal data taking, but is very useful for debugging and maintenance, because the console port is the only access way to the PPCs in case of problems. The Terminal Server supports TCP/IP protocol, so it is possible to "talk" to all PPC from a single terminal via telnet.

- **Network Hub:** this is needed to guarantee the connection between the 5 PCs and the Gran Sasso local network. These PCs are connected via bxmon to this Hub, that is connected via the Ethernet line coming from the external laboratories; this connection is realized via a dedicated optical fiber link, with a maximum speed of 1 $Gbit/s$.

5.3.2 DAQ software architecture

The Borexino DAQ software is a complex system (see figure 5.16), composed of many software elements written in different languages and exploiting different technologies, that run on at least 22 CPUs under the Linux operating system.

We can divide these elements in the following groups (related to the computing architecture just described):

- **Power PC software:** the first stage of the software system is made of the different programs that run on the VME Power PCs and that are devoted to the data read-out from each hardware element. There are four kind of these programs for the different sub-systems: Laben crate (14 CPUs), Outer Muon (1 CPU), Sums (1 CPU) and Trigger crate (1 CPU). All these programs are written in C language;

- **Main DAQ software:** the main DAQ (event builder, event logger, run controller, etc.) is made of many different processes that run mainly on the Linux PCs bxbuild. They are written in C++ and Perl and they make use of the CORBA technology;

- **Slow control software:** the slow control software is mainly dedicated to the control of High Voltage power supplies and of VME crates. The main program is written in C++ and runs on bxslow machine;

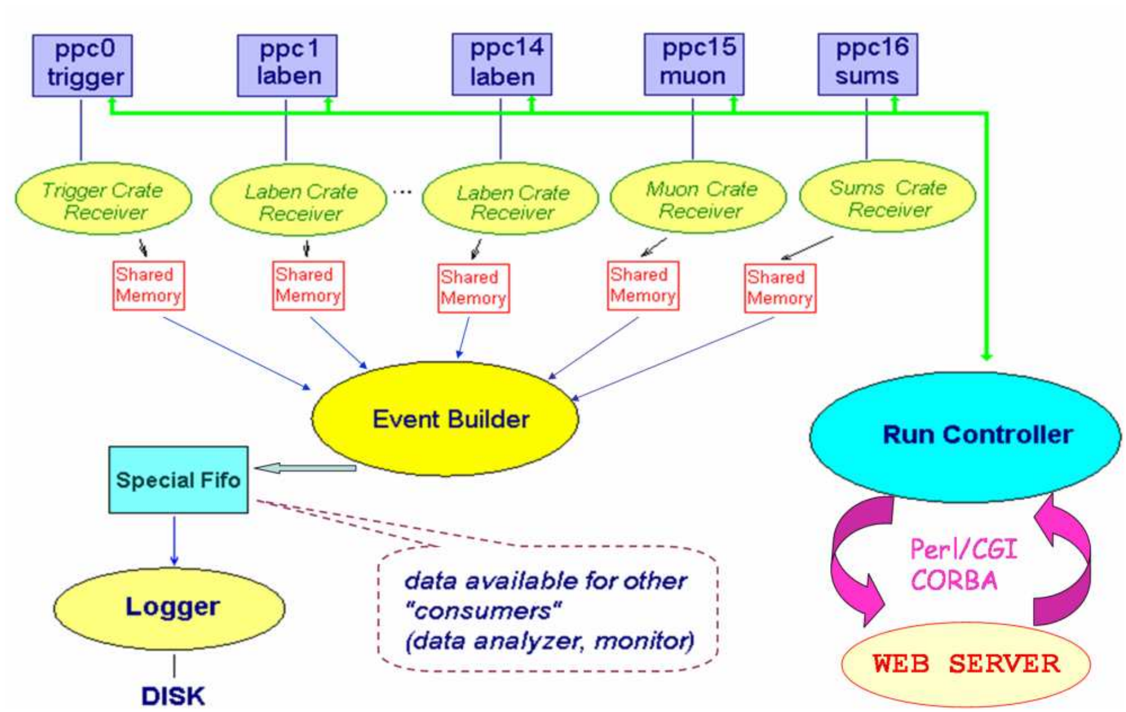

Figure 5.16: Block diagram of the Borexino Data Acquisition system.

- **Data Base server:** all parameters of the system are stored in PostgreSQL, which is a free client-server SQL Data Base distributed with the Linux operating system. This server runs on bxdb;

- **WEB server:** the human interface is based on WEB technologies. A set of HTML pages and Perl/CGI scripts provide the link between the human operator and the different elements of the system: in this way, all the system can be controlled and monitored remotely using this private WEB server. All the HTML pages are handled by a private WEB server (Apache) that is running on bxweb;

- **Event monitor (Analyzer):** this program is responsible for providing the people in charge of data taking a set of histograms and n-tuples required to check that everything is running fine. It is based on a set of Perl and HTML files; it uses the WEB technology.

5.3.3 Power PC software

Borexino DAQ is designed as a finite-state machine: all the components of its architecture share a common set of states and common set of commands (to perform

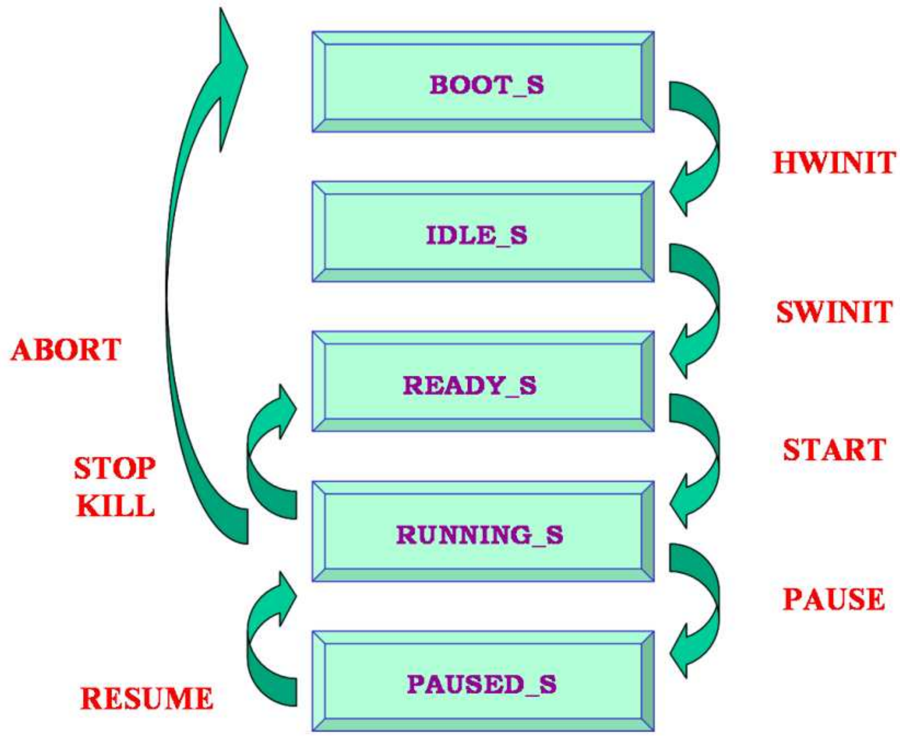

Figure 5.17: The common states of all the Power PCs, with the main commands.

transitions between different states). The core of the finite-state machine is executed by the Power PC software.

As already told, there are 4 kind of Power PC programs: Laben (running on 14 PPCs), Trigger (1 PPC), Muon (1 PPC), Sums (1 PPC). They share a common command interface and a common functional structure, while they may differ in the implementation details.

They share the following states (shown in figure 5.17): BOOT_S, IDLE_S, READY_S, RUNNING_S, PAUSED_S; they accept commands from Main DAQ via TCP/IP socket connections (on the port 5000); they read data from their specific hardware and send them to the Event Builder via (another) TCP/IP socket (port $10000 + n$, where n is the PPC number).

Whatever be the "flavor" of the Power PC software, it must acknowledge the following commands:

- HWINIT: perform all hardware initialization and load default values (if any); new state is IDLE_S;

- SWINIT: load parameters on the boards (those changed with a SET command after HWINIT); new state is READY_S;

- START: start run; new state is RUNNING_S;

- STOP: stop current run; flush the data in memory before stopping; new state is READY_S;
- PAUSE: pause the current run; new state is PAUSED_S;
- RESUME: resume the paused run; new state is RUNNING_S;
- ABORT: abort the run with no data flushing; new state is BOOT_S;
- KILL: abort the run with no data flushing; new state is READY_S;
- GET HWID: returns hardware ID (Ethernet) of the Power PC;
- GET STATUS, MACHINE_STATUS: return the program status, expressed as string (BOOT_S, etc.), or the system status, expressed as a number (1,2,4,8,16);
- (GET) SET TADD, TPORT, CID, TSEND: (get) set respectively: the TCP/IP address where DATA must be sent to (usually bxbuild); the TCP/IP port where DATA must be sent to (default is $10000 + n$); the logical crate ID; the event block size (data are sent to the network in blocks of TSEND events);
- REBOOT, TEST: reboot the Power PC; test the hardware.

Laben Power PC software

The Laben Software has a multi-process structure, featuring four logical functions identified (for historical reasons) with the names M1, M2, M3 and M4 (see figure 5.18). M1 reads data and sends them to the builder; M2 reads histograms and sends them to the histogram receiver; M3 and M4 handle commands and send error messages. M1 is in turn composed by three main processes: "main_t" receives commands issued by the M4 area; "cpu" continuously reads data from the VME backplane and store them in an internal Shared Memory; "sped" reads the Shared Memory and sends the data to the network.

The Laben power PCs keep 4 different Network connections during normal data taking, for handling commands, data, histograms and errors (see figure 5.18): S1 is used for commands and links each PPC to the Run Controller; S2 and S4 are used to send data respectively to the Event Builder and to the Histogram Server; S3 is used for error messages that are gathered by the standard UNIX Syslogd process running on bxmon.

Besides the common set of commands of all the PPCs, the Laben software features specific commands allowing to perform actions on the Laben Board set-up parameters: for example, it is possible to set (get) the threshold for each channel, to enable/disable specific channels (boards) from the DAQ or from the trigger, to set or check internal parameters.

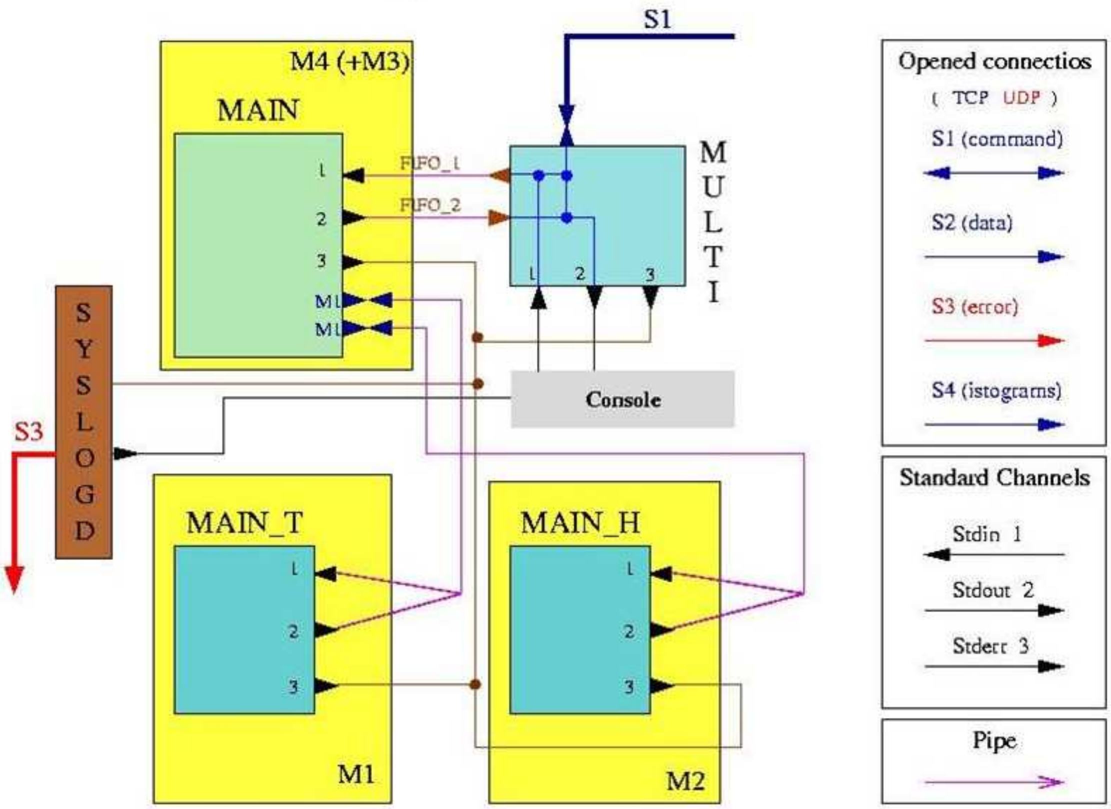

Figure 5.18: Structure of the Laben PPC software and list of the open connections.

5.3.4 Main DAQ software

The software running on the Linux workstations is a set of independent UNIX processes, mainly written in C++, that are designed to perform the DAQ functions of Event Building, Run Control, User Interface, handle the interaction with the Postgres Data Base server, and eventually send data to consumers like Event monitor (Analyzer). The following list collects the software elements that form the main DAQ system for Borexino (mostly running on bxbuild machine).

- **Crate Receivers:** each Power PPC is continuously read out by a dedicated process, that put the data in an internal RAM location (a UNIX Shared Memory Segment) that can also be accessed by the Event Builder (see figure 5.16). Receiver process exchanges commands with the remote PPC via socket connection: receiver 0 gets the trigger data ("Tcr"), receivers 1...14 get the Laben data ("Lcr1"..."Lcr14"), receiver 15 gets the outer muon data (Mcr) and receiver 16 gets the FADC data (Scr).

- **Event Builder:** the Event Builder continuously check for new data present in the internal Shared Memory written by the Crate Receivers. When some data are present in all the segments, the EB proceeds to identify the corresponding event blocks (using the 16 bit Trigger ID that each Power PC writes in the data), converts the hardware encoding of the channels in the logical map that is defined in the Data Base and writers each built event in a special FIFO, where data are available for the Logger process and other consumers like the Event Monitor.

- **Logger:** this is a very simple program that reads data from the special FIFO filled by the Event Builder and writes them in the final raw data file (presently, data can only be written on disk). To handle the FIFO, a special piece of Linux kernel code has been written, in order to allow the possibility that many different consumers can get the data during normal data taking without affecting the data flow.

- **Run Controller:** this is the core of the system. It is a program capable to get the commands from the WEB User Interface (see above) and to dispatch them to the different processes and/or to the Power PCs. It is also responsible to start the other processes of the system; finally, it receives exceptions from other streams and takes proper actions when these exceptions occur. The Run Controller communicates with the Event Builder (and other processes) via socket connections; the synchronization between the different streams is guaranteed by the use of standard UNIX semaphores.

5.3.5 The WEB interface

The human interface to DAQ software is based on WEB technologies. A set of HTML pages (dynamically generated via Perl/CGI scripts) provide the link between the human operator and the different elements of the system: in this way, all the system can be controlled and monitored remotely using this private WEB server.

The WEB interface handles all the DAQ operations: Borexino shifters can follow a sequence of allowed operations, for all needed procedures of data taking. For this reason, the interface has been designed to be reliable, easy to use, intuitive, and tolerant to operator errors (this last item is realized thanks to the weak interaction to the controlled finite-state machine: it can even be started and stopped with no influence on data taking).

It provides five main functions (see figure 5.19):

- **run controller:** it handles the controller of the finite-state machine, allowing to configure the system, the trigger setup, to perform the main data taking actions, etc.; a screenshot of the main run controller page is in figure 5.20: DAQ is in PAUSED_S state and the allowed operations are RESUME or ABORT (see also figure 5.17);

- **profile manager:** it allows the management of the Borexino Data Base collection (see below);

Figure 5.19: Starting page of the Borexino DAQ WEB interface.

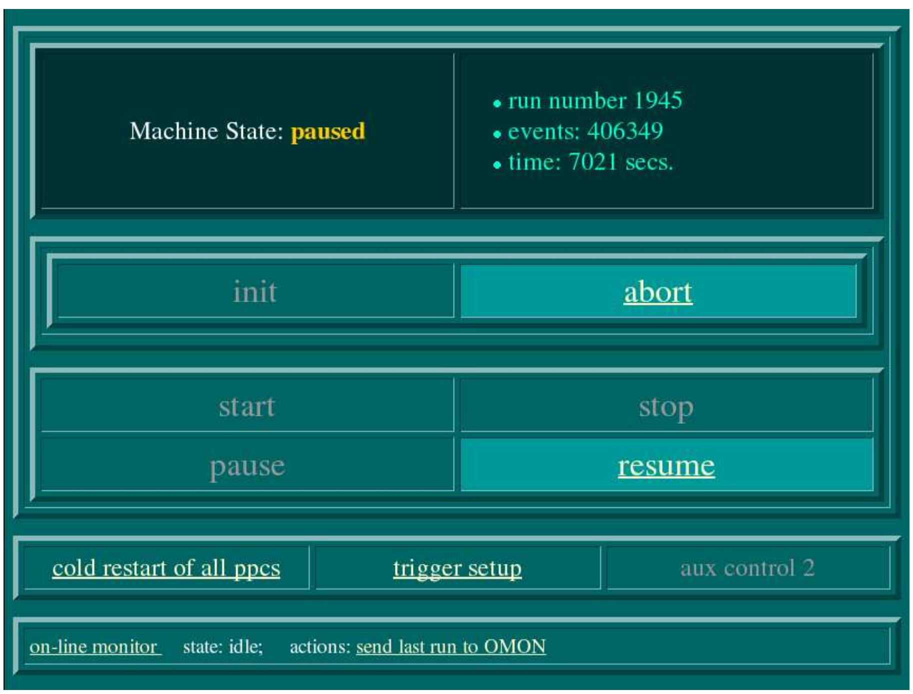

Figure 5.20: Run Controller page: main DAQ is in PAUSED_S state.

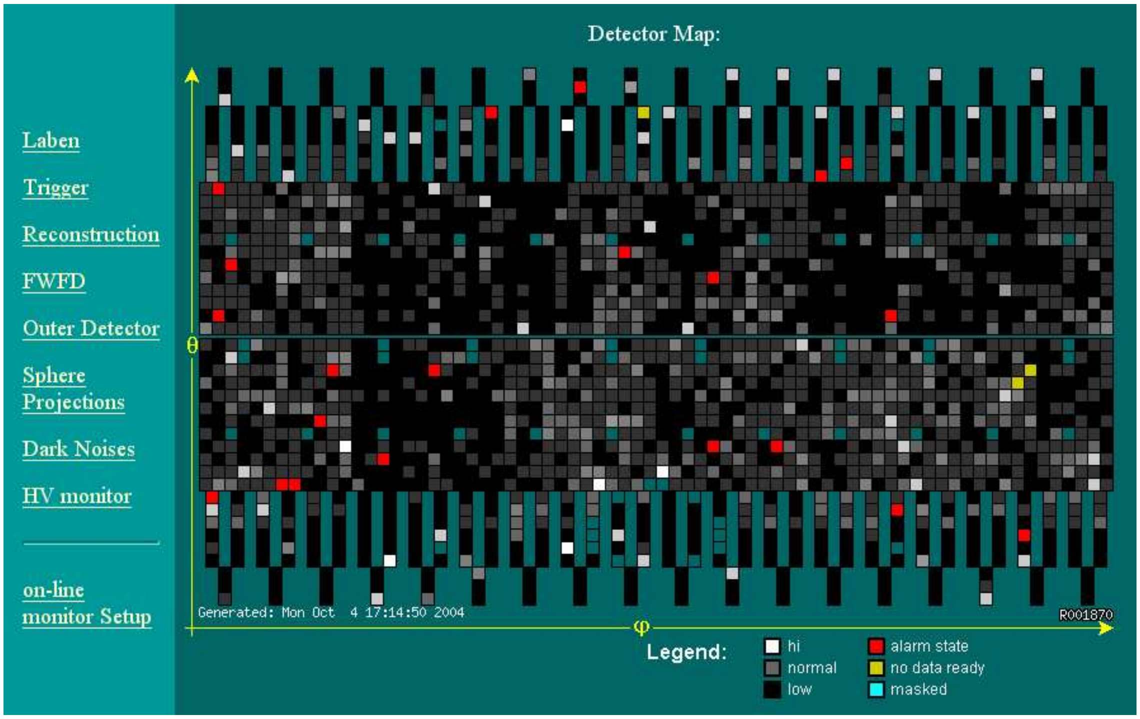

Figure 5.21: The starting page of the On-line monitor, with the detector rates map.

- **on-line monitor:** it provides the interface to the event monitor, which allows to monitor the detector status during the data taking (see below);
- **system monitor:** it checks the state of the PCs and PPCs in the DAQ network and of all the software processes composing the global on-line system;
- **slow control:** it provides the complete interface to the Slow Control system (see below);

5.3.6 The event monitor

The On-line Monitor (or Analyzer) is responsible for providing the people in charge of data taking a set of histograms and n-tuples required to check that everything is running fine. It is based on a set of Perl and HTML scripts and, as usual, it uses the WEB technology.

The monitoring program is not designed to estimate neutrino fluxes, but to keep track on parameters of machine (rates, backgrounds, amplification, etc.). The main goal of the project is to perform diagnostics of the system and, in case of error, to suggest possible failure locations: this purpose distinguishes the monitor from the real off-line software, even if the analyzer core is based on a simplified version of the off-line event reconstruction program.

The starting page of the Analyzer is a full PMT map in plain projection (see figure 5.21): the countrate for each PMT is reported in gray scale, while alarmed channels are lighted in red. The detector map is a "clickable" figure: pointing on one of the channels on the map, a new page is opened, showing main parameters (histograms) for that channel: the total count rate, the amplitude (charge) distributions; the timing distributions.

Different subsets of the detector can be displayed and, in particular, the PMT map can be organized according to the Front-End or Digital board arrangement. Moreover, general detector monitoring histograms are available (total countrate, trigger rate, event size, event energy, etc.), allowing an idea of the general behavior of the data to be displayed, while the run is underway.

5.3.7 The Data Base collection

Borexino owns a Data Base system, collecting all the detector parameters that can be relevant both for Data Acquisition and analysis. The Data Base server is PostgreSQL, which is a free client-server data base package, SQL compatible. Many different software products can access the Data Base from any remote host machine, to read data or write data in it, both using an interactive interface or any software program, through an Application Program Interface (Postgres API libraries are available for many languages: in our case the most used are the C and the Perl interfaces).

Borexino Data Base server hosts 8 different Postgres data bases, which accomplish different data storage functions. Data Base collection is listed in figure 5.22, where each component of the collection is associated to the program family which is in charge of interacting with it. The organization of the single Data Base is hierarchical (see figure 5.23): each Data Base collects a set of tables and each table is a

• access • daq_config • channelhistory	DAQ/on-line
• bx_geometry • bx_calib • bx_physics	off-line
• bx_slow	slow control
• bx_fluid	FH system

Figure 5.22: List of Borexino Data Bases: they are divided in 5 main groups, depending on the program family that is in charge to write and read the stored informations.

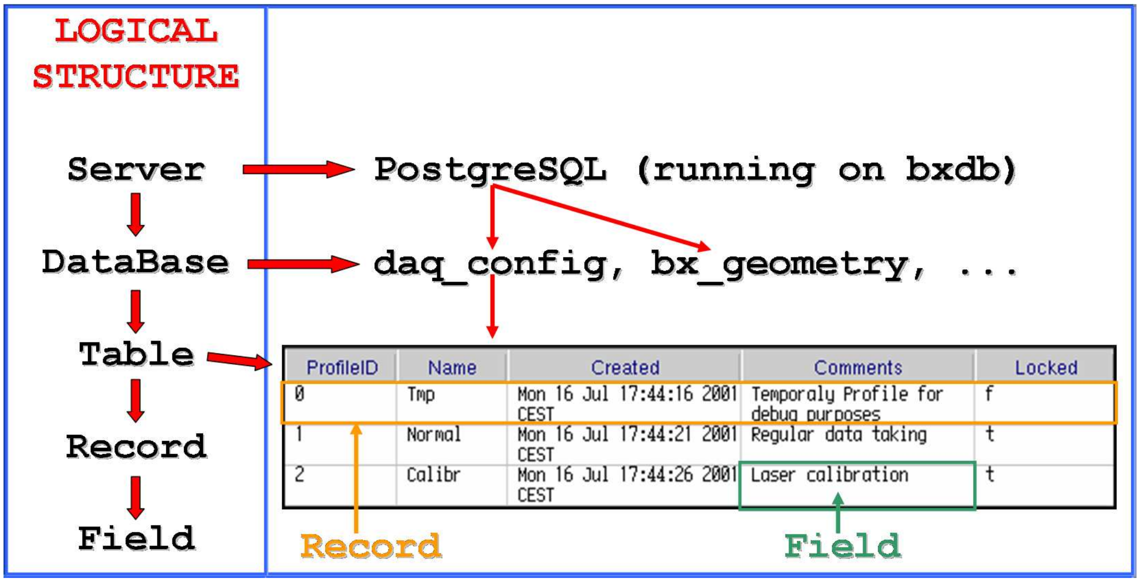

Figure 5.23: The Data Base logical structure, with an example (table "Profiles").

list of records; each record is in turn a collection of fields.

The "DAQ-related" data bases store all the detector informations needed by the on-line programs, such as the Crate Mapping, the Channel Setting, the Run Informations (some of these informations are directly written by the DAQ during the data taking, while some others are just read by the various programs). The **bx_slow** data base handles the parameters stored by the Slow Control program (see below): the most important feature is the storage of all the parameters from the High Voltages control program. Finally, the Borexino Fluid Handling system (see section 2.2) is completely remote controlled: the central control software stores into its own data base (**bx_fluid**) all the fluid handling informations that can be relevant for detector monitoring and data analysis (temperatures, pressures, etc.).

The "off-line" databases collect all the informations needed to reconstruct raw-data, as produced by the DAQ system: in **bx_geometry**, the complete electronics mapping and hard-wired parameters needed to build up the detector geometry are stored; this is a crucial data set, because it allows to reconstruct the complete geometrical information of the detected photons, from the PMT location on the SSS to the "channel-labelled" data structure written on disk. **bx_physics** contains the parameters of the detector with a physical meaning, like the scintillator photon yield, the quenching factor, the time decay constants, the media refraction indexes. Finally, **bx_calib** handles the physical parameters of the detector which are determined through a calibration procedure (of any type). Some of these parameters concern the scintillator properties, and are supposed to be updated when a specific measurement of the scintillator (like a chemical laboratory measurement) takes place; other parameters are connected to the detector read-out system, such as the

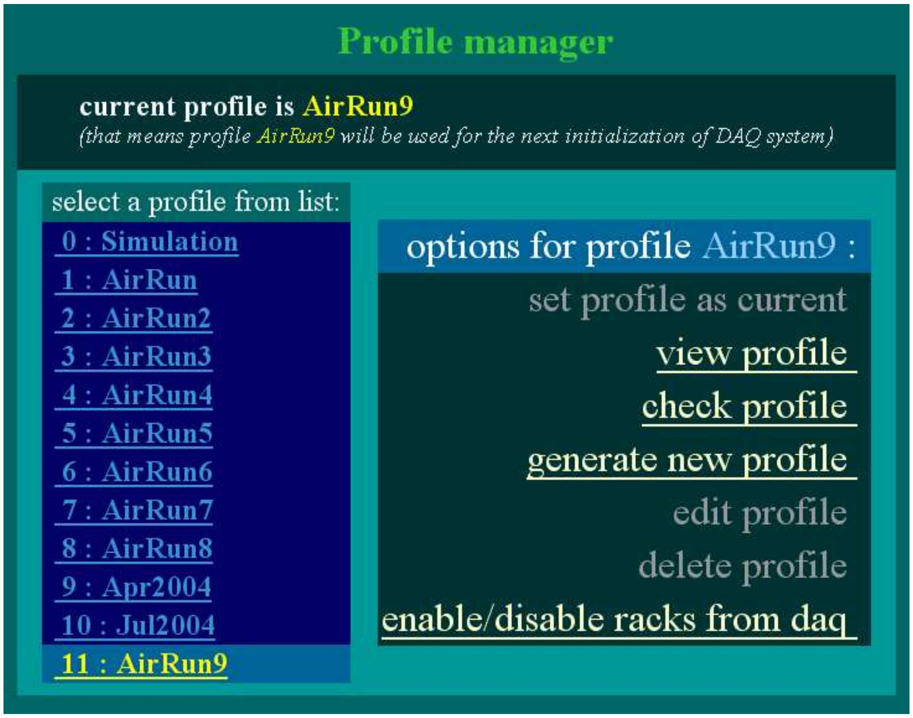

Figure 5.24: The "profiles manager" page of the Borexino WEB interface: a list of valid detector configuration is proposed to the user for data taking.

Laben channels pre-calibration parameters (see chapter 6) or PMTs time and charge equalization constants (chapter 7): this second set of parameters is computed, on request, by specific functions of the events reconstruction program and is directly written by the program into the appropriate Data Base tables.

Like all the other components of the Borexino DAQ system, the Data Base collection has its own WEB interface, devoted to the setting (and displaying) of the main Data Base parameters that are relevant for data acquisition. In figure 5.24, the main "profiles manager" page is shown: it offers the user a list of valid detector setups ("Profiles"), that are available for data taking; user can choose one of the existing profiles as "current profile" for running (if needed, small modifications can be brought in the configuration, such as the number of active crates); if major modifications are needed, the user can follow a guided procedure to create a new configuration, which will be checked and validated by the interface before being used.

5.3.8 The slow control

The slow control chain is intended to handle the control and feedback system that allows to maintain the stability of the read-out apparatus. Two major functions are

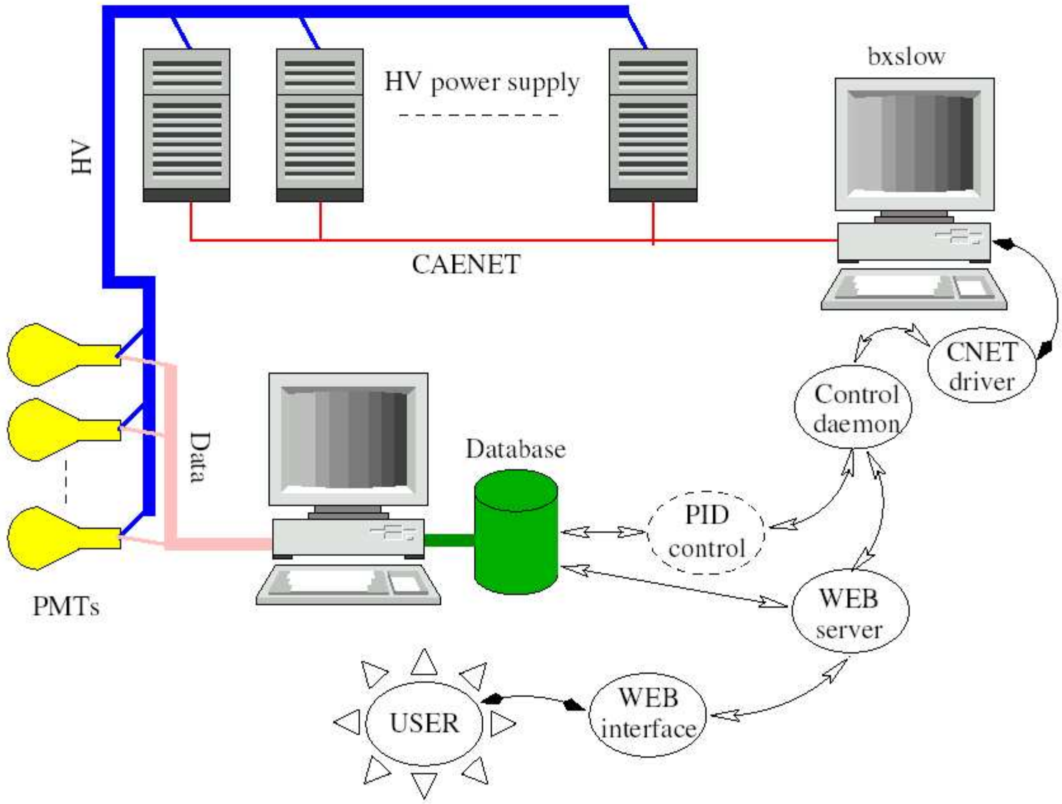

Figure 5.25: Logic scheme of the HV controls in the Slow Control System.

currently available:

- the control of the VME crates, which monitors the status of the crates (signaling possible alarm states) and allows to perform a remote power-on/off or reset of the single crates or groups of crates;
- the complete control of the High Voltage Power Supplies, including the voltages setting, the power-on and power-off procedures, the currents and voltages monitoring, the alarm handling and reporting, and the Data Base storage of all the relevant parameters (this task is schematized in figure 5.25).

All these control tasks are performed by a single server, running on a dedicated Linux machine (bxslow). This software is completely independent from the remaining DAQ processes and also has its own WEB interface. From this page, the user can remotely power on/off single crates/boards/channels, change the default high voltage values, and monitor the status of the HV/VME system.

Chapter 6

Tests of the Borexino read-out system

In the period from February 2002 to August 2004, the Borexino detector underwent many global tests of its read-out system. These tests are operated in the form of "Air-Runs"; an Air-Run consists in a real run of the detector, with all PMTs on and the electronics and DAQ chain enabled. They are called Air-Runs because the Borexino detector is not yet filled with water or scintillator. The complete list of Borexino Air-Runs is reported in table 6.1.

The main purposes of these tests are:

- check of the general status of the photomultipliers and of the HV power supplies; if needed, fine tuning of the working conditions of the single PMT;

- test of the electronics status, with the complete event read-out chain: Front-End and digital modules are tested, but also sums system (see chapter 8); this will result in a general improvement of the electronics performances, as well as in the fine debugging of single boards or channels;

- set-up and finalization of the trigger system, allowing the possibility of different trigger configurations (dark noise runs, laser runs, etc.; details are given in section 5.2.4);

- complete test of the on-line software, including the main DAQ system, the On-line Monitor, the Slow Control, the Data Base collection, etc. (the system is described in section 5.3);

- finalization and test of the PMT laser calibration apparatus (see chapter 7);

- check and improvement of many components of the events reconstruction program (splitting algorithm, position reconstruction software, etc.).

Four types of measurement have been performed:

Nr.	Date	Measurement Types	Main Results
1	Feb 2002	Pulser/Dark Noise	First PMT debugging
2	Apr 2002	Pulser/^{222}Rn source	PMT debugging and electronics checks
3	Jun 2002	Pulser/Laser	Identified a time measurement problem
4	Aug 2002	Pulser/Laser	Solved the time measurement problem
5	Dec 2002	Laser/^{210}Po source	Identified a charge measurement problem
6	Apr 2003	Outer detector only	First debugging of the outer detector
7	Aug 2003	Dark Noise/Laser	Solved the charge measurement problem
8	Dec 2003	Laser/^{222}Rn source	Good energy and position performances
9	Aug 2004	Dark Noise/Laser	Electronics saturation studies

Table 6.1: List of the Borexino Air-Runs, with the measurement types and the main achieved results.

- **pulser data:** in this run configuration, all the front-end channels receive a synchronous pulse, generated through a timing unit and a fan-out module (see section 5.2.4); this kind of data allowed to improve the time measurement performances of the detector, with the introduction of an upgraded time reconstruction algorithm (see below);

- **dark noise data:** these data are acquired delivering asynchronous pulses to the trigger ("random" triggers); in this way, it is possible to measure the dark rate of the single PMTs (and generally to monitor their status);

- **timing laser data:** in this case, all the PMTs are illuminated by a synchronous light pulse, delivered by the calibration system; these data allow to check the overall timing resolution of the detector, as well as the charge measurement capabilities (the single photoelectron response of the PMTs can be studied);

- **radioactive source data:** three radioactive sources have been measured in Borexino; all the sources were composed of a small quartz vial, filled with some cm^3 of scintillator, which had been previously ^{222}Rn loaded through exposure to a ^{226}Ra radioactive source; this last type of data allowed higher level debugging of the detector and of the event reconstruction program.

6.1 General status of detector: from the first PMT test to the detector completion

The first Air-Run took place in February 2002. It allowed the first test of the PMTs status, because it was the first time that the 1993 installed PMTs were turned on, after their mounting in SSS.

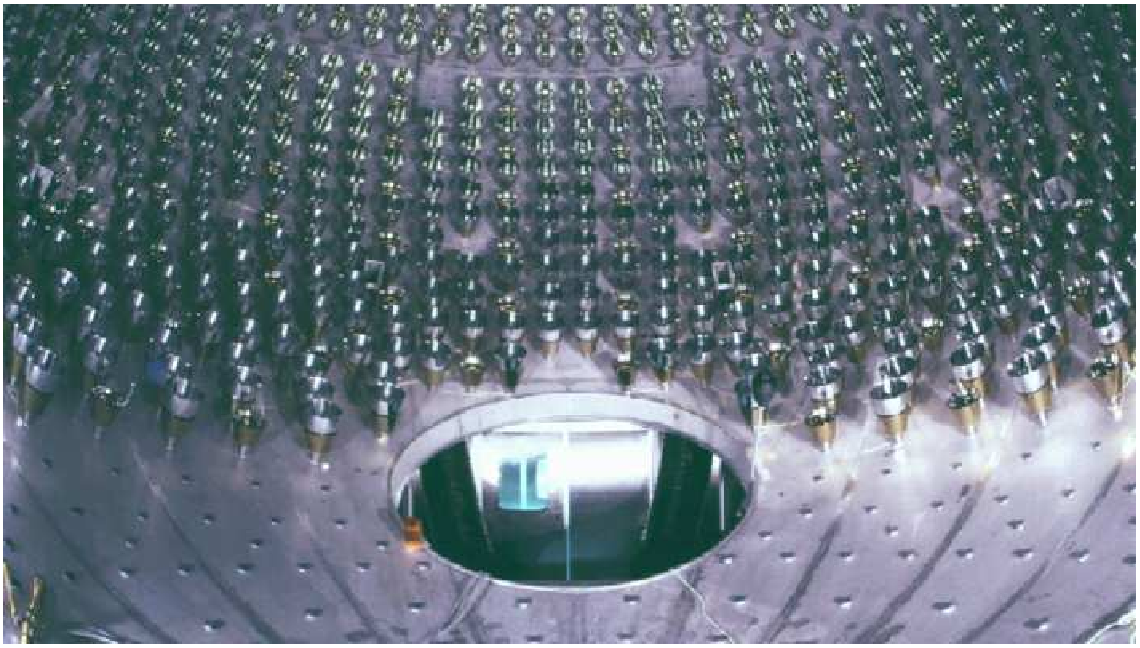

Figure 6.1: An internal view of the SSS, with the 1993 installed PMTs and the empty regions on the floor and around the access door (Feb 2002).

Such a test was very critical, because the newly installed PMTs had been tested both at the production site and in the Gran Sasso testing facility (section 5.1), but the possible failures due to transport to the Hall C and installation in SSS had to be evaluated. Furthermore, the PMTs had never been tested with the final HV power supplies, nor with the Borexino Front-End boards (Front-End boards are very critical for PMTs, because they feature the decoupling stage from the HV to the signal): therefore, their performances were not guaranteed to be the same.

The run preparation was very accurate and the main preparation steps were:

1. **Data Base setup:** the complete cabling data have been inserted in Data Base (as described in section 5.1); before starting the data taking, all the database content has been checked carefully (an integrity control procedure has been implemented in the WEB interface); a new "profile" has been created, describing a valid detector setup and the corresponding run conditions;

2. **High Voltages setup:** for each PMT, the HV working conditions (as tested in the Gran Sasso facility) had been stored into a dedicated data base; before the run, these values have been recovered and loaded into the HV mainframes through an automatic procedure;

3. **careful darkening of the SSS:** the Borexino Sphere has been sealed in June 2004, after the last PMTs installation; in 2002, many open flanges and air

filters were present: before the run, all these holes have been darkened with black light-proof materials; the same work has been performed on the clean rooms in communication with the SSS;

4. **pulser runs:** before turning on the PMTs, many pulser runs have been acquired, in order to check the electronics status; damaged Front-End or Laben boards have been replaced with spare ones;

5. **individual PMT check:** many PMTs have been turned on individually and visually checked with the Scope: if needed, the HV settings have been modified in order to meet the optimal working condition.

6.1.1 The "flashing" phototubes

When a new PMT group is turned on for the first time, an important cross-talk effect may be observed. Indeed, when a phototube is getting broken (for any reason), it may happen to electrically discharge, emitting light flashes that illuminate all the others PMTs in the group. In this case, a very high rate of correlated light pulses is observed in all the surrounding PMTs.

This effect was observed during the first Borexino Air-Run: a general very high rate was present in the detector ($> 100\ kHz$, while in normal condition a few Hz of dark noise activity should be observed at most). A complicated "flasher-hunting" procedure was established; first, all the detector was kept on: counting rate on some reference channels was measured by means of a set of scalers; then, each crate was turned off in turn, until a significant rate decrease was observed on reference channels: in this case, the crate just turned off should host the flashing PMT. At this point, the full crate was turned on again, and the procedure was repeated on the single HV boards (they were turned off one by one, until the one containing the flashing PMT was found); once the board was identified, the flashing channel was found (in a similar way) and physically disconnected from its power supply (the maximum of 900 V difference between the channels in the same HV board does not allow to turn off completely the single channels: this is especially delicate in case of a discharging PMT, which can continue flashing also at a low voltage).

In this way, three big flashers were found, that induced a very high rate in the detector ($> 100\ kHz$ on each PMT); other ~ 80 PMTs were turned off or disconnected, because they showed an irregular or instable behavior, or simply because they were too noisy for a "quiet" data taking. All these disconnected PMTs have been analyzed and checked afterwards, and most of them were re-connected: in AirRun9 (August 2004), only 19 PMTs were still disconnected because of their instability ($< 1\%$ of the 2212 installed PMTs).

Figure 6.2 shows the countrate on the single PMTs, as measured with the Online Monitor, in a detector map presentation; the top figure represents the situation before a big flasher ($\sim 600\ kHz$) was identified: a pattern of correlated light emis-

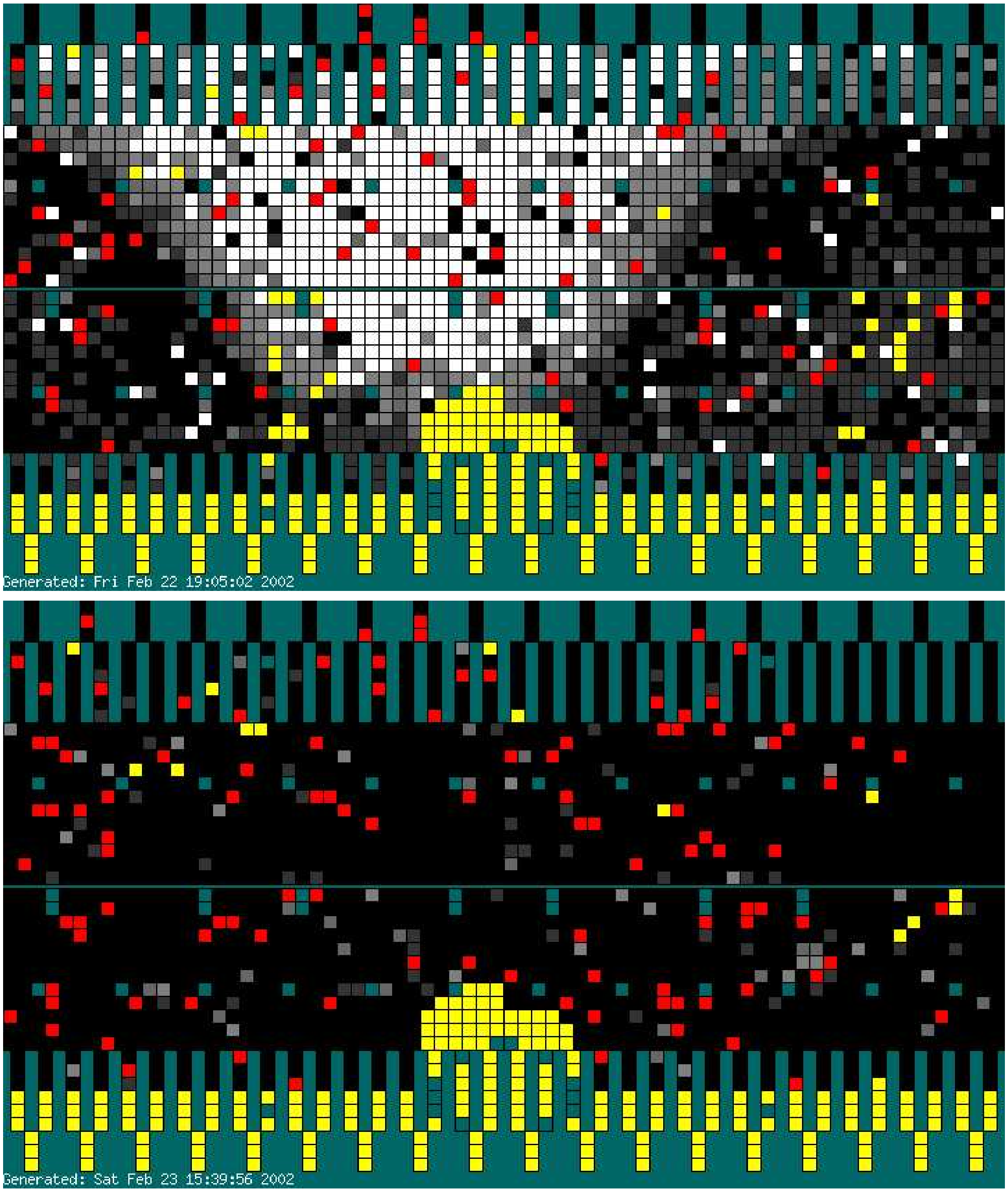

Figure 6.2: Single channel countrate during the AirRun1, in a detector map presentation (from the On-line Monitor): detector is “photographed” before (top) and after (bottom) the disconnection of a flashing PMT. Countrate is expressed in grayscale: the white area is illuminated by the flasher. Yellow and red spots represent respectively not installed PMTs (~ 220) and dead channels (~ 150).

sion is clearly visible. The lower picture shows the detector situation after the disconnection of the big flasher: an uniform count-rate can be observed.

In figure 6.2, are also visible the non-installed PMTs, represented with yellow points. The red points show completely dead channels: during the AirRun1 the dead channels were ~ 150. Of course, the channels classified as "bad" can suffer any possible problem (bad cables, bad front end channel, bad digital channel, dead PMT, software problems). These channels (which include the 80 disconnected PMTs) have been checked afterwards and repaired or recovered: in AirRun9, only 20 channels + 30 PMTs look dead (see section 7.4).

6.1.2 PMTs and electronics debugging

Detailed results about the PMTs and electronics status are given in chapter 7; here only the final results are summarized:

- the number of dead electronics channels decreases from ~ 80 (2002) to ~ 20 (2004), thanks to an intensive repair and substitution work on entire boards and single channels; this work has to be added to the one performed to improve the global electronics performances, as will be explained later;

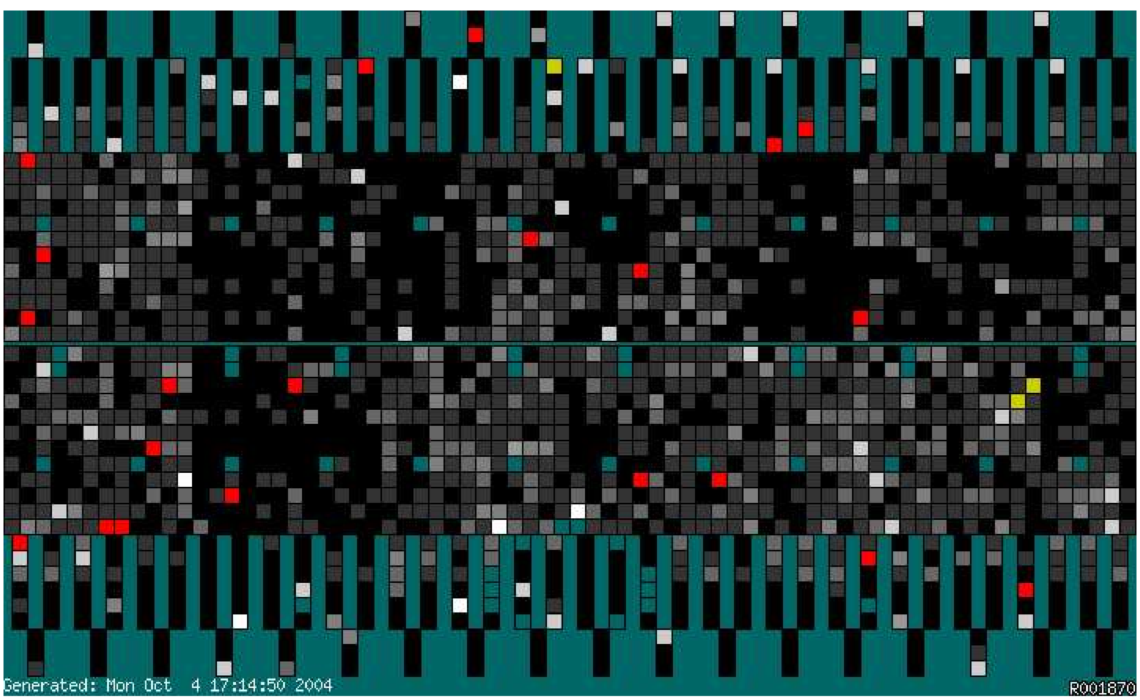

Figure 6.3: Single channel countrate during the AirRun9, in a detector map presentation: all the PMTs are installed in the SSS and the dead channels are ~ 20 (to be compared with situation in figure 6.2, bottom).

- the number of dead or disconnected PMTs decreased from ~ 80 (2002) to ~ 30 (2004); this improvement is due to different reasons: some dead PMTs were directly replaced in SSS (along with some other PMTs that were damaged during a cleaning work in the sphere); some other were simply recovered, through an accurate setting of their HV operating conditions.

6.2 A time measurement problem

During the AirRun3 (June 2002), a problem in the single hit time reconstruction was found: illuminating the PMTs with the synchronous light pulses delivered by the laser calibration system, the reconstructed time distribution showed a complex structure, with three peaks at 50 ns distance (plus a reflected light peak, 40 ns delayed from the main peak), as shown in figure 6.4.

Further measurements, performed with the PMTs off and with the Front-End pulsing system, confirmed this result and allowed the identification of some problems in the hit time reconstruction, due to the non-ideal behavior of the Laben boards.

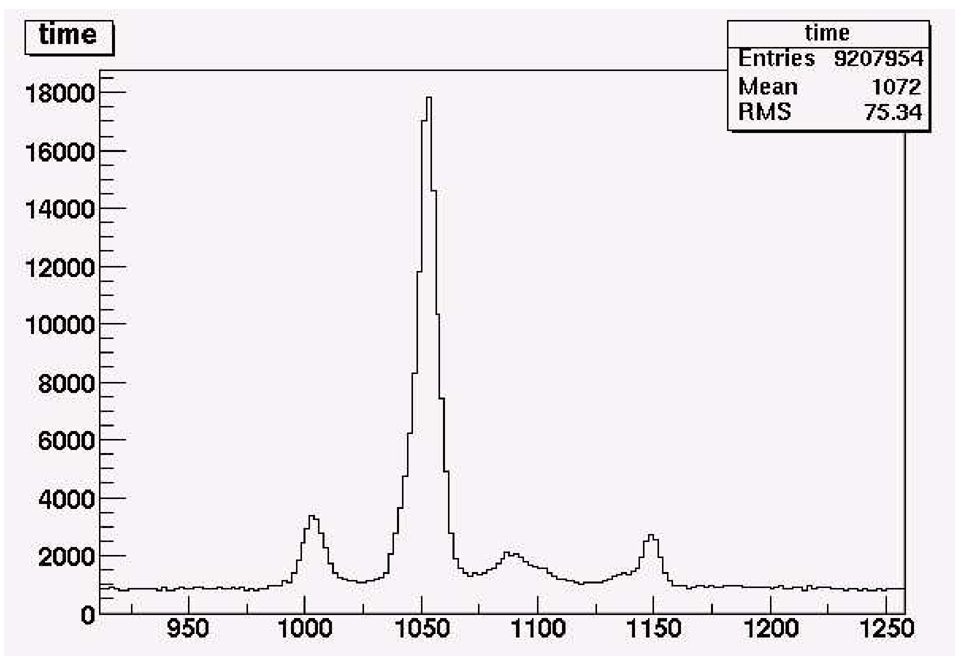

Figure 6.4: The peak structure in a timing laser run, during AirRun3: direct light peak is at about 1050 ns, reflected peak is 40 ns later, while the two peaks at 1000 and 1100 ns are due to a time measurement problem.

6.2.1 The single hit time reconstruction

The time information of the single hit is reconstructed from the data measured by the Laben board (described in section 5.2.2), by means of the following algorithm:

1. the value of the 16 bit counter ($gray\_count$) and the first sample of the 10 MHz ramp ($ramp_1$) are read;
2. the rough time is calculated as: $time\_gray = gray\_count \cdot 50\ ns$;
3. the slope of the ramp (positive or negative slope) is deduced from the last bit of $gray\_count$ (parity of the sample), and then (see figure 6.6):
   - if positive slope (even $gray\_count$), $\Delta t = (ramp_1 \cdot 50\ ns)/255$
   - if negative slope (odd $gray\_count$), $\Delta t = 50\ ns - (ramp_1 \cdot 50\ ns)/255$
4. the relative arrival time is evaluated as: $t = time\_gray + \Delta t$

In principle, this algorithm would require only one sampling of the 10 MHz triangular wave and would give a theoretical resolution smaller than 100 ps, in a time window of 3.2 ms (fixed by the 16 bit gray counter crossing). Actually, the non ideality on the Laben boards slightly complicates the picture, and the above described algorithm can give inexact results. Mainly three effects were found:

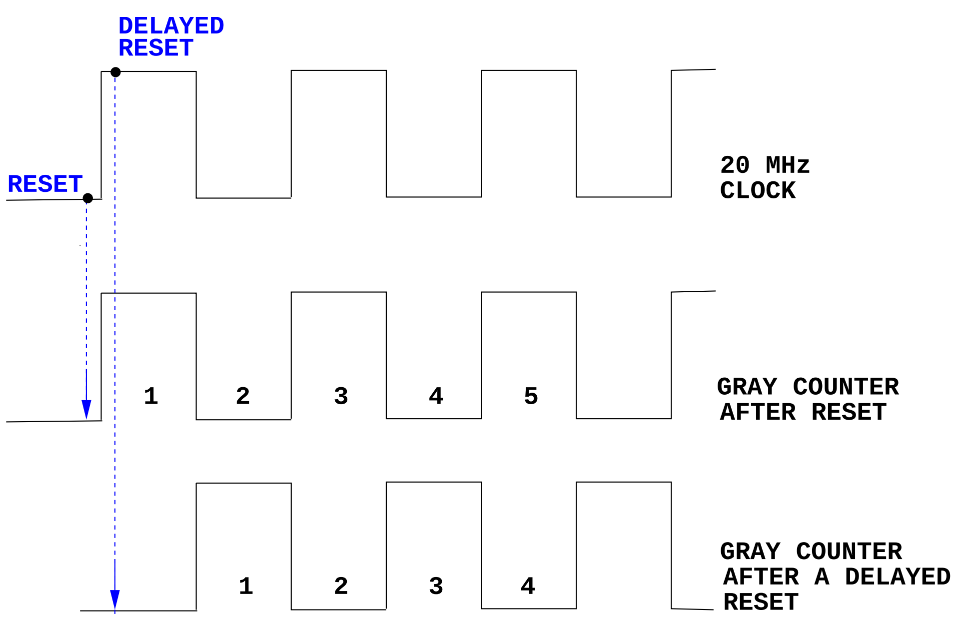

Figure 6.5: Possible systematic shift of 50 ns due to small delays between the arrival times of the reset signal on different boards.

- **non linearity of the ramp:** the ramp is not a perfect triangular wave but has smoothed angles and can also be saturated; for this reason, if a hit arrives too close to the ramp edge, the second sample of the triangular wave (80 ns delayed) has to be used for time measurement: the time of the first sampling is then recovered by subtracting the delay time. To increase the precision of this subtraction, the effective value of the nominal 80 ns delay time is measured for each channel in every run;

- **misalignment of gray counters on different boards:** at the start of each run, the BTB delivers a reset signal to each Laben crate, in order to synchronize both the triangular waves and the gray counters. Due to small delays in the delivery lines, some boards can receive these signals with some ns delay: in this case, a situation like the one presented in figure 6.5 could happen, causing systematic shifts of 50 ns. To solve this problem, a programmable number of pulser events (usually 1000) is delivered to the system at the beginning of each run: these synchronous events (also called "pre-calibration" events) allow a software re-alignment of the gray counters on all the boards;

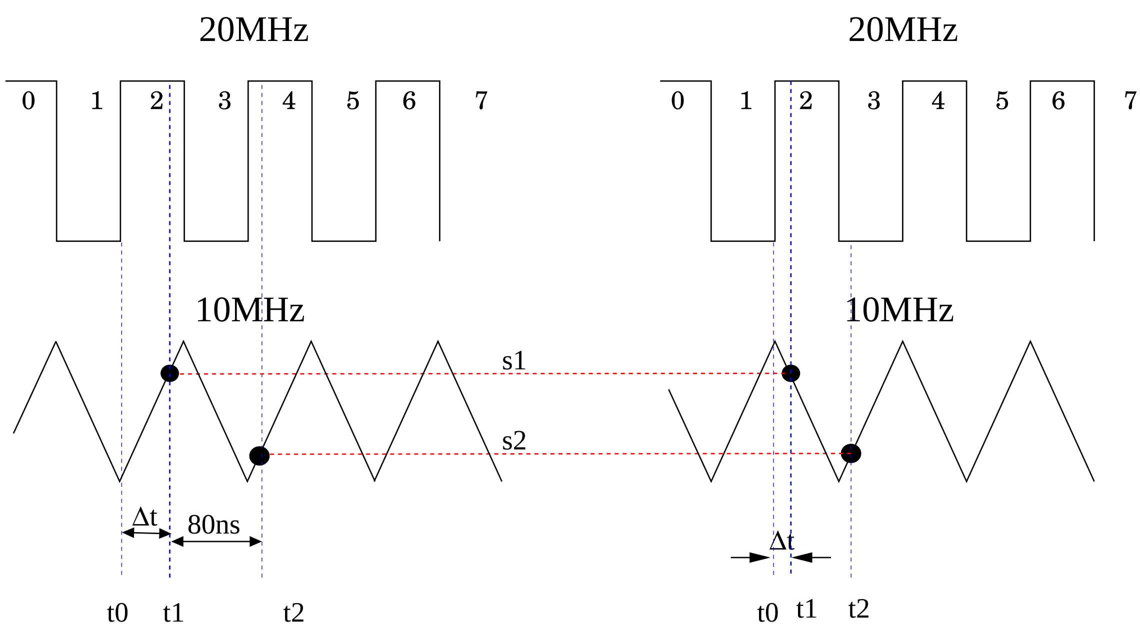

Figure 6.6: The reconstructed Δt value in the two cases of rising (left) or falling (right) slope for the triangular wave (with respect to the parity of the gray counter).

- **not fixed relationship between the parity of the gray counter and the slope of the ramp:** the 10 MHz triangular wave is obtained by the 20 MHz clock, but unfortunately there is no warranty to have a fixed relationship between the gray counter and the slope. The absence of a known relationship can introduce another 50 ns error in the time measurement, as shown in figure 6.6. Nevertheless, this relationship can vary from run to run, but is guaranteed to remain constant during a single run: therefore, it can be measured at the beginning of the run, using the "pre-calibration" events delivered to all the channels, in the same way as it is done for the gray counters alignment.

6.2.2 The "pre-calibration" events

To study the efficiency of the above described algorithm, some pure pulser runs were acquired, with all the PMT high voltages off (in order to exclude any possible contribution to the time spread due to the photomultipliers). The time resolution estimated in this way, is therefore an estimation of the intrinsic resolution of the electronics and it has to be added to the photomultiplier intrinsic time spread to obtain the resolution of the whole chain (see section 7.3).

The first data analysis was performed without any software realignment of the gray counters: a relevant number of channels, about 1% of the detector, showed systematic shifts of 50 ns. If we plot the difference of the reconstructed hit times of each Laben channel with the time of one reference channel, we can clearly see these shifts (figure 6.7, left); this is even more clear in the projection of this plot: figure 6.7 (right) shows the double time peak on rack 1.

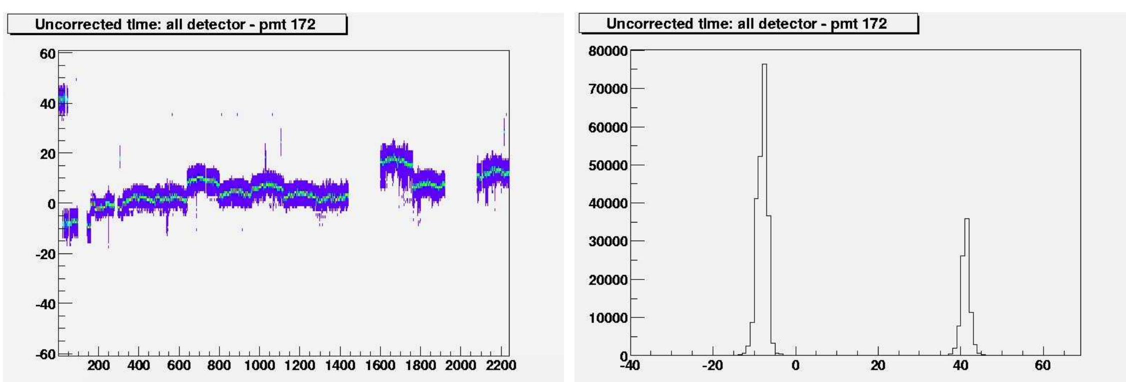

Figure 6.7: Left: difference of the reconstructed times of the hits with one reference channel, before the software realignment of the gray counters. Right: projection of the same histogram for rack 1 only (the 50 ns shift is clearly visible).

After the correction of the gray counters, all the racks are internally synchronized, and the remaining shifts among one rack and another are real hardware delays: they can be assumed to be constant and treated as systematic delays. After a subtraction of these values, we find the plots of figure 6.8: the intrinsic electronics spread on the whole detector results in about 1.2 ns. The small fraction of hits falling outside the central peak (about 0.1% of the hits) still shows a systematic shift of 100 ns: this is the unavoidable fraction of hits where the pre-calibration routine fails to evaluate the relative slope.

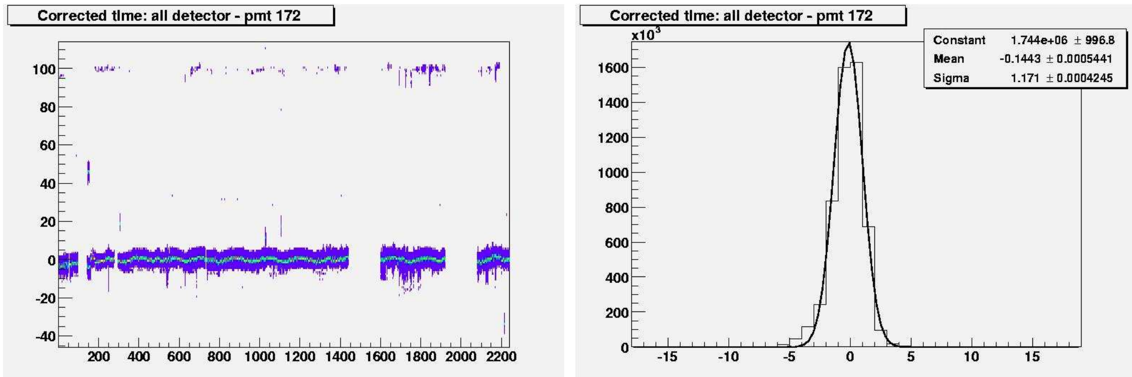

Figure 6.8: Left: difference of the reconstructed times of the hits with one reference channel, after the software realignment of the gray counters and a subtraction of the systematics delays. Right: projection of the same histogram, showing the final resolution of the pre-calibration algorithm.

Once the good performances of the algorithm were evaluated, the generation of the pre-calibration events has been permanently inserted in the BTB firmware (and in trigger configuration): since June 2002, they are automatically delivered at the beginning of each Borexino run. A further complete test of the time reconstruction capabilities has been performed in AirRun4 (August 2002), using the PMTs laser calibration system: the results of this test are described in section 7.3.

6.3 A charge measurement problem

After the correction of the timing problem through the introduction of a new “pre-calibration” procedure, also a charge measurement problem was identified in the Air-Runs laser data. Actually, a rather high number of channels ($\sim 30\%$) got a zero charge measurement in a big fraction of the hits, resulting in a total 15% of zero charge hits on the whole detector in a standard timing laser run (the typical charge spectrum with the big “zero charge” bin is shown in figure 6.9, left).

This effect was especially puzzling, because it was found to be independent from the High Voltages; moreover, the channels showing the problem were spread out on the whole detector and changed from one run to another (in figure 6.9, right, is shown a typical histogram of all the channels, displaying the distribution of the zero charge hits in the detector).

The problem was traced back to the bad quality of the cables connecting the Front-End modules to their (low voltage) power supply. The bad connections induced randomly some low frequency noise on the charge signals: therefore the charge

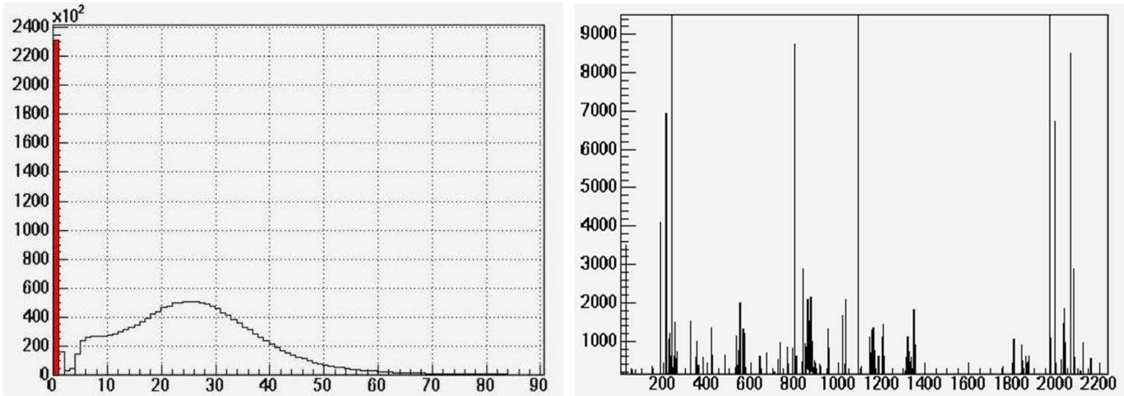

Figure 6.9: The charge spectrum measured in a standard timing laser run (left): the zero charge bin is highlighted in red; the corresponding detector map, representing the channels which measure the zero charge hits (right).

baselines were drifted outside the ADC range; for the concerned oscillating channels, the two charge samples were always measured 0 or 255 (resulting in a null charge value). This noise was not stable, thus it was not easy to identify it in normal test conditions.

All the cables and connectors between the Front-End modules and their power supplies were replaced in June 2003, with better quality connectors and shielded cables. The result, for a pulser run taken immediately after the modification, was a decrease of the zero charge bin down to 3%. Afterwards, during the AirRun7 (August 2003), the performances of the system were evaluated again, by means of a series of "timing" laser runs.

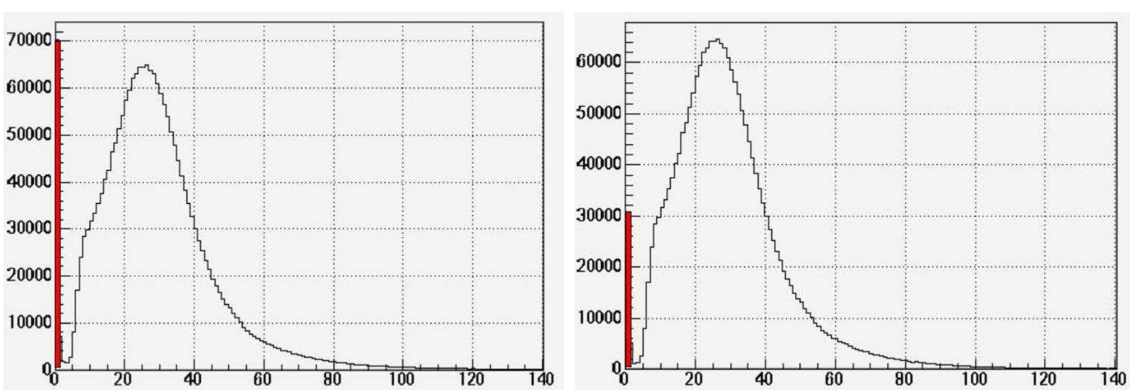

Figure 6.10: The charge spectrum measured in a standard timing laser run, after the Front-End cables modification: considering all the channels (left) and excluding the 40 channels which still have the zero charge problem (right).

The result of these runs is shown in figure 6.10 (left): after the modification, $\sim 4\%$ of the hits still show the charge measurement problem. The good news is that the channels with a high zero charge bin are now a small number of the total (~ 40) and are always the same: then the problem can be further reduced simply by repairing or replacing these channels. Excluding these 40 channels from the analysis, the zero charge peak reduces down to $< 2\%$ of the total hits (figure 6.10, right). Further results about charge measurement performances in laser data (allowing PMTs charge calibration) are described in section 7.4.

6.4 The radioactive source tests

Three radioactive source runs have been performed in Borexino between April 2002 and December 2003. These runs allowed a global test of the complete read-out system, in a "realistic" operative condition. The three sources were composed of a small quartz vial, filled with some cm^3 of scintillator, which had been previously ^{222}Rn loaded through exposure to a ^{226}Ra radioactive source.

1. **April 2002 (AirRun2):** a ^{222}Rn loaded source was produced, via a prolonged exposure to a high intensity ^{226}Ra source; the quartz cell had a spherical shape; it was suspended on a rope and inserted in the SSS from the top flange; the rope allowed source displacement along the detector $z-$axis.

2. **December 2002 (AirRun5):** a ^{210}Po source was prepared through the exposure to a 2 MBq ^{226}Ra source: once loaded in ^{222}Rn, the source has been conserved for many months before the run, waiting for the complete ^{222}Rn decay and the ^{210}Po build-up; residual ^{222}Rn has been eliminated by nitrogen stripping of the source, just before the measurement; the source quartz cell had still a spherical shape and the usual suspension system was employed.

3. **December 2003 (AirRun8):** a new ^{222}Rn loaded source was produced, with the usual loading method with ^{226}Ra; the quartz cell had a cylindrical shape and, as usual, it was suspended on the rope.

The first radioactive source run gave poor results, because the detector status was too bad (the time and charge measurement problems was not solved yet): nevertheless, the ^{214}Bi –^{214}Po delayed coincidences present in the ^{222}Rn chain allowed the first test of the measurement system for the absolute time of the event. As explained in section 5.2, for each event the GPS time information is acquired and stored in the trigger record; this information has a 100 ns resolution, which is much smaller than the ^{214}Po decay time (236.6 μs).

A standard delayed coincidence analysis can be applied to the AirRun2 source data: using the absolute time information, the time differences between consecutive events are computed; in this way, a plot like the one showed in figure 6.11 is obtained. The time difference histogram can be fitted with the sum of two exponential

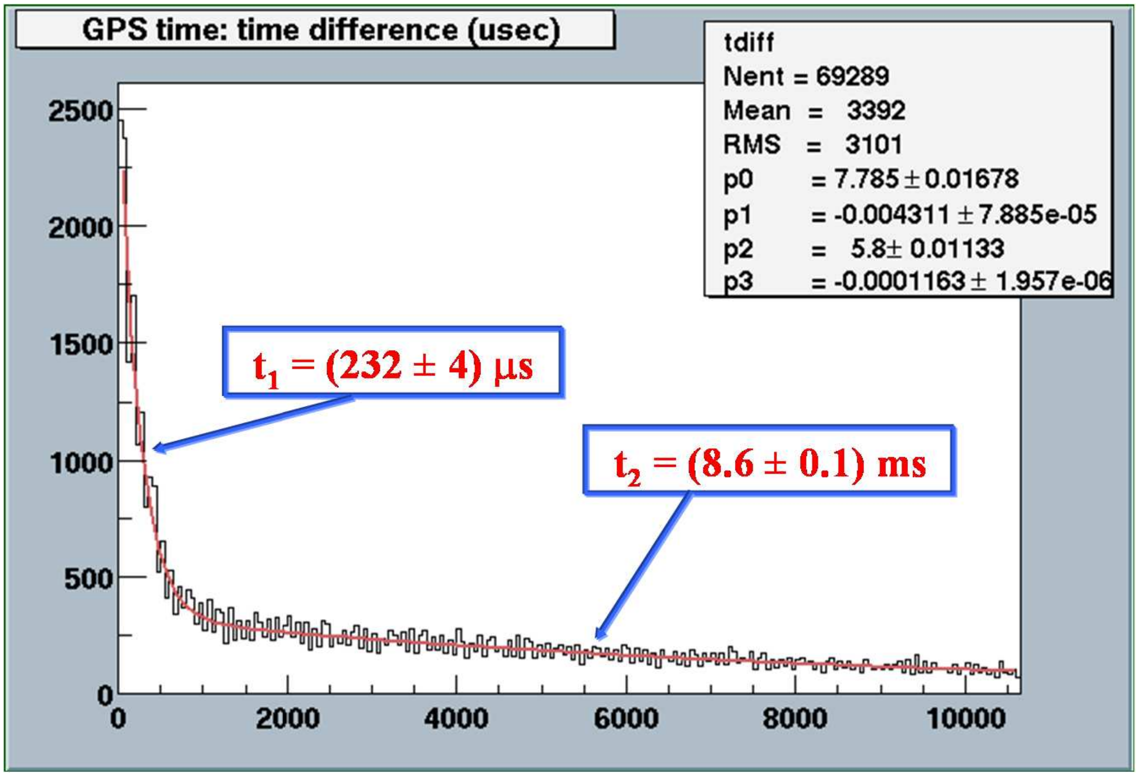

Figure 6.11: The time difference between consecutive events, as measured in a ^{222}Rn source run, during the AirRun2.

components: a short time component ($\tau = 232 \pm 4$ μs), which represents the ^{214}Bi $-^{214}Po$ coincidence; and a longer time component ($\tau = 8.6 \pm 0.1$ ms), accounting for the global trigger rate of the detector (~ 120 Hz, independently measured by means of a scaler).

This first result (even if it is almost trivial) allowed to draw three main conclusions:

- the GPS data are acquired correctly, correctly stored in the raw-data file and correctly reconstructed; therefore, the absolute time information is reliable;

- the trigger efficiency is satisfactory, otherwise the events in coincidence could not be detected and reconstructed with this precision; of course, deeper tests on this issue have been performed afterwards, confirming this first result;

- the overall DAQ chain can sustain a rate of at least 120 Hz for a reasonable amount of time (in the figure, ~ 70000 acquired events are shown); this DAQ rate is much larger than required for the standard Borexino run conditions (also acquiring ^{14}C spectrum, the rate should be in the 10 Hz range), and should represent a safe condition also in case of a supernova event, when a rate of a few 10 Hz is expected (see section 3.2).

6.4.1 Delayed coincidence analysis

This delayed coincidence analysis has been repeated with the data from AirRun8, when a new ^{222}Rn source was studied: in that case, the electronics status was much better (both the time and charge measurement problems had been solved) and some very simple "physics" informations could be deduced from the data.

First of all, the time difference study was repeated with the new source, giving again a very good result: the short time component of the detector activity was found at $\tau = 238 \pm 4\ \mu s$, well consistent with the ^{214}Po decay time (236.6 μs). Then the energy spectrum of the ^{214}Bi –^{214}Po events was studied: the result is shown in figure 6.12, where both the ^{214}Po α peak and the ^{214}Bi $\beta + \gamma$ spectrum are clearly visible.

The ^{214}Po α peak is fitted with a gaussian function: the center of the distribution is located at 343 $p.e.$ and has a width of 21 $p.e.$ (5% resolution, at 1 MeV energy); the

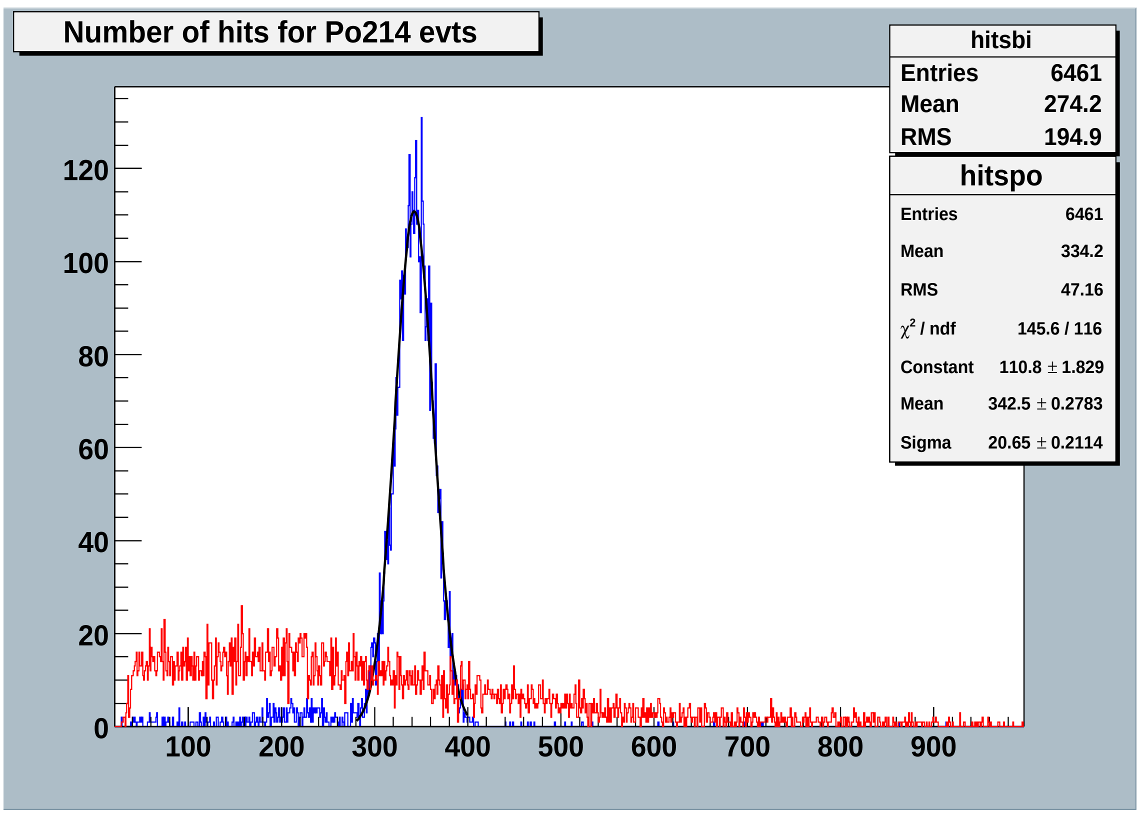

Figure 6.12: The energy spectra of ^{214}Po (blue) and ^{214}Bi (red) events, as acquired during the AirRun2 (the $x-$scale is in photoelectrons).

light yield of the source can be estimated to be about 460 $p.e./MeV$, if a standard quenching factor is assumed for alphas (see section 4.3). Concerning the ^{214}Bi $\beta+\gamma$ spectrum, its high energy component is clearly suppressed (the end-point of the spectrum should be at 3.3 MeV, while in this case very few events have an energy bigger than 1.5 MeV): this effect is due to the bad γ containment inside the source volume (amounting for a few cm^3).

The ^{214}Bi –^{214}Po events offer also two pure α and β samples for α/β discrimination studies. A very detailed work on this item has been performed using AirRun8 data [69]: here only the preliminary results obtained with the a simple "tail to total" method are reported (this method is described in section 4.2). In figure 6.13 is shown the behavior of the α/β discriminating parameter for a sample of ^{214}Bi –^{214}Po events: the discriminating parameter is obtained integrating the time signal of each event, in the interval between 15 and 100 ns. From this distribution, the resulting α/β discrimination efficiency can be estimated as follows: if we fix the β acceptance to 93%, the 98% of the α events are successfully rejected (neglecting non-gaussianities of the β signal, which are due to the presence of very low energy

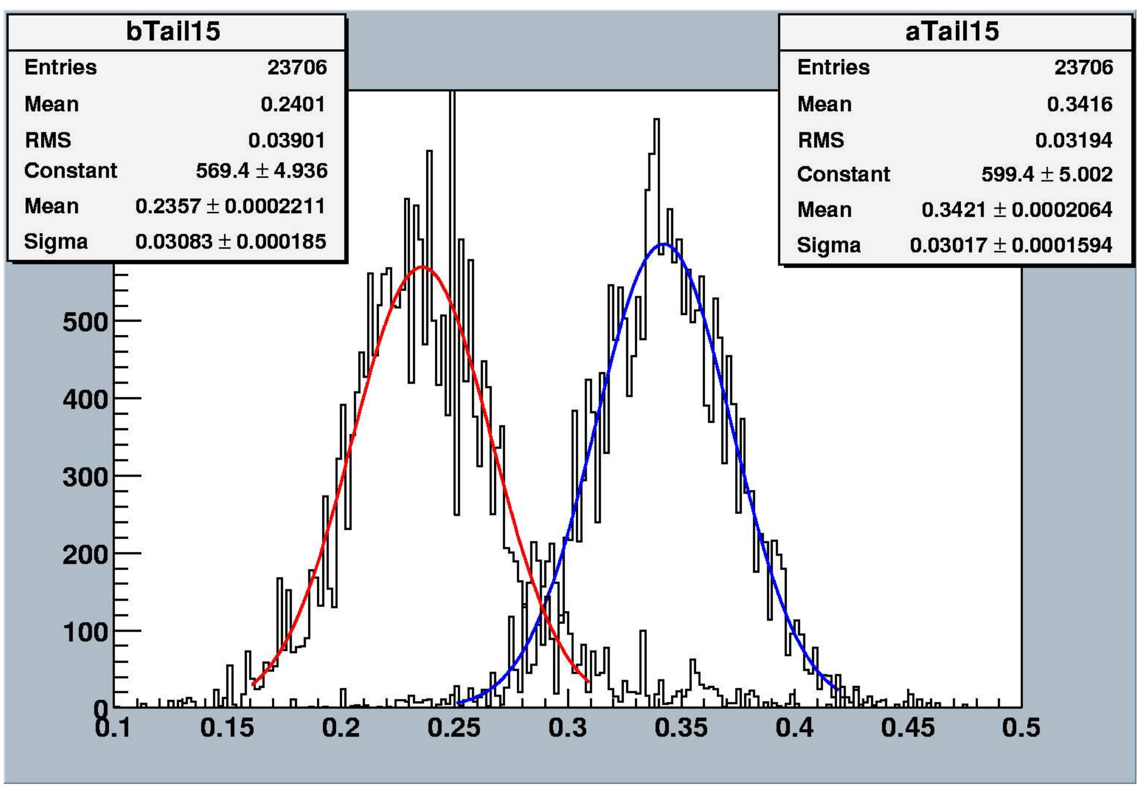

Figure 6.13: The "tail to total" α/β discrimination parameter, applied to ^{214}Bi –^{214}Po pairs as acquired in AirRun8 data; the ^{214}Bi (red) and ^{214}Po (blue) events are fitted with two gaussian functions.

events in the sample).

Of course, this discrimination method is just too trivial to give an idea of the final pulse shape analysis capabilities of Borexino: nevertheless, its efficiency confirms the general good status of the detector, especially concerning the time measurement issue.

6.4.2 Analysis of the energy spectra

In AirRun5 and AirRun8 data, the global energy spectra of the radioactive ^{210}Po and ^{222}Rn sources were measured. The AirRun5 spectrum showed a complex structure (see figure 6.14), instead of the α peak expected from the ^{210}Po decay. The explanation of this result relies on the total reflection mechanism: due to the spherical shape of the source quartz cell, a significant fraction of the scintillation photons undergoes a total reflection on the cell/air interface and is absorbed by the quartz before escaping the cell (a similar phenomenon has been observed also in CTF data, concerning the PC/water interface). According to this hypothesis (confirmed by a Monte Carlo study), the ^{210}Po events produced in the center of the source should produce a full energy peak (at ~ 150 *p.e.* in the figure), while the events closer to

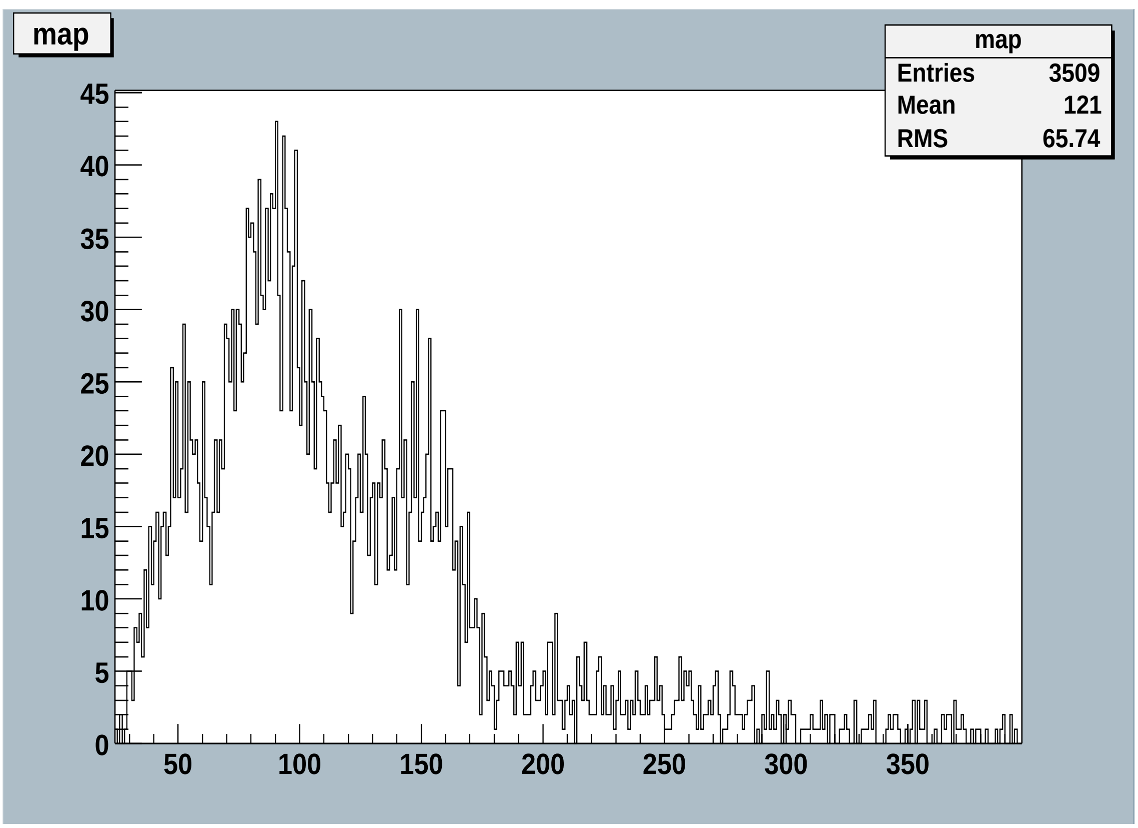

Figure 6.14: The energy spectrum of the ^{210}Po source, as measured during AirRun5.

the surface should experience a reduction in the detected light (broad structure at ~ 80 $p.e.$ in the figure).

The situation in the AirRun8 looks much more "comfortable": a structure with two peaks and an underlying continuous spectrum is observed, as expected; this fact indirectly confirms the total reflection hypothesis for the ^{210}Po source data, since the ^{222}Rn source was contained in a cylindrical cell, instead of a spherical one. In figure 6.15, this energy spectrum is shown: actually, this is the first energy spectrum ever measured in Borexino.

The two peaks visible in the spectrum are respectively: the ^{214}Po α peak already seen in the delayed coincidence analysis (it is the peak at ~ 350 $p.e.$ in the figure), and the summed contribution from the ^{222}Rn and the ^{218}Po α peaks (the resulting peak is at ~ 200 $p.e.$). These two α peaks show consistent values for reconstructed energy and resolution; the light yield deduced from the low energy peak confirms what measured on ^{214}Po events, resulting in about 460 $p.e./MeV$. Furthermore, the area of the low energy peak is exactly twice the area of the higher energy one, as expected in secular equilibrium hypothesis (^{222}Rn reaches the equilibrium with its daughters ^{218}Po and ^{214}Po in less than one hour). Finally, the underlying continuous spectrum is the summed contribution of the $\beta + \gamma$ decays in the ^{222}Rn sub-chain:

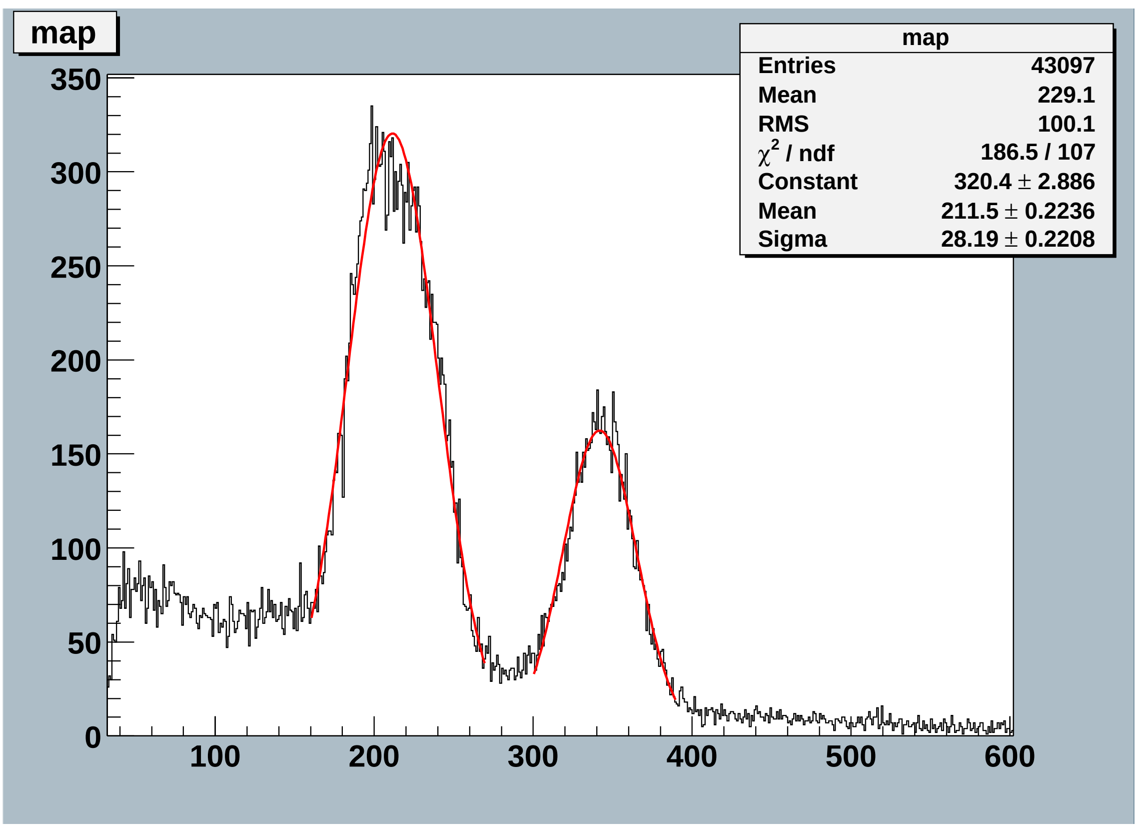

Figure 6.15: The energy spectrum of the ^{222}Rn source, as measured during AirRun8.

namely, the ^{214}Pb and the ^{214}Bi (with γ escaping the vial).

6.4.3 The position reconstruction code

The Borexino position reconstruction code relies on the time information of the single hit, as provided by the Laben electronics. The algorithm starts its minimization process from the barycenter of the collected charge on the phototubes. Then the MINUIT minimization package is invoked, which computes the best estimation for the event position through a maximum likelihood method. The minimization procedure is performed by comparing the intrinsic time distribution of the scintillation light with the measured arrival times of the photoelectrons; the *p.e.* arrival times are corrected for the time of flight information, which is the parameter related to the event position.

Before applying the position reconstruction algorithm to the scintillation events, the starting time of the physical pulse (i.e. the first hit in event) must be correctly identified. This is not a completely trivial issue, since the Borexino trigger gate starts $\sim 2\ \mu s$ before the real beginning of the event and the hits belonging to the pulse have to be disentangled from the underlying dark noise distribution. An algorithm has been written to compute the real starting point of the event [69], based on a simulation of the trigger behavior: such an algorithm has proved to satisfy the event identification requirements.

In both the source Air-Runs, the Borexino position reconstruction system has been tested, thanks to the source suspension system, which allowed the displacement of the source along the vertical axis of the detector. The results about reconstructed position are listed in table 6.2, compared to the nominal positions. Before describing these results, it is necessary to point out that the employed source insertion system is very "primitive" and therefore the absolute source positions are known with a precision of order 10 cm.

From the results listed in table 6.2, the following conclusions can be drawn:

- the general performances of the system are good, since the nominal source position is always reconstructed with a $< 10\ cm$ error (consistent with the uncertainty on the source position);

- the resolution for the ^{210}Po source is worse than for the ^{222}Rn source: this is consistent with the lower visible energy of the ^{210}Po events (see figure 6.14);

- looking at the ^{222}Rn data, it is easy to conclude that the z resolution is worse than the x and y resolution; furthermore, these resolutions decrease when the source approaches the north pole of the SSS: these two effects can easily been explained by recalling that at the time of the AirRun8 200 PMTs were still missing on the SSS floor (see picture 6.1);

- the drift on the reconstructed x position (in ^{210}Po data) is not due to a bug

^{210}Po source position	x	σ_x	y	σ_y	z	σ_z
$x=0;\ y=0;\ z=0$	-1.7	25	2.6	16	8.4	25
$x=0;\ y=0;\ z=100$	4.6	20	5.0	13	93	29
$x=0;\ y=0;\ z=200$	-0.4	22	5.0	18	192	25
^{222}Rn source position	x	σ_x	y	σ_y	z	σ_z
$x=10;\ y=0;\ z=60$	12	13	0.7	12	71	18
$x=10;\ y=0;\ z=z_1$	10	13	1.3	12	-21	15
$x=10;\ y=0;\ z=z_1+53$	11	13	-1.6	12	24	16
$x=10;\ y=0;\ z=z_1+153$	12	13	2.3	13	112	20
$x=10;\ y=0;\ z=z_1+253$	13	14	1.0	14	219	22
$x=10;\ y=0;\ z=z_1+403$	14	16	-0.8	16	373	28

Table 6.2: Nominal and reconstructed positions, for the ^{210}Po and ^{222}Rn sources, as measured respectively in AirRun5 and in AirRun8. All numbers are quoted in cm.

in the program (or to a misalignment of the SSS axis), but to a real source displacement due to the rope movement;

- the x and y position resolutions, for events close to the SSS center, are in the range $12 \div 13$ cm (without any cut on the energy of the events); with the completed detector, the z resolution should be of the same order.

Chapter 7

The PMT calibration system

A multiplexed system of optical fibers has been designed for the photomultiplier calibration of the Borexino detector. Both time and energy calibration are of capital importance in Borexino for the measurement of the solar ^{7}Be neutrino flux.

Accuracy in the time measurement of the single hit infers the accuracy on position reconstruction, which is required to define the Borexino Fiducial Volume; position resolution is limited by the scintillator fluorescence decay time of 3.5 ns (effectively increased to 5.5 ns after light propagation effects [6]), by the PMT transit-time jitter of ~ 1 ns and by the inter-PMT time equalization, which should be maintained at sub-nanosecond level and regularly checked. The accuracy of the time measurement is also crucial for α/β discrimination, based on the different fluorescence time profiles for α and β scintillation events (see chapter 4). An accurate energy determination and resolution are crucial for the spectral shape recognition of the neutrino signal: the energy resolution of the detector depends on good PMT charge calibration, the energy being determined, through a proportionality relation, from the number of detected photons.

The size of the detector, its tightness and radioactivity constraints require special care in the material selection and mechanical handling of the system. The solution of multiplexed fiber chains has been realized for the first time in a large underground detector.

7.1 System design

In the design of the calibration system for the time and charge response of the Borexino PMTs, the following requirements have been taken into account:

1. accuracy in time equalization: inter-PMT equalization inaccuracy should be contained within the PMT time jitter, which is ~ 1 ns;

2. accuracy in charge calibration: the system must illuminate all 2212 PMTs at the single photoelectron level in order to measure the Single Electron Response

(SER) parameters of each PMT. If we require less than 1% contamination from multi-electron pulses and from the dark noise accidental coincidences, the illumination level should be, respectively, lower than a mean value $\mu = 0.05\ p.e.$ and higher than $\mu = 0.01\ p.e.$ [33];

3. linearity check: the PMT illumination level should be adjustable, in order to verify the linearity of the PMT response. The value of $\sim 8.6\ p.e.$ per PMT corresponds to the saturation limit of the front-end electronics (in a 80 ns interval): higher intensity calibration source would allow non-linearity studies;

4. calibration rate: the PMT calibration should be performed at the fastest rate allowed by the DAQ system (a few kHz at an illumination level of $\mu = 0.05\ p.e.$), in order to minimize the duration of the measurement;

5. operational convenience: the system should allow a high level of automation for frequent use and must be operable from outside (a remotely controllable system meets also the requirement for a synchronization with the main electronics);

6. radioactivity: the contamination induced by the calibration system materials must not add a significant rate to the dominant (unavoidable) background generated by the PMTs;

7. long-term reliability, for at least 10 years of data taking.

Several alternative solutions were considered, that could suit the detector geometry consisting of consecutive shielding regions. The simplest method would be a light diffuser in the center of the detector (as in the SNO experiment [31]), illuminating simultaneously all the PMTs; though, a permanent diffuser would not be acceptable since it would represent a constant source of radioactivity in the innermost region, while a removable one would not allow for the easiness and safety of operation needed for frequent calibrations. Permanent light diffusers could be placed in the buffer region (as in the LSND experiment), or light beams could be generated by optical fiber couplers in the SSS; but in both these solutions the light would cross several meters of the buffer and scintillator regions, requiring off-line corrections to the light-pulse arrival time: the consequent dependence on the scintillator properties (such as index of refraction and attenuation length), which could drift in time, would compromise the calibration accuracy.

A preferable design would be one where the light is generated outside the active volume, to avoid internal contamination, and reaches the PMTs without crossing the scintillator but being transported via optical fibers. The basic concept of the system described here is thus a channel-by-channel calibration using the distribution of an external fast light pulse to all the PMTs through consecutive multiplexing of optical fiber bundles, split at the various detector interfaces as shown in figure 7.1, and following a criterium of mechanical decoupling of the internal/external regions to facilitate the mounting operations:

- air/water interface: a fast light pulse emitted by an external laser is focused onto a bundle of 35 external fibers 40 m long, running in the water buffer region;

- water/SSS interface: the 35 external fibers reach different locations on the sphere supporting the PMTs. Each single external fiber couples to a proper optical feed-through on the SSS itself;

- SSS/PC buffer interface: each feed-through is coupled to a bundle of 90 internal fibers 6 m long, running inside the SSS and reaching each single PMT.

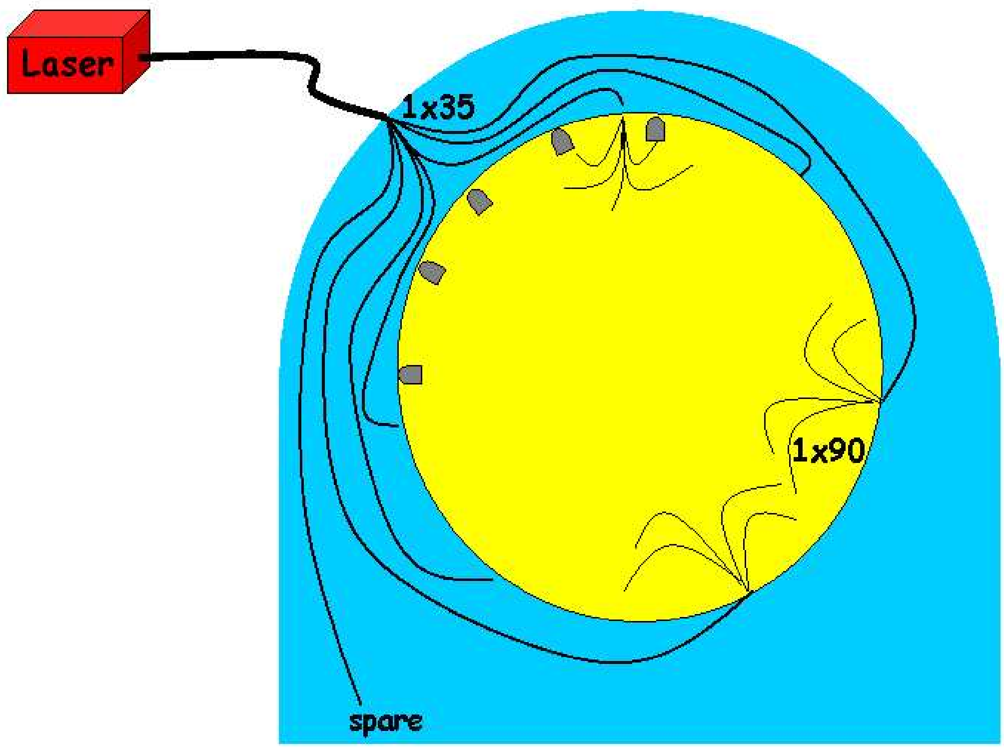

Figure 7.1: Scheme of the multiplexed system for PMT calibration.

7.1.1 Light source

The light source is a diode laser (*PicoQuant* LDH400), emitting a fast (50 ps time width) light pulse at a wavelength of 394 nm, where the photocathode quantum efficiency is about 27%. The maximum peak power is 400 mW, corresponding to 1.7×10^7 photons/pulse. The laser driver (PDL 800-B) allows a maximum repetition rate of 40 MHz (well above the maximum rate of the Borexino DAQ system) and can be triggered by an external pulse (to allow synchronization with both main electronics and DAQ); laser intensity can be selected by means of a potentiometer, which by design is only manually adjustable (an upgrade of the controller allowing remote setting of the intensity is under study).

The optical components associated with the coupling of the laser to the first segment of the calibration system consist of a series of neutral density filters for attenuation and a lens focusing the beam on the surface of a 2.5 mm diameter rigid quartz fiber that then distributes the light to the 35 fiber bundle. The lens is a $10\times$ standard microscope lens; focusing is necessary since the area of the laser spot (2×3.5 mm), is larger than the quartz fiber core. The rigid quartz fiber is 10 cm long and its numerical aperture is lower than the 35 fiber bundle area, for better optical transmission. The optical apparatus is mounted on a passive anti-vibration platform and enclosed in a light-proof stainless steel box; the laser controller can be activated from outside the box.

7.1.2 External fibers

The laser beam illuminates the fiber bundle of the first splitting point through a focusing lens and an optical rod that renders it uniform and wide enough to cover 35 quartz fibers. The diameters of the fiber core and cladding are, respectively, 300 and 325 μm. The fibers enter the detector through a single feed-through on the top

Figure 7.2: A bundle of 90 fibers connected to the feed-through and illuminated.

of the Water Tank. From then on they form separate cables, with Kevlar strands (for mechanical resistance) and a polyethylene coating, until they reach their entry points on the SSS. The PMTs are grouped in 28 clusters of about 80 elements and, for mounting reasons, the tubes installed on the 3 m main entrance door require an extra fiber bundle; the locations on the SSS are chosen as the central position of each PMT cluster. Six out of the 35 fibers will be spare.

7.1.3 Light-transmitting feed-through

A delicate part of the system is the feed-through on the SSS, since it must distribute the light from 1 input to 90 output fibers as uniformly as possible, while maintaining a high level of tightness against liquid diffusion between both sides of the SSS. The body and the connectors are made of electro-polished stainless steel, the sealing with the stainless steel flange is realized with a Viton *O-ring*. A quartz fiber, of length 10 cm and diameter 1.5 mm, is placed inside the connectors, optically coupling the PC and the water buffer side. The sealing against PC diffusion by capillarity near the fiber is assured by filling the inner part of the feed-through with a PC-proof, quartz-steel adherent epoxy resin.

7.1.4 Internal fibers

The second step of the multiplexed chain is formed by coupling the SSS feed-through to a bundle of 90 quartz fibers of 110 μm core diameter (figure 7.2). Taking into account the packing ratio of circles on a plane, 90 closely packed fibers with a diameter of 120 μm (cladding) occupy an area of 1.12 mm^2. The section of the 1.5 mm diameter fiber in the feed-through is 1.76 mm^2, thus a tolerance of 50% for non-optimal packing of the fiber bundle is achieved.

Both internal and external fibers, as well as the lens and clad rod used at the beginning of the optical path, have a quartz core, in order to optimize light transmission efficiency in the ultraviolet wavelength region. The cladding of the external fibers can be made of plastic, while the strong chemical reactivity of Pseudocumene determines the choice of quartz for the cladding of the internal fibers. This is one of the reasons for using Teflon for the coating of the internal cable; in addition, measurements carried out by the collaboration showed that Teflon has a very low rate of radon emanation. A Teflon support attached to the PMT light concentrator, points the fiber termination in the direction of the photocathode, at a 20 cm distance.

7.2 System feasibility tests

During the design phase, several tests were performed to guarantee the feasibility of the system for Borexino. On the one hand, the compliance of the system with the general requirements of the experiment in terms of radioactivity and chemical compatibility had to be verified and on the other, the total light transmission expected

Figure 7.3: An installed PMT: the optical fiber is visible, as well as the Teflon support attached to the light concentrator.

at the end of the chain had to be measured. The attenuation due to geometrical effects and fiber transmission can indeed be safely gauged from the a priori known fiber characteristics, while the inefficiency caused by losses at the optical couplings can only be measured in the final experimental conditions.

7.2.1 Radioactivity and chemical measurements

The radioactivity of the fibers, Kevlar, Teflon and the epoxy resin were measured using gamma spectroscopy; the radioactivity levels of the fiber material resulted to be comparable or lower than the values for the PMT glass. Since the fibers have a much lower total mass than the PMTs, the external background we expect from them is negligible. All the materials, immersed in Pseudocumene and subjected to accelerated ageing tests, did not manifest deterioration caused by the high chemical reactivity of Pseudocumene; the scintillator itself did not show any attenuation length variation. The mechanical tightness of the system was tested through a helium leak detector, that measured a leak rate at the level of 10^9 $mbar/l/s$, three orders of magnitude better than the general requirement set by the experiment.

7.2.2 Light transmission test: the two-liquid test tank

A prototype of the fiber chain was built to reproduce the full-scale system, both in terms of type and length of the fibers and materials for the cable and feed-through, and was installed in the Two-Liquid Test Tank (TLTT). It consists of two concentric cylindrical tanks with, respectively, 2.7 and 3.7 m diameter and 1.3 m height. The inner tank is filled with 7 t of Pseudocumene and the outer region with 6 t of ultra-pure water. The main goal of the TLTT was to test the most important technical aspect of the PMT construction, i.e., the sealing and its resistance to the chemical aggression of Pseudocumene over long periods of time. Owing to its large scale and working conditions similar to those of Borexino, the TLTT naturally became a facility to test other aspects of the Borexino design, in particular, the calibration systems. Photomultipliers, complete with $\mu-$metal shielding and fiber optics supports, are mounted in 49 of the 54 holes of the inner wall, with the body of the PMT immersed in Pseudocumene and the connector and cable in water. Three of the five remaining holes are used for the PMT calibration system test. A top view of the TLTT, during PMT installation, is shown in figure 7.4: the structure of the facility is clearly visible.

Tests in the TLTT make use of a laser, its associated optics and a prototype of the multiplexed optical fiber distribution system. Four fiber bundles were built according to the full-scale design, both in terms of fiber type (110 μm core diameter, quartz core, quartz cladding, teftzel buffer), cabling (Kevlar, Teflon), terminations and length (6 m). Three bundles with 28 fibers each were installed in the TLTT and the last one, having 90 fibers (as in full-scale design), was tested outside the tank to study light transmission uniformity (further details on the TLTT setup for the test of calibration system can be found in [33]).

7.2.3 TLTT results: time/charge calibration and uniformity

The time calibration parameters consist of time differences among the responses of all the PMTs to a common and simultaneous light pulse. Since there is a slight correlation between the charge and the PMT pulse rise time, an accurate time calibration should be performed at the typical illumination level of the experiment (the single photoelectron level). The time resolution of the single channel resulted to be about 1 ns for all channels, the same as the nominal time jitter of the PMTs, which means that the time spread due to the laser and fiber system is negligible, as expected.

The charge calibration procedure consists in finding the conversion factor between the measured charge on the channel and the number of detected photoelectrons. The centroid of the SER peak is the calibration parameter and can be calculated for all channels with a simple gaussian fit. Using this method, the illumination

Figure 7.4: Top view of the TLTT during the PMT installation.

level μ was also calculated for every channel and the average result was 1.5%: this is a low illumination level, expected from the low power laser, but still within the region required for the SER calibration.

Another critical parameter for a design with high number of optical fibers is the light uniformity. The calibration in Borexino will be carried out at the single photoelectron level; good uniformity is required to collect high statistics spectra for each photomultiplier in a reasonable dedicated time. The 90 fiber bundle prototype (internal fibers of 110 μm) was built and tested and the uniformity was measured to be of the order of 20%.

7.2.4 Assembled system results

The final calibration system has been mounted in Borexino detector and preliminarily tested. The total light transmission is measured to be $(4.2 \pm 1.4) \times 10^{-6}$, factorized in: $(1 \pm 0.3) \times 10^{-3}$ caused by the splitter of the 300 μm external fibers, $(77 \pm 4) \times 10^{-2}$ by the 29 feed-through and $(5.5 \pm 0.6) \times 10^{-3}$ by the second splitter of 100 μm internal fibers. As an example, figure 7.5 shows the light transmission of a typical 90 fiber bundle. The average of the light transmission of the best 80 fibers of each bundle is 5.5×10^{-3} and the standard deviation is 12%. The purely geometrical efficiency for the light transmission is 5.9×10^{-3}, so the fiber couplings present very few losses. The measured ratio between the transmission of the worst and best channels is about 0.5, which guarantees a good operation condition.

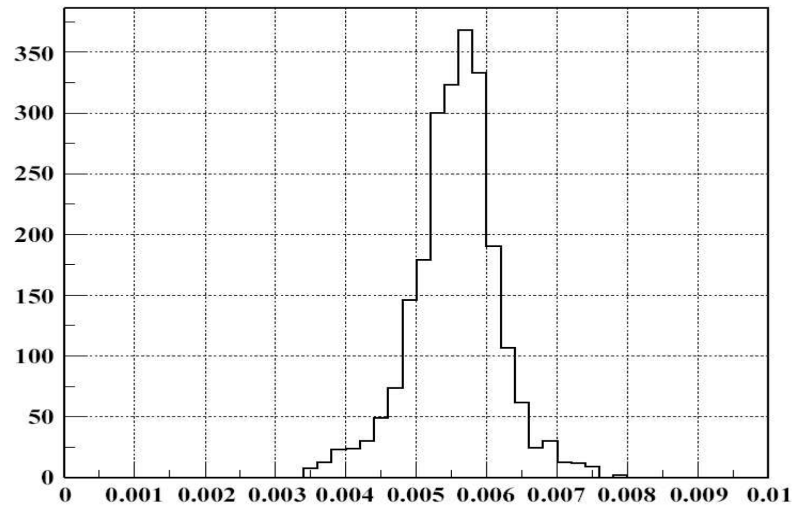

Figure 7.5: Fraction of transmitted light for each fiber in a 90 fibers bundle [33].

7.3 Test of the Borexino PMT calibration system

In August 2002, several data were taken with the 1993 PMTs installed in Borexino sphere, with high voltages on, by means of the PMT laser calibration system. This period of data taking has been a good test for the trigger and for the electronic systems and allowed an accurate debugging of the time reconstruction algorithm described in section 6.2, since the synchronous events provided by the laser timing system are a natural test of its efficiency. A PMT timing calibration test was performed and the applied time equalization algorithm was found to reduce the time spread of the whole detector to its theoretical value. Finally, the laser data could be used for a very preliminary estimation of the Stainless Steel Sphere reflectivity.

7.3.1 Description of the calibration data

As already mentioned in section 5.2.4, during normal data taking the laser system will be run with an external trigger. A NIM timing unit, placed in the trigger rack, automatically delivers a programmable rate of pulses to the Borexino Trigger Board; if the laser condition is disabled the BTB simply ignores these external inputs. Otherwise, not only the trigger signals, but also the driving signal that enables the laser light pulse, are generated. To allow a precise measurement of the time delay between this laser pulse and the arrival time of the light on the PMTs, a copy of the signal is sent to a dedicated Laben channel[1].

The run conditions of the AirRun4 data were the following:

- trigger either from TABs sum, with thresholds of $30 \div 40$ PMTs in trigger, or from an external trigger;
- timing laser system turned on, laser intensity 5;
- timing laser system triggered by an external pulse: single and double pulses (with variable delays: 0.5, 0.8, 1, 1.5 μs) and 100 Hz rate.

The time reconstruction algorithm used in the off-line code is quite complex (see section 6.2). Some non linearities and non ideal behaviors of the Laben boards forced us to develop a pre-decoding routine: a first pre-analysis of the raw data is needed to align the electronics; the synchronous events delivered by the time equalization system to the whole detector are a natural test of the precision of the method.

The typical plot of the difference between the reconstructed time of the laser signal and of the light pulses on the PMTs, summing over thousands of events, is shown in figure 7.6, for double pulse events. These plots show clearly the pattern of the 7 μs trigger gate, populated with the hits due to the constant and uncorrelated random noise of the PMTs, and the two light pulses, 1 μs delayed, of the double laser trigger.

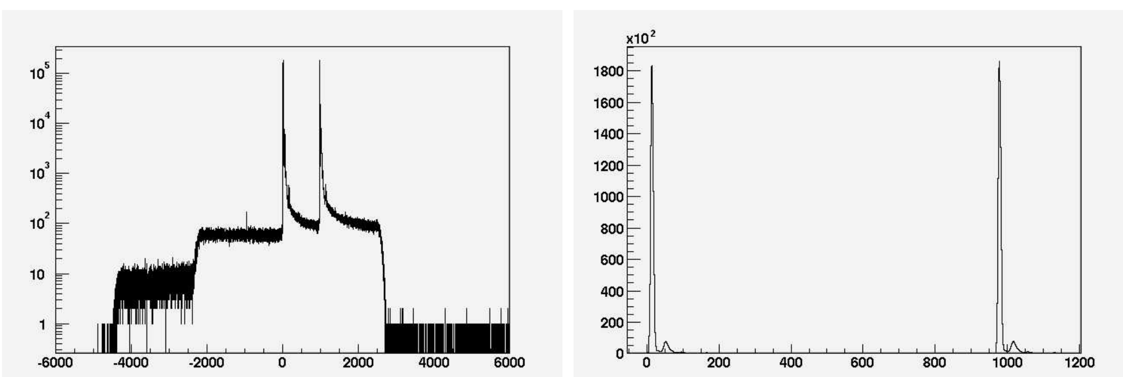

Figure 7.6: Time difference between the laser pulse and the light collected on all the PMTs, summing on about 40000 double pulse events, in logarithmic (left) and linear (right) scale; $x-$scale is in ns (time scale is zoomed in the right plot).

Looking more in detail (figure 7.7), each light pulse shows a complex structure: in the logarithmic scale at least three peaks, about 41 ns delayed, are well separable.

[1]About ten channels of the whole electronic system have been devoted to sample the time of the trigger and of the laser signals; this allow us to avoid the jitter time of the trigger and to have, event by event, very precise time reference values.

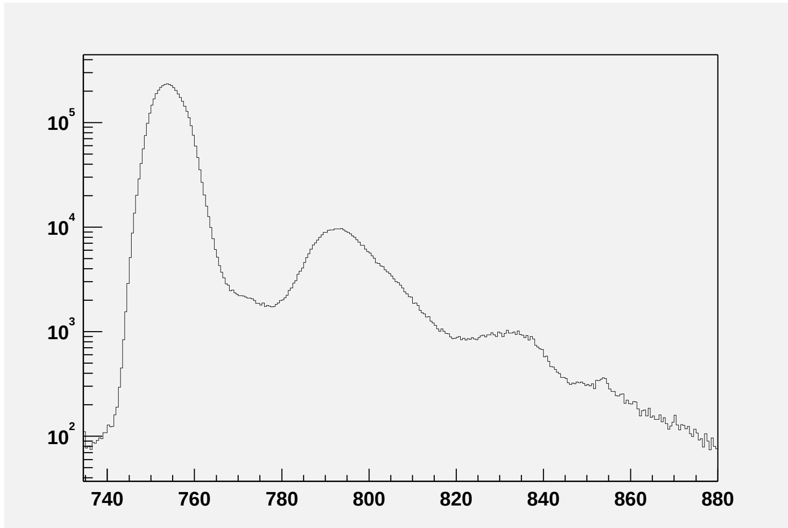

Figure 7.7: Zoom on the single laser pulse, in logarithmic scale ($x-$scale is in ns).

The first peak is obviously the direct light peak; its width gives an estimation of the time spread of the detector, before any calibration: the sigma value of the gaussian fit of the peak is lower than 4 ns (figure 7.8).

The second peak in figure 7.7 is due to the light reflection on the photocathode: a small fraction of the photons can be reflected on the PMT glass and detected by the PMTs on the opposite side of the sphere. This is confirmed by the time delay between the two peaks, about 41 ns, which is consistent with the distance between the center of the sphere and the photocathodes: the ratio between the areas under these two peaks can be, therefore, a rough estimation of the photocathodes reflectivity. In the same way, the third peak features the second reflection of the reflected photons: since these photons can be reflected both from the photocathodes and from the sphere, the ratio between the two peak is related to the overall detector's reflectivity.

7.3.2 The time calibration algorithm

As shown in figure 7.8, the direct light peak has a narrow time spread (about 4 ns); nevertheless, the inter-PMT time equalization must be improved through an accurate time calibration of the detector. The time calibration constants are calculated using the single time spectra of the PMTs illuminated by the synchronous light pulses of the timing system; the computed constants are then treated as systematic shifts in the reconstruction code.

The routine to compute the time calibration constants is a part of the general event reconstruction package: it has to be enabled with a proper configuration (preventing unauthorized update of the data base tables) and can be run only on

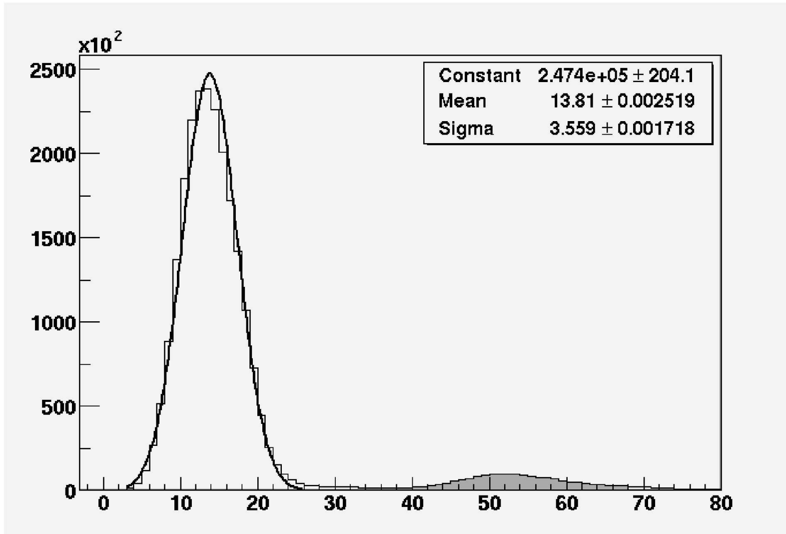

Figure 7.8: Gaussian fit of the direct light peak, summing on all the 1993 PMTs, before any calibration: the time spread on the whole detector is less than 3.6 ns.

high statistics timing laser data. Actually, in order to keep the calibration strategy as flexible as possible and to have a run-time monitor of the detector, a small rate of laser events is foreseen even during normal data taking; but these events have a very low rate and the real calibration constants should always be computed using dedicated laser runs.

During data processing only the events tagged as laser events are decoded: 2240 single channel histograms are filled with the difference between the time of the laser pulse and the time of the hits. The typical time distribution histogram obtained for the single PMT is shown in figure 7.9.

All good PMTs show a similar behavior: a constant and low background in the whole gate window, a sharp central peak in coincidence with the direct laser pulse and a much smaller peak, the reflected light peak, about 41 ns later. In order to exclude the reflected light from the gaussian fit of the direct light, the selected fit range is a ± 20 ns interval around the central value. The typical widths of the obtained gaussian fits are between 1.2 ns and 1.6 ns, very close to the PMTs jitter times (see chapter 5). The time spread due to the laser and fiber system is therefore negligible, as expected.

At the end of computations, the obtained gaussian mean values are written in a dedicated table of the "bx_calib" Data Base and, when a normal run is reconstructed, these calibration parameters are read from the table and added as constant shifts to the hit time of each PMT.

The calibration code has been set-up and tested with the AirRun4 timing laser data: the very first run has been used to compute the calibration parameters and fill the Data Base table; then the following runs were reconstructed using the computed

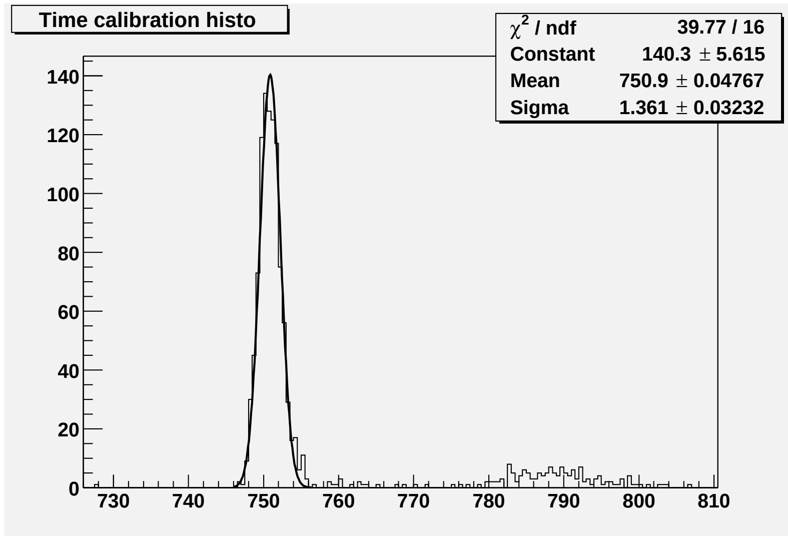

Figure 7.9: Typical time distribution for a single PMT, illuminated with the timing laser calibration system.

calibrations. Figure 7.10 shows the comparison between the width of the direct light peak before and after the calibration procedure: from the starting point of $\sigma = 3.6\ ns$, we finally obtain the excellent result of $\sigma = 1.6\ ns$. Since the mean PMT jitter time is about 1.1 ns and the intrinsic resolution of the time reconstruction algorithm is about 1.2 ns (see chapter 6): this value matches exactly the theoretical resolution expected from the squared sum: $\sqrt{(1.1)^2 + (1.2)^2} \sim 1.6\ ns$.

7.3.3 Status of the detector

The timing laser data are very useful to test the general status of the detector: channel-by-channel, it is possible to check the whole chain from the PMT and optical fiber to the electronics and data acquisition. In August 2002, the status of the detector was the following: 1862 PMTs out of the 1993 installed had high voltages on (64 PMTs from the upper hemisphere had been un-cabled in order to allow some works in the water tank, while the remaining 67 PMTs had been temporarily turned off because they needed further checks). Among these 1862 PMTs, 1686 have been successfully calibrated, while the remaining ones show different problems:

- 85 channels had electronics problems (on Front-End or Laben boards). Most of these channels were connected to a small number of boards, so the great part of them have been fixed in a few months after the AirRun4;

- 12 PMTs are suspected to be dead, since they give no signal. Following Air-Runs allowed deeper tests and checks of their status;

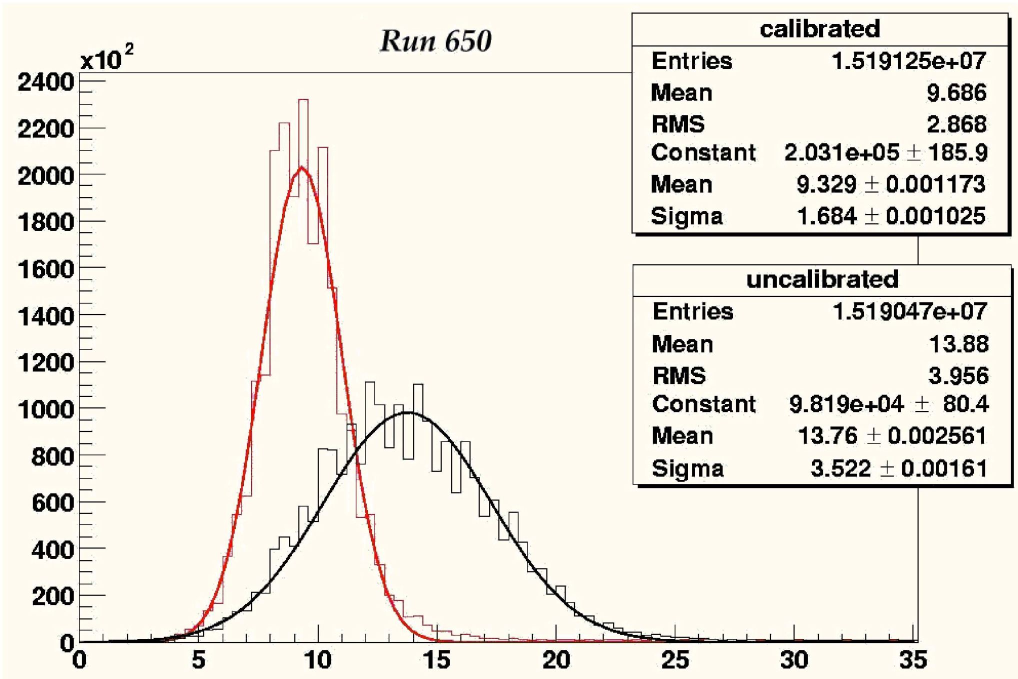

Figure 7.10: Time distribution for the whole detector illuminated by a timing laser pulse, before (red) and after (black) the time calibration.

- 79 PMTs have problems with the laser fiber: they clearly do not receive any light from the laser. Luckily, 40 of them belong to the same fiber cluster, that was disconnected from the light source during some works in the water tank: therefore, the real fiber problems to be further investigated regards only 39 PMTs.

Figure 7.11 shows the typical time distribution for a PMT with no direct light (the fiber belongs to the disconnected cluster): the light peak, compared to the standard situation (see figure 7.9) is about 41 ns delayed, while the statistics is much lower. The PMT is clearly not illuminated by its own fiber, but it sees the light reflected from the photocathode of the PMTs lying on the opposite side of the sphere. These PMTs have been excluded from the timing calibration routines, otherwise a time offset of about 41 ns would have been added to their hits; the exclusion algorithm is based both on the total rate on the PMT (which is much lower than in case of directly illuminated PMTs) and on the average value of the hits time (which is at least 30 ns delayed with respect to the other channels).

7.3.4 Rough estimation of the SSS reflectivity

We already mentioned and showed the different reflected-light peaks which are visible in the typical time distribution for the whole detector illuminated by a timing laser

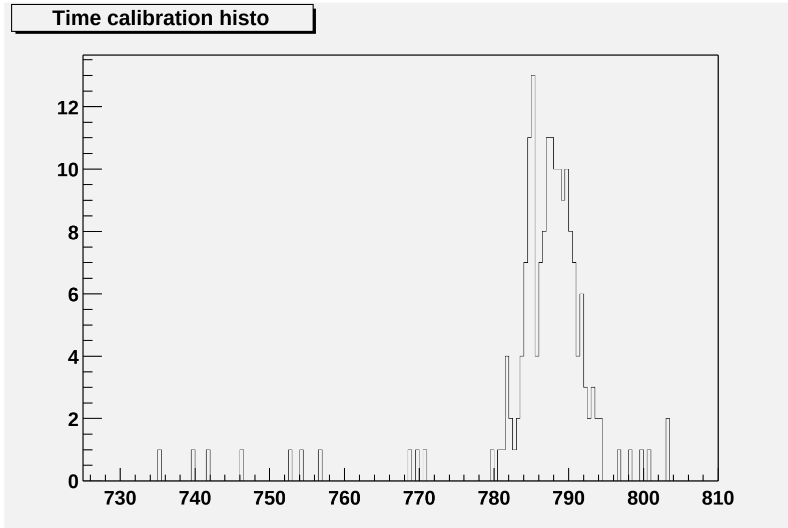

Figure 7.11: Typical time distribution for a single PMT which does not receive direct laser light, but only reflected light (direct peak should be at $\sim 750\ ns$).

pulse. From these data we can attempt a very preliminary and rough estimation of the reflectivity value of the Stainless Steel Sphere: actually what we can estimate is not the direct SSS reflectivity, but the integrated reflectivity, that means both the SSS and the photocathodes contributions.

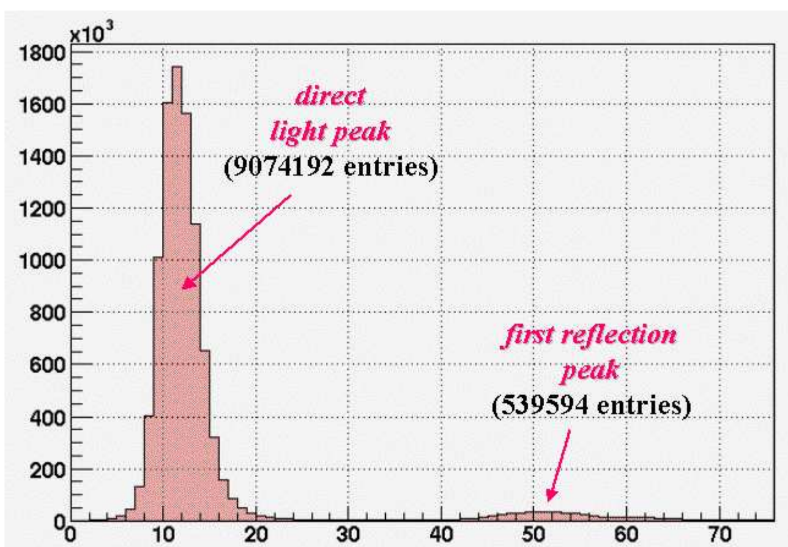

Figure 7.12: The direct light peak and the first reflection peak, obtained with the AirRun4 timing laser data (linear scale).

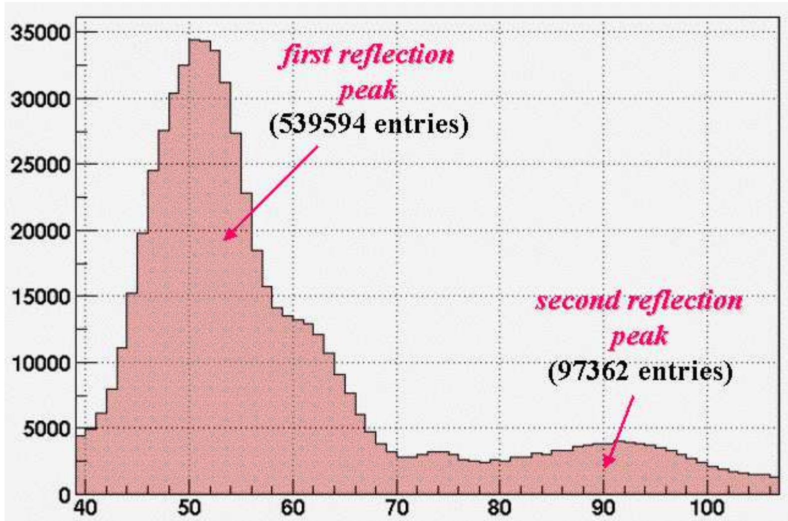

Figure 7.13: The first and the second reflection peaks obtained with the AirRun4 timing laser data (linear scale).

Since the fiber terminations point directly to the photocathode, the first reflected peak is due only to the reflectivity of the PMT glass. This is a known value and the ratio between the direct light peak and this second peak can be used only as a consistency test: the ratio of the number of entries under the second and the first peaks is about 10 %, and this is consistent with the photocathode reflectivity value measured in the laboratory.

More interesting is the ratio between the second and the third peak. As already explained, this ratio should give an estimate of the overall detector reflectivity, averaging both the photocathode and the sphere contributions. With the same technique used before, that is evaluating the ratio of the areas under the two peaks, we obtain a reflectivity value of about 20 %. This method is obviously too trivial to estimate a precise and reliable reflectivity value, but we can exclude with a certain confidence reflectivity values greater than $30 \div 40\%$.

7.4 Calibration test of the complete detector (AirRun9)

Laser calibrations have been run in all the Borexino Air-Runs (see chapter 6); in this section, the test with the complete detector (2212 installed PMTs) will be described.

In the AirRun9, many laser data have been acquired, with the aim to check both the newly installed PMTs and the whole read-out chain. Several runs have been taken with different laser intensities, in order to study the dynamics of the Laben electronics at high energies (above 1 MeV); in the meanwhile, the same study was performed with Flash-ADC electronics (see chapter 8), in order to compare the performances of the two systems.

At the beginning of data taking, an accurate study of the PMT illumination conditions has been preformed, in order to define the optimal laser intensity for calibrations, meeting both the single photoelectron condition and a reasonable duration for the measurement. A special "mixed" run, with both laser and "random" (dark noise) events, was taken at a laser intensity 4.5 (on the potentiometer scale), with the aim of evaluating the separate contribution of the laser light and of the dark noise to the signal of each PMT; the result of the run is shown in figure 7.14, where the number of hit PMTs per event is displayed, for random and laser triggers.

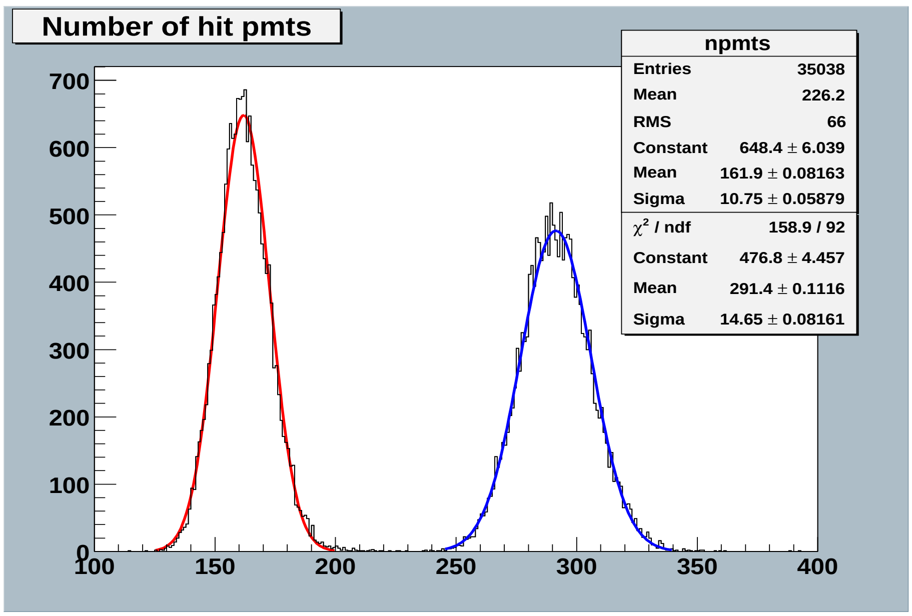

Figure 7.14: The random noise (red) and laser (blue) contributions to the number of hit PMTs in each event.

The pure dark noise contribution has a mean value of $\mu = 162$ PMTs, while the laser events show a mean hit PMT number of $\mu = 291$; from these numbers, the pure laser contribution yields: $\mu \simeq 130$ hit PMTs, corresponding to a PMT occupancy of 5.8%. Under the Poisson hypothesis (in these conditions, $\mu = 6.0\%$), the probability for a PMT to receive more than one *p.e.* in a single event ($P_{>1}/P_1$), is lower then 3%, therefore the single *p.e.* condition is reasonably fulfilled. On the other hand, a further decrease in laser intensity would not improve very much the measurement, because the random noise and laser contributions would become closer, and the laser peak would suffer from significant dark noise contamination.

The conclusion of this first measurements sequence is that a "nearly optimal" intensity for the laser is about 4.5, in case of standard timing calibrations.

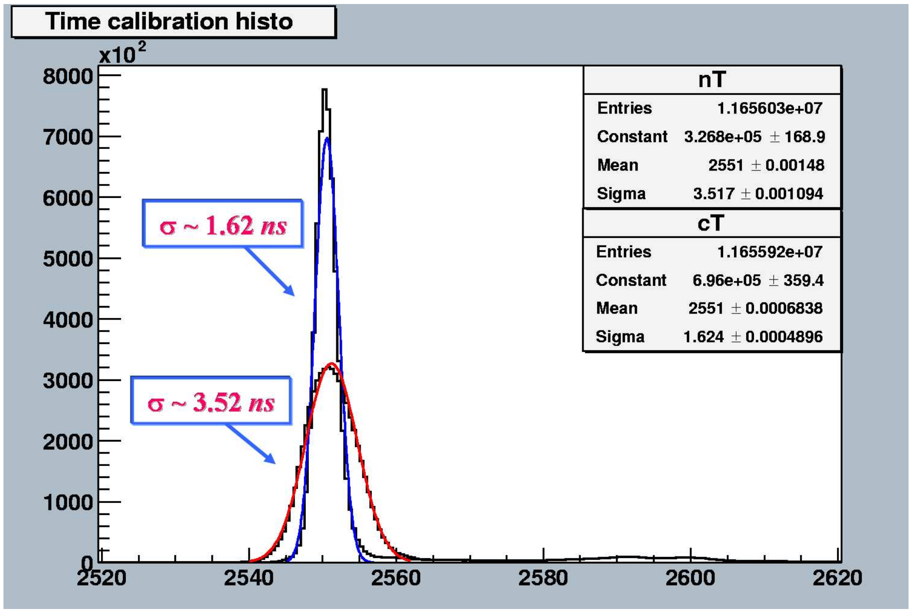

Figure 7.15: Time distribution for the whole detector illuminated by a timing laser pulse, before (red) and after (blue) the time calibration.

7.4.1 Time calibration results

Once determined the "optimal" illumination condition for PMTs, a new timing calibration test has been performed, with the aim of checking the performances of the procedure for the completed detector, as well as to measure the overall time resolution of the 2212 installed PMTs.

Results are shown in figure 7.15: the global detector resolution before time alignment procedure is 3.5 ns, while after timing calibrations the resolution is enhanced to 1.6 ns. These numbers confirm the previous results (AirRun4): this confirmation is a good result in itself, since the $\sim$ 220 newly installed PMTs had never been tested before in SSS (as well as their channels, HV supply, etc.); actually, all the detector (including the last installed 10%) shows similar timing performances.

In figure 7.15, is also possible to notice a decrease of the reflected peak, with respect to the previous conditions (see figure 7.8): the amount of light detected in the reflected peak is $\sim$ 5% of the direct peak. This reduction can be explained thanks to the presence of the Nylon Vessels, that have a refraction index significantly different from the air, which induces scattering and diffusion processes on the photons.

The main software improvement introduced during the AirRun9 is an upgraded calibration procedure for the PMTs which receive a very weak (but not null) laser signal: for these PMTs, the reflected light peak is larger than the direct one, therefore the standard algorithm would calibrate them on a $\sim$ 41 ns delayed pulse. The new procedure requires a special run, with higher laser intensity (in order to increase

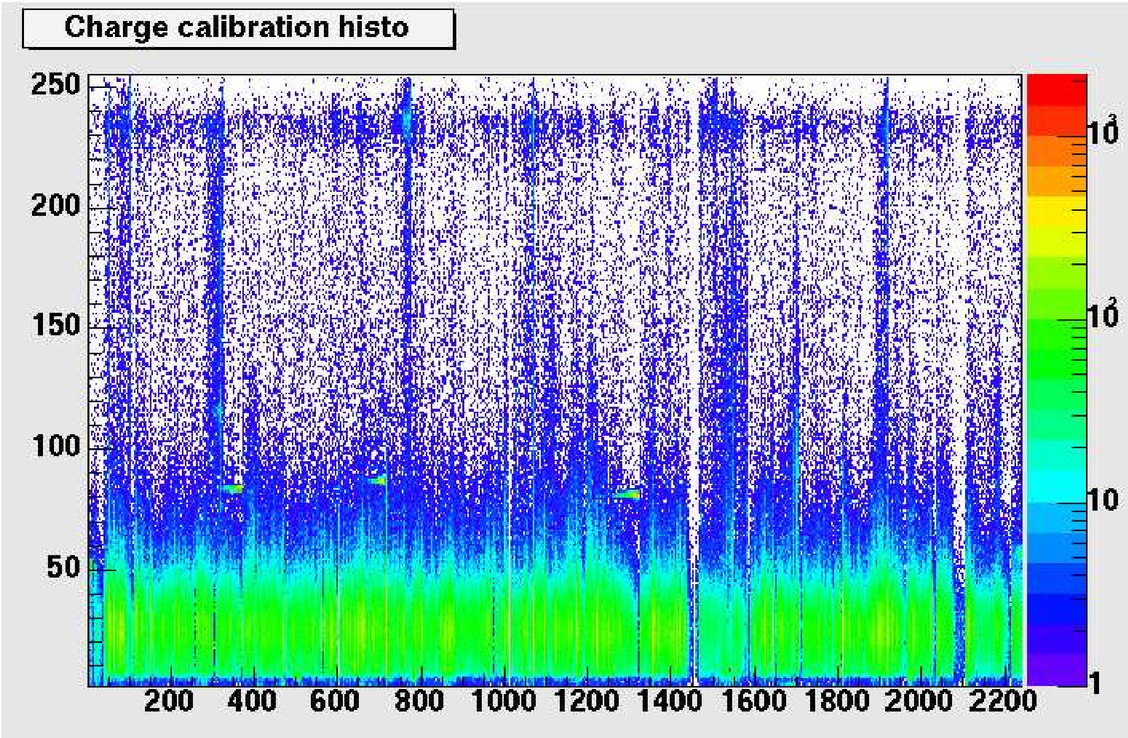

Figure 7.16: Charge spectrum (in ADC units) versus the channel number, before any calibration: the charge peak is represented by the green band, which is uniformly distributed on the whole detector.

statistics in the direct light peak); then a new fitting procedure computes the time alignment constants, discarding the reflected light and fitting the direct peak only: with this procedure, it was possible to “recover” 39 out of the 71 the PMTs showing illumination problems, that is to say that these channels were correctly calibrated.

7.4.2 Charge calibration routine

The charge calibration procedure consists in finding out, for each channel, the single photoelectron peak position in ADC units, that is to say the right conversion factor from the ADC information to the number of detected photoelectrons.

The charge calibration algorithm was first set-up during the AirRun7 (August 2003), after the fixing of an electrical problem on Front-End boards that prevented a correct behavior of the charge measurement (see section 6.3). Here only the results on the complete detector (AirRun9) will be reported, for simplicity purpose.

In figure 7.16, is shown the scatter plot of the detected charge (in ADC units) for laser events versus the channel number in the detector, before any calibrations; this spectrum was measured in a standard timing laser run with intensity 4.5. It is easy to notice that the position of the charge peak is quite uniform on the whole detector (if compared to the width of such a peak). The alignment of the non-calibrated charge spectrum is actually due to the very accurate setting of the PMT gain: this means that the first step of the charge calibration procedure consists in an appropriate setup of the PMTs (for this reason, the automated control of the High Voltages is crucial, as explained in section 5.3).

The ideal single photoelectron charge spectrum (on a single channel) is shown in figure 7.17 (left): this plot corresponds to a pure dark noise condition, realized during a special PMT test by means of light-proof plastic bags covering the PMTs; in this case, the single channel threshold was very low and the whole charge spectrum was detected. In the figure, the spectrum is fitted with a gaussian and an exponential: the gaussian component corresponds to the thermionic emission on the photocathode (equivalent to a single *p.e.* spectrum), while the exponential component takes into account the thermionic emission on the PMT dynodes. In real Borexino conditions, the single channel threshold is higher, therefore the exponential contribution is cut away (figure 7.17, right).

This suppression of the exponential component actually simplifies the calibration procedure, since the single channel spectrum can be easily fitted with a gaussian function (this holds in real single photoelectron conditions: otherwise, the fit should take into account the contribution from the second and third photoelectrons). The use of a very simple fitting function is a big advantage when an automatized calibration procedure is set-up: even in case of low statistics channels, it is possible to

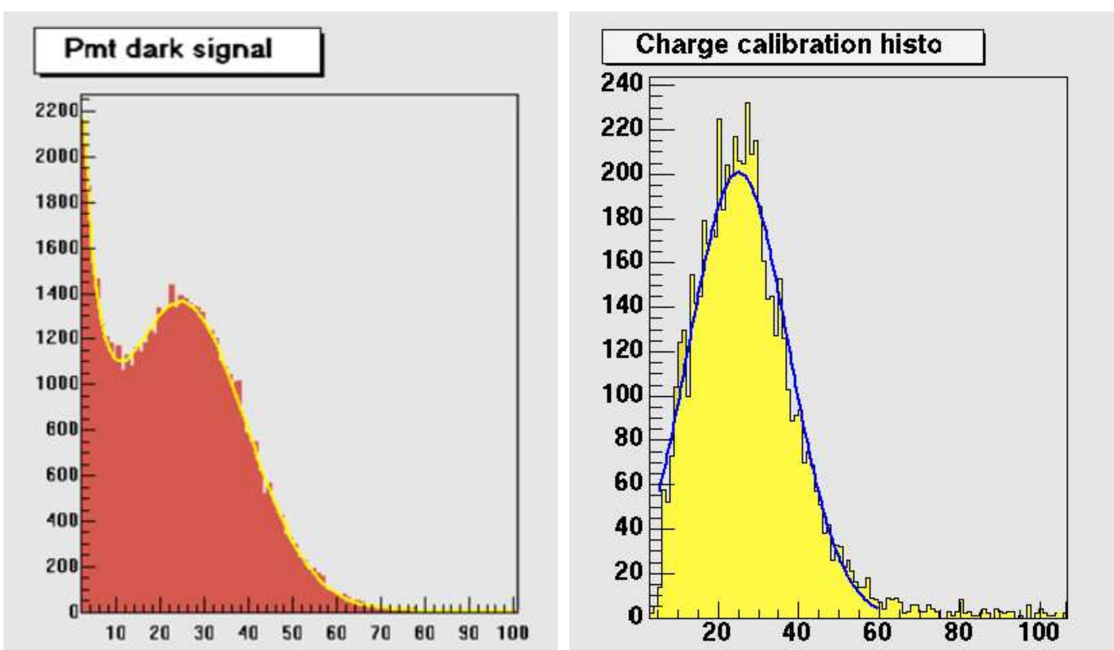

Figure 7.17: Charge spectrum (in ADC units) with different channel threshold conditions: very low threshold (left) and in normal Borexino threshold condition (right).

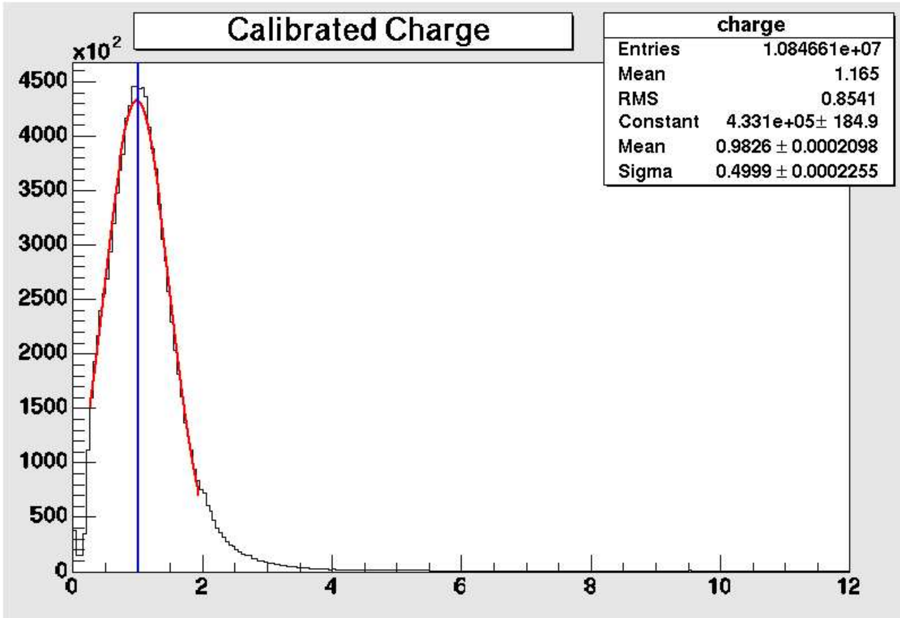

Figure 7.18: Overall charge spectrum on the detector, after calibration; only the first photoelectron peak is fitted: central value of the peak is located at ~ 1 *p.e.*.

get reliable results, without the need for manual intervention.

As usual, charge calibration parameters are computed using a dedicated laser run (a standard timing laser run, with intensity 4.5). After the computation of the parameters, they are written in Data Base, and are available for data reconstruction. The global charge spectrum on the whole detector, after the calibration, is shown in figure 7.18: the charge in each event has been converted into the number of photoelectrons and the central value of the peak is located at ~ 1 *p.e.*.

7.4.3 Status of the detector

During the AirRun9, the measurement of the detector status was somewhat complicated, because 5 entire fiber clusters were disconnected for technical reasons (related to installation works in the Water Tank); therefore, the irregular illumination conditions of the PMTs did not allow a very reliable study of their status (see figure 7.19).

In this case, the electronics and PMTs must be analyzed separately: electronics is checked by means of the pulser events (see section 6.2), while PMTs are studied using the results of the charge calibration procedure. In fact, in spite of what happens for the time calibration, the charge information can be successfully exploited even if a PMT does not receive enough direct light, because the light reflected on the opposite PMT's glass has the same charge spectrum than the direct one.

Combining all the available informations, the status of the 2212 installed PMTs is the following:

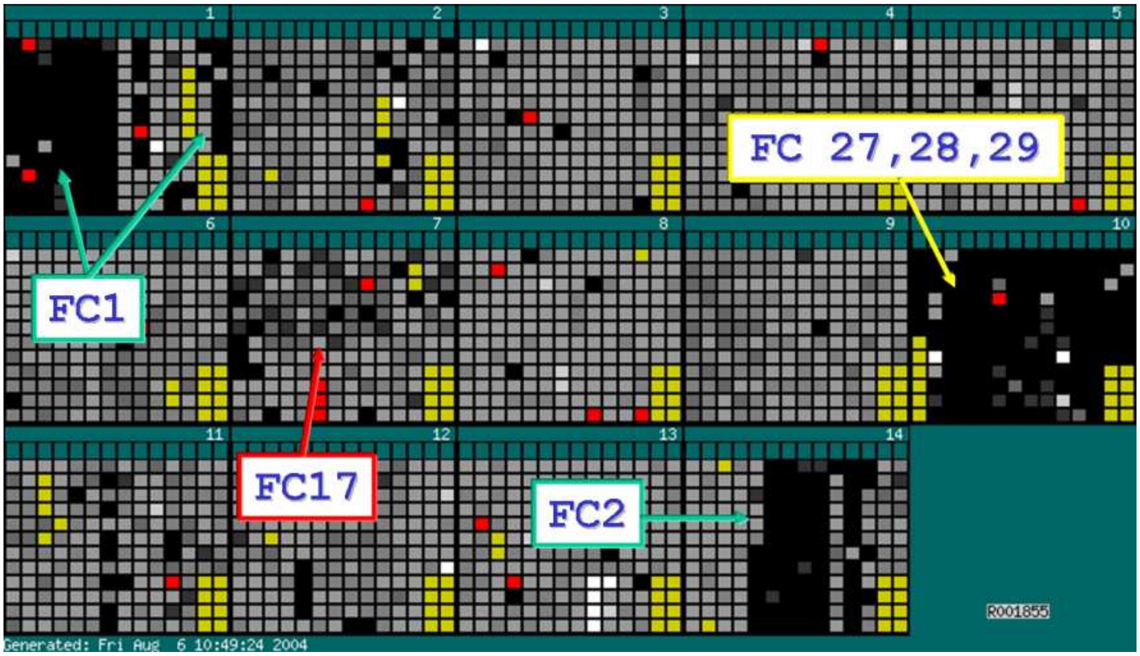

Figure 7.19: Single channel countrate during an high intensity laser run, in a Front-End map presentation, as displayed by the On-line Monitor (see section 5.3): the large dark zones correspond to PMTs illuminated by a disconnected fiber cluster (FC 1, 2, 27, 28, 29). The channel zone corresponding to cluster 17 is also labelled, because this fiber is the less efficient one in light transmission; the other (small) dark zones correspond to disconnected or dead PMTs, whose channels receive only the pre-calibration events. Finally, yellow and red spots represent respectively not installed PMTs (channel number is redundant) and dead electronics channels.

- 55 channels had electronics problems (on Front-End or Laben boards): 20 channels looks electrically dead, 20 show problems on time measurement and 15 give a bad charge information. The electronics status looks significantly improved, with respect to the AirRun4 situation, thanks to an intensive repair work accomplished before this run; of course, this debugging job will continue until all the channels will be fixed;

- 30 PMTs are either disconnected (20) or suspected to be dead (10), since they give no signal. Also the PMT situation is drastically improved since the AirRun4 period ($\sim$ 80 PMTs were classified as "probably bad" and disconnected): this improvement is due to a very accurate checking work on the PMTs, which allowed to recover many of them (mostly via a better setting of the HV operating condition);

- the number of PMTs with illumination problems is the most critical issue (due to the disconnected fiber clusters): excluding the 5 unplugged fibers, 30 PMTs does not receive enough light for timing calibration, when an high intensity run is performed (see above), while all the "alive" PMTs can be successfully calibrated in charge, exploiting the reflected light.

7.4.4 Charge saturation study

The last measurement performed in the AirRun9 was a scan in laser intensity, with the double purpose to recover weakly illuminated channels for timing calibrations (see above) and to study saturation effects on Front-End channels (the linearity on Front-End channels is guaranteed up to ~ 8.6 *p.e.* per event in an 80 *ns* window [66]).

The study of the detector dynamics by means of Laser events is somehow misleading, because the saturation effects does not depend only on total event energy, but also on its position inside the detector: if the event happens in the SSS center, the emitted photons are supposed to be uniformly collected on the surrounding PMTs; but for events close to the Inner Vessel, the closest PMTs will receive much more light than the farers ones (for a simple geometrical reason): therefore, in case of high energy events, the closest PMTs will undergo a bigger saturation effect than the farers ones; thus the saturation behavior will differ significantly from the case of events in the SSS center.

Laser events simulate real scintillation events located in the SSS center, because the laser light emission is uniformly distributed in the detector; nevertheless, extrapolation to an uniform events distribution is not completely unreliable, because the position reconstruction of the single event will allow to correct saturation effects on close PMTs, for events far from the detector center.

The scan in laser intensity was performed at different points: up to a laser intensity of 5.65, no charge saturation effect is visible on the Front-End channels; this intensity corresponds to a reconstructed charge of ~ 1600 *p.e.*: therefore, it

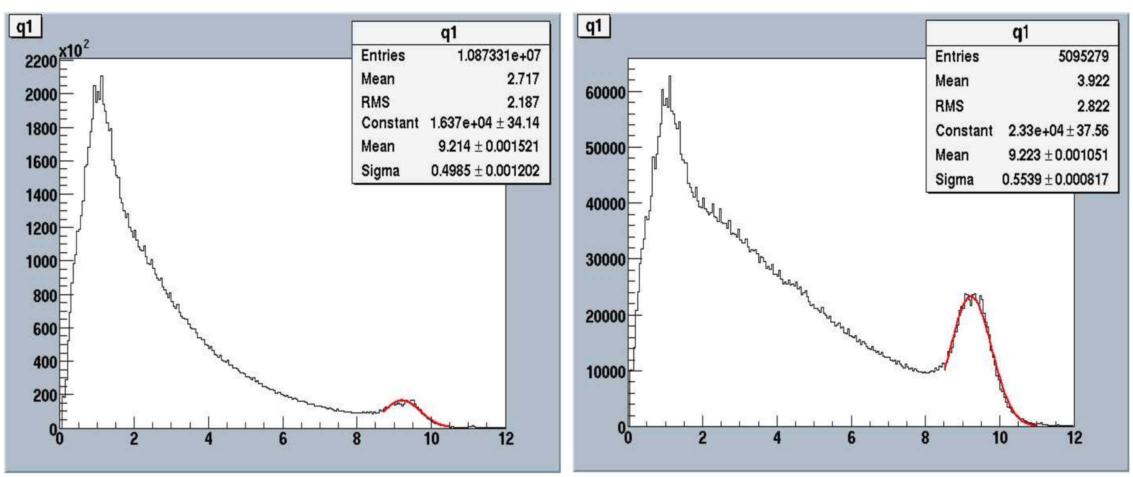

Figure 7.20: Charge spectra for high intensity laser runs: 5.75 (left) and 6 (right).

would be the saturation condition of an event at the SSS center, with an energy of 4 MeV (assuming a total light yield of 400 $p.e./MeV$). At the following intensity step (5.75) a small saturated peak appears (see figure 7.20, left), accounting for 3.6% of the hits; in this case, the reconstructed charge (without saturation correction) is $\sim$ 3900 $p.e.$, corresponding to a 9.7 MeV event at the SSS center. Finally, the laser intensity 6.0 was tried: in this case, 11% of the hits show a saturated charge (figure 7.20, right); the total reconstructed charge is $\sim$ 6650 $p.e.$ (without saturation correction), corresponding to a 16.8 MeV event in the detector center.

The energies of coincidence events in the NC and CC reactions on ^{12}C in scintillator from Supernova Neutrinos (section 3.2) are respectively 15.11 MeV (NC) and 13.37 MeV (CC, from $\bar{\nu}_e$) or 17.34 MeV (CC, from ν_e); these very preliminary saturation results allow to conclude that a reconstruction of event energy is possible for events up to $18 \div 20$ MeV (applying saturation corrections and reconstructed position extrapolations): therefore, in case of an high intensity supernova event, it will probably possible to distinguish the NC from the CC events.

Chapter 8

The high energy read-out system

The main acquisition system of Borexino has been designed and optimized for the detection of low energy neutrinos in the sub-MeV range, which are the main scope of the experiment.

As described in chapter 3, some interesting physics lies above this range, from the few MeV region (anti-neutrinos from reactors and from the earth's interior), up to the $\sim 15 \div 20$ MeV range (end point of the solar ^{8}B neutrino spectrum, CC and NC reactions on ^{12}C from supernova neutrinos).

Concerning the energy measurement in the 15 MeV range, some preliminary tests of the "solar neutrino" read-out system showed very encouraging results, as described in section 7.4: the limited amount of saturated channels in each event should guarantee the possibility to reconstruct the event energy in all the interesting interval.

Nevertheless, the energy measurement in the low energy spectrum is redundant, because in the single photoelectron regime (almost always valid in the sub-MeV region) the charge information can be integrated by a simple hit counting, allowing a cross check of the measurement. A similar redundancy would be desirable also in the higher energy range, where the hit counting information is no more reliable. In principle, a redundant read-out system in which no saturation correction has to be applied to events up to 20 MeV, would fit all the possible requirements.

A system based on phototubes clustering and waveform recording has been implemented, with the aim to cover at least the $1 \div 10$ MeV range. The phototubes are summed by groups of 24, and each of these 98 sums is recorded by a 400 MHz waveform digitizer.

The main physical interest in registering the full waveform of each event relies on the possibility to exploit the time shape information of the event for a pulse shape discrimination analysis (some application of the PSD techniques for α/β discrimination in CTF are described in section 4.2). In the single photoelectron regime, the pulse shape of each event can be reconstructed in the Laben system using the arrival time information for the single hit. In the high energy range, this information is not more available in the Laben electronics, since only the first hit in each channel will have its arrival time acquired.

A system based on waveforms recording, will provide the entire time evolution of the high energy signals: this will allow to perform PSD analysis in the whole energy range covered by the system. This information will be very important for the correct identification of anti-neutrino events from reactors and from the Earth's interior, since it will allow to tag the coincidence between the emitted e^+ and the delayed 2.2 MeV γ-ray (produced in the n capture). Moreover, the PSD discrimination will be crucial for the correct identification of the different reactions produced in a supernova event: $\bar{\nu}_e - p$ scattering will be identified trough an $e^+ - \gamma$ coincidence (with $E_\gamma = 2.2\ MeV$); the CC events trough an $e^+ - e^-$ coincidence (with $E_{e^-} = 13.37\ MeV$ for $\bar{\nu}_e$ capture and $E_{e^-} = 17.34\ MeV$ for ν_e capture) and the NC events will be tagged trough the identification of the 15.11 MeV γ.

8.1 Set-up of the sums acquisition in Borexino

The choice of a system based on phototubes clustering comes from the consideration that in the high energy range the single photoelectron information is not needed for energy reconstruction: therefore, there is no reason to record individually each of the 2200 signals. Moreover, the complete acquisition of 2200 channels would actually duplicate the existing system, and would be rather over-dimensioned if compared to its purpose.

In the implemented system, the signals from the photomultipliers are summed by solid angle sectors: in this way, we reduced the number of acquisition channels but not the precision of the energy measurement.

Each module of the Front-End electronics provides a sum of the fast signals of its 12 channels, obtained by a resistor network: this sum output has been designed to have a wider energy range than the sum of the 12 single channel outputs, that is to say it is designed to increase the maximum detectable energy.

A set of analog adders, active and passive, is used to build from these sums 98 groups of 24 phototubes, plus the total sum on the whole detector: these 99 channels are all recorded by fast waveform digitizers.

8.1.1 Summing devices

As just reminded, each Front-End board provides amplification and shaping for 12 channels and features a sum of these 12 amplified signals. A specific amplification device has been built to make various combinations from these sums:

- sum of 2 inputs, to build sums of up to 24 phototubes;
- sum of 8 inputs, to contribute building a total sum, which is used for triggering.

The gain of each sum is adjustable between 3.5 and 7 to fit to the range of the fast waveform digitizers.

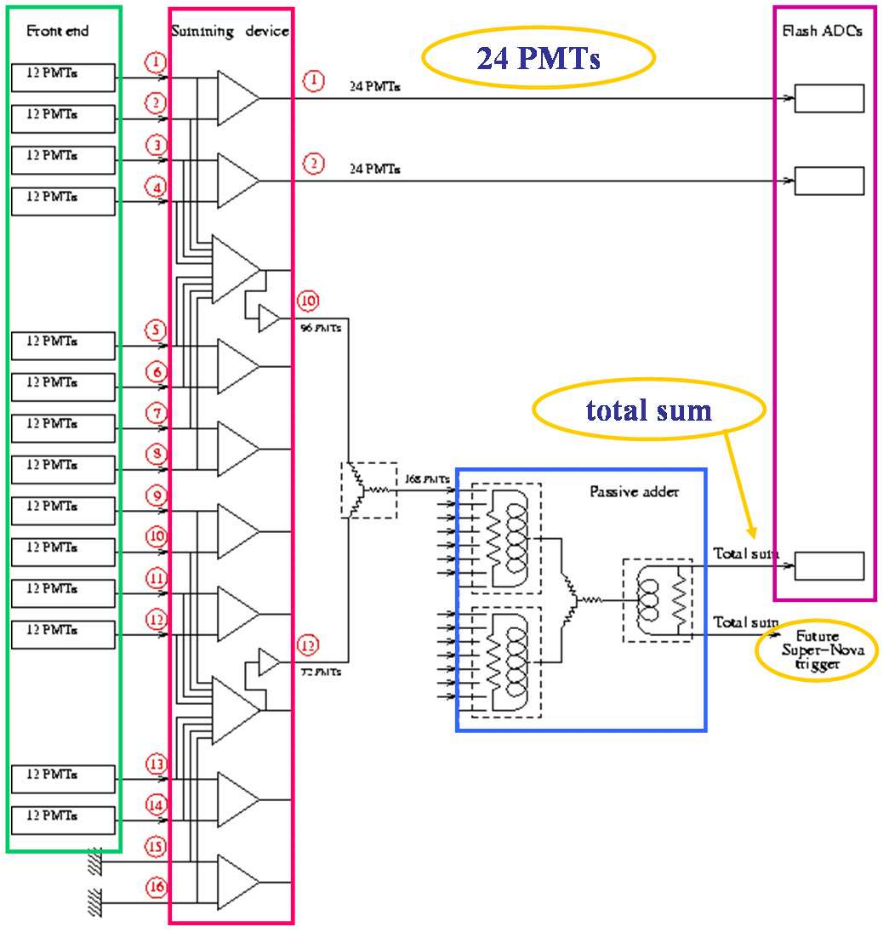

Figure 8.1: The layout of the sums system: the Front-End boards (in the green box), the summing devices (red box), the total sum circuit (blue box) and the fast waveform digitizers (purple box).

The total sum of the PMT signals from the whole detector is realized by a network of completely passive resistors, starting from the 8-channels sum output produced by the summing devices. The total sum circuit produces two outputs: the first one is acquired by the first channel of the fast waveform digitizers and is used by the trigger system; the second one is available either for attenuated total sum acquisition or for a future very-high-energy system acquiring only the total sum of all the PMTs signals[1].

[1]A system capable to register the full supernova neutrino spectrum, up to 50 MeV, would be suitable for Borexino needs: this very-high-energy system could be realized either acquiring an attenuated copy of the total sum signal, or with an intermediate summing stage, which could assemble in ~ 8 groups the output of the summing devices.

The complete layout of the system is displayed in figure 8.1, where the summing devices are highlighted in the red box, while the total sum circuit is shown in blue.

8.1.2 The Fast Waveform Digitizers

The used device was originally designed at Collège-de-France, then developed in collaboration with CAEN and produced by this company as *model V896*. It is a VME module housing 3 analog channels, with internal or external clock, a multi-event capability and zero dead time read-out, as long as the read-out sustains the trigger rate. The dynamic is 8-bit and the sampling period 2.5 ns.

The V896 is based on a 100 MHz 8$-$bit flash ADC with a 475 MHz analog bandwidth. Four such flash ADCs components, driven by four 100 MHz clocks, contribute to digitize each analog channel. These four clocks, with $\pi/2$ phase shifts, are internally generated from the common external 50 MHz clock. The four ADCs in each channel are designed to work in parallel, with time shifts of 2.5, 5 and 7.5 ns, since each of them is triggered by one of the four 100 MHz clocks: being the clocks $\pi/2$ shifted, the resulting time difference between subsequent samplings is 2.5 ns, so that the final sampling frequency is 400 MHz.

The waveform digitizers operate in stop mode; the four ADCs digitize continuously, writing into a circular buffer which is called "page". The storage capacity is 655.36 μs, divided into a configurable number of pages. In Borexino, they are configured as 64 pages of 10.24 μs: this long range could allow to accommodate to the latency of the main trigger (only the useful amount of data will actually be read).

On receipt of a trigger, the boards simply leave that page with all the data it contains and start writing to the next page. The written pages can be read anytime by a VME master. This VME master frees the pages if no longer needed, thus allowing the V896 to rewrite them (the principle of digitization and page switching is schematized in figure 8.2).

The V896 features a 16-bit TTL front panel input on its front panel (see figure 8.3). This pattern is sampled on trigger detection and logged for each page. In Borexino, the 16-bit event counter generated by the main trigger logic will serve as pattern input. These tags will be used by the event builder, to associate to each page the event number generated by the main trigger logic.

8.1.3 Read-out system layout

The system includes 34 digitizer modules with 3 input channels each, located in 4 VME crates; 33 boards account for the 99 analog signals and the last is used to record logical signals such as the trigger. The 4 VME crates are interconnected by a PVIC extension bus and read by a single VME master.

To allow accurate off-line usage of the wave forms, the time scales of all waveform digitizers must be identical. This is achieved by distributing a common 50 MHz

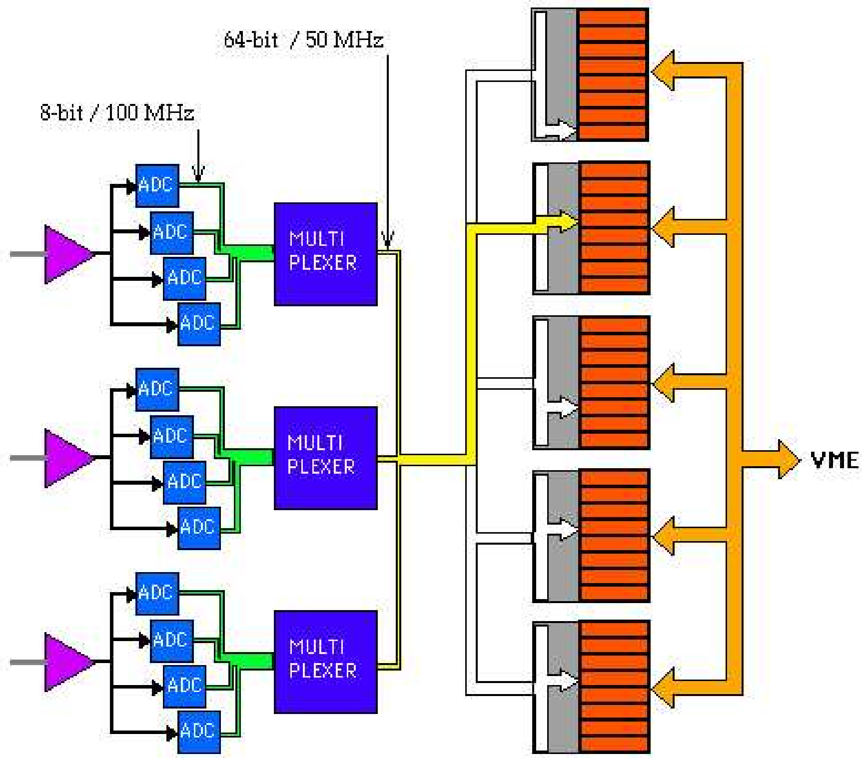

Figure 8.2: The principle of digitization and page switching of the V896 boards.

clock to all the 34 boards, so that the four 100 MHz clock of each board can be derived from this external clock. To provide in the same time the synchronization with Laben electronics, this 50 MHz clock is derived from the 20 MHz clock delivered by the Clock Generator of the main trigger system. A 100 ns period triangular wave in phase with the 20MHz clock is also acquired in one of the FADC channels, allowing the precise off-line alignment of the two systems.

The trigger signal issued by the main trigger logic is detected and synchronized with the 50 MHz clock by NIM logic and distributed to all the V896 modules: it provides the trigger signal to each board (the synchronization with the clock grants that all waveform digitizers detect the trigger on the same clock edge). The main trigger signal is also converted into a 100 ns triangular pulse and acquired in one of the FADC channels, to perform the off-line alignment of the two systems.

Summarizing all the above mentioned analog signals, in addition to the 98 PMT sums, 3 signals will be recorded by the Waveform Digitizers: the total sum on all the PMTs, which will provide a second level trigger (see below), a 100 ns period triangular wave in phase with the 20 MHz clock, a 100 ns triangular pulse in time with the main trigger. This leads to a total of 101 Waveform Digitizer channels, that is to say 34 boards.

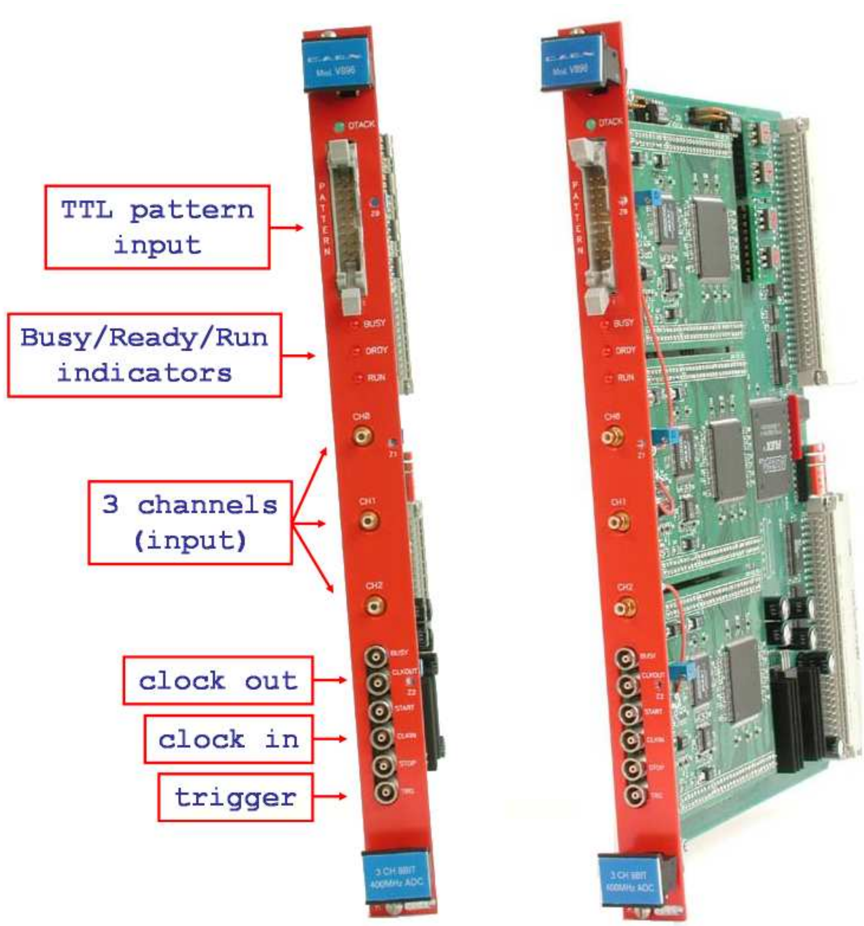

Figure 8.3: A picture of the V896 board, with the description of the input and output connectors on the front panel; in the lateral view, the three channels of the board are visible, as well as a portion of the motherboard.

As a security factor regarding heat evacuation, it has been decided to distribute the 34 boards into 4 VME crates (actually the board could fit in only 2 crates, but the fan layout suggested a sparse arrangement). These 4 crates are interconnected by a PVIC bus and read by a single VME master processor. This processor will follow the same protocol as the other VME masters of the Borexino read-out (see section 5.3) and transfer data via its Ethernet connection.

8.1.4 Online data processing

A second level of triggering, equivalent to an energy cut, is performed online by the acquisition process to reduce the huge amount of data. This second level trigger is done by analyzing the total sum signal and is composed of four steps (see figure 8.5):

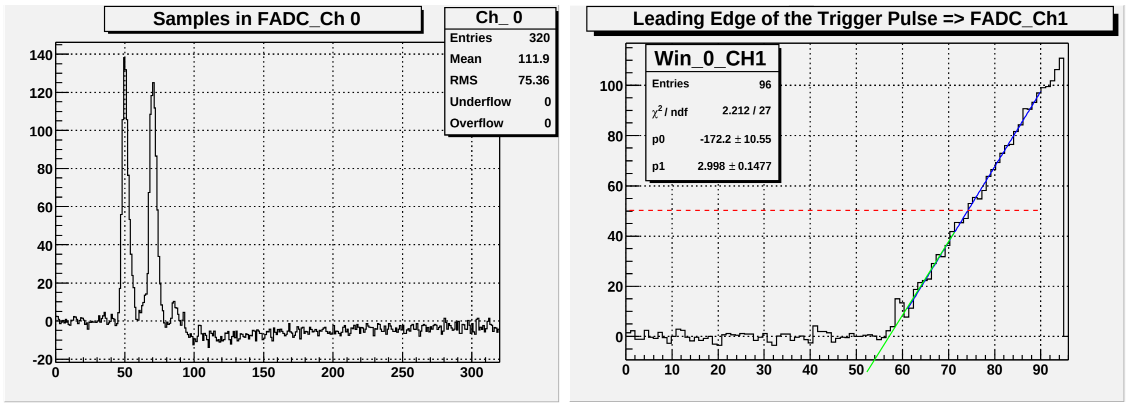

Figure 8.4: The total sum signal and the 100 ns triangular wave in phase with the trigger signal, as acquired during the AirRun7, for a double pulse laser event.

1. when the amplitude of the total sum signal exceeds a parameterizable threshold (THR_MIN), the event is marked to be read, and the on-line starts to compute the integral of the total sum signal, in the interval where its amplitude exceeds the THR_MIN value;

2. if the integrated total sum signal exceeds a second threshold (THR_WIN), a time "window" is created. We call "window" a portion of the FADC data, corresponding to a time interval selected inside the 10.24 μs of the page duration, which contains significant data. Outside the windows, only the electronics noise (and pedestal measurement) is present, which can be discarded: for this reason, after the windows creation, the portion of the data falling outside any window is rejected (this is actually a "zero suppression" procedure). This second step reduces the data by a factor around 20, since only the interesting parts of the total 10.24 μs interval are conserved;

3. the window integral is finally compared to a third threshold (THR_EVT), which is the real energy cut of the event: if the window energy exceeds this threshold, the event is marked as "valid" and the window interval is acquired;

4. otherwise, the on-line looks for other windows in coincidence with this one (before or after), within a parameterizable delay (TIMEOUT_READ): if two windows in coincidence are found, then the event is marked as "valid" and both windows are acquired; otherwise, the current window is

   discarded.

At the end of this process, only the relevant part of the data is read from the VME, formatted, and sent to the event builder.

The presence of a double threshold system (THR_WIN $\neq$ THR_EVT), is optimized for delayed coincidence studies and can be very useful for anti-neutrino physics

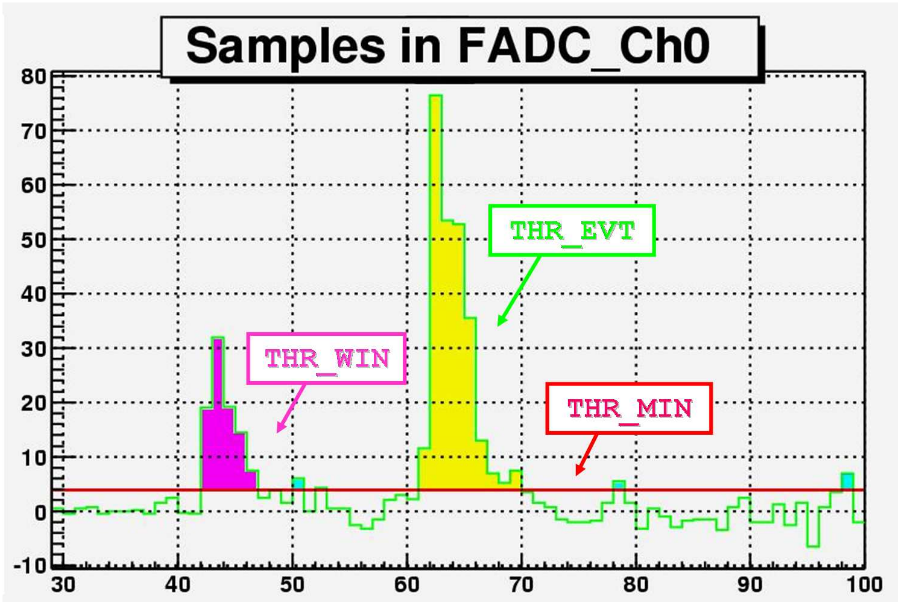

Figure 8.5: The three thresholds of the on-line data reduction algorithm for the FADCs: THR_MIN is an amplitude measurement, while THR_WIN and THR_EVT are charge measurements (with THR_WIN $\leq$ THR_EVT).

(see chapter 3). In this case, a suitable threshold condition would be: THR_WIN $\leq 1.02\ MeV \leq$ THR_EVT ($1.02\ MeV$ is the minimum energy of the e^+ signal) and TIMEOUT_READ $= 1\ ms$ (equivalent to $5\ \tau$ of the n capture).

In addition to the physical considerations, the four parameters of the algorithm (3 thresholds + 1 timeout) must be tuned in order to produce a sustainable FADC data flow: a detailed threshold study has been carried out during the last three Air-Runs, when the complete sums system was installed and operative (see below).

In the present configuration of the sums, the dynamics range was kept very low (see section 8.2.2), in order to allow better comparison with the Laben system. Thanks to this, it was possible to put a very low threshold on the single event (THR_EVT $\simeq 125\ keV$), so that all the interesting events in coincidence exceeded separately the threshold. For this reason, we temporarily set THR_WIN = THR_EVT and TIMEOUT_READ= $10\ \mu s$[2]: this choice is equivalent to disable the double threshold system, and allowed to speed-up the DAQ rate to an impressive value of $\sim 70\ Hz$[3].

[2]This timeout correspond to the duration of the FADC page.

[3]This number refers to a constant rate, as measured during a standard timing laser run.

8.2 Test of the sums system in Borexino Air-Runs

The installation of the FADCs started in 2002, and the integration of the DAQ in the main system was completed and optimized at the beginning of 2003. The sums system was tested for the first time in its final configuration during the AirRun7 (August 2003), with laser data only. A second test was performed in AirRun8 (December 2003), with the measurement of the ^{222}Rn radioactive source. Finally, laser data acquired in AirRun9 (August 2004), allowed an extensive test of the sums, including also a preliminary study of the dynamic range.

8.2.1 Laser data

The synchronous light pulses delivered from the PMT laser calibration system offer a very good tool to check the time alignment of the electronics: this is valid also for the sums system, since the relative synchronization of all the boards must be checked carefully. During AirRun7, many laser data were acquired, both in single and in double pulse configuration; double pulses were produced with different delays, in order to check the time reconstruction capabilities of the FADC system.

The results of these measurements are shown in figure 8.6 (in all the plots the $x-$scale is in 2.5 ns bins): the displayed pulse shape ("All channels samples") is the so-called "digital sum", that is to say a software sum obtained by summing up off-line the signals from all the single FADC channels (this signal differs from the analog total sum because of its wider dynamics range).

The first plot represents the single laser pulse (for 1 event): the time width of the pulse is $\sigma \sim 5$ ns, well consistent with the 4 ns measured by the Laben system (see section 7.3). The second and third plot show double pulses delayed respectively by 50 and 30 ns: the distances between the center of the two laser peaks reproduce correctly the time delays. In the last plot (bottom, right), a double pulse 600 ns delayed is visible: also in this case the time distance is correctly reproduced, even if the two pulses belong to two separate windows and the time delay is computed using the internal 50 MHz clock.

The very good result from these time measurement tests is crucial for the physics implications of the sums system utilization: for example, it could provide a key tool to separate the events in the fast ^{212}Bi –^{212}Po coincidence ($\tau_{Po} = 432.8$ ns). Furthermore, these good time reconstruction performances guarantee an appropriate behavior of the algorithm to define event windows; especially important is the result shown in figure 8.6 (bottom, right): since in this case the time difference (600 ns) is very close to the ^{212}Po mean-life, we can assume a good efficiency of the system in detecting the ^{212}Bi –^{212}Po coincidences on two separate windows (that is to say, to identify separately the two consecutive events).

Besides the time measurement studies, the laser data offered the possibility of a first comparison of the Laben and FADC performances. It was evaluated the linearity of the measured FADC total charge in each event, with respect to the

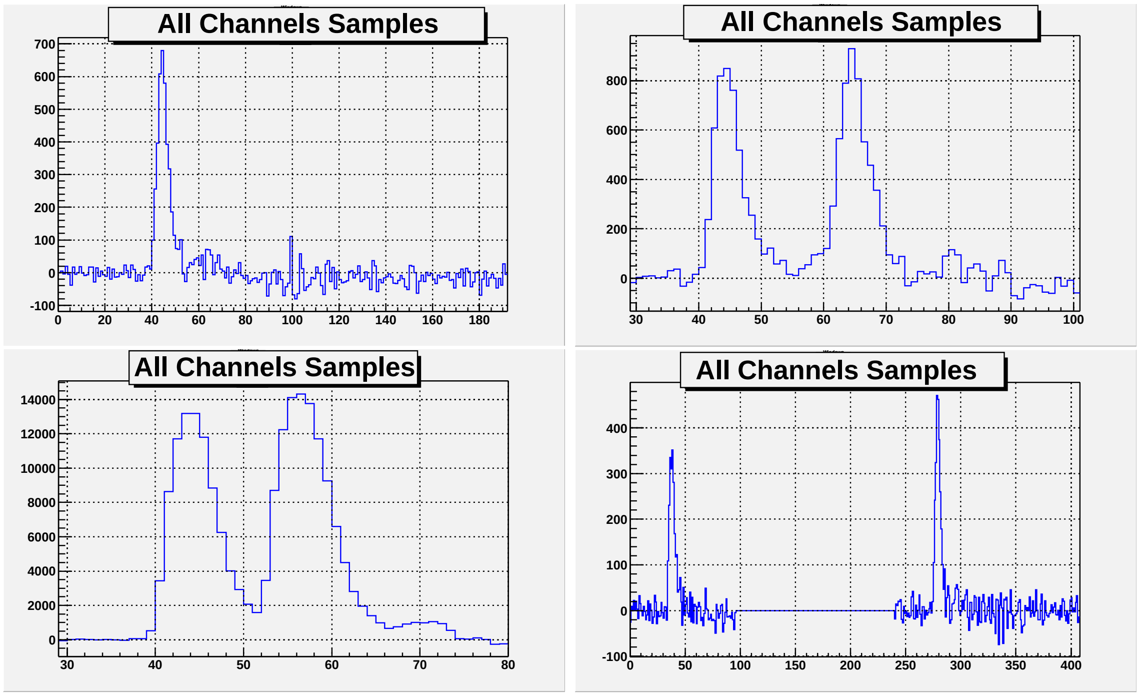

Figure 8.6: Laser data from single and double laser pulses, as acquired by the FADCs during the AirRun7. The displayed pulse is the "digital sum" and $x-$scale is in 2.5 ns bins (each plot represent a single event). From left to right and from top to bottom: a single pulse, a double pulse with $\Delta t = 50$ ns, a double pulse with $\Delta t = 30$ ns, a double pulse with $\Delta t = 600$ ns.

corresponding total charge measured by the Laben boards: this comparison was performed at different illumination levels for the PMTs, as allowed by our calibration system. A detailed analysis on this issue is still ongoing, but a preliminary result (obtained in the AirRun9) is shown in figure 8.7: the total charges, as measured in the two systems, appear rather aligned. Of course, this plot is not a conclusive result, but is nevertheless important, because it demonstrates the feasibility of an inter-calibration of the two systems, which will be crucial to guarantee the measured event energies to be the same in both electronics.

8.2.2 Dynamics study

The gain of the active adders is adjusted for to reach a mean amplitude of 5 ADC counts for 1 photo-electron. This would lead to a maximum of about 45 photo-electrons per channel if they were all synchronous, leading to a theoretical maximum of 11 MeV at the center of the detector and much less at the limit of the fiducial volume, considering a light yield of 400 $p.e./MeV$.

Actually, due to the dispersion in the emission time of the photons, the mean

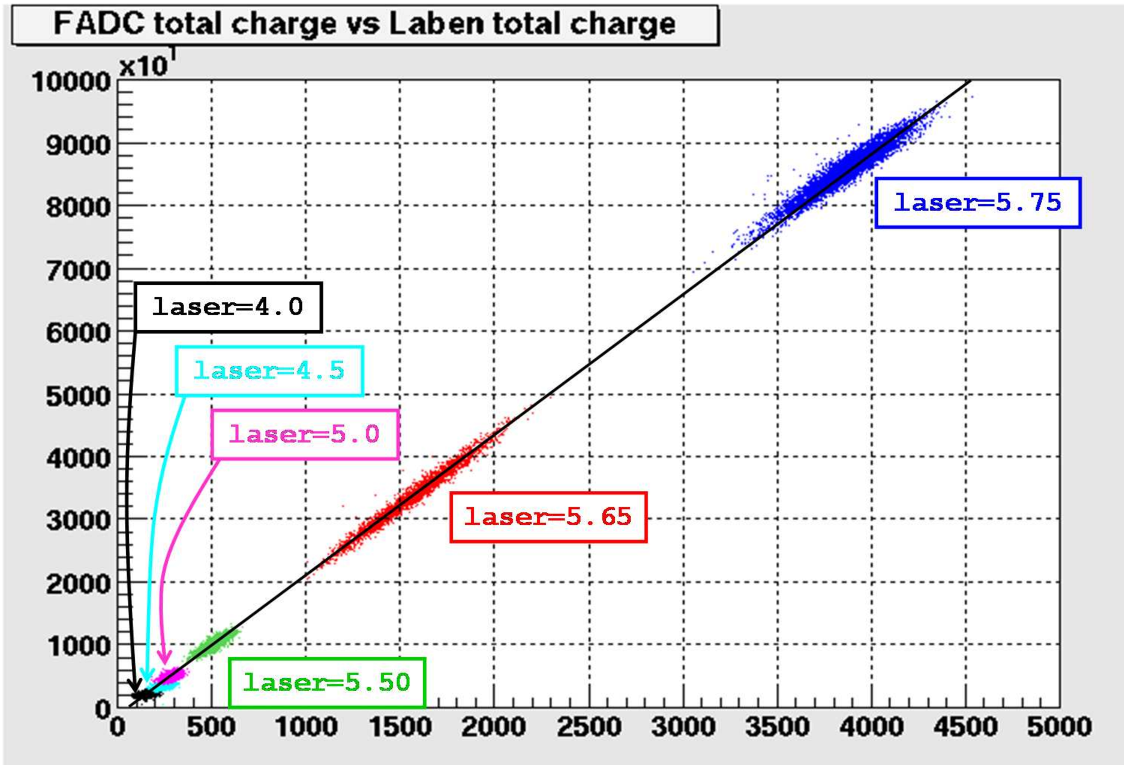

Figure 8.7: The total event charge detected by FADCs (in ADC units), versus the total event charge detected by Laben boards (in photoelectrons), for 6 different laser intensities, as measured during the AirRun9.

value of the energy loss due to saturation should reach about 1% at 10 MeV, for uniformly distributed events in the whole fiducial volume (this statement was demonstrated by means of a Monte-Carlo simulation). Since saturation occurs, by definition, with high amplitude signals which are not subject to large statistical fluctuations of their shape, the lost energy is recoverable by fitting the expected pulse shape on the unsaturated part of the signal.

In the following, it will be described the FADC saturation effect as measured by means of the laser calibration system (in different illumination conditions): as already explained, laser events simulate scintillation events occurring at the detector center, but with the substantial difference that in laser pulses all the photons are emitted synchronously, while in scintillation events the time spectrum has a $\sim 1\ \mu s$ duration (see figure 4.5): for this reason, these measurements on channel saturation cannot be extended to scintillation events and have to be considered as an "order of magnitude" estimation.

The amplitude spectra for all the FADC channels in laser events are shown in figure 8.8, as measured in two laser runs with intensities 5.65 (left) and 5.75 (right): in the first case, no saturation peak is present, while in the second case the saturated

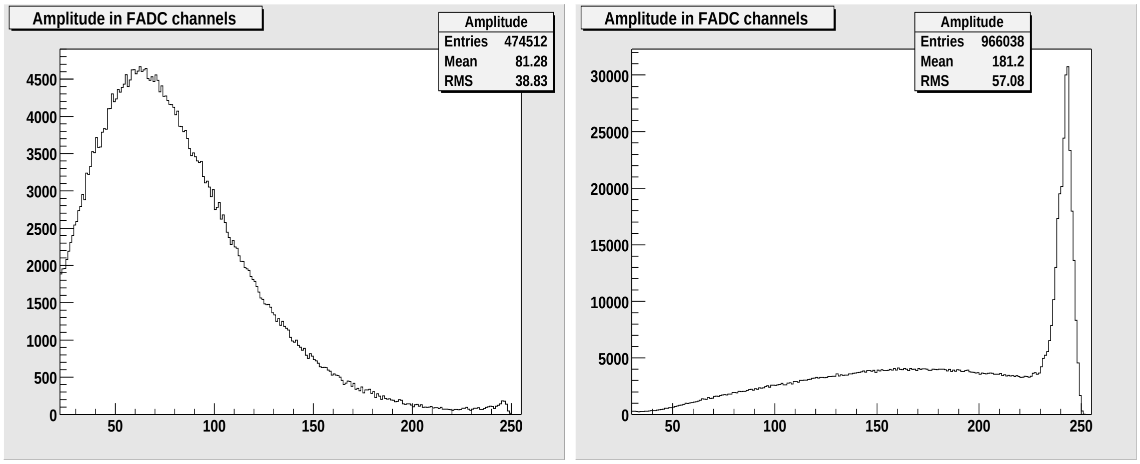

Figure 8.8: The charge spectra on all the FADC channels, summed over all the events in an entire run, with laser intensities 5.65 (left) and 5.75 (right).

peak accounts for $\sim 1/3$ of the total spectrum. A comparison of this result with the Laben data (see section 7.4), shows that the present performances of the sums system are quite unsatisfactory in the high energy range: the corresponding spectrum for laser intensity 5.75 showed only $< 4\%$ of saturated hits in Laben data (figure 7.20, left), while with FADCs the saturated fraction amounts to $\sim 1/3$.

Nevertheless, this issue is not a real problem in such an electronics system, because the gain of the summing devices can be lowered at will: in the final configuration of the system, the gain will be reduced by a factor 3. In this case, the saturation on the FADC channels would appear around the 25 MeV, allowing a full energy reconstruction (with very good resolution) of NC and CC events in case of a Supernova explosion. Moreover, thanks to the saturation recovery, the full Supernova neutrino spectrum up to 50 MeV (or at least a significant fraction of it) will be covered, even if with a worst resolution: in this way, the dynamics of the sums would be completely satisfactory to explore all the interesting physics range.

A test of the system with lowered gain conditions on the sums system is scheduled for the near future; on the other hand, the present dynamics conditions allowed to perform an extensive comparison of FADC and Laben electronics, since the two systems had a wide common range (see for example figure 8.7).

8.2.3 Radioactive source data

The ^{222}Rn source used during AirRun8 for the Borexino read-out test (see section 6.4), was measured also with the sums system.

The delayed coincidence analysis of ^{214}Bi –^{214}Po events has been repeated with FADC electronics, using the internal time informations of the system (namely, the 50 MHz clock) to determine the time difference between consecutive events; the

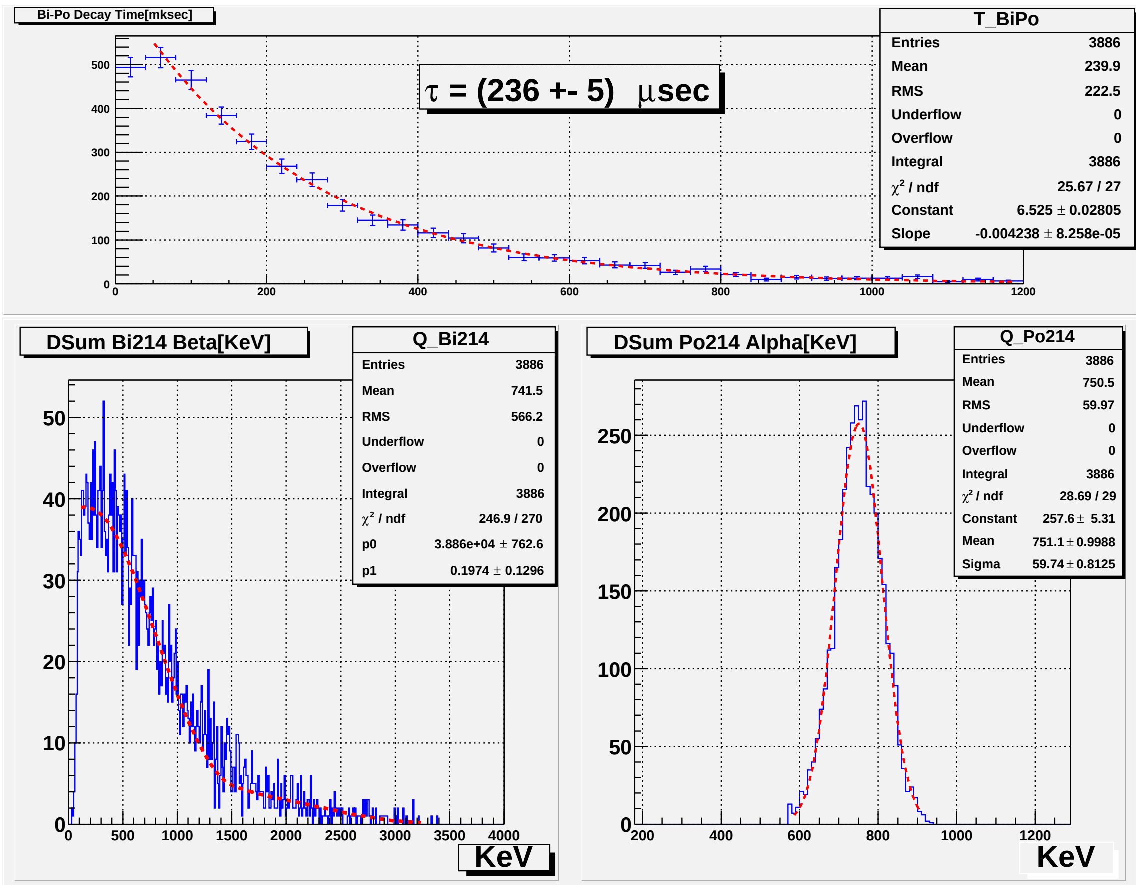

Figure 8.9: The ^{214}Bi $-^{214}Po$ coincidence events, as observed by the sums system during AirRun8: the time difference between consecutive events, consistent with ^{214}Po mean-life (top) and the energy spectra for ^{214}Bi (left) and ^{214}Po (right) events. Source was placed in the SSS center.

computed time differences are displayed in figure 8.9 (top): they are fitted with an exponential decay ($\tau = 236 \pm 5\ \mu s$), consistent with the ^{214}Po mean life ($236.6\ \mu s$).

Using the time difference information, the ^{214}Bi $-^{214}Po$ pairs have been selected (by means of a 5 τ cut on the ^{214}Po mean-life): in figure 8.9 (bottom) is shown the corresponding charge spectra (measured on the "digital sum") for ^{214}Bi and ^{214}Po events. ^{214}Po α peak (right) is fitted with a gaussian, centered exactly on 751 keV (the light yield of the source have been computed using the position of this peak). The ^{214}Bi $\beta + \gamma$ spectrum (figure 8.9, bottom, left) has been fitted with the main components of the theoretical spectrum, excluding γ contributions (γ energy is suppressed by the bad γ containment in the few cm^3 source volume).

The global energy spectrum of the source has also been studied, as shown in figure 8.10. In the plot, the source energy spectrum has been fitted with its main components: the three α peaks from ^{222}Rn, ^{218}Po and ^{214}Po (the first two peaks

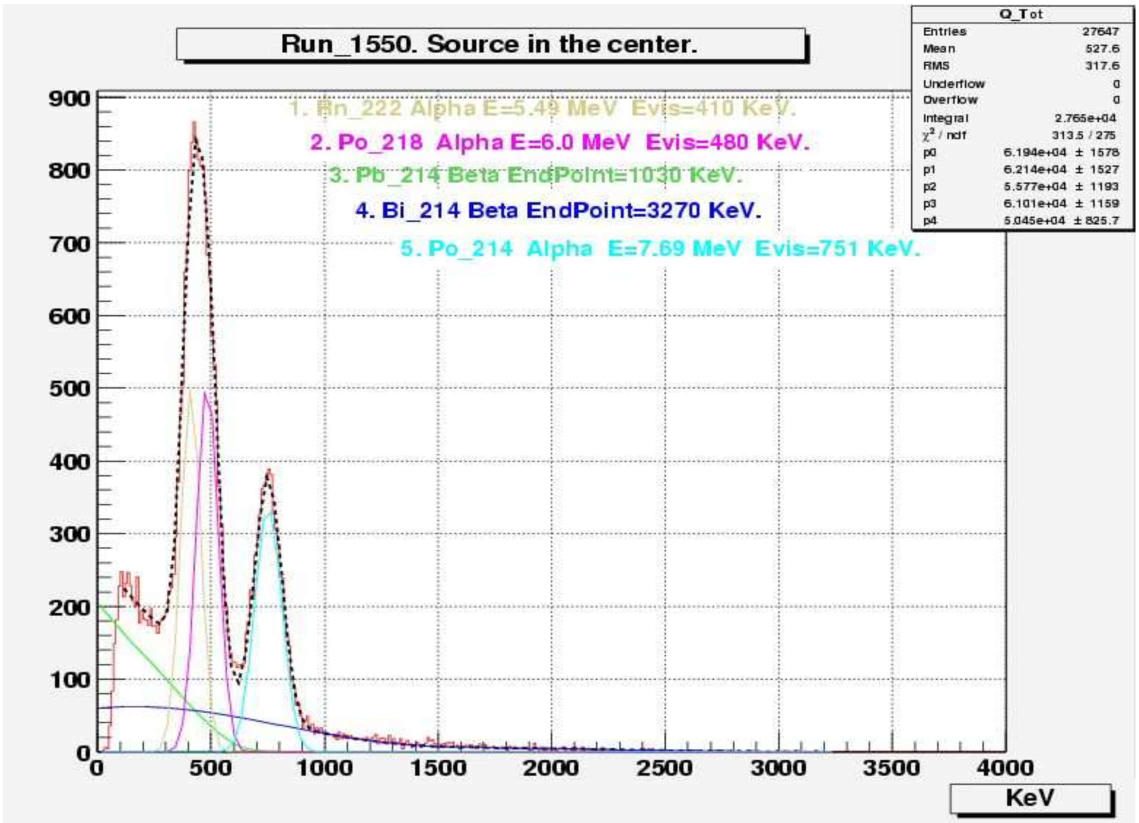

Figure 8.10: The global energy spectrum of the AirRun8 ^{222}Rn source, with the fit to its five components: ^{222}Rn, ^{218}Po, ^{214}Po, ^{214}Pb and ^{214}Bi. Source was placed in the SSS center.

are overlapping in a single peak) and the two β spectra from ^{214}Pb and ^{214}Bi (with suppressed γ components). In the spectral fit, the secular equilibrium constraint has not been imposed and the measured activities are consistent with the secular equilibrium hypothesis within 10%: this fact confirms that the secular equilibrium can always be assumed within the ^{222}Rn sub-chain.

These results with the source data are very important for the qualification of the sums system: as in the Laben case, the ^{214}Bi –^{214}Po coincidences allow to conclude that the event detection efficiency is satisfactory, while the energy spectra show, for the first time, the good energy reconstruction capabilities of this electronics.

8.3 Simulation of the sums system

In the framework of Borexino simulations, a package reproducing the behavior of the Front-End and Laben electronics has been written: this package reads as input the data produced by the general Borexino simulation codes[4] and transforms them into a real data structure, identical to the one produced by the DAQ system. Not only the basic performances of the electronics are reproduced by the simulation, but also all its known "non ideal" behaviors.

In order to compare correctly the results from FADC and Laben electronics, is very important to have a common simulation of the two electronics. The addition of the sums system to the general Borexino electronics simulation, is in principle a simple operation, because the package is based in an Object Oriented design and is written in C++: by definition, this technology guarantees a simple and safe integration of new functionalities in the code.

The main components of the sums electronics which need to be simulated are:

1. the summed signals, in groups of 16 or 24 PMTs (depending on the mapping), and also the total sum on 2212 PMTs;

2. the digitization procedure (i.e. the output of the FADC channels, including the noise on channel and the pedestal generation);

3. the behavior of the zero suppression algorithm;

4. other signals present in the system, such as the attenuated sum and the trigger ramp.

In the Borexino electronics simulation, a "channel" is an object (in the C++ sense) performing 3 main operations: it can receive a photoelectron; it triggers (when detector is triggered); it writes event on the file. The same implementation has been chosen for the "fadc_channel" object: each of the simulated FADC channels owns a list of the frontend hits produced in the associated PMTs (16,24,2214); this list represents the interface of the channel to the main detector object.

In the code logic, the operations requested to the FADC channels are performed in the following way:

1. receiving a photoelectron means that a new frontend hit is added to the internal list of frontend hits (of course, only photoelectrons produced in the associated PMTs can be received by a FADC channel);

2. when the channel is triggered, the frontend hit list is transformed into a digitized signal; this operation consists of five steps: hits are ordered in time; a simple shape is simulated for each hit; the shape of the single hit is divided into the 2.5 ns bins; hits are summed, to obtain total signal; for each bin, the total signal is converted into an integer number (from 1 to 255).

[4]Two simulation programs have been written for Borexino: a fast one, FORTRAN based, and a more complex one, based on the GEANT4 package from CERN.

3. the procedure for writing events to file reproduces the behavior of the zero suppression algorithm (for this reason, the total sum is processed first); to guarantee the most realistic result, this step is performed by a code identical to the one running in the FADC on-line program (it has just been "re-coded" in C++). The noise and pedestal informations are generated (for each of the four ADCs in the channel) only inside the windows (it would have been useless to generate noise in the preceding step in order to rejected it now[5]).

This simulation code has been written and is in its test phase: in particular, the parameters of the code, such as the gains, pedestals and noise are undergoing a fine regulation based on real data. When the project will be finished, it will provide a powerful tool for understanding the FADC data and for comparison with Laben results.

[5]A similar strategy has been chosen for the Laben section: the dark noise hits on each PMT are generated only inside the trigger gate.

Conclusions

In this thesis, the characterization and calibration of the Borexino detector have been performed, both for sub-MeV solar neutrino detection, and for detection of the high energy neutrinos emitted during Supernova events.

The CTF-3 measurement campaign (focussed on the assessment of the scintillator properties) is described: during this campaign, several purification methods have been tested on the scintillator and showed encouraging results. A detailed data analysis of the different purification tests is presented in this work, concerning the effectiveness of the methods in removing from the scintillator the most dangerous contaminants for Borexino.

The Borexino detector has been operated at the performance level demanded by physics and its overall capabilities have been carefully studied. The read-out system of the experiment has been completed, finalized and fully tested in realistic operation conditions; these tests happened during the 9 "Air-Runs": several run configurations were applied, allowing a global study of the system performances, as well as an accurate debugging on a single channel basis (both on the electronics and on the photomultipliers).

The PMT calibration system has been thoroughly tested, providing the assessment of the time measurement precision of the complete read-out system, along with an estimation of the final time resolution of the detector. Several runs have also been performed through the insertion of some radioactive sources in the Borexino sphere: these measurements represented a realistic test of our read-out system in operating conditions. In this way, the behavior of the complete chain was analyzed, showing very good global performances.

In particular, the energy and position reconstruction capabilities of the detector have been evaluated, demonstrating that the system is ready and operational for Borexino data taking: the good performances of the read-out chain will allow the neutrino signal identification in a wide energy range and the measurement of the ^7Be neutrino flux.

Appendix

The ^{238}U radioactive chain

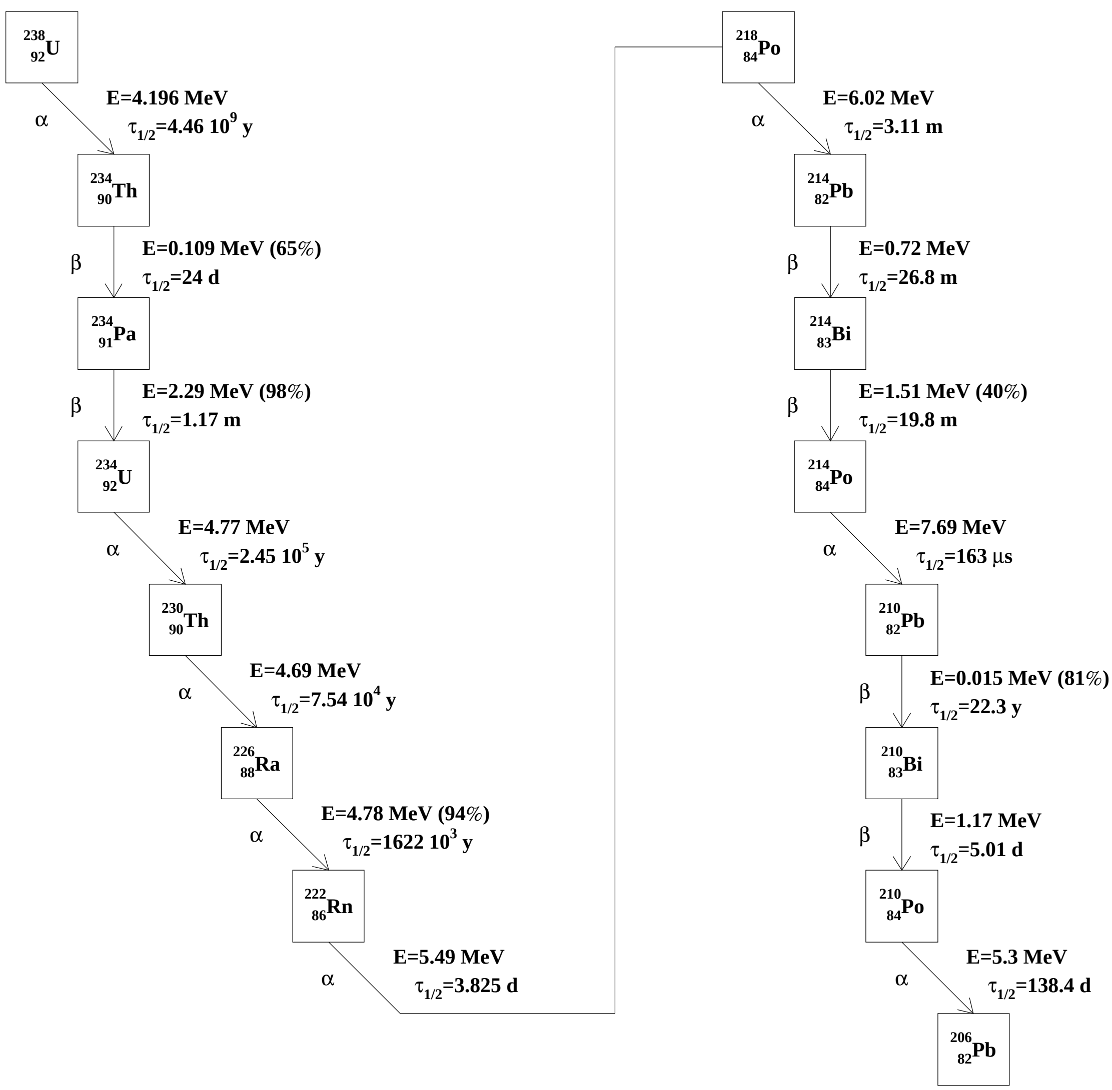

The ^{232}Th radioactive chain

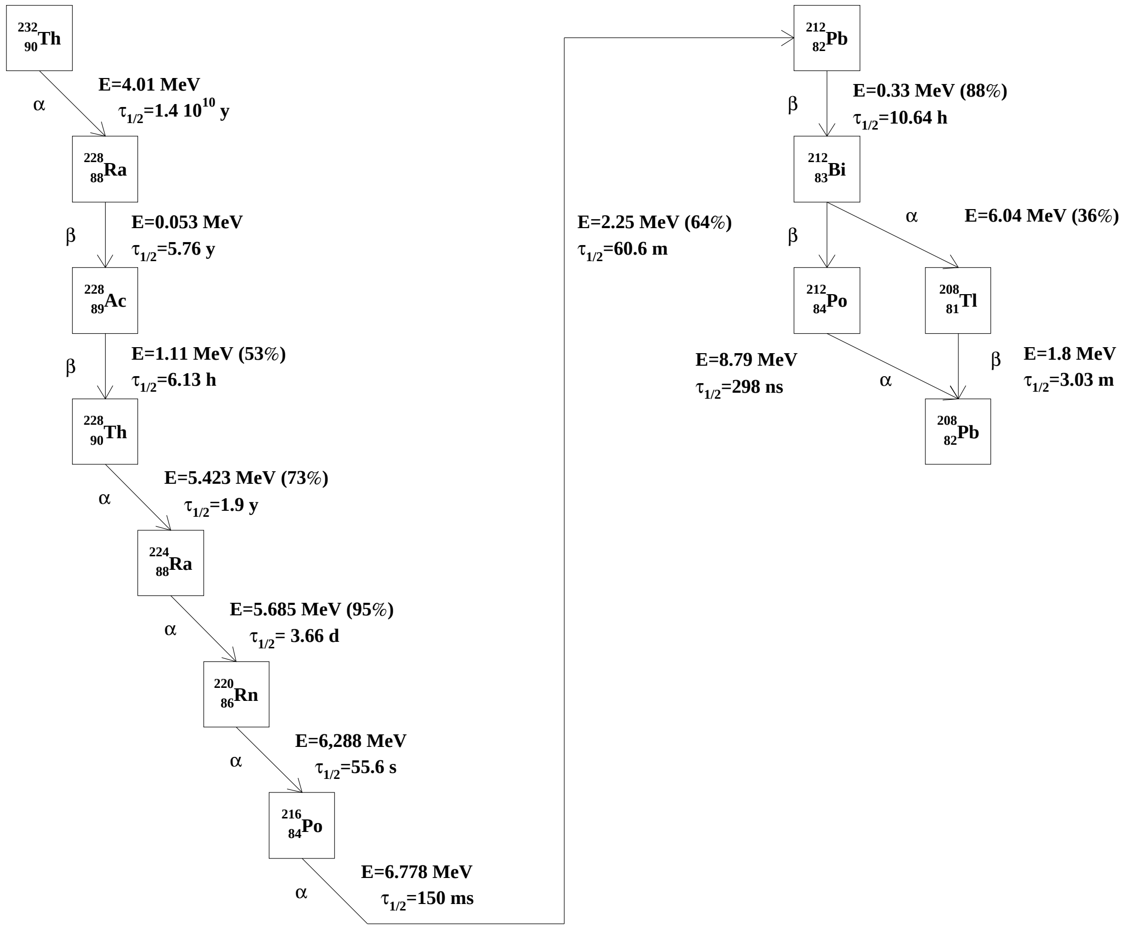

Bibliography

[1] J.N. Abdurashitov *et al.* [SAGE Collaboration], J. Exp. Theor. Phys. **95**, 181 (2002).

[2] Q.R. Ahmad *et al.* [SNO Collaboration], Phys. Rev. Lett. **87**, 071301 (2001).

[3] Q.R. Ahmad *et al.* [SNO Collaboration], Phys. Rev. Lett. **89**, 011301 (2002).

[4] S.N. Ahmed *et al.* [SNO Collaboration], Phys. Rev. Lett. **92**, 181301 (2004).

[5] G. Alimonti *et al.* [Borexino Collaboration], *A large-scale low background liquid scintillator detector: the counting test facility at Gran Sasso*, Nucl. Instrum. Meth. A **406**, 411 (1998).

[6] G. Alimonti *et al.* [Borexino Collaboration], *Light propagation in a large volume liquid scintillator*, Nucl. Instrum. Meth. A **440**, 360 (2000).

[7] G. Alimonti *et al.* [Borexino Collaboration], *Measurement of the C-14 abundance in a low-background liquid scintillator*, Phys. Lett. B **422**, 349 (1998).

[8] G. Alimonti *et al.* [Borexino Collaboration], *Science and technology of Borexino: A real time detector for low energy solar neutrinos*, Astropart. Phys. **16**, 205 (2002).

[9] G. Alimonti *et al.* [Borexino Collaboration], *Ultra-low background measurements in a large volume underground detector*, Astropart. Phys. **8**, 141 (1998).

[10] C. Arpesella *et al.* [BOREXINO Collaboration], *Measurements of extremely low radioactivity levels in BOREXINO*, Astropart. Phys. **18**, 1 (2002).

[11] M. Apollonio *et al.* [CHOOZ Collaboration], Phys. Lett. B **420**, 397 (1998).

[12] M. Apollonio *et al.* [CHOOZ Collaboration], Phys. Lett. B **466**, 415 (1999).

[13] T. Araki *et al.* [KamLAND Collaboration], arXiv:hep-ex/0406035 (2004).

[14] K. Assamagan *et al.*, Phys. Rev. D **53**, 6065 (1996).

[15] H.O. Back *et al.* [Borexino Collaboration], *New limits on nucleon decays into invisible channels with the BOREXINO Counting Test Facility* Phys. Lett. B **563**, 23 (2003).

[16] H.O. Back *et al.* [Borexino Collaboration], *Phenylxylylethane (PXE): A high-density, high-flashpoint organic liquid scintillator for applications in low-energy particle and astrophysics experiments*, arXiv:physics/0408032.

[17] H.O. Back *et al.* [Borexino Collaboration], *Study of the neutrino electromagnetic properties with prototype of Borexino detector*, Phys. Lett. B **563**, 35 (2003).

[18] J.N. Bahcall, Astrophys. J. **467** 475 (1996).

[19] J.N. Bahcall, Nucl. Phys. B (Proc. Suppl.) **118**, 77 (2003).

[20] J.N. Bahcall, M.C. Gonzalez-Garcia, C. Peña-Garay, JHEP **0207**, 054 (2002).

[21] J.N. Bahcall, M.C. Gonzalez-Garcia, C. Peña-Garay, Phys. Rev. Lett. **90**, 131301 (2003).

[22] J.N. Bahcall, P.I. Krastev, A.Y. Smirnov, JHEP **0105**, 015 (2001).

[23] J.N. Bahcall, M.H. Pinsonneault, Phys. Rew. Lett. **92**, 121301 (2004).

[24] J.N. Bahcall, M.H. Pinsonneault, S.Basu, Astrophys. J. **555**, 990 (2001).

[25] R. Barate *et al.* [ALEPH Collaboration], Eur. Phys. J. C **2**, 395 (1998).

[26] J.F. Beacom, W.M. Farr, P. Vogel, Phys. Rev. D **66**, 033001 (2002).

[27] J.F. Beacom, P. Vogel, Phys. Rev. D **58**, 093012 (1998).

[28] J.F. Beacom, P. Vogel, Phys. Rev. D **58**, 053010 (1998).

[29] R.M. Bionta *et al.*, Phys. Rev. Lett. **58**, 1494 (1987).

[30] F. Boehm *et al.*, Phys. Rev. D **64**, 112001 (2001).

[31] J. Boger *et al.* [SNO Collaboration], Nucl. Instrum. Meth. A **449**, 172 (2000).

[32] J. Bonn *et al.*, Nucl. Phys. Proc. Suppl. **91**, 273 (2001).

[33] B. Caccianiga *et al.*, *A multiplexed optical-fiber system for the PMT calibration of the Borexino experiment*, Nucl. Instrum. Meth. A **496**, 353 (2003).

[34] L. Cadonati, *The Borexino Solar Neutrino Experiment and its Scintillator Containment Vessel*, Ph. D. Thesis, Princeton University (2001), UMI-99-93687.

[35] L. Cadonati, F.P. Calaprice, M.C. Chen, *Supernova neutrino detection in Borexino*, Astropart. Phys. **16**, 361 (2002).

[36] C. Cattadori, talk given at *Neutrino 2004* conference, 14-19 June 2004, Paris.

[37] M. Chen *et al.*, Nucl. Instrum. Meth. A **420**, 189 (1999).

[38] B.T. Cleveland *et al.*, Astrophys. J. **496**, 505 (1998).

[39] R.J. Davis, D.S. Harmer, K.C. Hoffman, Phys. Rev. Lett. **20**, 1205 (1968).

[40] K. Eguchi *et al.* [KamLAND Collaboration], Phys. Rev. Lett. **90**, 021802 (2003).

[41] K. Eguchi *et al.* [KamLAND Collaboration], Phys. Rev. Lett. **92**, 071301 (2004).

[42] S. Eidelman *et al.* [Particle Data Group Collaboration], Phys. Lett. B **592**, 1 (2004).

[43] K. Eitel, eConf **C020620** SAAT03, arXiv:hep-ex/0209019 (2002).

[44] B. Faid *et al.*, Astropart. Phys. **10**, 93 (1999).

[45] G.L. Fogli *et al.*, Phys. Rev. D **66**, 093008 (2002).

[46] D. Franco, *The Borexino Experiment: Test of the Purification Systems by the Counting Test Facility*, Ph. D. Thesis, Università degli Studi di Milano (2005).

[47] Y. Fukuda *et al.* [Kamiokande Collaboration], Phys. Rev. Lett. **77**, 1683 (1996).

[48] Y. Fukuda *et al.* [Super-Kamiokande Collaboration], Phys. Lett. B **436**, 33 (1998).

[49] Y. Fukuda *et al.* [Super-Kamiokande Collaboration], Phys. Rev. Lett. **81**, 1562 (1998).

[50] Y. Fukuda *et al.* [Super-Kamiokande Collaboration], Phys. Rev. Lett. **82**, 2644 (1999).

[51] S. Fukuda *et al.* [Super-Kamiokande Collaboration], Phys. Rev. Lett. **86**, 5651 (2001).

[52] E. Gatti and F. De Martini, *A new linear method of discrimination between elementary particles in scintillation counters*, IAEA Wien, pp.265-276 (1962).

[53] F. Gatti *et al.*, Nucl. Instrum. Meth. A **461**, 474 (2001).

[54] F. Gatti *et al.* [BOREXINO Collaboration], Nucl. Phys. Proc. Suppl. **78**, 111 (1999).

[55] G. Gelmini, E. Roulet, Rept. Prog. Phys, **58** 1207 (1995).

[56] A. Goretti, P. Lombardi and G. Ranucci, *Pulse Shape Discrimination of liquid scintillators*, Nucl. Instr. Meth. A, **412**, 374 (1998).

[57] T. Hagner *et al.*, Astropart. Phys. **14**, 33 (2000).

[58] W. Hampel *et al.* [GALLEX Collaboration], Phys. Lett. B **447**, 127 (1999).

[59] W. Hampel *et al.* [GALLEX Collaboration], Phys. Lett. B **420**, 114 (1998).

[60] G. Heusser *et al.*, Appl. Rad. Isot. **52**, 691 (2000).

[61] K. Hirata *et al.* [KAMIOKANDE-II Collaboration], Phys. Rev. Lett. **58**, 1490 (1987).

[62] K. Ishihara, Nucl. Instrum. Meth. A **503**, 144 (2003).

[63] T. Ishii [K2K Collaboration], arXiv:hep-ex/0406055.

[64] M. Ishitsuka *et al.* [Super-Kamiokande Collaboration], hep-ex/0406076 (2004).

[65] H.V. Klapdor-Kleingrothaus *et al.*, Mod. Phys. Lett. A **16**, 2409 (2001).

[66] V. Lagomarsino and G. Testera, Nucl. Instrum. Meth. A **430**, 435 (1999).

[67] V.M. Lobashev *et al.*, Nucl. Phys. Proc. Suppl. **91**, 280 (2001).

[68] F. Mantovani *et al.*, Phys. Rev. D **69**, 013001 (2004).

[69] D. Manuzio, *Towards the detection of subMeV solar neutrinos in Borexino: data reconstruction and analysys tools*, Ph. D. Thesis, Università degli Studi di Genova (2004).

[70] S.P. Mikheev, A.Y. Smirnov, Sov. J. Nucl. Phys. **42**, 913 (1985).

[71] M.E. Monzani, *Metodi di identificazione delle particelle α/β in grandi volumi di scintillatore liquido, per la reiezione del fondo radioattivo nell'esperimento Borexino*, Tesi di Laurea, Università degli Studi di Milano (2001).

[72] R. D. Peccei, AIP Conf. Proc. **490**, 80 (1999).

[73] A.P. Pocar, *Low background techniques and experimental challenges for Borexino and its nylon vessels*, Ph. D. Thesis, Princeton University (2003), UMI-31-03047.

[74] B. Pontecorvo, Sov. Phys. JETP **26**, 984 (1968).

[75] R.S. Raghavan *et al.*, Phys. Rev. Lett. **80**, 635 (1998).

[76] G. Ranucci *et al.*, *A sampling board optimized for pulse shape discrimination in liquid scintillator applications*, Ieee Trans. Nucl. Sci. **51**, 1784 (2004).

[77] G. Ranucci *et al*, *Scintillation decay time and pulse shape discrimination of binary organic liquid scintillators for the Borexino detector*, Nucl. Instr. Meth. A, **350**, 338 (1994).

[78] W. Rau, G. Heusser, Appl. Rad. Isot. **53**, 371 (2000).

[79] The Royal Swedish Academy of Sciences, *Press Release: The 2002 Nobel Prize in Physics* (2002).

[80] R. Saakian [MINOS Collaboration], Phys. Atom. Nucl. **67**, 1084 (2004).

[81] D.N. Schramm, Comments Nucl. Part. Phys. **17**, 239 (1987).

[82] M. Schwarzschild, *Structure and Evolution of the Stars*, Princeton University Press, 1958.

[83] D.N. Spergel *et al.* [WMAP Collaboration], Astrophys. J. Suppl. **148**, 175 (2003).

[84] G. ‘t Hooft, Phys. Lett. B **37**, 195 (1971).

[85] S. Turck-Chieze and I. Lopes, Astrophys. J. **408**, 347 (1993).

[86] S. Turck-Chieze *et al.*, Phys. Rev. Lett. **93**, 211102 (2004).

[87] L. Wolfenstein, Phys. Rev. D **17**, 2369 (1978).